University of Valencia
Department of Applied Physics and Electromagnetism

Optical, Structural and Electrical Characterization of GaN/AlN Nanostructures: Quantum Wells, Quantum Dots and Nanowires

Thesis elaborated by

Rafael Mata Sanz

under the supervision of

Professor Dr. Ana Cros Stötter

to obtain the Phylosofical Doctor degree in Physics

VNIVERSITAT DE VALÈNCIA

Valencia (Spain)
2011

UNIVERSITAT DE VALÈNCIA
BCA. DE CIÈNCIES EDUARD BOSCÀ
DATA: 29-9-2011
SIGNATURA: TD-F 649
Nº ITEM: 122531531
25cm

UMI Number: U607769

All rights reserved

INFORMATION TO ALL USERS
The quality of this reproduction is dependent upon the quality of the copy submitted.

In the unlikely event that the author did not send a complete manuscript
and there are missing pages, these will be noted. Also, if material had to be removed,
a note will indicate the deletion.

UMI U607769
Published by ProQuest LLC 2014. Copyright in the Dissertation held by the Author.
Microform Edition © ProQuest LLC.
All rights reserved. This work is protected against
unauthorized copying under Title 17, United States Code.

ProQuest LLC
789 East Eisenhower Parkway
P.O. Box 1346
Ann Arbor, MI 48106-1346

To my Family

Los que aseguran que es imposible
no deberían interrumpir a los que
estamos intentándolo.

Thomas Alva Edison

Agradecimientos

Quiero resaltar antes de nada, que todo el mundo que ha estado cerca de mí durante el periodo de la elaboración de esta Tesis me ha aportado, de una forma u otra, una ayuda indispensable para la realización de este trabajo. Sin embargo, si esta inmensa lista de personas tiene que empezar con un nombre ese tiene que ser el de Ana Cros Stötter, mi Directora de Tesis.

Antes de empezar con este proyecto, había oído de distintas fuentes que el desarrollo de una tesis doctoral se podía convertir en los cuatro peores años de tu vida, o por el contrario en los cuatro mejores, dependiendo principalmente de tu director de tesis. Basándome en mi experiencia, ahora puedo decir que he vivido los cuatro mejor años que he tenido a lo largo de mi vida. Además del desarrollo intelectual que me ha aportado, he sentido a nivel personal una gran satisfactión al trabajar junto a mi Directora. En gran parte de las ocasiones no hemos compartido las mismas ideas; sin embargo, tengo que destacar la gran capacidad de que dispone para escuchar, y en cosecuencia para convencer o ser convencida. Duras han sido las discusiones que hemos tenido durante estos cuatro años, pero a la vez fructíferas. Creo que el ímpetu y desenfreno que tengo por llevar a cabo mis ideas ha sido equilibrado por la paciencia y cautela de mi Directora. El haber trabajado durante estos años en el mejor punto de equilibrio que pudiéramos haber encontrado me ha hecho sentir que he aprendido de una de las mejores personas y espectroscopistas Raman del mundo. Gracias Ana.

En el siguiente lugar tengo que recordar a un excompañero que no llegó a terminar su tesis doctoral. Juan Fresneda tiene la culpa de que haya invertido cuatro años de mi vida en realizar este trabajo, ya que él fue quien me advirtio de esta vacante y quien gestionó los trámites administrativos cuando yo aún me encontraba en Alemania buscando trabajo posteriormente a mi licenciatura. Gracias también a todos los componentes del Grupo de Espectroscopía de Sólidos de la Unversidad de Valencia, liderado por el Profesor Andrés Cantarero Sáez. Gracias tanto a los profesores titulares, postdocs, estudiantes de doctorado y técnicos de laboratorio que han estado entre los años 2007 y 2011. Además, quiero mencionar la increible

relación que he tenido con compañeros de otros grupos de investigación ubicados en el Instituto de Ciencias de Materiales de la Universidad de Valencia, así como, con el Profesor Juan P. Martínez Pastor, con Juan Francisco Sánchez Royo y con compañeros como Josep Canet Ferrer y Jesús Álvarez Álvarez. A los cuales, en parte les tengo que agradecer la ayuda prestada para la realización de partes de esta Tesis. Gracias a todos.

Sobrepasando las fronteras, es de recibo mencionar y agradecer el tiempo invertido en enseñarme durante mis estancias en el extranjero: a todo el Grupo de Espectroscopía de la Universidad de Florencia dirigido por la Dra. Ana Vinattieri por haberme enseñado fotoluminiscencia resuelta en tiempo, a la Dra. Rachel Oliver de la Universidad de Cambridge y a todo su grupo por haber invertido su tiempo enseñándome a manejar el microscopio de barrido electrónico y el microscopio de fuerza atómica conductivo, a todo el departamento de microestructuras del CEA en Grenoble dirigido por el Dr. Bruno Daudin por haberme enseñado a crecer mediante epitaxia de haces moleculares y por haberme hecho pasar durante un invierno en Francia una de mis mejores estancias en el extranjero y, finalmente, tengo que agradecer a la Dr. Maria do Rosario por haberme enseñado la técnica de caracterización infrarrojo en la Universidad de Aveiro en Portugal. Gracias a todos.

Logotipos de las Universidades, Instituciones o Grupos de investigación que me han otorgado el placer de realizar una estancia o una colaboración junto a ellos. Gracias a todos.

Finalmente, tengo que apuntar a las personas que no se ven pero que siempre están ahí, a mi Familia. Desde los primeros años en la Universidad, ellos han estado ahí, apoyándome y aguantando mis cambios de humor, que no han sido pocos ni suaves. Respetando mis decisiones aunque no estuvieran de acuerdo, como cuando decidí realizar mis últimos años de carrera en el extranjero. Aquellos fueron tiempos duros, en Alemania, yendo a estudiar con un metro de nieve, haciéndose de noche a las cuatro de la tarde y con el dinero justo para subsistir. Y aún en la distancia, ellos estuvieron ahí. Aún a pesar de los malos años pasados en el extranjero, esos años han servido para realizar experiencias tan gratificantes como este trabajo de investigación que, finalmente, hacen que sonría al pensar en todos aquellos malos momentos pasados. Esos periodos de tiempo, no hubira sido posible superarlos sin el apoyo de mi Familia. Por eso y por lo que me dan cada día, quiero darles las gracias y dedicarles esta tesis doctoral, la primera y espero que no la última, realizada por un miembro de mi Familia. Gracias Familia.

Contents

Introduction xvii

Publications xxi

Definitions and Notations xxiii

1 Fundamental properties of group III-nitride semiconductors and Metal-Semiconductor contacts 1

1.1 Crystal structure 1

1.1.1 The wurtzite crystal structure 2

1.1.2 Internal polarization in Wurtzite structure 4

1.1.3 Strain in epitaxial films grown along different directions . . . 7

1.2 Electronic properties 9

1.2.1 Bulk GaN band structure 10

1.2.2 Effect of strain on the electronic band structure 13

1.3 Vibrational properties 14

1.3.1 Phonon modes 14

1.3.2 Strain effect on the phonon modes 16

1.3.3 Doping and phonon-plasmon coupled modes 17

1.4 The internal electric field in heterostructures 19

1.4.1 Quantum confined Stark effect 20

1.5 Metal-Semiconductor contact 22

1.5.1 The formation of a barrier 22

1.5.2 Current transport processes 25

1.5.3 Ohmic contact 27

2 Growth and characterization techniques 31
2.1 Plasma Assisted Molecular Beam Epitaxy 31
2.1.1 Principle of Molecular Beam Epitaxy 32
2.1.2 Experimental equipment 35
2.2 Scanning electron microscopy 37
2.2.1 Principles of scanning electron microscopy 38
2.2.2 Imaging the topography 39
2.3 Photoluminescence 40
2.3.1 Optical properties of bulk GaN 47
2.3.2 Time Integrated Photoluminescence setup 49
2.3.3 Time Resolved Photoluminescence setup 50
2.4 Micro Raman Scattering 53
2.4.1 Microscopic theory of inelastic light scattering by phonons . 54
2.4.2 Micro Raman Scattering setup 60
2.5 Atomic Force Microscopy 61
2.5.1 Fundamentals of Atomic force microscopy 61
2.5.2 Surface topography measurements 64
2.5.3 Conductive measurements 67

3 Characterization of non-polar GaN/AlN heterostructures 71
3.1 Non-polar heterostructures 71
3.2 Characterization of *a*-plane GaN/AlN quantum wells 72
3.2.1 Description of the samples 73
3.2.2 Structural characterization 74
3.2.3 Polarized photoluminescence emission 81
3.2.4 Theoretical description and interpretation 84
3.3 Characterization of *a*-plane GaN/AlN quantum dots 88
3.3.1 Description of the samples 88
3.3.2 Morphological characterization 89
3.3.3 Structural characterization 91
3.3.4 Polarized photoluminescence characterization 93
3.3.5 Theoretical description and interpretation 97

4 Growth and morphology of GaN nanowires 103
4.1 GaN nanowires in nanoscience 103
4.2 Growth conditions of GaN nanowires by PA-MBE 105
4.2.1 Effective temperature and its related NWr density 108
4.2.2 Growth of GaN nanowires using an AlN buffer layer 111
4.2.3 Growth of GaN nanowires directly on Si(111) 113
4.3 Nucleation and morphology of GaN NWrs grown directly on Si(111) 115

5 Vibrational and optical characterization of GaN nanowires 125
5.1 Vibrational properties of GaN nanowires 125
5.1.1 Surface optical modes 128
5.2 PL emission properties of GaN nanowires 129
5.2.1 Temperature dependence 133
5.2.2 Polarization of the emission 137
5.2.3 Power dependence study 140
5.3 Effect of density on the optical properties GaN nanowires 142
5.3.1 Sample description and Raman Scattering 142
5.3.2 Surface optical phonon modes as a function of NWrs density 145
5.3.3 PL analysis and discussion 146

6 GaN/AlN heterostructures grown in GaN nanowires 153
6.1 Nanowires based heterostructures 153
6.2 GaN/AlN quantum disks: axial heterostructures 155
6.2.1 Description of the samples 155
6.2.2 Structural analysis and Raman experiments 155
6.2.3 PL emission from GaN/AlN axial insertions 159
6.2.4 Theoretical support and discussion 160
6.3 Core/shell GaN/AlN NWrs heterostructures: Their properties as a function of shell thickness 162
6.3.1 Description of the samples 162
6.3.2 Morphological analysis and Raman measurements 163
6.3.3 PL emission characteristics 165
6.3.4 Theoretical modeling and discussion 167
6.4 Core/shell GaN/AlN NWrs heterostructures as a function of density 172
6.4.1 Raman scattering analysis 173
6.4.2 PL characterization 175
6.4.3 HRTEM analysis and discussion 179

7 Silicon doped GaN nanowires 185
7.1 Growth parameters and description of the samples 185
7.2 Morphological and structural properties 186
7.3 Carrier recombination 190
7.4 Electrical properties 192

Conclusions 203

Resumen en español 207

Bibliography 229

Curriculum Vitae in Science 247

Introduction

Since almost twenty years, the III-Nitride semiconductors have experienced a strong development, both in material quality and commercial applications. These III-V compounds are formed by Al, Ga and In as group-III elements and Nitrogen as the group-V component. The semiconductors of this material system present a direct band gap that can be tuned from 0.63 eV for InN to 3.5 eV for GaN and 6.3 eV for the AlN [1]. Therefore, by the formation of the ternary alloys of these materials it is possible to cover the electromagnetic spectrum from the infrared to the ultraviolet wavelength, as can be observed schematically in Figure 7.10. Moreover, these materials present excellent mechanical and thermal properties. The technological applications involving III-N semiconductors have largely extended those praised by the development of the light emitting diode (LED) technology, discovered by Oleg Losev in 1920 [2]. The new generation of electronic devices requires faster response, needs to support higher powers and temperatures and manage large capabilities. The properties of group III-Nitride semiconductors can overcome these necessities, and make them perfect candidates for the construction of new optoelectronic devices. Actually, a huge amount of devices have been already made and commercialized, such as: high electron mobility transistors, green, blue and ultraviolet laser diodes or solar cells. The nowadays common illumination systems based on high power LEDs such as traffic lights and the replacement of the incandescent light bulbs by white LEDs are based on GaN LEDs. In addition, there is an increasing interest in the development of ultraviolet (UV) detectors, which could be based on GaN, AlN and their heterostructures. The group III-Nitride semiconductor family crystalizes in different structures, but the most stable is the wurtzite phase, which has its optical axis along the c direction. Its inherent anisotropy allows the nitride materials to be used as polarized detectors in the UV range. Of course, the fabrication of these new technologies have only been possible due to key advances in the growth methods. From the different methods commonly used for the growth of III-Nitride semiconductors the most relevant are metal-organic chemical vapor deposition and molecular beam epitaxy (MBE). To-

gether with the use of appropriate substrates and buffer layers and the accurate control of growth conditions, the fabrication of high quality nanostructures has become possible. This allows the design of the electronic and optical properties of the materials including quantum confinement and surface effects.

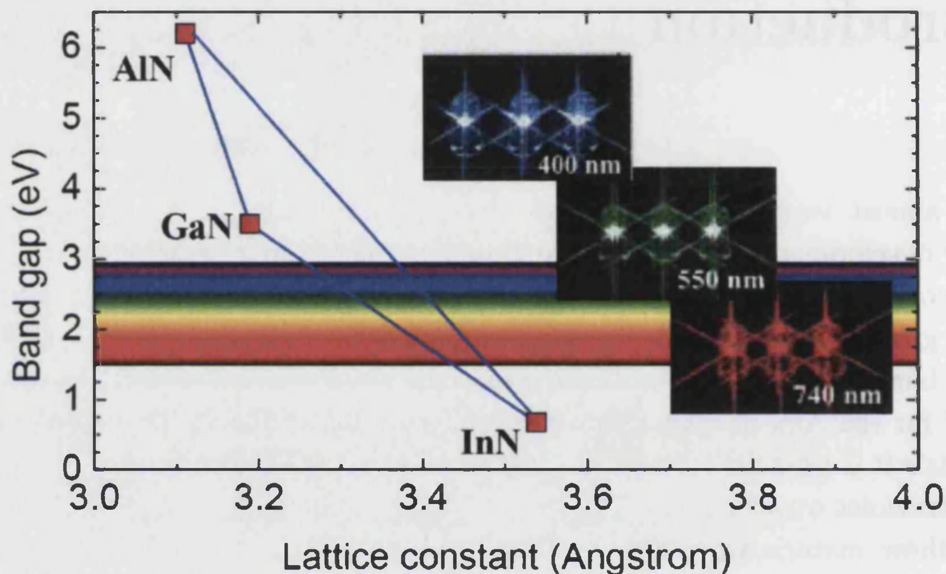

Figure 1: Band gap energy and lattice constant a of III-N semiconductors. Image taken from [3].

Behind the technological implementations of these materials in our daily life, there is a deep research effort on their physical properties. This effort has lead, for example, to the exploitation of the piezoelectric and spontaneous polarization properties of nitride semiconductors for the development of high electron mobility transistors and chemical detectors. In optoelectronic devices, however, the electrical polarization characteristic of nitride semiconductors has to be avoided, since it influences negatively their performance through the quantum confined Stark effect. With this aim, the growth of heterostructures along non polar directions of the wurtzite structure was proposed ten years ago [4]. Besides avoiding the effect of the internal electric field, heterostructures grown along non polar directions present optical anisotropy that can be exploited for the development of polarized optoelectronic devices. Despite the deep research effort performed up to now on the III-N material system, there are still many fields open for research, specially around the properties of nanostructures based on these materials. For example, the parameters that control their emission characteristics, such as strain, size, shape,

orientation or doping, have not been studied in depth yet. It is the aim of this Thesis to analyze some of them.

With this goal in mind, this Thesis is organized in the following Chapters. In Chapter 1 we give a general view of the basic properties of nitride semiconductors: crystal structure, electronic, vibrational and optical properties. Chapter 2 presents the basis of the growth and characterization techniques used in this work. This covers structural characterization techniques such as scanning electron microscopy and atomic force microscopy; optical characterization techniques such as Raman scattering and Photoluminescence; and, finally, conductive atomic force microscopy for electrical characterization. In Chapter 3 we study the influence of several physical parameters on the polarized emission of a-plane GaN/AlN quantum well superlattices, as well as a-plane quantum dots in relation to their morphology. Chapter 4 treats the basic properties of GaN nanowires. The growth conditions to reach columnar nanostructures are discussed, and a statistical analysis of their morphological features as a function of substrate temperature is also shown. The analysis of the optical properties of GaN nanowires is presented in Chapter 5. A study of the optical and structural properties of GaN/AlN nanowire heterostructures, both radial and axial, is presented in Chapter 6. Finally, in Chapter 7 we have performed a study of the optical, structural an electrical properties of n-type GaN nanowires doped with Si. To summarize this work, the main conclusions are exposed at the end of this Thesis.

For the elaboration of this work the collaboration with other scientists was necessary, both from the University of Valencia and from other research groups. The theoretical simulations were performed by Dr. Alberto García-Cristóbal and Dr. Jorge Budagosky, from the Group of Spectroscopy of Solids (University of Valencia), and by Dr. Yann-Michel Niquet, from CEA (Grenoble). Experimental facilities that complemented those available at the University of Valencia were accessed through short stays at various laboratories. The growth of the samples was performed in Grenoble (France) in the group leaded by Dr. Bruno Daudin. Most of the SEM and TEM measurements for morphological analysis were also performed in this laboratory. Time resolved photoluminescence studies were developed in Florence (Italy) in the group of Dr. Anna Vinattieri. The learning of the electrical measurements of Si-doped GaN nanowires was accomplished in Cambridge (England) under the supervision of Dr. Rachel Oliver, and through fruitful discussions with Dr. Luis Colchero, from Nanotec. Finally, the rest of the techniques, such as time integrated photoluminescence, Raman spectroscopy and electrical measurements by means of atomic force microscopy were performed at the Institute of Material Science of the University of Valencia.

Publications

The following list correspond to parts of this thesis already published:

- R. Mata, N. Garro, A. Cros, J. A. Budagosky, A. García-Cristóbal, A. Vinattieri, M. Gurioli, S. Founta, E. Bellet-Amalric y B. Daudin, *Anisotropic polarization of non-polar GaN quantum dot emission*, Phys. Stat. Sol. C, **6**, S541-S544 (2009).
- C. Bougerol, R. Songmuang, D. Camacho, Y. M. Nique, R. Mata, A. Cros, and B. Daudin, *The structural properties of GaN insertions in GaN/AlN nanocolumn heterostructures*, Nanotechnology, **20**, 295706 (2009).
- R. Mata, A. Cros, J. A. Budagosky, A. Molina-Sánchez, N. Garro, A. García-Cristóbal, J. Renard, S. Founta, B. Gayral, E. Bellet-Amalric, C. Bougerol, and B. Daudin, *Reversed polarized emission in highly strained a-plane GaN/AlN multiple quantum wells*, Physical Review B, **82**, 125405 (2010).
- K. Hestroffer, R. Mata, D. Camacho, C. Leclere, G. Tourbot, Y. M. Niquet, A. Cros, C. Bougerol, H. Renevier and B. Daudin, *The structural properties of GaN/AlN core-shell nanocolumn heterostructures*, Nanotechnology, **21**, 415702 (2010).
- R. Mata, K. Hestroffer, J. Budagosky, A. Cros, C. Bougerol, H. Renevier, B. Daudin, *Nucleation of GaN Nanowires Grown by Plasma-Assisted Molecular Beam Epitaxy: The Effect of Temperature*, Submitted (2011).
- R. Mata, A. Cros, S. Agouram, B.Gayral, B. Daudin, *Surface phonon modes of MBE grown GaN nanowires: dependence on nanowire density*, Under elaboration (2011).

Definitions and Notations

Abbreviation	Definition
ADC	Analogical Digital Converter
AFM	Atomic Force Microscopy
AM-AFM	Amplitude Modulation Atomic Force Microscopy
BZ	Brillouin Zone
CAFM	Conductive Atomic Force Microscopy
CB	Conduction Band
CCD	Charge Coupled Device
CEA	Commissariat à l'Énergie Atomique
CH	Crystal Field Hole
CL	Cathodoluminescence
DAFS	Diffraction Anomalous Fine Structure
DOP	Degree of Polarization
DOS	Density of States
EFM	Electrical Force Microscopy
e-h	Electron Hole
FM-AFM	Frequency Modulation Atomic Force Microscopy
FWHM	Full Weight at Half Maximum
GIMAD	Grazing Incidence Anomalous Diffraction
GPA	Geometrical Phase Analysis
HH	Heavy Hole
HR-TEM	High Resolution Transmission Electron Microscopy
IR	Infrared Absorption
KP-AFM	Kelvin Probe Atomic Force Microscopy
LH	Light Hole
MBE	Molecular Beam Epitaxy
MCA	Multi-Channel Analyzer
MCPT	Micro-Channel Photomultiplier
	...the list continues in the next page...

Abbreviation	Definition
MEIS	Medium Energy Ion Scattering
NWrs	Nanowires
PA-MBE	Plasma Assisted Molecular Beam Epitaxy
PDP	Phonon Deformation Potential
PL	Photoluminescence
QDs	Quantum Dots
QWs	Quantum Wells
RF	Radio Frequency
RHEED	Reflection High Energy Electron Diffraction
RS	Raman Scattering
SCM	Scanning Capacitance Microscopy
SEM	Scanning Electron Microscopy
SPM	Scanning Probe Microscopy
STEM	Scanning Transmission Electron Microscopy
STM	Scanning Tunneling Microscopy
TAC	Time Amplitude Converter
TES	Two Electron Satellite
TTs	Transit Time Spread
UHV	Ultra High Vacuum
VB	Valence Band
WZ	Wurtzite
XRD	X Ray Diffraction

Chapter 1

Fundamental properties of group III-nitride semiconductors and Metal-Semiconductor contacts

In the present Chapter we pretend to introduce the general properties of group III-nitride semiconductors, focalizing on GaN with the wurtzite structure. A detailed structural description of the unit cell will be done, and we will dedicate a Section to describe the spontaneous and piezoelectric polarization characteristic of these semiconductors. We will show the basis of the electronic properties of bulk GaN considering also the effect of strain. A description of the vibrational properties of the III-N compounds studied in this work will also be given. Finally, we will address the influence of the Stark effect on the optical properties of GaN/AlN heterostructures.

1.1 Crystal structure

There are two common crystal structures existing for group III-nitrides at normal pressure: the wurtzite (WZ) and the zincblende structures. While WZ is the thermodynamically stable phase, the zincblende phase is metastable. However, it has been stabilized by epitaxial growth of thin films on cubic substrates such as Si and GaAs. Considering that the work developed in this Thesis is centered on the properties of III-N semiconductors with WZ structure, in the following Sections we will give a description of the structural, optical and vibrational properties of this phase.

1.1.1 The wurtzite crystal structure

The WZ crystal structure has an hexagonal unit cell. The schematic diagram of the WZ cell is shown in Fig. 7.11, where the yellow big spheres represent the Ga atoms and the grey small ones the N component. The crystallographic directions corresponding to the c, a and m axis are shown on the right part. The stacking sequence of the atoms is ABA along the [0001] direction, as it is also labeled in the Figure.

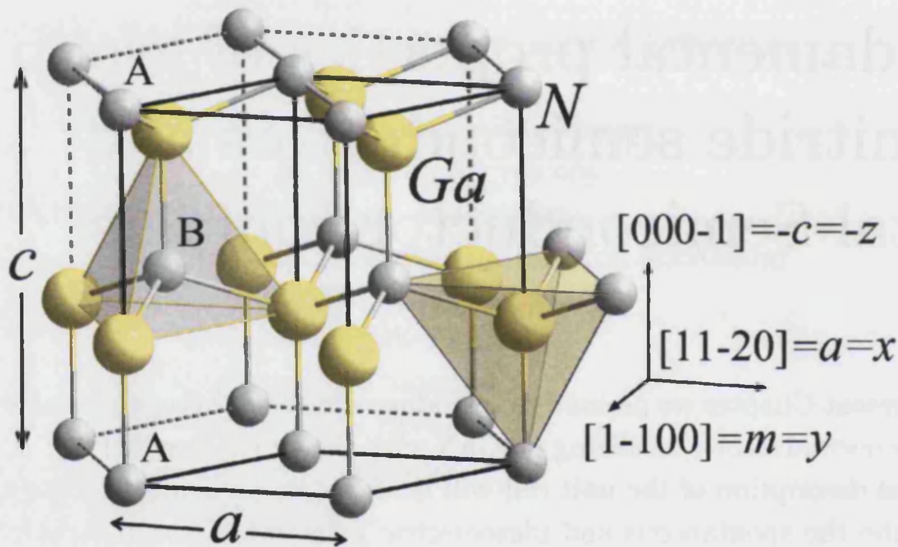

Figure 1.1: Schematic diagram of the WZ cell. Yellow big spheres represent Ga atoms, while grey small spheres denote the N atom positions. The stacking sequence of atoms ABA is labeled, as well as the lattice parameters a and c. The axes indicate the most common crystallographic directions.

The cell is characterized by two lattice parameters a and c, shown by arrows in the Figure. The primitive unit cell contains two atoms of each type and belongs to the space group $P6_3mc$ in Hermann-Mauguin notation. It means that the Bravais lattice is primitive, that there is a six fold screw rotation of vector $\frac{1}{2}c$, a mirror plane perpendicular to the a axis and a glide mirror plane perpendicular to the m axis with translation vector $\frac{1}{2}c$. The values of the lattice parameters a and c for the materials treated in this work have been taken from [1] and are listed in Table 1.1.

The two Ga atoms in the unit cell are placed at positions $(0, 0, 0)$ and $(\frac{2}{3}, \frac{1}{3}, \frac{1}{2})$, and the two N atoms at positions $(0, 0, u)$ and $(\frac{2}{3}, \frac{1}{3}, \frac{1}{2}+u)$, in units of the hexagonal cell. The cell internal parameter u is defined as the anion-cation distance along the c-axis in units of the lattice parameter c. Therefore, the WZ crystal structure

Compound→	GaN	AlN
a(Å)	3.189	3.112
c(Å)	5.185	4.982
u	0.378	0.390

Table 1.1: Measured lattice parameters for GaN and AlN. Values extracted from [1]. The internal parameter u is dimensionless and it is shown in the last row of the table.

can be described by two hexagonal compact lattices, one composed of metal atoms and the other of nitrogen atoms, shifted a distance uc along the [0001] direction. For the ideal WZ cell $u = 0.375$. However, in real crystals with WZ structure u deviates from the ideal value. The value of u for GaN and AlN is shown in the last row of Table 1.1. One can appreciate that u is larger than in the ideal case. As we will see later, this fact has important consequences on the properties of the materials, in particular on its polarization properties.

Polarity

Noncentrosymmetric compound crystals exhibit two different sequences of the atomic layering in the two opposing directions parallel to certain crystallographic axes. For binary compounds with wurtzite structure, such as GaN, for example, the sequence of the atomic layers of the constituents Ga and N is reversed along the [0001] and $[000\bar{1}]$ directions. As a consequence, a crystallographic polarity along this axes can be observed. The corresponding [0001] and $[000\bar{1}]$ oriented surfaces are named the Ga-face and N-face, respectively. Figure 1.2 presents a schematic illustration of the polarity along the c-axis for the case of GaN.

In the case of heteroepitaxial growth of thin films of a noncentrosymmetric compound, the polarity of the material cannot be predicted in a straightforward way, and must be determined by experiments [5]. This is the case for GaN epitaxial layers and GaN-based heterostructures with the most common growth direction normal to the (0001) basal plane, where the atoms are arranged in bilayers. As we have seen in the previous Section, these bilayers consist of two closely spaced hexagonal layers, one formed by cations and the other formed by anions, leading to polar faces. Thus, in the case of GaN, a basal surface should be either Ga- or N-faced. A simple consideration must be taken into account to distinguish both polarities. In the wurtzite structure, the Ga atoms have four bonds along the vertices of a tetrahedron. As can be appreciated in Fig. 7.11, one of the bonds is aligned along the c axis. The other three form a certain angle with this axis. A Ga-face is obtained when the anion-cation bond parallel to the c axis is

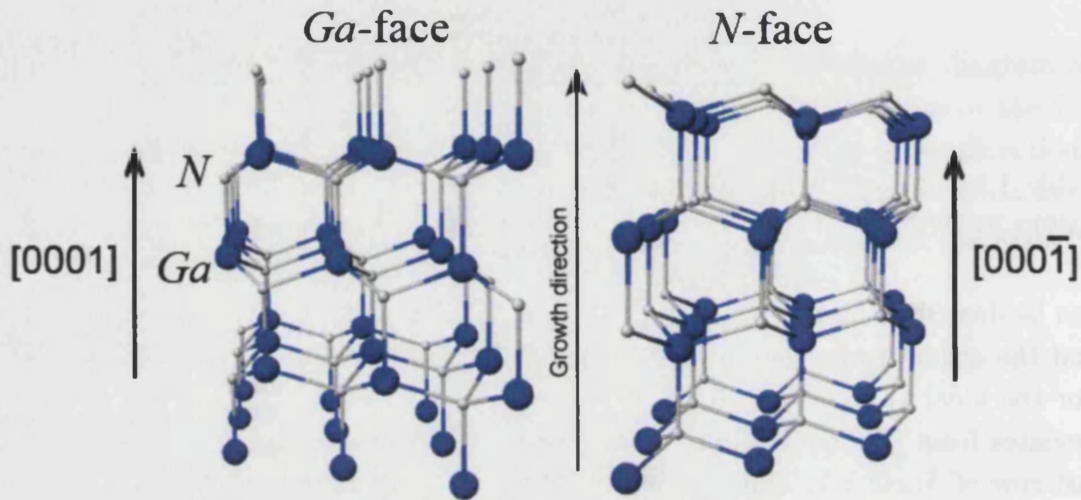

Figure 1.2: The small and large spheres indicate N and Ga atoms, respectively. GaN with Ga-face polarity on the left side and GaN with N-face polarity on the right side.

pointing towards the free surface (figure on the left). If the situation is inverted, the material is N-face (figure on the right).

1.1.2 Internal polarization in Wurtzite structure

The natural WZ structure of the III-V nitrides is the crystal structure with highest symmetry compatible with the existence of spontaneous polarization. When the crystal structure is changed by an applied strain, the polarization of the structure may change, giving rise to piezoelectric polarization. Therefore, in a general situation the macroscopic polarization is the contribution of two factors: the spontaneous polarization $\boldsymbol{P}^{sp}$, and the piezoelectric polarization $\boldsymbol{P}^{pz}$. In the following we will explain separately with more detail both contributions.

Spontaneous polarization

The symmetry of the WZ crystal belongs to the point group $6\,mm$, then the resulting total spontaneous polarization should be along the direction [0001], $\boldsymbol{P}^{sp} = P^{sp}\boldsymbol{u}_z$. The metal atoms and nitrogen present a difference in electronegativity, which is larger for nitrogen. This means that the electron cloud along the III-N bond is somewhat shifted towards the nitrogen. This effect, together with the low symmetry of the wurtzite structure, shifts the center of the positive and negative charge so that they are at different positions even in an ideal wurtzite structure.

This shift creates microscopic dipoles in the primitive cell which give rise to the macroscopic polarization of the crystal structure. This would be the only cause of spontaneous polarization for an ideal wurtzite crystal. Another consideration to be taken into account is that, in real nitride semiconductor crystals, the value of the internal parameter u differs from the ideal one. Consequently, the lattice cannot be represented by regular tetrahedra, but they are deformed along the c axis, contributing even more to the displacement of the center of the positive and negative charges. This represents the most important contribution to the macroscopic polarization. Bernardini *et al.* [6] have provided *ab initio* calculations using a Barry-phase approach in order to obtain the spontaneous polarization for different III-N materials. Their results for GaN and AlN are shown in Table 1.2. Considering the value of the calculated spontaneous polarization for GaN and

(Cm^{-2})	GaN	AlN
P^{sp}	-0.029	-0.081

Table 1.2: Calculated values of the spontaneous polarization. From Ref. [6].

AlN, we can observe that because of the sensitive dependence of the polarization on the structural parameters, there are quantitative differences in their values. This dependence becomes clear if we consider that the internal parameter u is larger for AlN than for GaN. As a consequence, AlN presents a larger spontaneous polarization than GaN.

Piezoelectric polarization

The piezoelectric effect in noncentrosymmetric crystals is characterized by the induction of a macroscopic polarization as a consequence of the deformation of the unit cell. A general deformation in a solid is described in terms of a continuous deformation field $\boldsymbol{u}(\boldsymbol{r})$, where $\boldsymbol{r}$ specifies the vector displacement in the solid. The deformation field is related to the strain tensor ε_{jk}. In presence of a deformation, the induced piezoelectric polarization $\boldsymbol{P}^{pz}$ can be expressed as:

$$P_i^{pz} = e_{ijk}\varepsilon_{jk}, \tag{1.1}$$

where e_{ijk} defines the piezoelectric tensor of rank 3. The subindexes ijk vary from 1 to 3, where 1, 2 and 3 correspond to the three spatial directions. The tensor e_{ijk} has $3^3 = 27$ components. Due to the tensor symmetry, there are 18 independent components. Using the notation introduced by Voigt it is possible to reduce the indexes jk to one following the rules exposed in Table 1.3.

Tensor notation	11	22	33	23,32	31,13	12,21
Voigt or matrix notation	1	2	3	4	5	6

Table 1.3: Relation between tensor and Voigt notation.

It is important to note that, as a consequence of this transformation, a factor 2 appears in the non diagonal tensor components. For example, the relation between e_{14} (Voigt notation) and e_{123} (tensor notation) is $e_{14}=2e_{123}$. Similar relations are obtained for the transformed strain tensor components ε_{jk}. Furthermore, taking into account that the WZ structure is isotropic in its basal plane, the number of non vanishing components is reduced to 5, being only 3 of them independent. With these considerations the tensor e_{ij} becomes:

$$e_{ij} = \begin{pmatrix} 0 & 0 & 0 & 0 & e_{15} & 0 \\ 0 & 0 & 0 & e_{15} & 0 & 0 \\ e_{31} & e_{31} & e_{33} & 0 & 0 & 0 \end{pmatrix}. \tag{1.2}$$

Now, we introduce the piezoelectric tensor 1.2 in Eq. 1.1, and we obtain the total contribution of the piezoelectric polarization. Adding this contribution to the spontaneous polarization, we obtain the total intrinsic macroscopic polarization given by:

$$\begin{pmatrix} P_1 \\ P_2 \\ P_3 \end{pmatrix} = \begin{pmatrix} 0 \\ 0 \\ P^{sp} \end{pmatrix} + \begin{pmatrix} 0 & 0 & 0 & 0 & e_{15} & 0 \\ 0 & 0 & 0 & e_{15} & 0 & 0 \\ e_{31} & e_{31} & e_{33} & 0 & 0 & 0 \end{pmatrix} \begin{pmatrix} \varepsilon_{11} \\ \varepsilon_{22} \\ \varepsilon_{33} \\ 2\varepsilon_{23} \\ 2\varepsilon_{13} \\ 2\varepsilon_{12} \end{pmatrix} \tag{1.3}$$

Values of the piezoelectric components reported in the literature are compiled in Table 1.4. A wide variation of the values is found. In this work we will consider the piezoelectric coefficients reported by Bernardini *et al.* [6], since their values are in good agreement with the available experimental values for the piezoelectric constants of other materials, such as ZnO (e_{33} = 1.2 C/m^2 and BeO e_{33} = 0.09 C/m^2, showing some slight overall improvement over the Berry phase calculations [7]. The third independent component of the piezoelectric tensor, e_{15}, is related to the polarization induced by a shear strain, and will not be considered in this work.

(Cm^{-2})	e_{33}	e_{31}	e_{15}
GaN	0.73[6]	-0.49[6]	-0.3[8]
	0.44[9]	-0.36[8]	-0.33[10]
	0.65[10]	0.33[10]	-0.22[9]
	-	-0.22[9]	-
AlN	1.46[6]	-0.60[6]	-0.48[11]
	1.55[11]	-0.58[11]	-

Table 1.4: Values of the piezoelectric coefficients of GaN and AlN compiled from several works.

1.1.3 Strain in epitaxial films grown along different directions

When a film is grown on a substrate, the lattice constants and the thermal expansion coefficients may be different between the grown material and the substrate. A stress in the grown film may appear that can be described by the stress tensor σ_{ij}. For a sufficiently small stress, the amount of strain is, according to Hooke's law, proportional to the magnitude of the applied stress and is given by the following expression:

$$\sigma_{ij} = C_{ijkl}\varepsilon_{kl}. \tag{1.4}$$

The proportionality constants, C_{ijkl}, define the stiffness tensor. By using Voigt notation again and considering the symmetry of the WZ structure, it is possible to reduce the indexes to two: $ij \rightarrow l$ and $kl \rightarrow m$, as well as the number of independent components. Then, the relation between strain and stress can be expressed as $\sigma_l = C_{lm}\varepsilon_m$ and the stiffness tensor becomes:

$$C_{ij} = \begin{pmatrix} C_{11} & C_{12} & C_{13} & 0 & 0 & 0 \\ C_{12} & C_{11} & C_{13} & 0 & 0 & 0 \\ C_{13} & C_{13} & C_{33} & 0 & 0 & 0 \\ 0 & 0 & 0 & C_{44} & 0 & 0 \\ 0 & 0 & 0 & 0 & C_{44} & 0 \\ 0 & 0 & 0 & 0 & 0 & \frac{C_{11}-C_{12}}{2} \end{pmatrix}. \tag{1.5}$$

Elastic constants for wurtzite GaN have been obtained from a number of experiments and calculations. We choose the values recommended by Vurgaftman *et al.* [1] as a result of an exhaustive comparison between parameters from different works. The values are compiled in Table 1.5. Vurgaftman *et al.* recommend these theoretical parameters since they present the best concordance with the experimental data of Polian *et al.* [12]. Regarding the elastic constants for wurtzite AlN, they were experimentally measured by several authors. Several theoretical results

are also available. Vurgaftman *et al.* recommend the values exposed in the Table because Wright *et al.* [13] provide a detailed discussion of their expected accuracy.

(GPa)	GaN	AlN
C_{11}	390	396
C_{12}	145	137
C_{13}	106	108
C_{33}	398	373
C_{44}	105	116

Table 1.5: Elastic constants for GaN and AlN extracted from Ref. [1].

For the interpretation of the experimental data on strain obtained from several techniques, throughout this Thesis we have adopted some approximations that simplify the strain-stress relations given above. In the first place, we have neglected the shear strain components, i.e., σ_{ij} with $i \neq j$ are taken equal to zero. This approximation is easily justified for thin films, since shear is expected to be very small. For three dimensional heterostructures, such as quantum dots, the small magnitude of the shear strain is not so clear, but in any case it is very difficult to quantify experimentally. With these considerations the stiffness tensor can be simplified to a 3×3 matrix.

In what follows, we will make explicit use of the spatial directions x, y and z by replacing the indexes in the following way: $1 \rightarrow x$, $2 \rightarrow y$ and $3 \rightarrow z$. To clarify this notation, we remit the reader to the coordinate axis in Fig. 7.11. We will keep this notation throughout the whole Thesis. Finally, strain and stress will be related by only four elastic coefficients according to:

$$\begin{pmatrix} \sigma_{xx} \\ \sigma_{yy} \\ \sigma_{zz} \end{pmatrix} = \begin{pmatrix} C_{11} & C_{12} & C_{13} \\ C_{12} & C_{11} & C_{13} \\ C_{13} & C_{13} & C_{33} \end{pmatrix} \begin{pmatrix} \varepsilon_{xx} \\ \varepsilon_{yy} \\ \varepsilon_{zz} \end{pmatrix} \tag{1.6}$$

In the case of WZ materials the values of the strain tensor components can be obtained from the change in the lattice parameters a and c, that is:

$$\varepsilon_{zz} = \frac{c - c_0}{c_0} \text{ and } \varepsilon_{xx,yy} = \frac{a - a_0}{a_0}, \tag{1.7}$$

where the value of the lattice parameter a along the directions x and y may be different, as occurs for nanostructures grown along non-polar directions.

Strain state for films grown along [0001]

The growth direction for the c-plane GaN films is along the z direction, which is parallel to [0001]. c-plane films are mostly grown on substrates having an hexagonal symmetry, such as c-plane SiC, c-plane sapphire or (111) silicon. In this case, the film strain in the growth plane is isotropic, i.e., $\varepsilon_{xx} = \varepsilon_{yy}$. Within the biaxial approximation, it is assumed that the material grows free of stress along the growth direction. In these conditions, $\sigma_{\parallel} = 0$, and using Eq. 1.6 we obtain the following Poisson's relation:

$$\frac{\varepsilon_{zz}}{\varepsilon_{xx}} = -2\frac{C_{13}}{C_{33}}. \tag{1.8}$$

The resulting equation relates the in-plane and the out of plane strain components through the stiffness coefficients.

Strain state for films grown along $[11\bar{2}0]$ and $[1\bar{1}00]$

When the film is grown along non-polar directions, such as $x = [11\bar{2}0]$ or $y = [1\bar{1}00]$, the c axis of the WZ structure lies in the growth plane, as can be clearly seen in Fig. 3.2. In contrast to the previous case, here the strain in the growth plane is usually anisotropic, since the lattice mismatch between film and substrate is different along the c axis and perpendicular to it. In the case of films grown along $y = [11\bar{2}0]$, within the biaxial approximation $\sigma_{yy} = 0$. Using Eq. 1.6 one obtains Poisson's relation:

$$\varepsilon_{xx} = -\frac{\varepsilon_{yy}C_{11} + \varepsilon_{zz}C_{13}}{C_{12}}. \tag{1.9}$$

Due to the symmetry of the matrix 1.5, one can obtain the corresponding Poisson's equation for the growth direction $[1\bar{1}00]$, just by exchanging the index x and y:

$$\varepsilon_{yy} = -\frac{\varepsilon_{xx}C_{11} + \varepsilon_{zz}C_{13}}{C_{12}}. \tag{1.10}$$

In these cases, as commented before, the values of ε_{xx}, ε_{yy} and ε_{zz} will be usually different.

1.2 Electronic properties

As we have already studied, III-N semiconductors normally crystalize in the WZ crystal structure. These materials have a direct band gap and with their alloys the energy gap (E_g) ranges from 0.6 eV for InN to 6.3 eV in the case of AlN. The energy

gap of GaN is located in the middle of this range at 3.5 eV. In this section we will describe the electronic bands of this semiconductor. Moreover, its band structure will be described by the effective mass approximation along different directions in **k**-space. Finally, we shall consider calculations performed by Chuang *et al.* [14] of the electronic band structure. The effect of a compressive biaxial strain will be considered in order to analyze the influence of strain on the electronic band structure.

1.2.1 Bulk GaN band structure

The active material of the nanostructures studied in this Thesis is GaN. Consequently, in this section we will center our attention on the band structure of this direct band-gap semiconductor in the proximity of the conduction band (CB) minimum and the valence band (VB) maximum, which are located at the Γ point. Chuang *et al.* [14] computed the electronic band structure of GaN within the framework of an 8×8 Hamiltonian in the $\mathbf{k} \cdot \mathbf{p}$ theory. The quasi-cubic approximation allows the introduction of the spin-orbit interaction as a perturbation [15]. In this way, it is possible to calculate the energies of the bands at the Γ point. Using irreducible representations of group theory, the former states in the valence bands are labeled as Γ_9 for the upper valence band, Γ_7^+ for the second one and Γ_7^- for the lowest valence band. The energy splitting between Γ_7^+ and Γ_7^- is known as crystal-field splitting, Δ_{cr}, since it is induced by the hexagonal symmetry of the WZ structure. For similar reasons, the energy splitting between Γ_9 and Γ_7^+ levels is known as spin-orbit energy splitting, Δ_{so}. It is possible to obtain an approximate expression for the energies of the conduction and the three valence bands at the Γ point, which are given as:

$$\begin{aligned} E_{cv} &= E_g + \Delta_1 + \Delta_2 \\ E_{\Gamma_9} &= \Delta_1 + \Delta_2 \\ E_{\Gamma_7^+} &= \frac{\Delta_1 - \Delta_2}{2} + \sqrt{\frac{\Delta_1 - \Delta_2}{2}^2 + \Delta_3^2} \\ E_{\Gamma_7^-} &= \frac{\Delta_1 - \Delta_2}{2} - \sqrt{\frac{\Delta_1 - \Delta_2}{2}^2 + \Delta_3^2} \end{aligned} \quad (1.11)$$

where,

$$\Delta_1 = \Delta_{cr} \text{ and } \Delta_2 = \Delta_3 = \frac{\Delta_{so}}{3}. \quad (1.12)$$

These calculations have been reproduced by my colleague Jorge Budagosky [16]. The corresponding electronic band structure of GaN near the Γ point, considering

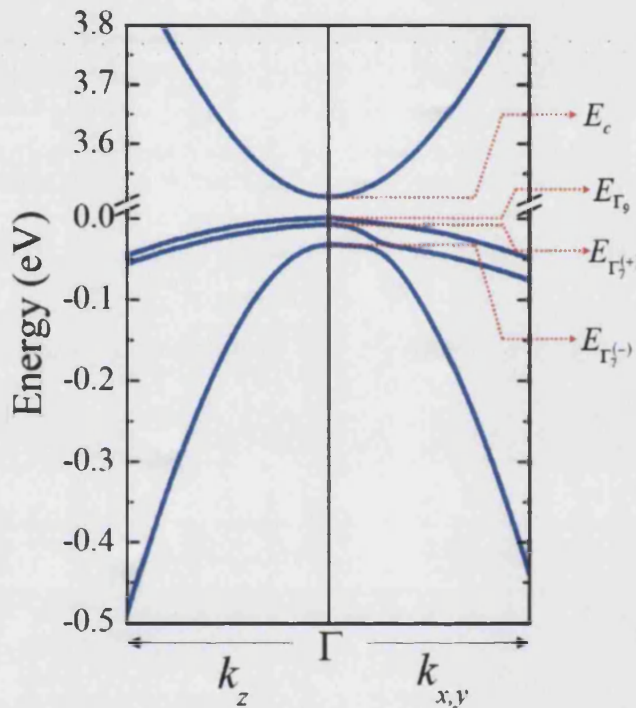

Figure 1.3: Band structure of GaN with the WZ structure near the Γ point. Note that the origin of energies is taken at the maximum of the valence band Γ_9. Figure taken from [16].

spin-orbit interaction, is shown in Fig. 1.3. The bands are labeled on the right part the of the Figure. The electronic bands are represented along $\mathbf{k_z}$ and $\mathbf{k_x}$. It can be observed that both directions are not equivalent. However, for bulk GaN, and due to the symmetry of the wurtzite structure, the directions $\mathbf{k_x}$ and $\mathbf{k_y}$ are equivalent. Note that the bands are not degenerate at the Γ point, a feature that differentiates the nitride semiconductors from other most common III-V semiconductors with the zinc-blende structure. Moreover, an anticrossing between the Γ_9 and Γ_7^+ bands, and between Γ_7^+ and Γ_7^- along $\mathbf{k_{x,y}}$ can be observed.

In order to understand the polarization characteristic of the photoluminescence emission of the different nanostructures studied later in this work, it is necessary to determine the nature of the atomic orbitals involved in the formation of the energy bands[17]. The minimum of the conduction band is located at the Γ point and the bands in the vicinity of this point are originated from N and Ga s-states (wavefunction $|S\rangle$-like orbitals). The three valence bands arise from N $2s$, $2p$ and Ga $4s$, $4p$ states, but at the vicinity of the Γ point the valence bands consists almost exclusively of N $2p$ states. In particular, the first valence band (Γ_9) consist entirely of p_{xy} orbitals (wavefunction $|X \pm iY\rangle$-like), the second (Γ_7^+) of p_{xy} with a small fraction of p_z orbitals (wavefunction $|Z\rangle$-like). Finally, the lowest energy valence

(m_0)	m^z_{CB}	m^{xy}_{CB}	m^z_{HH}	m^{xy}_{HH}	m^z_{LH}	m^{xy}_{LH}	m^z_{CH}	m^{xy}_{CH}
GaN	0.20	0.18	1.76	1.61	1.76	0.14	0.16	1.04
AlN	0.33	0.25	3.53	10.42	3.53	0.24	0.25	3.81

Table 1.6: Effective mass values for the electron, heavy hole, light hole and crystal field hole bands at the Γ point in units of the free electron mass m_0. Values extracted from [18].

band (Γ_7^-) consists almost entirely of p_z orbitals. This composition, characteristic of bulk GaN, can be altered by strain and confinement, as will be discussed later in this Thesis.

Effective masses

Within the parabolic approximation, in the vicinity of the Γ point the curvature of the energy bands can be described in terms of the effective mass tensor. Taking into account the anisotropy of the WZ structure, a general expression for the CB and the three VB can be written as:

$$E_i(k) = E_i + \frac{\hbar^2(k_x^2 + k_y^2)}{2m_i^{xy}} + \frac{\hbar^2 k_z^2}{2m_i^z}, \tag{1.13}$$

where the subindex i refers to the conduction band CB and the different valence bands Γ_9, Γ_7^+ and Γ_7^-, labeled here as HH, LH and CH respectively. These labels are historically used for bulk GaN and arise from the names heavy hole, light hole and crystal field hole, respectively. They make reference to the value of the effective masses of the different bands along k_x or, equivalently, k_y, and to the origin of the third (crystal field) band. In Table 1.6 we show the effective mass values for GaN and AlN along the directions perpendicular and parallel to the WZ c axis at the Γ point in units of the free electron mass m_0. Stands out the strong anisotropy of the WZ structure along z, specially in the valence bands. The values have been compiled from [18]. In the case of GaN, one can observe that the effective mass is "heavy" along $\mathbf{k_z}$ for both HH and LH bands, compared with the effective mass of the CH band along the same direction. However, along $\mathbf{k_{xy}}$, the HH band is "heavy" while the other two bands are "light". AlN presents similar characteristics than GaN along $\mathbf{k_z}$, but its "heaviest" effective mass corresponds to the HH band along $\mathbf{k_{xy}}$.

1.2.2 Effect of strain on the electronic band structure

The electronic band structure of unstrained GaN has been exposed above. However, normally it is usual to grow heterostructures where the active region (GaN) is compressed or elongated due to the lattice mismatch between the GaN and the barriers (AlN) or substrate. Unlike the spin-orbit interaction, the crystal field splitting Δ_{cr} is very sensitive to strain. Therefore, some of the valence bands will be more strongly modified due to strain than others. In order to illustrate the impact of strain on the electronic structure, we present in Fig. 7.12 the band structure of bulk GaN. A biaxial compressive strain along the [0001] (a) and the [11$\bar{2}$0] (b) directions is applied. The calculation has been performed by Dr. Jorge Budagosky [16] considering the following values of strain that are derived for epitaxial growth of GaN on AlN and taking into account Eqs. 1.7, 1.8, 1.6 and 1.5:

$$\begin{array}{ll} \varepsilon_{xx} = \varepsilon_{yy} = -2.4\% \text{ and } \varepsilon_{zz} = 1.3\% & \text{for } [0001] \\ \varepsilon_{xx} = 9.3\%, \ \varepsilon_{yy} = -2.4\% \text{ and } \varepsilon_{zz} = -3.9\% & \text{for } [11\bar{2}0] \end{array} \quad (1.14)$$

The applied strain will modify the energy of the conduction and valence band edges. In the case of a compressive biaxial strain along the WZ [0001] axis, Fig 7.12(a), the conduction band blue shifts by ~164 meV. The valence bands also shift in the same direction but by a smaller amount of ~18 meV. As a consequence, the gap increases ~146 meV. Note that the energy splitting between Γ_9 and Γ_7^+ bands remains constant, while the splitting between them and the valence band Γ_7^- increases by ~220 meV. Therefore, the anticrossing between Γ_7^+ and Γ_7^- takes place farther away from the Γ point.

In the same way, Fig. 7.12 (b) represents the bulk GaN band structure that results after applying a biaxial compressive strain in the (11$\bar{2}$0) plane. In contrast to the case analyzed before, under this deformation the conduction band blue shifts ~200 meV. On the contrary, the valence bands suffer a larger displacement towards low energies, around ~95 meV. This gives an increment of the gap energy of ~300 meV, two times larger than in the previous case. The splitting between Γ_9 and Γ_7^+ increases ~53 meV, as well as that between Γ_9 and Γ_7^-, by an amount of ~300 meV in this case. Finally, the most notable difference between the biaxial deformation in the (0001) and (11$\bar{2}$0) planes is the anisotropy of the energy bands along both directions of the WZ basal plane ($\mathbf{E}(\mathbf{k_x}) \neq \mathbf{E}(\mathbf{k_y})$).

Once we have discussed the characteristics of the electronic band structure, we will introduce the vibrational properties of the crystalline structure, which will be also used in the following to characterize the nanostructures.

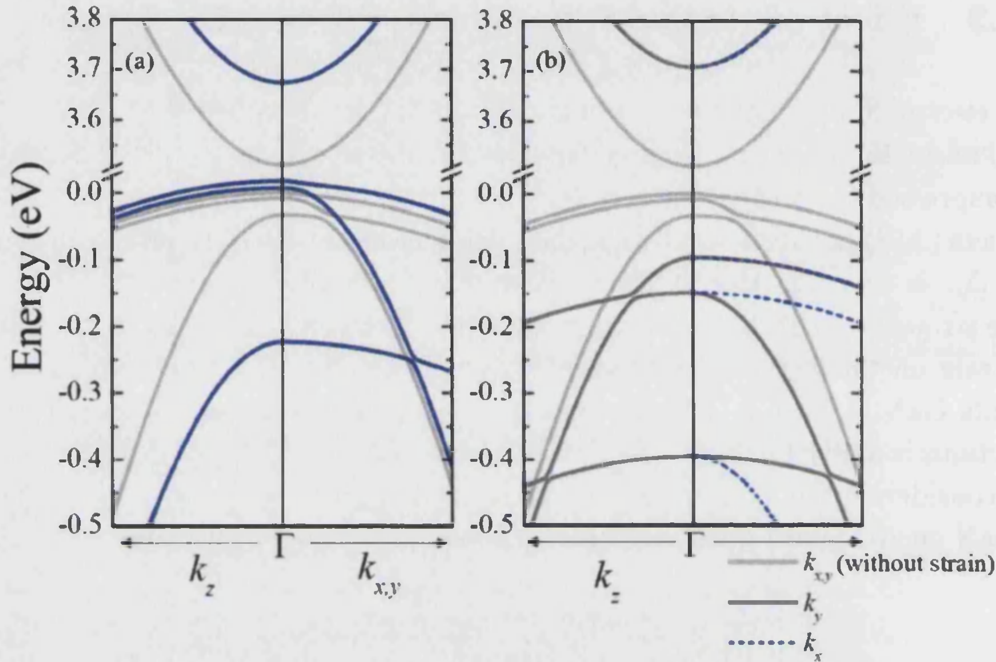

Figure 1.4: (a) Band structure for GaN near the Γ point applying a biaxial compressive strain in the plane (0001) (blue line) and unstrained (gray line). (b) The same but the biaxial compressive strain is applied in the plane $(11\bar{2}0)$ (dark gray line and dashed blue line) and unstrained (gray line). Figure taken from [16].

1.3 Vibrational properties

The normal modes of vibration of the atoms of a crystal, also known as phonons, are almost entirely the responsible of the thermal properties of the materials, such as thermal conductivity, thermal expansion, etc. Some of them interact directly with light and can be responsible for strong absorption and reflection. Taking profit of this fact, information about the crystalline structure can be extracted from them. The most common experimental techniques to study the phonon modes are neutron scattering, infrared absorption (IR) and Raman scattering (RS). This last technique will be explained in more detail in the next Chapter. In this Section we shall present the characteristics of the phonon modes for the III-N compounds treated in this work, and finally we will consider the effect strain on them.

1.3.1 Phonon modes

A crystal has a huge number of phonons. Each one is characterized by a wavevector $\overrightarrow{q}$ in the first Brillouin zone (BZ). The related frequencies, $\omega(q)$, are given by 3N

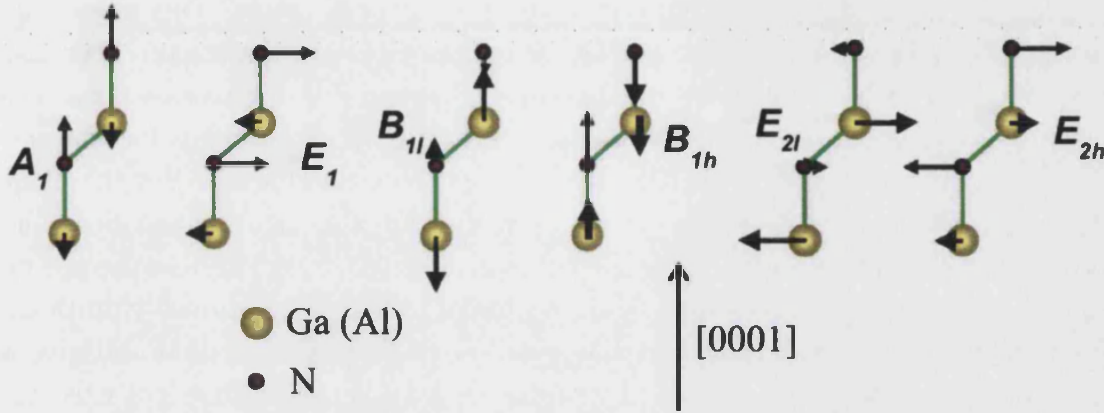

Figure 1.5: Sketch of the four atoms of the WZ unit cell, including the atomic displacements for the optical phonon modes at the Γ point. The big spheres represent the Ga atoms while the small spheres correspond to N atoms. Images taken from [20].

functions of $\vec{q}$, where N is the number of atoms per unit cell. This results in three acoustic branches, for which $\omega(0) = 0$. The rest 3N-3 branches, nine in our case, correspond to the optical modes, with $\omega(0) \neq 0$.

The normal coordinates can be transformed under the operations of the crystal symmetry, in the same way that the base functions of the irreducible representation [19] of the point group. Therefore, the different types of phonons in a crystal can be classified by the irreducible representation of their point group. The irreducible representations can be normally expressed as contributions of a reducible representation Γ. In the case of WZ structure it is formed by the following irreducible representations:

$$\Gamma_{ac} + \Gamma_{op} = (A_1 + E_1) + (A_1 + E_1 + 2E_2 + 2B_1) \tag{1.15}$$

The first set of modes corresponds to the acoustic branch and the second parenthesis includes the optical modes. Modes A_1 and E_1 are both IR and RS active, while E_2 are only RS active, since they do not have associated a dipolar momentum. The mode B_1 is silent, i.e., both RS and IR inactive. On the other hand, a phonon is called longitudinal when the atoms vibrate along the same direction than the propagation, and it is called transversal if the direction of vibration of the atoms is perpendicular to the direction of propagation.

We represent schematically the magnitude and sign of the atomic displacement of the phonon modes at the Γ point in Fig. 1.5. The two first figures from the left correspond to the polar modes A_1 and E_1. In the case of these phonons, the

two Ga atoms move in phase, but out of phase with the N atoms. This movement creates an electric dipole that gives these phonons their polar character. The last two figures on the right represent the non-polar phonons E_2. In this case Ga atoms vibrate out of phase, as do the N atoms. Consequently, no dipole is formed and the modes are non-polar. A similar out of phase movement characterizes the silent B_1 modes, shown in the middle. Accordingly, they are also non-polar modes. The presence of the dipole induced by the polar modes also gives rise to a frequency splitting between the transverse (TO) an longitudinal (LO) optical vibrations. For the LO mode the dipoles sum along the direction of propagation and give a macroscopic electric field associated with the oscillation, which does not exist for TO modes. For the non-polar modes no such splitting occurs. The two E_2 (and similarly for the B_1) are labeled as high and low attending to their frequency. In both cases, the low frequency is attributed to the movement of the Ga atoms while the high frequency of the modes are originated by the movement of the N atoms, with a smaller mass. The frequencies of the Raman active phonon modes of bulk GaN and AlN at the Γ point are listed in Table 1.7. These values are compiled from [21] and are taken as bulk reference for the rest of the work.

(cm^{-1})	GaN	AlN
$A_1(LO)$	734.0	890.0
$A_1(TO)$	531.8	611.0
$E_1(LO)$	741.0	912.0
$E_1(TO)$	558.8	670.8
E_{2l}	144.0	248.6
E_{2h}	567.6	657.4

Table 1.7: Phonon frequencies corresponding to wurtzite GaN and AlN at the Γ point. Values taken from [21].

1.3.2 Strain effect on the phonon modes

The frequency of the phonon modes can be affected by strain. This fact can be used as a tool to characterize the deformation in crystals [22]. The relation between the phonon modes and the strain can be established within the framework of the linear deformation potential theory. This approximation has been developed in detail for crystals with WZ structure by Briggs *et al.* [23]. This theory describes the shift of the phonon modes, $\Delta\omega_\lambda = \omega_\lambda - \omega_0$, with respect to the frequency of the unstrained mode, ω_0, by means of the phonon deformation potentials (PDPs) characteristic of each mode λ. Under deformation, the energy shift suffered by the

modes belonging to the A_1 representation is given by:

$$\Delta\omega_{A_1} = a_{A_1}(\varepsilon_{xx} + \varepsilon_{yy}) + b_{A_1}\varepsilon_{zz}, \tag{1.16}$$

where a_{A_1} and b_{A_1} are the corresponding PDPs of the mode A_1. The modes belonging to the E_1 and E_2 representations are doubly degenerated. The application of strain may break this degeneracy, giving rise to two separate modes. The resulting frequencies are given as a function of strain by:

$$\Delta\omega_\lambda = a_\lambda(\varepsilon_{xx} + \varepsilon_{yy}) + b_\lambda\varepsilon_{zz} \pm c_\lambda\sqrt{(\varepsilon_{xx} + \varepsilon_{yy})^2 + 4\varepsilon_{xy}^2}, \tag{1.17}$$

with $\lambda = E_1, E_2$. Note that the PDPs take different values for TO and LO phonons. The values of the PDPs have been reported for various modes in the literature. The most accepted values together with their corresponding uncertainties have been compiled in Table 1.8.

(cm^{-1})	a GaN	b GaN	c GaN[24]	a AlN[25]	b AlN[25]
$A_1(LO)$	-782 ± 174[25]	-1181 ± 245[25]	0	-643 ± 84	-1157 ± 136
$A_1(TO)$	-630 ± 40[26]	-1290 ± 80[26]	0	-930 ± 94	-904 ± 163
$E_1(TO)$	-820 ± 25[26]	-680 ± 50[26]	379 ± 43	-982 ± 83	-901 ± 145
$E_1(LO)$	-	-	678 ± 49	-	-
E_{2h}	-850 ± 25[26]	-920 ± 60[26]	379 ± 107	-1092 ± 91	-965 ± 161
E_{2l}	115 ± 25[26]	-80 ± 35[26]	-	-	-

Table 1.8: Deformation potential for the different GaN and AlN phonon modes.

1.3.3 Doping and phonon-plasmon coupled modes

In a doped semiconductor the free-carriers can be considered to behave like a gas of charged particles immersed in a uniform background of equal and opposite charges, namely the ions. This is called a plasma. In n-type material this plasma will consist of electrons while for p-type materials it consists of holes. Quantised oscillations of this plasma, i.e., fluctuations in the charge density are called plasmons. The plasmons naturally produce a longitudinal electric field which can couple to the LO phonons which also have an associated longitudinal electric field. The polar phonon modes generate electric dipoles and therefore give a contribution to the dielectric function ϵ of the material, and hence to the refractive index. The dielectric function $\epsilon(\omega)$ depending on the phonon and plasmon contributions can be expressed as :

$$\epsilon(\omega) = \epsilon_\infty \left[1 + \frac{\omega_{LO}^2 - \omega_{TO}^2}{\omega_{TO}^2 - \omega^2} - \frac{\omega_P^2}{\omega^2}\right]. \tag{1.18}$$

To obtain this expression we have considered negligible the damping of the plasma and the molecular vibration. ϵ_∞ is the high-frequency dielectric constant (at frequencies much higher that that of the phonons or plasmons but at lower frequency than that corresponding to the band gap energy). The LO-phonon frequency ω_{LO} and the TO phonon frequency ω_{TO} are those characteristic of the crystal in the absence of any plasmon effects. The plasma frequency ω_P is given by:

$$\omega_P = \sqrt{\frac{4\pi n e^2}{\epsilon_\infty m^*}}. \tag{1.19}$$

Here n is the free carrier concentration and m^* is the effective mass of electrons or holes in the n- or p-type semiconductors respectively. The Gauss equation $\nabla \boldsymbol{D} = 0$ applies since there are no excess charges present and hence it can be shown that $(\mathbf{k} \cdot \mathbf{F})\epsilon(\omega) = \mathbf{0}$, where $\mathbf{F}$ is the electric field. The transverse solutions are given by $(\mathbf{k} \cdot \mathbf{F}) = \mathbf{0}$ while the longitudinal solutions are given by $\epsilon(\omega) = 0$ [27]. Solving the Eq. 1.18 for the longitudinal solutions we obtain:

$$\omega_\pm^2 = \frac{\{\omega_{LO}^2 + \omega_P^2\}}{2} \pm \frac{\sqrt{[\omega_P^2 - \omega_{LO}^2]^2 + 4\omega_P^2[\omega_{LO}^2 - \omega_P^2]}}{2}. \tag{1.20}$$

We use the values of $\omega_{A_1(TO)} = 531.8$ cm^{-1}, $\omega_{A_1(LO)} = 734$ cm^{-1}, $\epsilon_\infty = 5.35$ and $m^* = 0.2m_0$ (where m_0 is the mass of the free electron) applicable to n-type GaN, as indicated in [28]. The solutions of Eq. 1.20 are labeled as L^+ and L^- and plotted in Fig. 1.6 versus n with full lines. The plasma frequency is also included (dashed line).

At low concentration ($< 10^{17}$ cm^{-3}) the observed RS spectrum will be nearly identical to the spectrum for completely undoped material with only RS signals observed form LO and TO phonons at the frequency of $\omega_{A_{1,LO}}$ and $\omega_{A_{1,TO}}$ respectively. As the carrier concentration increases, the frequency of the LO phonon increases. In addition a new mode labeled L^- in the Figure appears and approaches the TO phonon frequency as the carrier concentration is increased. The intensity and line-shape of the observed modes vary and in general the Raman signal of the L^+ mode is weaker and broader than that of the uncoupled LO phonon mode. This characteristics are enhanced for increasing carrier concentration.

Observation of the L^+ and L^- modes in n-type material in good agreement with theory have been obtained in GaN by Harima *et al.* [29] (indicated by black circles in the graph), by Perlin *et al.* [30] (shown by empty squares) and by Kozawa *et al.* [31] (empty triangles in the graph). The branches of the L^+ and L^- modes can be used to determine the free carrier concentration in GaN nanostructures by

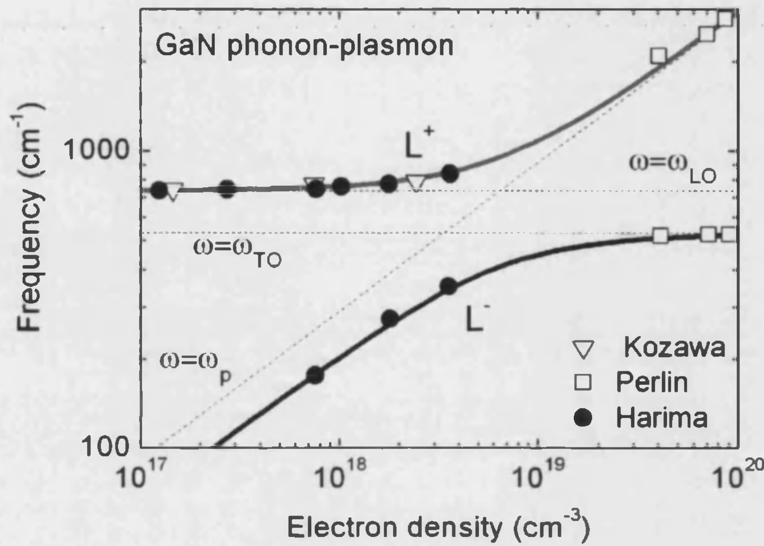

Figure 1.6: Carrier-density dependence of the LOPC-mode frequency in n-type wurtzite GaN. The data are taken from Harima *et al.* (filled circles) [29], Perlin *et al.* (squares) [30] and Kozawa *et al.* (triangles) [31].

the observed Raman shift of the $A_{1,LO}$ mode. This estimation will be considered in following Chapters.

1.4 The internal electric field in heterostructures

We have already seen in Sec. 1.1.2 that in WZ III-nitride semiconductors there exists an internal macroscopic polarization. This internal macroscopic polarization induces a volume charge density given by $\rho_P = -\boldsymbol{\nabla P}$. With the formation of heterostructures, a change in the polarization may take place at the interfaces. This change produces a sheet carrier density at the interfaces expressed by $\sigma_P = \boldsymbol{\Delta P \cdot n}$, with $\boldsymbol{n}$ being the normal to the interface. For instance, in the case of a [0001] oriented GaN quantum well between AlN barriers, each interface will carry a charge sheet of opposite sign. These charge sheet acts as a capacitor, creating an huge electric field. The value of the electric field has been found to be as high as 7 MV/cm in GaN/AlN quantum dots grown along the [0001] direction [32]. Now, in order to clarify the direction of the electric field in GaN/AlN heterostructures, we should first consider the polarization component along the c axis extracted from Eq. 1.3:

$$P_z = P_{sp} + e_{33}\varepsilon_{zz} + e_{31}(\varepsilon_{xx} + \varepsilon_{yy}). \tag{1.21}$$

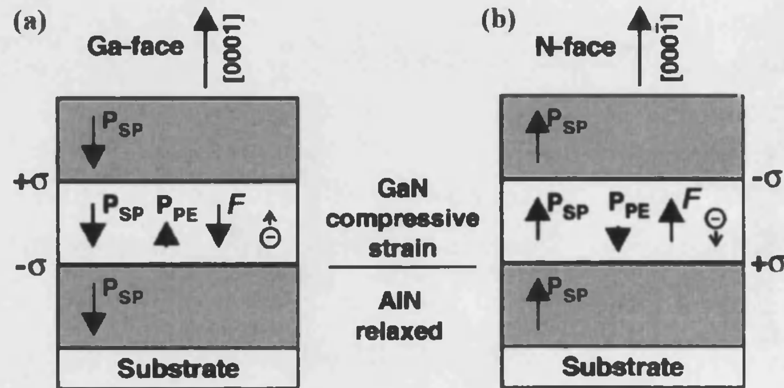

Figure 1.7: Polarization induced sheet charge density and directions of the spontaneous and piezoelectric polarizations, together with the resulting electric field, in Ga- (a) and N-face (b) compressive biaxial strained GaN/AlN heterostructures.

By applying Eq. 1.8, we obtain that $[e_{31} - e_{33}(C_{13}/C_{33})] < 0$ for GaN and AlN. Then, the piezoelectric polarization is negative for tensile and positive for compressive strained material. Furthermore, the spontaneous polarization for GaN and AlN was found to be negative [6], meaning that for Ga-face heterostructures it points towards the substrate. The directions of the spontaneous and piezoelectric polarization are given for GaN/AlN heterostructures, together with the direction of the resulting electric field $\boldsymbol{F}$ in Figure 1.7 depending on the polarity of the nanostructure: Ga-face (a) and N-face (b).

1.4.1 Quantum confined Stark effect

A consequence produced by the existence of internal electric fields is the appearance of the quantum confined Stark effect (QCSE) [33]. Quantum wells (QWs) grown along the crystallographic c-axis exhibit an internal electric field in the MV/cm range. This strong electric field pulls to opposite directions the electrons and holes, towards the interfaces of the QW. Their spatial separation causes a decrease of the overlap of the electron and hole wavefunctions, and in consequence a decrease of the radiative recombinations with respect to nonradiative ones, diminishing its optical efficiency. Additionally, due to the change in the potential profile, the energy of the optical transitions also decreases. This effect is significantly enhanced for thick QWs. One of the ways to prove the existence of the QCSE is performing photoluminescence experiments. This technique will be extensively explained in the next Chapter. But, for the moment we will describe the PL experiments performed by Craven *et al.* [34] on QWs grown along two different

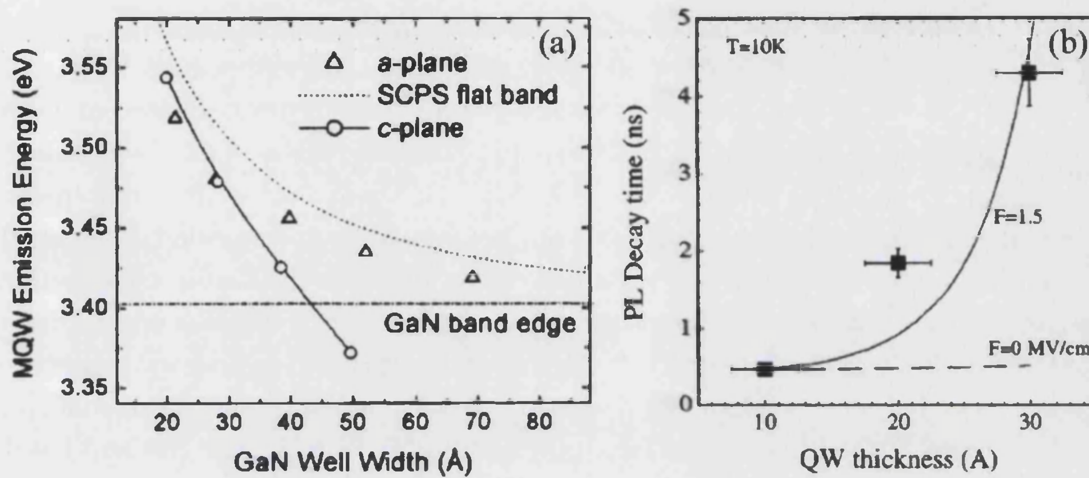

Figure 1.8: (a) Well width dependence of the room temperature PL emission energy of *a*- and *c*-plane QWs. The dotted line is the result of self-consistent Poisson-Schrödinger (SCPS) calculations. Images taken from [34]. (b) Experimental time decay constants (solid squares) as a function of QW thickness. Images taken from [35].

directions. Figure 1.8 (a) shows the PL emission at room temperature from *c*- and *a*-plane GaN/AlN quantum wells with circles and triangles respectively as a function of well thickness. The dashed-dotted line represents the energy of the band gap of GaN at room temperature of 3.44 eV [1]. We can observe that for very narrow nanostructures the confinement dominates over the effect of the electric field and the energy of the optical transitions is higher than the gap of bulk GaN for both orientations. For sufficiently large nanostructures the effect of confinement decreases and the electric field dominates. It is observed that the energy of the optical transitions for *c*-plane GaN/AlN quantum wells is below the gap of bulk GaN. On the other hand, the emission from *a*-plane GaN/AlN quantum wells is always above the gap of GaN for all QW thicknesses. This behavior indicates the absence of QCSE, characteristic of non-polar nanostructures [4]. Further evidence of the strong electric field present in *c*-QWs is provided by PL decay measurements at low temperature. In Fig. 1.8 (b), R. Langer *et al.* [35] plotted the PL decay time of the emission from various *c*-QWs with different thicknesses (d). We observe a strong increase of the PL decay time with increasing d, from a few hundred ps to several ns, a consequence of the spatial separation of electron and holes in the polar QWs.

1.5 Metal-Semiconductor contact

The electrical connections necessary for the development of devices based on GaN require high-quality contacts. Both ohmic and Schottky contacts can be obtained by the deposition of Ti/Al on n-GaN [36] after an adequate thermal treatement. However, the characteristics of the GaN surface states result in a Schottky contact with most metals, resulting in a rectifying behavior. It is the aim of this Section to introduce the principal physical processes involved in a metal-semiconductor contact, in order to understand the I-V characteristics of GaN nanowires investigated later in this work. A complete and extensive explanation of the concepts introduced in this Section can be found in the third edition of S. M. Sze and Kwok K. Ng [37].

1.5.1 The formation of a barrier

When a metal-semiconductor contact is made, a barrier between both materials is formed at the interface. Here, we will consider the basic energy-band diagrams leading to the formation of the barrier height and some effects that can modify the value of this barrier. A schematic view of the electronic bands at the contact, with indication of the parameters used for the description of its physical properties, is shown in Fig. 7.13. When a metal and a semiconductor are in contact, the charge starts flowing from the semiconductor to the metal until thermal equilibrium is established. In this situation the Fermi levels at both sides line up. Relative to the Fermi level in the metal, the Fermi level of the isolated semiconductor is lowered by an amount equal to the difference between the work functions of both materials. The work function is denoted by $q\phi_m$ for the metal, and is equal to $q(\chi+\phi_n)$ for the semiconductor, where $q\chi$ is the electron affinity measured from the bottom of the conduction band E_C to the vacuum level, and $q\phi_n$ is the energy difference between E_C and the Fermi level. The potential difference between the two work functions $q\phi_m - (\chi + \phi_n)$ represents the contact potential. As the separation between both materials, δ, decreases, the electric field in the gap increases and an increasing negative charge is built up at the metal surface. When δ is small enough to be comparable to the interatomic distances, the gap becomes transparent to electrons. It is clear that the limiting value of the barrier height $q\phi_{Bn0}$ is given by

$$q\phi_{Bn0} = q(\phi_m - \chi - \Delta). \tag{1.22}$$

where Δ is the potential across the interfacial layer. Electrons near the interface tend to diffuse into the metal region. As electrons diffuse, they leave positively

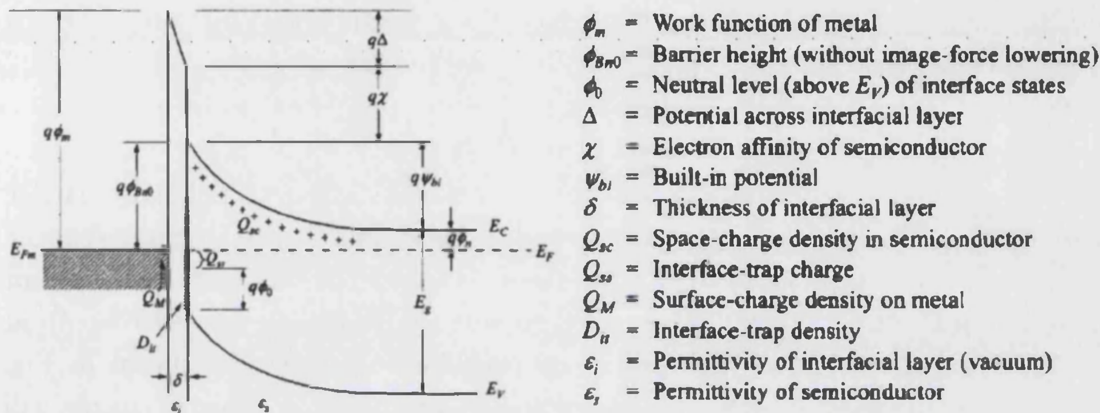

Figure 1.9: Schematic energy band diagram of a metal n-type semiconductor contact with an interfacial layer (vacuum) of the order of the atomic distances. Image extracted from [37].

charged ions in the n region. The regions nearby the junction interface lose their neutrality and become charged, forming the space charge region or depletion layer. The electric field created by the space charge region opposes the diffusion process. When the equilibrium is reached a potential difference, called built-in potential ($q\psi_{bi}$) is formed across the junction. If we polarize the metal-semiconductor system with a forward bias, V_F, the electrons in the n-type region are pushed towards the junction. This reduces the width of the depletion zone and the potential $q\psi_{bi}$ is also reduced by an amount of qV_F. Therefore the Schottky barrier decreases. If the metal-semiconductor system is reverse biased with a voltage qV_R, the voltage at the semiconductor is higher than that at the metal. Therefore, no current will flow until the junction breaks down. This increases the voltage barrier causing a high resistance to the flow of charge carriers, thus allowing minimal electric current to cross the junction. The increase in resistance of the junction results in the junction behaving as an insulator until the electric field intensity increases beyond a critical level. At that moment, the junction depletion zone breaks-down and current begins to flow, usually by either the Zener or avalanche breakdown processes. Both of these breakdown processes are non-destructive and are reversible. The barrier heights of metal-semiconductor systems are, in general, determined by both the metal work function and the interface states. For III-V compounds, extensive measurements using photoemission spectroscopy indicate that the Schottky-barrier formation is due mainly to defects generated near the interface by deposition of the metal [38]. It has been shown that on a few compound semiconductors such as GaAs, GaSb, and InP, the surface Fermi-level positions obtained from a number of metals are pinned at an energy level quite independent of the metal [39]. This pinning of surface Fermi level can explain the fact that for most III-V compounds,

the barrier height is essentially independent of the metal work function.

Images-Force lowering

The image-force lowering, also known as the Schottky effect or Schottky-barrier lowering, is the image-force-induced lowering of the barrier energy for charge carrier emission, in the presence of an electric field. Consider a metal-vacuum system first. The minimum energy necessary for an electron to escape into vacuum from an initial energy at the Fermi level is the work function $q\phi_m$ as shown in Fig. 7.13. When an electron is at a distance x from the metal, a positive charge will be induced on the metal surface. The force of attraction between the electron and the induced positive charge is equivalent to the force that would exist between the electron and an equal positive charge located at -x. This positive charge is referred to as the image charge. Making use of the attractive force, one can calculate the work done to an electron in the course of its transfer from infinity to the point x. This energy corresponds to the potential energy, *PE*, of an electron placed at a distance x from the metal surface, and is measured downwards from the x-axis. When an external field $\mathcal{E}$ is applied in the -x direction one can calculate the total potential energy, that *PE* has a maximum value. The image-force lowering $\Delta\phi$ and the location of the lowering x_m at the potential maximum are given by the condition $\frac{dPE}{dx} = 0$. Therefore:

$$x_m = \sqrt{\frac{q}{16\pi\varepsilon_0|\mathcal{E}|}} \text{ and } \Delta\phi = \sqrt{\frac{q|\mathcal{E}|}{4\pi\varepsilon_0}}, \tag{1.23}$$

where q correspond to the electron charge. Thus at high fields the Schottky barrier is considerably lowered, and the effective metal work fucntion is reduced. These results can be applied to metal-semiconductor systems. However, the field should be replaced by the appropriate field at the interface, and the free-space permittivity ε_0, should be replaced by an appropriate permittivity ε_s characterizing the semiconductor medium, that is:

$$\Delta\phi = \sqrt{\frac{q|\mathcal{E}|}{4\pi\varepsilon_s}}. \tag{1.24}$$

In a practical Schottky-barrier diode, the electric field is not constant with distance, and the maximum value at the surface based on the depletion approximation can be used:

$$\mathcal{E} = \sqrt{\frac{2qN_D\phi_0}{\varepsilon_s}}. \tag{1.25}$$

An finally, substituting this $\mathcal{E}$ into the Eq. 1.24 we obtain:

$$\Delta\phi = \sqrt{\frac{q|\mathcal{E}|}{4\pi\varepsilon_s}} = \left[\frac{q^3 N_D \phi_0}{8\pi^2\varepsilon_s^3}\right]^{1/4}. \tag{1.26}$$

1.5.2 Current transport processes

Current transport in metal-semiconductor contacts is mainly due to majority carriers. Figure 1.10 shows five basic transport processes under forward bias: (1) Emission of electrons from the semiconductor over the potential barrier into the metal. This process is dominant in Schottky diodes with moderately doped semiconductors operated at moderate temperatures such as 300 K. (2) Quantum mechanical tunneling of electrons through the barrier. This process is very important for heavily doped semiconductors and it is responsible for most ohmic contacts. (3) Rccombination in the space-charge region. (4) Diffusion of electrons in the depletion region. (5) Holes injected from the metal that diffuse into the semiconductor. In addition, we may have edge leakage current due to a high electric field at the metal-contact periphery or interface current due to traps at the metal-semiconductor interface. For common high-mobility semiconductors the transport can be adequately described by the thermionic-emission-diffusion theory, which is a combination between the thermionic-emission and the diffusion theories.

In order to complete our description of the meta-contact and transport processes, finally we will present the tunneling current, which is significant in heavily doped semiconductors.

Thermionic-Emission-Diffusion theory

The thermionic-emission theory is derived from three assumptions: the barrier height $q\phi_{Bn}$ is much larger than kT, the thermal equilibrium is established at the plane that determines emission, and the existence of a net current flow does not affect this equilibrium. We can then superimpose two current fluxes: one from metal to semiconductor and its inverse, each described by a different quasi Fermi level. If thermionic emission is the limiting mechanism, when E_{Fn} is flat throughout the depletion region (see Fig. 1.10). Additionally, the diffusion theory gives account of the effect of electron collisions within the depletion region. We consider that the carrier concentrations are unaffected by the current flow and that the impurity concentration of the semiconductor is non degenerate. The synthesis of thermionic-emission and diffusion approaches is derived from the boundary

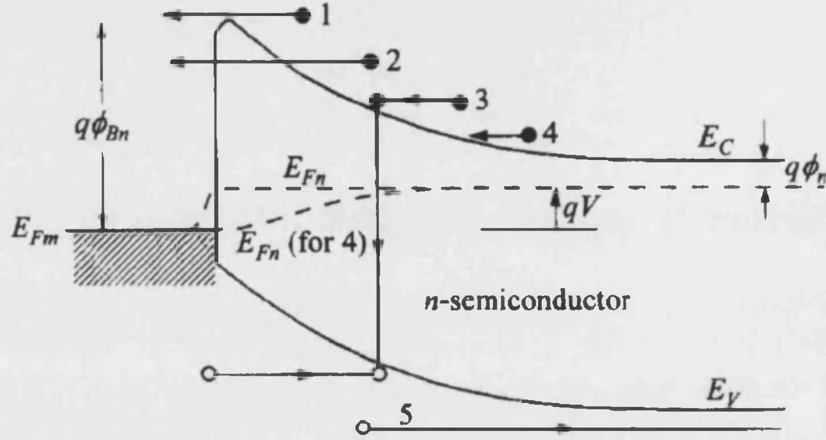

Figure 1.10: Five basic transport processes under forward bias, (1) Thermionic emission, (2) Tunneling, (3) Recombination, (4) Diffusion of electrons and (5) Diffusion of holes. Image extracted from [37].

condition of a thermionic recombination velocity v_R near the metal-semiconductor interface. We consider the case where the barrier height $q\phi_{Bn}$ is larger than the energy given by the charge density between the metal surface and the end of the depletion region. In that case, an applied voltage $V > 0$ between the metal and the semiconductor will decrease the barrier by an amount qV, and it will produce a flow of electrons towards the metal. We can describe the current flow in terms of an effective recombination velocity v_R. Hence, the electron density when the current is flowing will be described by:

$$n_0 = N_C \exp\left(-\frac{q\phi_{Bn}}{kT}\right). \tag{1.27}$$

where N_C is the effective density of states in the conduction band. Taking as boundary condition $E_{Fm} = 0$, an expression for the current density across the junction is obtained:

$$J_{TED} = A^{**}T^2 \exp\left(-\frac{q\phi_{Bn}}{kT}\right)\left[\exp\left(\frac{qV}{kT}\right) - 1\right]. \tag{1.28}$$

In this equation, A^{**} is the reduced effective Richardson constant given by the following equation:

$$A^{**} = \frac{4\pi e k_B^2 m_e^*}{h^3} = 120\left(\frac{m_e^*}{m_e}\right), \tag{1.29}$$

where m_e^* is the GaN electron effective mass.

Tunneling Current and measurement of barrier height

For more heavily doped semiconductors, the tunneling current may become more significant. In the extreme case of an ohmic contact, which can be described as a metal contact on a degenerate semiconductor, the tunneling current is the dominant transport process. The tunneling current from semiconductor to metal is proportional to the quantum transmission coefficient (tunneling probability) multiplied by the occupation probability of the electronic states of the semiconductor and the probability of unoccupied states in the metal. We note that the total current density, which consists of both thermionic emission and tunneling, can be conveniently expressed as

$$J = J_0 \left[\exp\left(\frac{qV}{\eta kT} \right) - 1 \right] . \tag{1.30}$$

where J_0 is the saturation current density obtained by extrapolating the current density from the log-linear plot to $V = 0$, and η is the ideality factor, related to the slope. With little or no tunneling current or depletion-layer recombination, J_0 is determined by the value given by the thermionic emission and η is close to unity. For moderately doped semiconductors, the I-V characteristics in the forward direction is given by Eq. 1.28. Since both A^{**} and $\Delta\phi$ (image-force lowering) are weak functions of the applied voltage, the forward J-V characteristics are represented by Eq. 1.30. The extrapolated value of current density at zero voltage is the saturation current J_0, and the barrier height can be obtained from the equation

$$\phi_{Bn} = \frac{kT}{q} \ln\left(\frac{A^{**}T^2}{J_0} \right) . \tag{1.31}$$

The value of ϕ_{Bn} is not very sensitive to the choice of A^{**}. The theoretical relationship between J_0 and ϕ_{Bn} at room temperature indicates that for an increase of J_0 the corresponding ϕ_{Bn} should decrease.

1.5.3 Ohmic contact

An ohmic contact is defined as a metal-semiconductor contact that has a negligible junction resistance relative to the total resistance of the semiconductor device. The macroscopic parameter-specific contact resistance is defined as the reciprocal of the derivative of the current density with respect to the voltage across the interface. When evaluated at zero bias, this specific contact resistance R_c is an important

figure-of-merit for ohmic contacts:

$$R_c \equiv \left(\frac{dJ}{dV}\right)^{-1}_{V=0}. \tag{1.32}$$

To derive the value of R_c analytically, the I-V relationships described earlier can be used. For low to moderate doping levels, the standard thermionic-emission expression (Eq. 1.28) is used to obtain

$$R_c = \frac{k}{A^{**}Tq} \exp\left(\frac{q\phi_{Bn}}{kT}\right). \tag{1.33}$$

Since only the case of small applied voltages is relevant, the voltage dependence of the barrier height can be neglected. Equation 1.33 shows that in order to obtain low values of R_c, high doping concentration, low barrier height, or both must be present. It has to be noted that the total contact resistance will increase with decreasing contact area. In our experiments, we will perform conductive measurements by using an atomic force microscopy metal coated tip. This kind of tips present a radius around 20 nm and the contact area will depend on the normal force applied between the tip and the sample. In range used in our experiments we expect a contact area of the order of $50 \cdot 10^{-14}$ cm^{-2} regarding the tip indentation. The set up of this experiment will be shown at the end of the next Chapter.

This Chapter contains a description of the fundamental properties of the group III-nitrides semiconductors. We have presented the general characteristics of the wurtzite crystalline structure, including the origin of the polarization along the c-axis. In particular, the structural properties of GaN have been given. The electronic properties of GaN have been addressed, including the effect of strain on the electronic band structure. The polarization selection rules of the optical transitions for bulk GaN were studied. Regarding the vibrational properties, the phonon modes of wurtzite GaN and AlN have been described. A Section has been dedicated to expose the influence of strain on the vibrational properties. In addition, the phonon-plasmon coupling and its consequences on the vibrational modes of doped nanostructures has been shown. We have presented the consequences on the optical properties of the internal electric field that appears in GaN/AlN heterostructures, and in consequence, the quantum confined Stark effect is described with the aid of experimental examples. Finally, the metal-semiconductor Schottky and ohmic contacts have been described through the Thermionic-Emission-Diffusion theory. The different processes involved in charge transport have been considered.

UNIVERSITAT DE VALÈNCIA BIBLIOTECA DE CIÈNCIES

Chapter 2

Growth and characterization techniques

This Chapter describes the main experimental methods that we use in this Thesis, pointing out as well the most important elements to perform the growth of the samples. At first, we describe the plasma assisted molecular beam epitaxy growth (PA-MBE). An introduction about reflection high energy electron diffraction in grazing incidence (RHEED) will be given. We will continue with *ex-situ* methods used to characterize the samples such as: scanning electron microscopy (SEM), technique used to study the morphology of the grown samples; photoluminescence (PL) used for the optical characterization; and μ-Raman Scattering (RS) used for structural characterization through the study of lattice vibrations. Finally, we will introduce the basic concepts of atomic force microscopy (AFM). This last technique will be used for morphological characterization as well as for electrical measurements.

2.1 Plasma Assisted Molecular Beam Epitaxy

Molecular beam epitaxy (MBE) was developed in the early 1970s as a means of growing high-purity epitaxial layers of compound semiconductors by A. Cho and J. Arthur [40, 41]. The word epitaxy is a contraction of two Greek words, *epi* signifying lie on and *taxis* signifying the arrangement. There are different types of epitaxial techniques, like Metal-Organic Chemical Vapour Deposition, Liquid Phase Epitaxy or MBE. In this Section we will describe the different parts of an MBE machine and their functionality, since it is the technique used for the growth of the samples studied in this work.

2.1.1 Principle of Molecular Beam Epitaxy

MBE technique produces epitaxial layers growth by the deposition of atoms of different species onto a heated crystalline substrate. The substrate is selected according to its crystallographic parameters and orientation. The molecular beams are produced by heating the elemental sources in separate effusion cells. The cells are also known as Knudsen cells and they can be schematically seen in Fig. 2.1. In the case of nitrides, the solid effusion cells are usually filled with metals of group III, as well as with Mg or Si elements for p- and n-type doping, respectively. Adjusting the cell temperature, it is possible to control the atomic flux. Each cell is equipped with a shutter, which responds in fractions of second. The rapid movement of the shutter allows to change the effused material almost instantly. In this way, it is possible to grow heterostructures with abrupt interfaces. To provide atomic N, a radio frequency (RF) plasma generator is used. The plasma is formed by the inductive coupling of the RF energy into a discharge chamber filled with nitrogen gas to a pressure in the 10^{-4} Torr range.

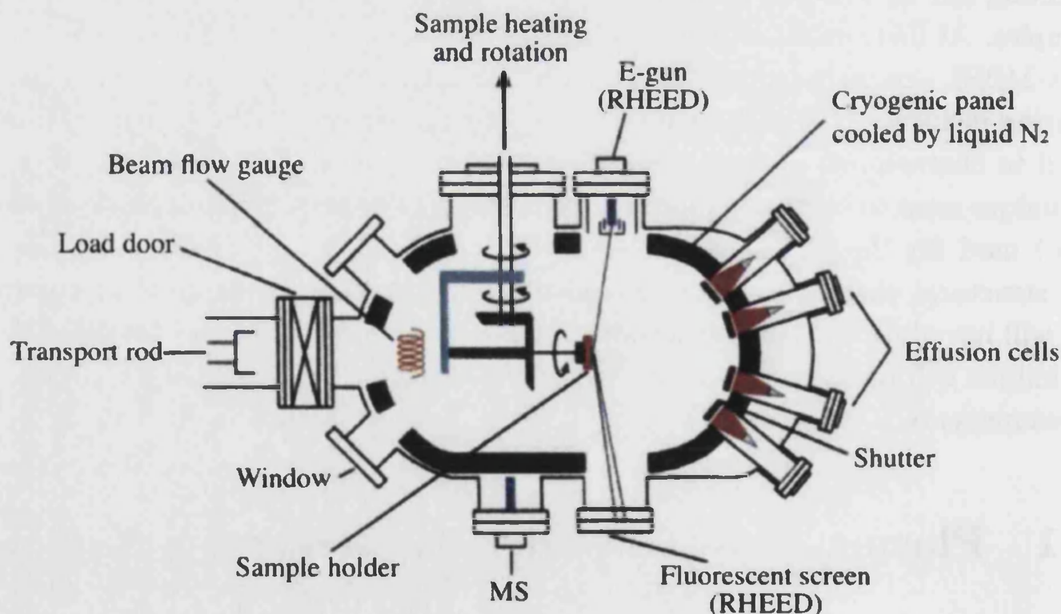

Figure 2.1: Diagram of a typical MBE growth chamber. All the main components are labeled.

To ensure that the reaction takes place on the substrate, the mean free path d of the particles in the effused beams should be larger than the geometrical size of the chamber. If one considers the mean free path as the distance between collisions, using kinetic theory of gases one can estimate that $d \propto 1/n\sigma$, where n is the atom

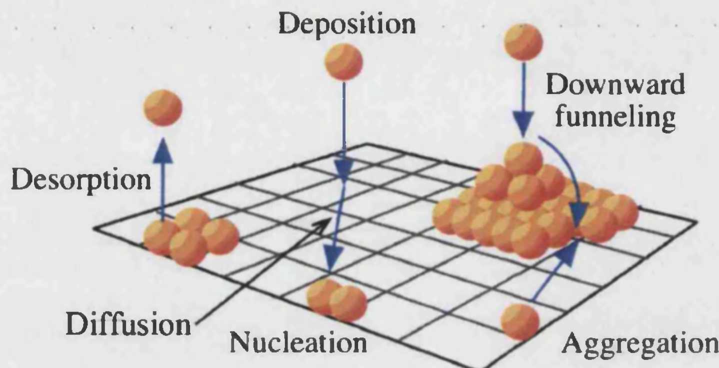

Figure 2.2: Schematic diagram of the principals processes involved during MBE growth.

concentration and σ the cross section per collision. In the case of commercial MBE chambers, atomic diffusion fulfills this simple relation provided that the pressure does not exceed 10^{-5} Torr.

The composition and morphology of the grown structure depends, mainly, on the flux rates of the constituent elements and the growth temperature. The growth rate is typically several hundreds of nanometers per hour. The most relevant processes involved during growth are graphically shown in Fig. 2.2. The atoms of the incoming beams from the Knudsen cells are deposited on the substrate. They can diffuse until they nucleate with other atomic constituent or aggregate to already formed 2D layers or nuclei. The diffusion rate increases with increasing temperature. However, it can also contribute against the nucleation or aggregation by increasing the desorption rate.

Some of the processes described above, such as incorporation or nucleation will depend strongly on the type of surface used for the growth process. A very clean surface is usually needed to reach proper growth, and the substrate used will play an important role. Among the most relevant substrates used for growing nitride semiconductors we have Sapphire (Al_2O_4), 6H-SiC or Si(111). However, the lattice mismatch between these substrates and nitrides is quite large, resulting in a large dislocation density of the nitride epilayer. In order to reduce the dislocation density, a usual procedure is to deposit a 2D layer of a material with intermediate lattice mismatch prior to nanostructure growth. This layer is named buffer layer. To give an overview about the mismatch of the materials used in this work, we list in Table 2.1 the mismatch in percentage between GaN and AlN and different substrates. The lattice mismatch for the lattice parameter a is shown in the upper part of the Table, and that for the lattice parameter c at the bottom.

a lattice mismatch(%)	GaN	AlN	6H-SiC	Si(111)
GaN	0	-2.4	-3.6	20.4
AlN	2.4	0.0	-1.2	23.4
c lattice mismatch(%)	GaN	AlN	6H-SiC	Si(111)
GaN	0	-3.9	-3.1	-9.3
AlN	3.9	0.0	0.0	-5.6

Table 2.1: Mismatch in percentage (%) between the materials used for the nanostructure, GaN and AlN in the first column, and different substrates. The lattice mismatch along the [0001] direction is shown in the upper part, and along the $[11\bar{2}0]$ direction in the bottom part.

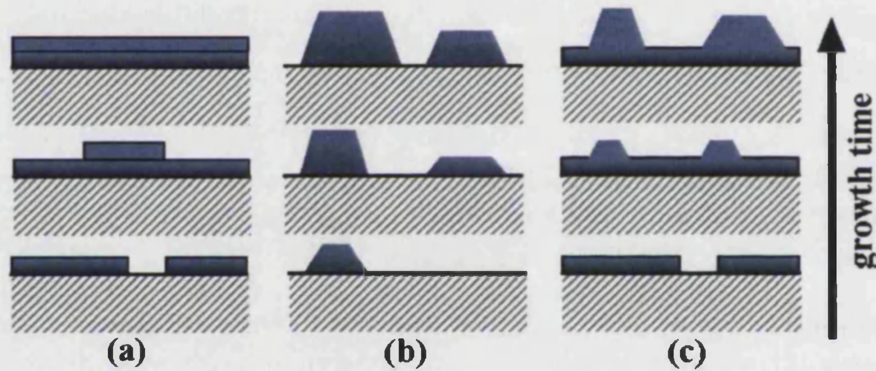

Figure 2.3: Schematic representation of the three crystal growth modes. On the left, we show the growth mode layer by layer named Frank-van der Merwe (a), in the middle Volmer-Weber growth (b). Finally we represent the Stranski-Krastanov growth mode (c). Figure taken from [42].

In epitaxy we can distinguish three possible crystal growth modes. Figure 2.3 shows them schematically. The case (a) is named Frank-van der Merwe. It corresponds to a full wetting of the substrate and the continuous deposition layer by layer of the growing material up to a critical thickness. For larger thickness the 2D layer relaxes the accumulated elastic energy by dislocation formation. The next growth mode (b) is by formation of islands and is called Volmer-Weber. In this growth mode the atoms do not wet the substrate, so that they cannot form a continuous 2D layer on it. They diffuse until their nucleation, forming many different 3D islands that grow independently. Finally, in the Stranski-Krastanow mode, shown schematically in (c), growth starts in a similar way as in (a), that is, by the layer by layer deposition of the growing material. The difference is that, once the critical thickness is reached, the elastic energy accumulated during growth does not relax plastically. Instead, the growth mode changes from a 2D growth mode to the formation of 3D islands. In this case, the 3D islands grow on a thin (1 or 2 monolayers thick) 2D layer called wetting layer.

2.1.2 Experimental equipment

In this Section we describe the different parts of a MBE machine together with their functionalities. For the growth of the samples described in this work experiments we have used a MECA2000 MBE provided with an Applied EPI Unibulb RF plasma cell. The growth machine belongs to the semiconductors group of CEA (Grenoble) and was used under the supervision of Dr. Bruno Daudin. In order to cite all the parts of the machine we will follow the path followed for the growth of a new sample, starting from the introduction of a new substrate until the finished sample comes out from the main chamber. It is important to note that growth must be performed in an ultra high vacuum (UHV) environment. To keep the vacuum level low in the main chamber, the MBE machine consists of several chambers separated by valves. Each chamber is equipped with its own vacuum system. The photography on the right part of Fig. 2.4 shows from right to left the path followed by the substrate through the different chambers. In first place, a transfer chamber is separated from both the main and the pre-chamber by valves. This chamber is equipped with a turbo molecular pump together with a mechanical pump, so that vacuum levels as high as 10^{-7} Torr can be reached. The transfer chamber is used to introduce new substrates and to transfer out the already grown samples. Once the new substrate is loaded into transfer chamber and evacuation has taken place, it can be transferred to the pre-chamber. The pre-chamber is equipped with a ionic pump that can reach vacuum levels of 10^{-9} Torr. Once the proper vacuum level has been reached, the sample can be transferred to the main chamber. In this way, a high vacuum level is always maintained in the main chamber, where the pressure can be in the order of 10^{-10} Torr. On the left part of the Fig. 2.4 we show a photography of the back side of the main chamber, where the effusion cells can be clearly distinguished.

Additionally to the mechanical pumps, the main chamber is equipped with cryogenic panels that can be localized in the sketch of Fig. 2.1. By the continuous flow of liquid nitrogen at 77 K, the unwanted particles of the chamber will be trapped, decreasing their kinetic energy by the low temperature. In this way, the sample holder region maintains a clean environment.

Reflection high energy electron diffraction

The reflection high energy electron diffraction (RHEED) is one of the most useful tools in the MBE growth systems. It allows the *in situ* control of growth [43]. This technique is based on the interaction of a high energy (10-50 keV) electron beam with the grown surface, falling at grazing incidence (0.5-2°). The electrons

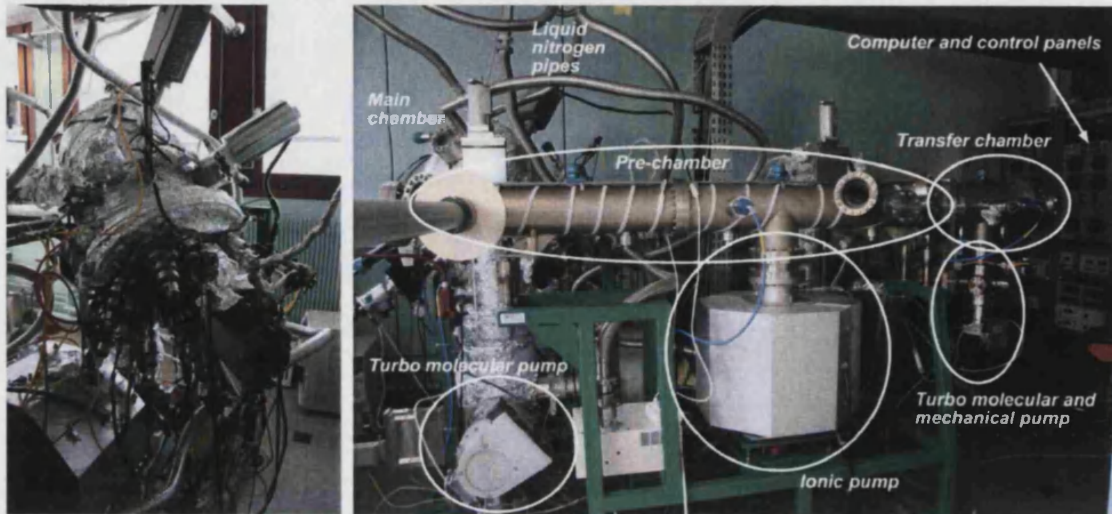

Figure 2.4: On the left, the back side of the main chamber, where the effusion cells can be seen. The photography on the right shows the different parts of a complete MBE machine. The transfer chamber, the pre-chamber and the different pumps of the vacuum system are labeled. The control computer, control panels and the main chamber are located at the background. The pipes from the roof are used to provide the liquid nitrogen for the cryogenic panels. With permission from CEA.

elastically dispersed form a diffraction pattern on a fluorescence screen located in front of the electron gun. The emplacement of the gun source and the fluorescence screen can be appreciated in Fig. 2.1. The diffraction pattern can be captured by a CCD camera and represented on a monitor. Due to the small angle between the electron beam and the surface of the substrate, the interaction region is limited to the surface. In the case of the growth of 2D layers the electrons will interact only with the first monolayers. However, in the case of 3D nanostructures, such as nanowires or quantum dots, the electrons will totally cross the nanostructures. In this case, as shown in Fig. 2.5, the technique may provide information of nanostructure alignment. Commonly, RHEED is used in different situations: before growth starts, in order to verify a very clean substrate surface; to control the initial growth stadium; to observe changes in the surface when growing heterostructures or to monitor growth stability. The intensity and shape of the diffraction patterns depend on the distribution of the dispersion centers in the surface of the crystal. By their analysis, RHEED diagrams provide qualitative information about the crystallinity and topology of the grown material. Regarding the crystallinity, the RHEED diagram of a monocrystalline 2D layer if formed by thin and bright streaks, with a separation between them characteristic of the material. In the case of two different crystalline orientations, the diagram can be described by the superposition of two such RHEED diagrams. The topology of the surface can be also be

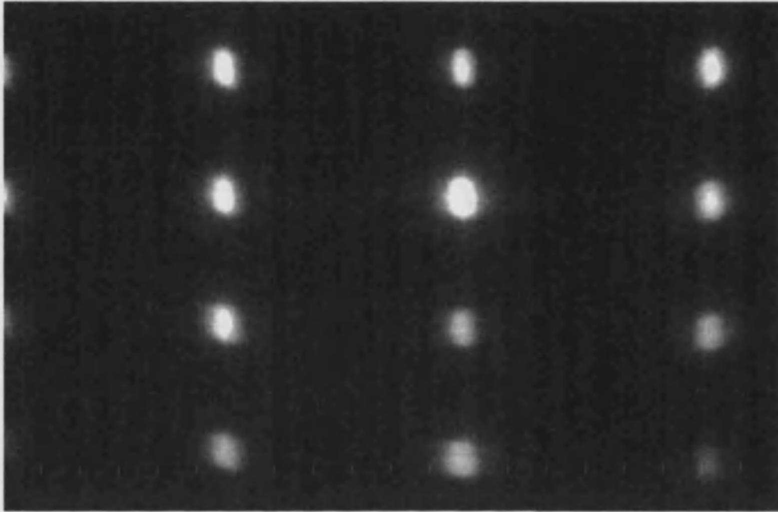

Figure 2.5: Spotty RHEED pattern characteristic of long GaN NWrs grown on Si(111) after the deposition of a thin AlN buffer layer. The slightly bright lines between spots are characteristic of very well aligned NWrs.

checked through the analysis of the corresponding RHEED diagram. For example, a rough surface produces a diffraction of the electron beam along the three spacial directions. This shows up as shiny spots in the RHEED pattern. The Figure 2.5 represents a characteristic RHEED pattern of well aligned long GaN NWrs. The bright spots correspond to 3-dimensional growth. The lightly bright lines between the dots in the RHEED pattern correspond to the reflections on the walls of the NWrs, indicating that these walls are parallel to each other [44]. Consequently, the nanowires are well aligned.

2.2 Scanning electron microscopy

The scanning electron microscopy (SEM) is a type of electron microscopy that images the sample surfaces by scanning them with a high energy electron beam. The electrons interact with the atoms of the sample producing signals that contain information about the surface topography, composition, electrical conductivity, etc. The first SEM image was obtained by Max Knoll in 1935. The signals produced by a SEM include secondary electrons, back-scattered electrons, characteristic X-rays, light and current. We will focus here our attention only on the process we have explored in our work: image formation by the extraction of secondary electrons.

2.2.1 Principles of scanning electron microscopy

An electron beam is thermodynamically emitted from a heated tungsten filament. Tungsten is chosen because it has the highest melting point and lowest vapor pressure of all the metals. The electron beam can be tuned in an energy range from 0.5 to 40 keV and is focused on the sample by several condenser lenses to a spot with a diameter between 0.4 and 5 nm. At the end of the electron column, scanning coils or deflector plates deflect the beam in the x and y axis in order to scan a square area on the sample's surface. When the primary electrons interact with the sample, the electrons lose energy by absorption and scattering within a droplet-like shaped volume. This droplet-like volume is known as the interaction volume. The dimensions of this excitation volume are close to the value of the penetration depth or range of primary electrons. According Ref. [45], the penetration depth R_e can be defined as:

$$R_e = \frac{0.0276A}{\rho Z^{0.889}} E_0^{1.67} [\mu\text{m}], \tag{2.1}$$

where A is the atomic weight in g·mol^{-1}, ρ is the density of the material in g·cm^{-3}, Z is the atomic number and E_0 is the electron probe energy in keV.

In order to illustrate the interaction volumen, in Fig. 2.6 we represent the penetration of an electron beam of 5 nm diameter with 5 keV of energy into a GaN bulk sample obtained using the Monte-Carlo simulation method [46]. On the right, the penetration distance is indicated in the images and it corresponds to ~200 nm.

Along the penetration path, the primary electrons exchange energy with the specimen. As a result of this interaction, different processes take place: the reflection of high energy electrons (elastic scattering), the emission of secondary electrons (inelastic scattering) and the emission of electromagnetic radiation (luminescence). Besides these processes, the beam creates a current through the sample. For that reason, it must be prepared adequately: for conventional imaging in SEM, the samples must be electrically conductive, at least at the surface, and electrically grounded to prevent the accumulation of electrostatic charge at the surface. Non conductive specimens tend to charge when scanned and this causes scanning faults and other image artifacts. To avoid this, non conductive samples are covered by a thin layer of gold ir order to improve their conductivity.

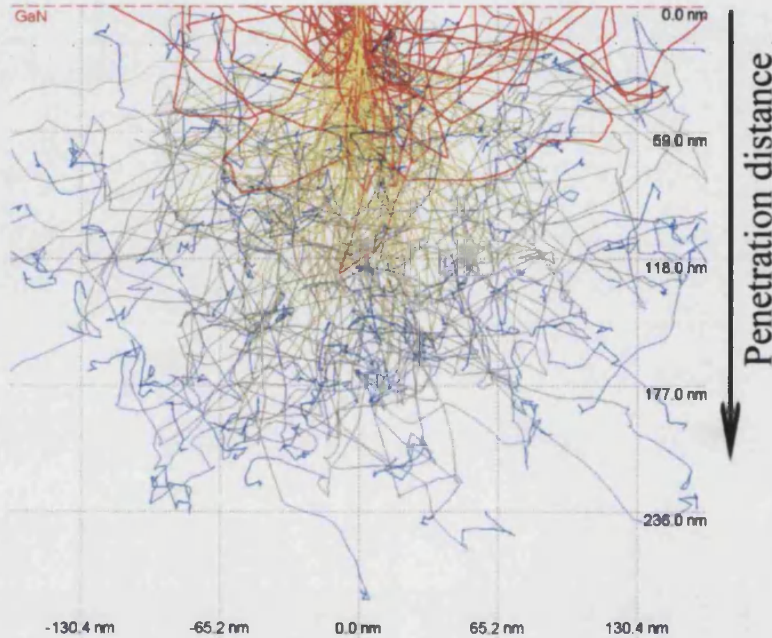

Figure 2.6: Monte-Carlo representation of the interaction volume in a GaN bulk sample. The simulated beam has a spot of 5 nm diameter and 5 keV energy. The lines represent the trajectories of the primary electrons. Colors red, yellow and blue represent, from high to low, the energy of the electrons.

2.2.2 Imaging the topography

The most common imaging mode collects low energy secondary electrons. These electrons are ejected from the external orbitals of the atoms after their inelastic interaction with the beam electrons. Due to their low energy, only the electrons that are a few nanometer away from the surface can escape from it. The mean rate of electron energy loss per unit length of its path s in the solid, with all the dissipation mechanisms included, can be described by Bethe's expression as:

$$\frac{dE}{ds} = -2\pi e^4 N_A \frac{\rho Z}{EA} \ln \frac{1.166E}{J}, \tag{2.2}$$

where e is the electron charge, N_A Avogadro's number, ρ is the density of the object material, A the atomic weight, Z the atomic number, E the mean electron energy and J the mean ionization potential. Once these secondary electrons are ejected from the surface, they are attracted toward the collectors, that produce an electric field about +400 V. Then, they are further accelerated towards a scintillator positively biased by +2000 V. The electrons are detected by an Everhart-Thornley detector [47] which is a type of scintillator-photomultiplier system. The electrons have sufficient energy to cause the scintillator to emit flashes, which are collected

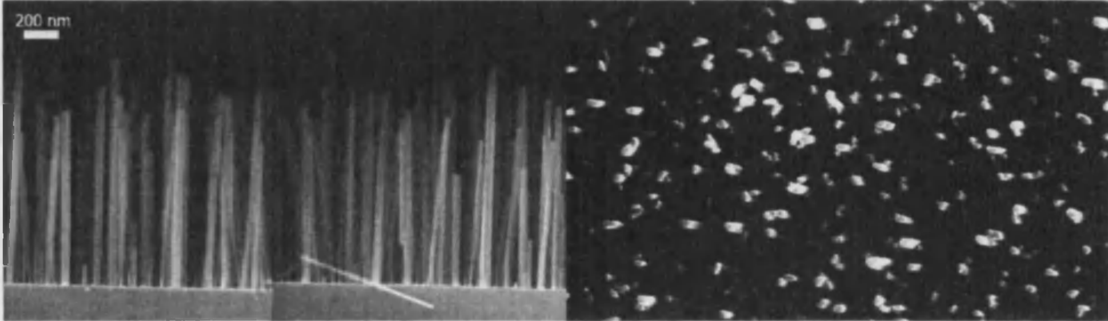

Figure 2.7: SEM picture of GaN NWrs in cross section and top view.

by a photomultiplier outside the SEM column. The light signal is converted and amplified in electrical signal by the photomultiplier. It is displayed as a two-dimensional intensity distribution that can be digitalized as image of topography. Figure 2.7 shows the SEM images of GaN NWrs characteristic of the samples studied in this work. Both cross section and top view are shown from left to right respectively.

The brightness of the signal depends on the number of secondary electrons that reach the detector. If the beam enters perpendicular to the surface of the specimen, the interaction volume will be symmetric with respect to the beam and a certain number of electrons will escape from the sample. As the angle of incidence decreases, the escape distance of one side of the interaction volume will decrease. In consequence, more secondary electrons will be emitted from that side. For a similar reason, steep surface and edges tend to shine more than flat surfaces, resulting in images with a well defined three dimensional visual effect. In Fig. 2.7 (right) we can observe GaN NWrs from top view. The bright effect on the edges of the NWrs is clearly visible. In the cross section view (left), a 3D visual effect can be seen. The first line of NWrs is brighter than the lines of wires behind. The resolution of this technique can reach values smaller than 0.5 nm in the scanning plane. However, the resolution along the z axis (depth) is very poor, although the 3D effect is present. For the SEM images performed in this work, we used a microscope Zeiss model Ultra 55 presented in Fig. 2.8.

2.3 Photoluminescence

Photoluminescence (PL) spectroscopy is a non-destructive technique that can be used to analyze intrinsic and the extrinsic properties of semiconductors. PL concerns the radiation emitted by a material after excitation with an electromagnetic

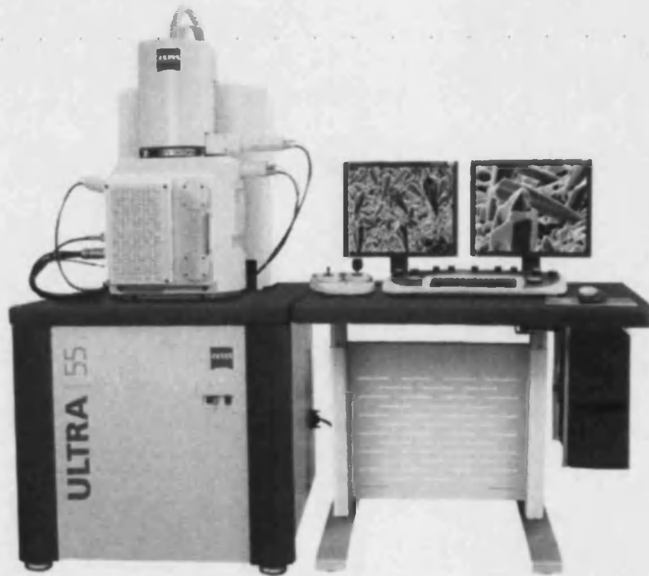

Figure 2.8: Photography of the SEM system used in this work. Image taken from [48].

wave with energy above the band gap. General information about the optical properties of the material can be obtained by the analysis of the PL spectrum as a function of different parameters, such as temperature, excitation energy, excitation intensity, magnetic field, etc. These characteristics render this technique very useful in the field of material science and solid state physics. To mention some examples, PL can be used as a simple feedback characterization technique to study the effect of the variation of the growth parameters on the optical properties. It also gives indications on the defects involved or produced by typical processing steps and by post-growth treatments.

Photoexcitation

Fig. 7.14(a) shows a schematic diagram of all the processes involved during PL. Photons are absorbed from a monocromatic excitation source, usually a laser, which energy $h\nu_L$ is larger than the band gap of the material. Their energy is transferred to the electrons, which can reach the conduction band, leaving a hole in the valence band. Depending on the material electronic structure, absorption can take place through direct transitions, where the electron does not change its wavevector, or through indirect transitions, where the electron changes its wavevector by it interaction with a phonon. Since GaN has a direct band-gap, the transitions will be direct.

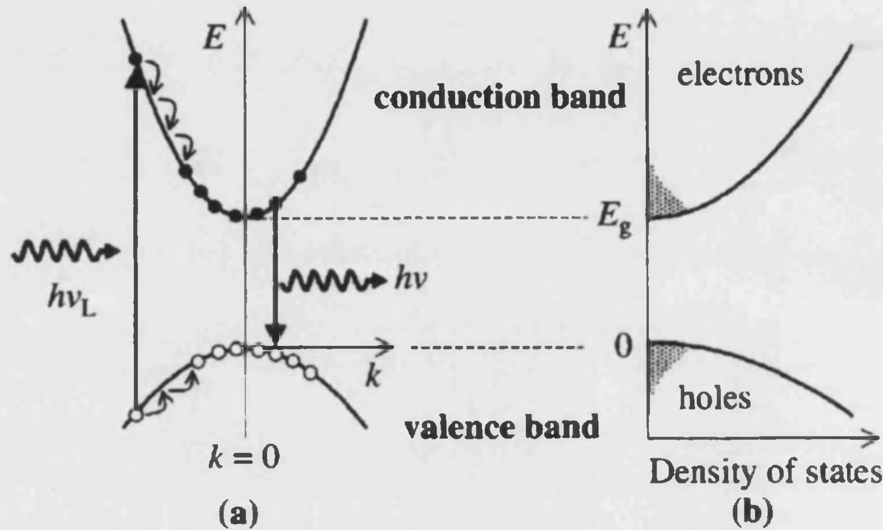

Figure 2.9: Sketch of the different processes involved during photoluminescence: excitation, thermalization and recombination (a). Part (b) of the figure represent the density of states (DOS) of electrons and holes. Images taken from [49].

Thermalization and diffusion

Once the electrons are photoexcited through the band gap, they transfer energy to the crystal lattice by thermalization. In a first stage, a very rapid relaxation occurs. The carriers partially lose their excess energy by collisions among themselves. They reach a hot thermal distribution characterized by a temperature different from that of the lattice (hot carriers). In a second stage, the hot distribution cools down towards the lattice temperature releasing optical phonons until they are no longer efficient to remove the excess energy. The first two stages span a time interval shorter than 100 ps. The third stage concerns the final cooling of the electrons to the lattice temperature through acoustic phonon emission and occurs on the nanosecond scale. This last stage is in competition with the depletion of the e-h pairs by recombination. As a consequence, the high energy tail of band-gap luminescence gives a direct indication of the carrier temperature T_e; in fact, it is expected to decrease exponentially with increasing energy, according to [50], following the equation:

$$I(\hbar\omega) \propto e^{-(\hbar\omega - E_g)/k_B T_e}, \tag{2.3}$$

where k_B is the Boltzmann constant. Moreover, in the case of high power excitation, the effective e-h pair temperature is usually larger than that of the lattice, since the thermalization time through emission of acoustic phonons is longer than that characteristic of the generation of e-h pairs.

Related with the thermalization process is the diffusion of the carriers. At the same time that they thermalize, they move through the lattice. In consequence, they can be trapped at impurities or defects, or may reach the interfaces o surfaces of the heterostructure, where non-radiative processes dominate.

Recombination

After the processes described above, the electrons and holes can reach the bottom of the conduction band and the top of the valence bands respectively, from where they can recombine in two ways: radiatively, when the excess of energy is released by the emission of a photon, or non radiatively, that is, transferring their energy through other processes such as interaction with the lattice. The radiative recombination is characterized by the minority carrier radiative lifetime τ_r. This lifetime depends on the carrier concentration, including intrinsic and excited carriers. On the other hand, the non-radiative recombination is characterized by the non radiative lifetime τ_{nr}. Thus, the total decay rate of the emitted photons by the recombination of e-h pairs is given by the total lifetime τ_{tot} of the recombination [51]:

$$\frac{1}{\tau_{tot}} = \frac{1}{\tau_{nr}} + \frac{1}{\tau_r}, \tag{2.4}$$

The internal efficiency of the material is defined as:

$$\eta = \frac{\tau_{nr}}{\tau_r + \tau_{nr}}. \tag{2.5}$$

Taking this into account, one can consider that a material is a good emitter when $\tau_r \ll \tau_{nr}$. In the following, we shall expose the elementary relation between the PL energy peak, line width and spectral dependence corresponding to the following radiative recombination channels: band-to-band transition, free excitonic transitions, bound excitonic emission, donor-acceptor pair recombination and free to bound recombination.

At intermediate and high temperatures, when bound states are ionized, the photoexcited carriers can recombine via band-to-band recombination. Considering a direct band gap semiconductor and assuming parabolic bands, the energy peak and the ful width at half maximum (FWHM) of these transitions are [50]:

$$h\nu_{CB-VB} = E_g + \frac{1}{2}k_BT, \text{ and FWHM} = 1.8k_BT. \tag{2.6}$$

Excitons are formed by the binding of electrons and holes through the Coulomb

interaction. This interaction reduces the energy of the electron-hole pair by an amount E_X and the emission occurs below the band gap energy. The energy of the emission is given by:

$$h\nu_X = E_g - \frac{R_X}{n^2} = E_g - E_X, \tag{2.7}$$

where $R_X = \frac{\mu}{m_0 \epsilon} R_H$ and accounts for the strength of the electron-hole interaction, with R_H the Rydberg energy. n is the principal quantum number, ϵ is the dielectric constant of the material, and $\mu = \frac{m_e m_h}{m_e + m_h}$ is the exciton reduced mass. Here, m_e and m_h are the effective electron and hole masses at the Γ point [49]. In general, the small value of the exciton binding energy makes it difficult to observe the emission corresponding to excited excitonic states ($n > 1$). However, at low temperature the $n = 1$ excitonic recombination dominates the band-gap luminescence spectrum.

A free exciton that travels through the lattice can be localized on a neutral or ionized donor or acceptor, giving place to the so-called exciton bound to impurity complex. An exciton bound to an ionized donor, conventionally indicated as (D^+X), is a complex consisting of a donor ion, an electron and a hole; an exciton bound to a neutral donor, conventionally denoted as (D^0X), consists of a donor ion, two electrons and a hole. The description of an exciton bound to an ionized (A^+X) or to a neutral (A^0X) acceptor is analogous, but substituting the electrons by holes. The recombination of bound excitons is an important recombination process in the near band edge spectral region as the donor or acceptor concentration is increased from very low levels. These transitions dominate the low temperature band edge PL spectra and their transition energies correspond to:

$$h\nu_{BX} = E_g - E_X - E_{BX}. \tag{2.8}$$

E_{BX} is the exciton localization energy, that is, the energy required to remove the exciton from the impurity. It may differ from one impurity to another. In general, the donor ionization energy E_D is smaller than the acceptor ionization energy E_A, at least in direct gap semiconductors. It is therefore expected that the PL signal originating from donor bound exciton recombination lies closer to the free exciton recombination than that of the acceptor bound exciton. Experimentally, it is observed that the bound exciton recombination line is narrower than the corresponding free exciton line. This is ascribed to the fact that the exciton localization at the impurity reduces the contribution to the broadening due to impurities, disorder, defects and thermal energy in the crystal lattice,increasing the lifetime of the complex. Besides, the ratio between the intensity of the peaks related to bound and free-exciton recombination directly reflects the impurity concentration. The

bound exciton recombination can be used to get information on neutral donor and acceptor binding energies, making use of the so-called two electron satellite (TES) transitions. The origin of the TES is a kind of Auger process, internal to the neutral donor-bound exciton. In this process, upon recombination of one electron with the hole, the remaining electron is promoted to some excited state of the neutral donor. In other words, the donor-bound exciton transition line results from the following recombination: $D^0X(0) \rightarrow D^0_{n=1} + h\nu$, where $h\nu_{D^0X}$ is the emission energy of the donor-bound exciton $D^0X(0)$, $X(0)$ stands for the ground state of the donor-bound exciton and $D^0_{n=1}$ denotes the final state of the transition, which is here the ground state (1s) of the neutral donor. However, there is some probability that the neutral donor be left in one excited state ($n = 2, 3, etc.$), giving rise to the TES lines, $D^0X(0, a, b, c...) \rightarrow D^0_{n=2,3,...} + h\nu_{TES}$, where 0,a,b,c, . . . stands for the ground state (0) and the so-called rigid rotational excited states of the D^0X complex $(a, b, c...)$. $n = 2, 3, ...$, represents the different possibilities for the principal quantum number of the D^0 final state. Thus, this transition is displaced at lower energies with respect to the principal bound exciton transition by energies that are directly related with the impurity binding energy. It is important to remark that the relative probabilities of the different recombination channels are very sensitive to the symmetry of both the initial and final states, as recently demonstrated by the detailed spectroscopic study of high-quality GaN [52]. In particular, the final state can be a p-state of the neutral donor, toward which the recombination is favored if the initial state is the first excited state (a-state) of the D^0X complex. Such excited states of D^0X in GaN have been studied both experimentally [53] and theoretically [54], being of great importance to explain the temperature dependence of TES related PL spectra. Indeed, when the temperature is raised above typically 5 K, the thermal population of excited states of the D^0X complex makes the transition to the 2p state of D^0 more probable than the transition to the 2s state. This results in the dominance of the $D^0X(a)$:2p transition lying 1.3 meV above the $D^0X(0)$:2s. These transitions are detectable only at low impurity concentration. This fact, together with the low intensity of the transitions, makes quite difficult their detection (see spectra in Fig. 2.10).

In the case of donor-acceptor (D-A) pair recombination, the emission energy is a function of the inter-pair distance r, defined as the separation between the location of the donor and the acceptor. We consider a D-A pair separated a distance r larger than the sum of the Bohr radii of the donor and the acceptor. Now, we assume that the overlap integral between the trapped hole and electron is sufficiently small so that there is a negligible contribution to the energy of the system in its initial state. Then, their interaction could be described by a Van der

Waals polarization interaction term (dipole-dipole interaction between the neutral D-A pair) which lowers the energy of the interacting pair by:

$$E_{VdW} = \frac{6.5e^2}{\epsilon_0 r}\left(\frac{a_D}{r}\right)^5, \tag{2.9}$$

where $a_D = \hbar/\sqrt{2m_e E_D}$ is the Bohr radius of the shallower impurity in the pair, usually the donor Bohr radius. In the final state, the electrostatic interaction potential between the charged donor and the charged acceptor gives rise to a Coulomb interaction term $e^2/\epsilon_0 r$. The energy of the emitted photon in a D-A transition is:

$$h\nu_{D-A} = E_g - (E_A + E_D) + e^2/\epsilon_0 r - E_{VdW}. \tag{2.10}$$

The donor-acceptor separation r has a discrete nature,inducing the appearance of discrete lines. However, in several cases the discrete line sequence is lost and is replaced by a wide asymmetric band. The condition for bound pairs is $E_A + E_D > e^2/\epsilon_0 r$, which yields $r \sim 700$ Å in GaN. For this r-value, the Van der Waals term is negligible in comparison with the Coulomb correction term. On the other hand, the very distant non-isolated pairs, which are numerous and have a large capture cross-section, are responsible for the low energy part of the D-A pair band. However, the recombination rates are very low for such distant pairs, so that these transitions easily saturate as the exciton intensity increases. Consequently, the D-A pair band energy blue-shifts with the excitation density.

As the temperature increases, the D-A pair band evolves to the free-to-bound recombination (CB-A). Since $E_D < E_A$, these effects can be attributed to the thermal ionization of the donor and to an increase in the conduction band electron concentration. The peak energy for these transitions is given by:

$$h\nu_{CB-A} = E_g - E_A + \frac{1}{2}k_B T, \tag{2.11}$$

where the term $\frac{1}{2}k_B T$ results from the thermal diffusion of free electrons in the conduction band.

Finally, when the optical transition involves a deep center, two different kinds of transitions can occur: recombination between an electron and a hole bound to different deep centers, and localized electron transitions from the excited state to the ground state of a molecular-like deep center. Due to the localized nature of the impurity states, the electronic states may couple strongly to the lattice. Through this interaction, phonons can cooperate to the recombination of carriers. This process may be so strong that the most probable transition may have an energy

much smaller than that of the no-phonon transition given in Eq. 2.10. This transmission of energy through lattice is known as "Stokes shift". The degree of coupling to LO phonons in a polar lattice increases very rapidly with localization, particularly for the holes, which have larger masses than the electrons.

2.3.1 Optical properties of bulk GaN

We have seen in Section 1.2, that in unstrained WZ GaN there are three closely spaced valence bands at the Γ point, labeled as HH, LH and CH. The excitons involving electrons in the conduction band and holes in the corresponding valence bands are labeled A, B and C for each valence band respectively. The energy gap of bulk GaN is 3.506 eV at 4 K [55] and it decreases down to 3.440 eV at 295 K [56]. Due to the binding energy of the complex formed in a crystal (excitons, donor bound excitons, donor acceptor pairs (DAP), etc.), the near band edge emission takes place at energies lower than the energy gap. The excitonic emission occurs when the sample has high crystal quality. Nevertheless, during growth some impurities can be accidentally introduced in the crystal lattice. Then, excitons may be bound to the impurities, giving place to complexes that give rise to emission at lower energies. These transitions dominate the low temperature ranges. Additionally, if the sample is intentionally doped, enough deep states can appear in the band gap so that their transitions reflect in the photoluminescence spectra.

We present in Fig. 2.10 the PL spectra of both polarization components $E \perp c$ (a) and $E \parallel c$ (b) of the emitted light detected with the light wavevector perpendicular to the wurtzite c axis (k $\perp$ c) in the range of temperatures between 25 and 100 K. The GaN crystals were grown on (0001)-oriented single-crystalline sapphire in a vertical reactor with a bottom-fed design [57]. The sample has a total thickness of 800 μm and for its growth the nitrogen-to-gallium flux ratio was fixed to 10. The growth was carried out at a temperature of about 1070°C with a growth rate exceeding 100 μm/h. Subsequently, the bulk GaN crystal was separated from the sapphire substrate by a laser-induced lift-off process utilizing the third harmonic of a Q-switched Nd:YAG laser with a wavelength of 355 nm. More details on the growth process can be found elsewhere [58].

The spectra in graph (a) correspond to the polarization component $E \perp c$ of the emitted light. The spectrum at low temperature has been fitted with gaussian functions to resolve the PL peaks. The emission at 3.481 eV is identified as the recombination of free exciton A (X_A). Additionally, the presence of chemical impurities in the crystal lattice produces potential traps, where the free excitons can be bounded. Normally, the binding energy of complexes formed by impurities

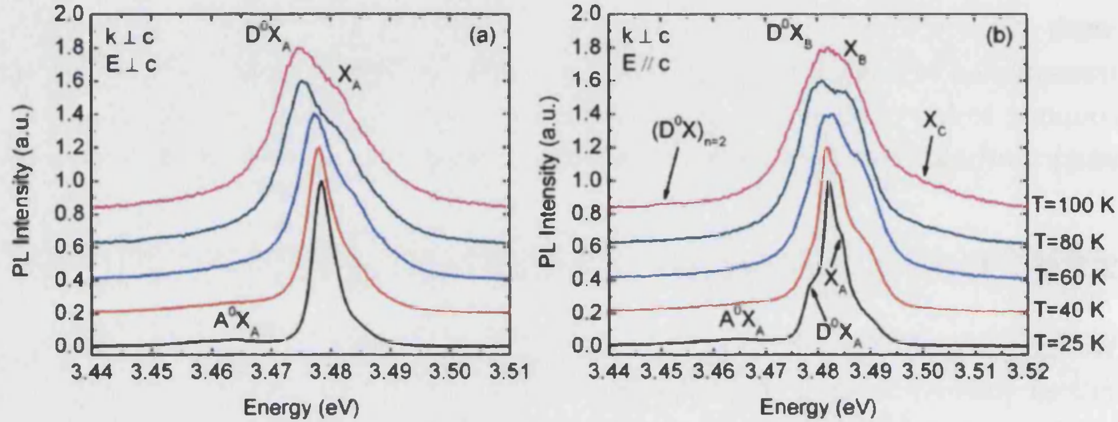

Figure 2.10: PL spectra of bulk GaN for the $E \perp c$ (a) and $E \parallel c$ (b) polarization components of the emission at different temperatures. The spectra are normalized to the D^0X_A (a) and D^0X_B (b) peaks and shifted for clarity.

is very low and they thermalize as the temperature increases. The impurities are commonly attributed to oxygen, silicon or vacancies in GaN. The transitions at energies 3.478 and 3.463 eV have been attributed to the emission from the recombination of the donor bound excitons D^0X_A and acceptor bound exciton A^0X_A, respectively. This last transition is assigned to acceptor bound exciton A^0X because of its lower emission energy and its related intensity compared with D^0X_A peak. As the temperature increases the donor bound exciton complex, D^0X_A, thermalizes, and its intensity decreases with temperature. At the same time, the peak related to X_A starts to dominate the intensity of the spectrum. Globally, all the peaks suffer a red-shift as the temperature increases. This behavior is due to the decrease of the band gap with increasing temperature [59].

Figure 2.10 (b) corresponds to the PL spectra of the polarization component E $\parallel c$ of the emission. In this case, the low temperature spectrum is dominated by the D^0X_B emission at 3.482 eV, which is consistent with the optical selection rules for B exciton. The main peak X_B in 3.485 eV at 25 K survives as the temperature increases, while the donor bound to exciton D^0X_B vanishes, consistent with the thermalization of this complex. According to the thermal band filling of the bands and the polarization selection rules, in this configuration the exciton X_C is visible above 100 K under a broad peak at 3.499 eV. Besides, it is possible to distinguish a broad shoulder close to 3.45 eV in the spectrum at 100 K. This could be the so-called "two-electron" transition $(D_2^0X)_{n=2}$ that emerges at 3.4530 eV when the donor is left in an excited $2s$-like state [50]. Although these transitions fulfill the optical polarization properties as corresponds with the character of the valence bands (see Section 2.3.1), forbidden peaks related with exciton A appear in this

(meV)	This work	[55]	[17]	[56]	[60]	[18]	[61]
Δ_{so}	5	6	5	6.4	11	1.2	5
Δ_{cr}	16	-	16	11.5	22	5.3	23

Table 2.2: Comparison of the values of the spin-orbit and the crystal field splitting energies obtained in this work and in previous ones.

configuration. This fact can be explained if we consider some relaxation of the selection rules, probably due to a small misalignment between the c-axis and the polarizer used for measurements. Moreover, in polarized PL measurements, the optical transitions from the conduction band to the three valence bands Γ_9, Γ_7^+ or Γ_7^- can be used to estimate the value of the splitting energies Δ_{so} and Δ_{cr}. For this purpose, we will make the assumption that all three excitons, A, B and C, have the same binding energy. Within this approximation, we can use the energy difference between the excitonic transitions to determine $\Delta_{so} = X_B - X_A$ and $\Delta_{cr} = X_C - X_B$. In Table 2.2 we compare the values obtained in this way with those determined, both experimentally and theoretically, by previous researches. The agreement found is quite good.

2.3.2 Time Integrated Photoluminescence setup

The instrumentation used in our TIPL setup is schematically shown in Fig. 2.11. The samples are placed into a cryostat Leybold model Coolpower 5/100. The cryostat was placed in a mechanical arm in order to move it along all spatial directions. We use a vacuum system consisting in a mechanical pump Leybold model Divac 2.5 VT together to a turbo-molecular pump Leybold model TW-300. The mechanical pump is used first in order to reache values of pressure of a few mbars. At this stage, the turbo-molecular pump is switched on to increase the vacuum level up to 10^{-7} mbars. In ordar to cool down the sample a He-gas closed circuit cryostat refrigerated by water Leybold model Coolpak 6000 is used. For measurements as a function of temperature, a temperature controller Cryo Vac Tic model 304-MA is used. This system uses an auto-tuning proportional-integral-derivative algorithm in order to improve the stability of the temperature. The excitation was done with different laser lines according to the specific requirements of each experiment. The excitation power was adjusted by using both the current control of the laser and neutral filters. In first place, a continuous wave Ar^+ laser Coherent model SBRC MotoFRED was used to excite the photoluminescence of nanostructures grown along non-polar WZ crystallographic directions. The 488 nm line of this laser was doubled by a non linear crystal, obtaining radiation of 244 nm and several mW power (working at maximum power). On the other hand, the laser employed to

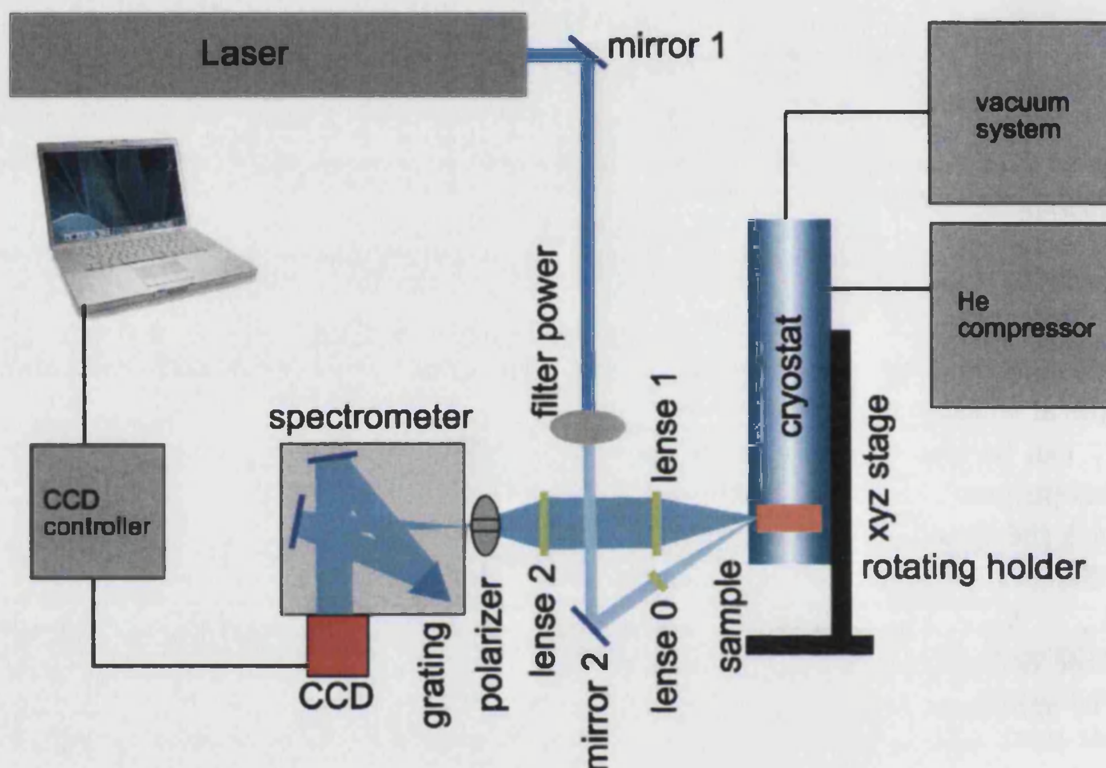

Figure 2.11: Schematic diagram of the setup used for TIPL experiments.

photo-excite GaN nanowires was a He-Cd Kimmon model IK3301R-G. We used the 325 nm line with a power of several mW. The emission from the sample was collected by adequate lenses and dispersed through the 2400 grooves/mm gratings of a Jobin Yvon spectrometer model Triax 190 with a focal distance of 0.19 m. A Si CCD camera Jobin Ybon model 3500V is used as detector. The resolution of the system is of the order of 3 meV. For measuring the polarization of the emitted light a polarizer placed in front of the entrance slit of the spectrometer in combination with a special rotating holder was used.

2.3.3 Time Resolved Photoluminescence setup

Time resolved PL (TRPL) measurements were performed at the Department of physics of the University of Florence, in Italy, where I had the pleasure to work with Dr. Ana Vinattieri. The experimental setup is shown in Fig. 2.12. The excitation power source used is a mode-locked pulsed wave solid state (Nd:YAG) laser Coherent model Antares-76s. It emits a radiation of 1064 nm wavelength with a power around 24 W. The pulses have a temporal width of 1 ps and their repetition

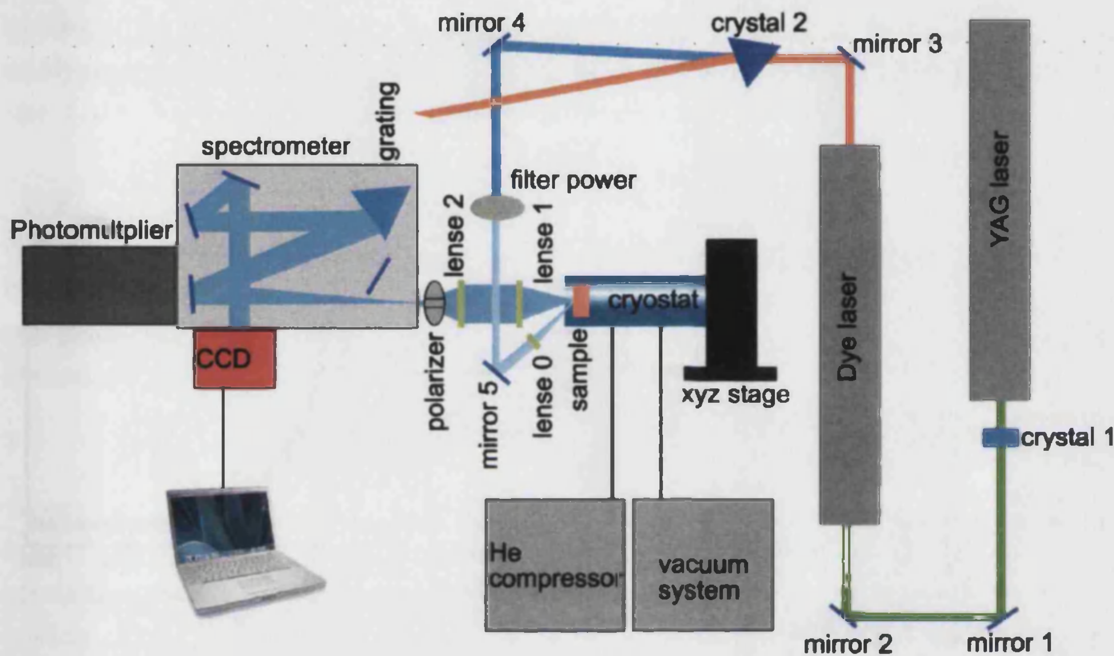

Figure 2.12: Schematic diagram of the setup used to performed TRPL.

frequency is of 76 MHz. This infrared radiation is duplicated in frequency by a non lineal crystal of Lithium Triboro, giving a radiation with 532 nm wavelength and an output power around 3.5 W. Through the doubling process the repetition frequency of the pulses is kept constant, but their width increases up to 3 ps. The resulting radiation is used to pump a Rhodamine 6G dye laser that gives an output power around 700 mW at 600 nm with the same frequency and temporal width of the original pulses. This radiation is doubled again by means of a non linear crystal of Lithium Iodate. Finally, we obtain a pulsed laser radiation with 300 nm wavelength and maximum power around 10 mW. The pulses have duration of 3 ps and their frequency is 76 MHz, as in the original excitation source. The sample is placed into a cryostat. The vacuum system consists in the coupling of a mechanical pump to a turbo pump and to cool down we use a He-gas closed circuit refrigerated by water similar to the one used in the TIPL setup. A 0.30 m focal length spectrometer Acton Research SP 300i is used as monochromator. It contains an adjustable entrance slit and a grating of 1200 groves/mm. The spectrometer is provided with two exit slits, where a CCD camera and a photomultiplier are placed. For the analysis of the polarization of the emission, a polarizer and a $\lambda/2$ sheet Halbo Optics Babinet Soleil Compensator are used.

With the aim of studying the temporal dynamics of the radiative recombination a microchannel photomultiplier (MCPT) Hamamatsu model R3809U51 was used.

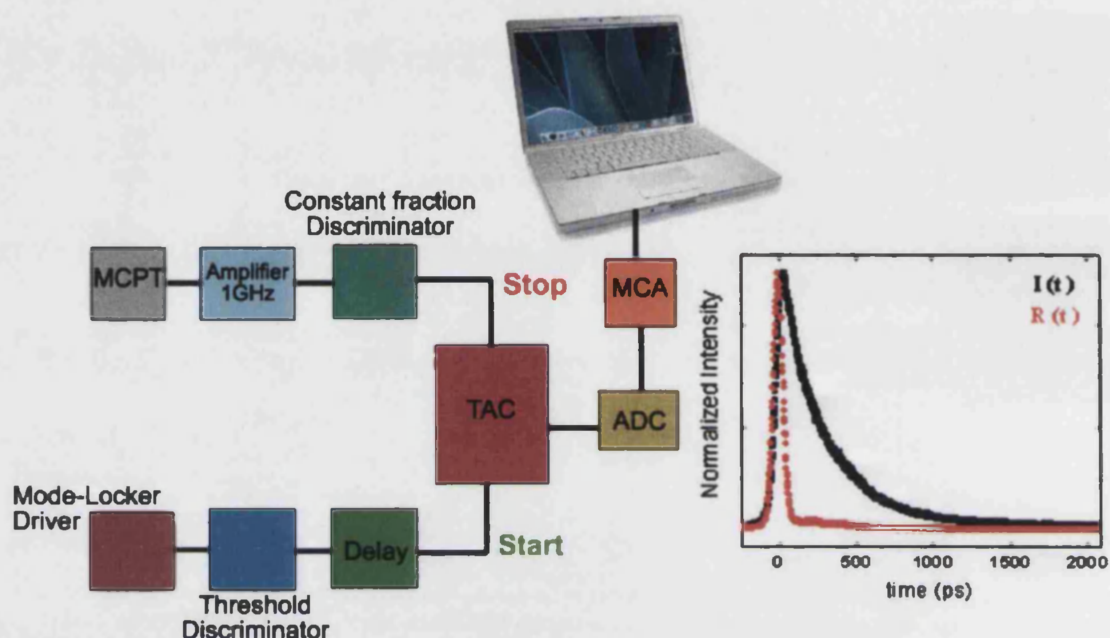

Figure 2.13: Schematic diagram of the different electronic controllers used to perform TRPL. The spectrum represents the resolution of the setup. It was taken at 10 K exciting at 300 nm and with 2 mW power.

Each channel has a diameter of 6 μm into a total area of 17 mm^2. The electronic pulse at the exit of the microchannel has a time of 150 ps and a transit time spread (TTs) smaller than 25 ps. The temperature in the MCPT is kept constant at 250 K by the cooling of a Peltier cell. The cathode is made by a multialcaline solution to allow the spectral response between 160 and 910 nm, where the maximum sensibility is at 600 nm (Quantum Efficiency of 10%). The technique used is the temporal correlation of a single photon. This technique consists in the measurement of the temporal delay between the emission of the first photon detected and the excitation pulse which generated it. The distribution of the delay time of the detected photons averaged out at a big number of events, reproduces the temporal distribution of the PL signal generated by a single laser pulse. To measure this distribution, the signal at the exit of the detector is discriminated and amplified by a fraction constant discriminator Ortec 9327. This signal is used as a start signal for the time-amplitude convertor (TAC). The sequence is schematically shown in Fig. 2.13. The pulse given by the mode-locking control system, which is associated to the pulse of the laser, is used as a stop signal for the TAC. Therefore, the TAC is only fitted out in presence of relevant events and not in correspondence to each excitation pulse. The TAC produces a pulse of amplitude proportional to the time elapsed between the start and stop signals. Then, the TAC signal is sent to the

analogical-digital converter (ADC) and immediately afterwards to a multi-channel analyzer (MCA), that records the amplitude distribution of the pulses coming from the TAC. It reproduces the temporal distribution of the detected events.

Finally, the resolution of the setup is checked by using a pulsed laser coming directly through the spectrometer, R(t) in the spectrum of Fig. 2.13. The broadening suffered by the pulse is mainly due to the transit time spread dispersion of the photo-electrons. If L(t) is the decay of the PL from the sample, the resulting measured decay is:

$$I(t) = \int_{+\infty}^{+\infty} L(\tau)R(t-\tau)d\tau, \qquad (2.12)$$

where I(t) is therefore the convolution between L(t) and the setup response. In the spectrum of Fig. 2.13 we can see the typical decay of one of the a-QDs samples studied in this work. The aim of this characterization technique is the determination of the order of magnitude of the decay time τ of the optical transitions. Since the FWHM of R(t) is about three times smaller than the measured decay, I(t), we will not perform a deconvolution of both signals in order to determine the absolute value of τ.

2.4 Micro Raman Scattering

Although most of the light traveling through a medium is either transmitted or absorbed following the standard laws of reflection and refraction, a very tiny fraction is scattered in all directions by inhomogeneities inside the medium. Static inhomogeneities such as dislocations in a crystal scatter the light elastically, i. e., without frequency change. However, fluctuations in the density of the medium that are associated with atomic vibrations scatter the light inelastically. Inelastic scattering of light by molecular vibrations was first experimentally reported by C.V. Raman [62]. Today, Raman scattering has become a standard spectroscopic tool in the study of semiconductors. In this section we shall first present a macroscopic theory of Raman scattering by phonons in solids. This is followed by the introduction of the Raman tensors for the WZ crystal structure and a discussion about the phonon mode selection rules. The rest of the Section is a description of the Raman setup used to perform the experiments.

2.4.1 Microscopic theory of inelastic light scattering by phonons

We consider an infinite medium with electric susceptibility χ. For the moment we shall assume the medium to be isotropic so that χ can be represented by a scalar. When a sinusoidal plane electromagnetic field described by

$$\boldsymbol{F}(\boldsymbol{r},t) = \boldsymbol{F}_i(\boldsymbol{k},\omega)\cos(\boldsymbol{k_i r} - \omega_i t) \tag{2.13}$$

is present in this medium, a sinusoidal polarization $\boldsymbol{P}(\boldsymbol{r},t)$ will be induced:

$$\boldsymbol{P}(\boldsymbol{r},t) = \boldsymbol{P}(\boldsymbol{k_i},\omega_i)\cos(\boldsymbol{k_i r} - \omega_i t) \tag{2.14}$$

Its frequency and wavevector are the same as those of the incident radiation while its amplitude is given by:

$$\boldsymbol{P}(\boldsymbol{k_i},\omega_i) = \chi(\boldsymbol{k_i},\omega_i)\boldsymbol{F}_i(\boldsymbol{k_i},\omega_i) \tag{2.15}$$

In the medium there are fluctuations in χ due to atomic vibrations. We have seen in Chap. 1.3 that the normal modes of atomic vibrations in a crystalline semiconductor are quantized into phonons. The atomic displacements $\boldsymbol{Q}(\boldsymbol{r},t)$ associated with a phonon can be expressed as plane waves:

$$\boldsymbol{Q}(\boldsymbol{r},t) = \boldsymbol{Q}(\boldsymbol{q},\omega_0)\cos(\boldsymbol{qr} - \omega_0 t) \tag{2.16}$$

with wavevector $\boldsymbol{q}$ and frequency ω_0. These atomic vibrations will modify χ. We assume that the characteristic electronic frequencies which determine χ are much larger than ω_0. In this conditions χ can be taken to be a function of $\boldsymbol{Q}$. This is known as the quasi-static or adiabatic approximation. Normally the amplitudes of these vibrations at room temperature are small compared to the lattice constant and we can expand χ as a Taylor series in $\boldsymbol{Q}(\boldsymbol{r},t)$:

$$\chi(\boldsymbol{k_i},\omega_i,\boldsymbol{Q}) = \chi_0(\boldsymbol{k_i},\omega_i) + \left(\frac{\partial\chi}{\partial\boldsymbol{Q}}\right)_0 \boldsymbol{Q}(\boldsymbol{r},t) + \ldots, \tag{2.17}$$

where χ_0 denotes the electric susceptibility of the medium with no fluctuations. The second term of the equation represents an oscillating susceptibility induced by the lattice wave $\boldsymbol{Q}(\boldsymbol{r},t)$. Substituting 2.17 into 2.15 we can express the polarization $\boldsymbol{P}(\boldsymbol{r},t,\boldsymbol{Q})$ of the medium in the presence of atomic vibrations as

$$\boldsymbol{P}(\boldsymbol{r},t,\boldsymbol{Q}) = \boldsymbol{P}_0(\boldsymbol{r},t) + \boldsymbol{P}_{ind}(\boldsymbol{r},t,\boldsymbol{Q}) \tag{2.18}$$

where

$$P_0(\boldsymbol{r},t) = \chi_0(\boldsymbol{k_i},\omega_i)\boldsymbol{F}_i(\boldsymbol{k_i},\omega_i)\cos(\boldsymbol{k_i r} - \omega_i t) \tag{2.19}$$

is a polarization vector vibrating in phase with the incident radiation and

$$\boldsymbol{P}_{ind}(\boldsymbol{r},t,\boldsymbol{Q}) = \left(\frac{\partial\chi}{\partial\boldsymbol{Q}}\right)_0 \boldsymbol{Q}(\boldsymbol{r},t)\boldsymbol{F}_i(\boldsymbol{k}_i,\omega_i)\cos(\boldsymbol{k_i r} - \omega_i t) \tag{2.20}$$

is the polarization wave induced by the phonon. Besides the phonon, other perturbations can modify the susceptibility of the medium, giving place to a change in the polarization. An example are plasmons, magnons or electrons. The case of plasmons is discussed in Sec. 1.3.3. To determine the frequency and wavevector of $\boldsymbol{P}_{ind}$ we rewrite $\boldsymbol{P}_{ind}(\boldsymbol{r},t,\boldsymbol{Q})$ as

$$\boldsymbol{P}_{ind}(\boldsymbol{r},t,\boldsymbol{Q}) = \left(\frac{\partial\chi}{\partial\boldsymbol{Q}}\right)_0 \boldsymbol{Q}(\boldsymbol{q},\omega_0)\cos(\boldsymbol{qr} - \omega_0 t) \tag{2.21}$$

$$\times\boldsymbol{F}_i(\boldsymbol{k}_i,\omega_i)\cos(\boldsymbol{k_i r} - \omega_i t)$$

$$= \frac{1}{2}\left(\frac{\partial\chi}{\partial\boldsymbol{Q}}\right)_0 \boldsymbol{Q}(\boldsymbol{q},\omega_0)\boldsymbol{F}_i(\boldsymbol{k}_i,\omega_i t) \tag{2.22}$$

$$\times \{ \cos[(\boldsymbol{k}_i + \boldsymbol{q})\boldsymbol{r} - (\omega_i + \omega_0)t]$$

$$+ \cos[(\boldsymbol{k}_i - \boldsymbol{q})\boldsymbol{r} - (\omega_i - \omega_0)t] \}$$

$\boldsymbol{P}_{ind}$ consists of two sinusoidal waves: a Stokes shifted wave with wavevector $\boldsymbol{k}_S = (\boldsymbol{k}_i - \boldsymbol{q})$ and frequency $\omega_S = (\omega_i - \omega_0)$ and an anti-Stokes shifted wave with wavevector $\boldsymbol{k}_{AS} = (\boldsymbol{k}_i + \boldsymbol{q})$ and frequency $\omega_{AS} = (\omega_i + \omega_0)$. The radiation produced by these two induced polarization waves is known, respectively, as Stokes scattered and anti-Stokes scattered light. Since the phonon frequency is equal to the difference between the incident photon frequency ω_i and the scattered photon frequency ω_S, this difference is referred to as the Raman frequency or Raman shift. The Raman shift is the difference between the frequencies of the inelastic light and the incident light. Raman spectra are usually given in terms of plots of the intensity of the scattered radiation versus the Raman frequency. Raman shifts are often measured in wavenumbers (cm^{-1}) where 1 cm^{-1} $\approx$ 0.124 meV. Notice that both frequency and wavevector are conserved in the above scattering processes. As a result of wavevector conservation, the wavevector q of phonons studied by one-phonon Raman scattering must be smaller than twice the photon wavevector. Assuming that visible lasers are used to excite Raman scattering in a sample with refractive index about 3, q is of the order of 10^6 cm^{-1}. This value is about $1/100$ of the size of the Brillouin zone in a semiconductor. Hence, one-phonon Raman

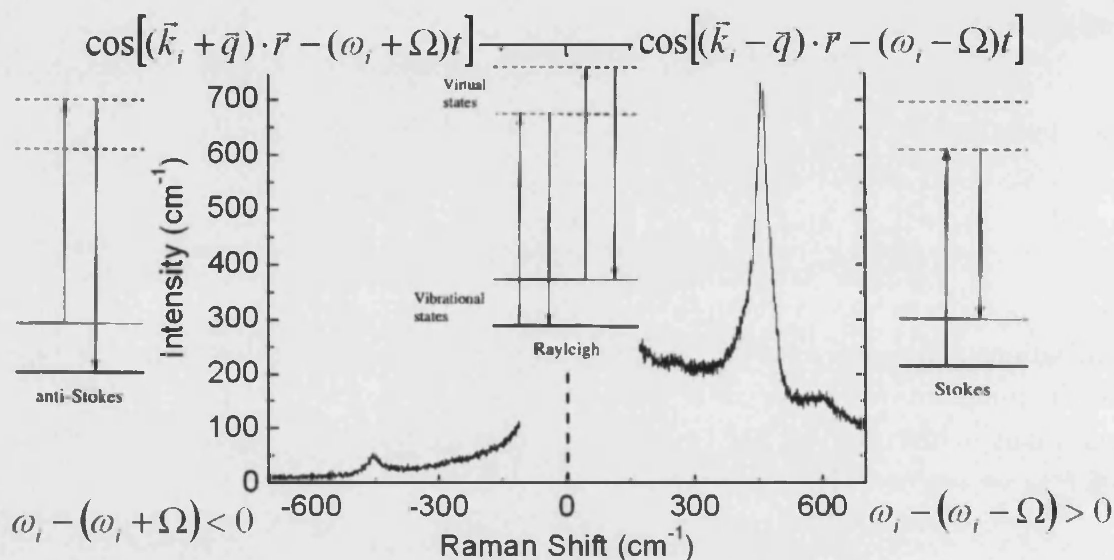

Figure 2.14: Schematic representation of Anti-Stokes, Rayleigh and Stokes RS emission. Insets: schematic diagrams of the microscopic processes involved in light scattering. The vertical arrows represent the virtual electronic transitions.

scattering probes only zone-center phonons. In such experiments q can usually be assumed to be zero.

Figure 7.15 shows a schematic spectrum of the emission corresponding to Stokes, Rayleigh and Anti-Stokes scattering versus frequency. The sharp lines are consequence of **k**-vector conservation. They are usually fitted by Lorentzian functions. Note that the Stokes and Anti-Stokes lines are equally displaced (ω_{ph}) from the Rayleigh line, because the energy of one phonon is either gained or lost by the incident light, as can be schematically understood in the energy diagram at the inset of the Figure. Rayleigh scattering arises from transitions with initial an final states at the same vibrational energy level. Stokes RS arises from transitions which start at the ground state vibrational energy and end at a higher vibrational energy level, whereas Anti-Stokes RS involves a transition from higher to lower vibrational states. At room temperature, most molecular vibrations are in the ground state. Therefore, Anti-Stokes transitions are less likely to occur than Stokes transitions resulting in the Stokes RS signal being more intense. This larger relative intensity becomes increasingly larger as the energy of the vibrations increases and the higher vibrational energy levels become less populated at any given temperature. For this reason, it is usually the Stokes RS which is routinely studied in Raman spectroscopy.

Raman tensors

The intensity of the scattered radiation can be calculated from the time-averaged power radiated by the induced polarizations $\boldsymbol{P}_{ind}$ per unit solid angle. This intensity will depend on the polarization of the scattered radiation, $\boldsymbol{e}_S$, as $|\boldsymbol{P}_{ind} \cdot \boldsymbol{e}_S|^2$. If we denote the polarization of the incident radiation as $\boldsymbol{e}_i$, the scattered intensity I_S calculated from 2.21 is proportional to

$$I_S \propto |\boldsymbol{e}_i \left(\frac{\partial \chi}{\partial \boldsymbol{Q}}\right)_0 \boldsymbol{Q}_0 \boldsymbol{e}_S|^2 \tag{2.23}$$

where $\boldsymbol{q}$ is approximated by zero for one-phonon scattering and χ may be complex. Notice that the scattered intensity is proportional to the vibrational amplitude $\boldsymbol{Q}$ squared. In other words, there will be no Stokes scattering if no atomic vibration is present. This result is a consequence of our classical treatment. Let us assume that $\boldsymbol{Q}$ is the vector displacement of a given atom induced by the phonon so that $\left(\frac{\partial \chi}{\partial \boldsymbol{Q}}\right)$ is a third-rank tensor with complex components. By introducing a unit vector $\widehat{\boldsymbol{q}} = \boldsymbol{Q}/|\boldsymbol{Q}|$ parallel to the phonon displacement we can define a complex second rank tensor $\mathfrak{R}$ as

$$\mathfrak{R} = \left(\frac{\partial \chi}{\partial \boldsymbol{Q}}\right)_0 \widehat{\boldsymbol{Q}}(\omega_0) \tag{2.24}$$

such that I_S is proportional to

$$I_S \propto |\boldsymbol{e}_i \mathfrak{R} \boldsymbol{e}_S|^2. \tag{2.25}$$

$\mathfrak{R}$ is known as the Raman tensor. By measuring the dependence of the scattered intensity on the incident and scattered polarizations one can deduce the symmetry of the Raman tensor and hence the symmetry of the corresponding Raman-active phonon. Thus Raman scattering can be used to determine both the frequency and symmetry of a zone-center phonon mode. In Sec. 1.3 we saw the different phonons in WZ structure. Each phonon has an associated Raman tensor or tensors and these are shown in the following for Raman active phonons of the WZ structure:

$$A_1(z) = \begin{pmatrix} a & 0 & 0 \\ 0 & a & 0 \\ 0 & 0 & c \end{pmatrix}, E_2 = \begin{pmatrix} d & 0 & 0 \\ 0 & -d & 0 \\ 0 & 0 & 0 \end{pmatrix}, E_2 = \begin{pmatrix} 0 & d & 0 \\ d & 0 & 0 \\ 0 & 0 & 0 \end{pmatrix}, \tag{2.26}$$

$$E_1(x) = \begin{pmatrix} 0 & 0 & e \\ 0 & 0 & 0 \\ e & 0 & 0 \end{pmatrix}, E_1(y) = \begin{pmatrix} 0 & 0 & 0 \\ 0 & 0 & e \\ 0 & e & 0 \end{pmatrix}.$$

a and c are found to be complex number and their relative phase $\Delta\alpha$ can be experimentally determined [63], as we will see in the following. The labels in parenthesis indicate the direction of the induced electric dipole in the case of the polar phonon modes. E_2 phonons (being, as well as E_1 phonons a two-dimensional representation) are described by two Raman tensors. For E_1, these tensors are labeled according to the polarization of the corresponding phonon.

Selection rules

The Raman tensor as defined in 2.24 appears to be a symmetric second-rank tensor, since the susceptibility is a symmetric tensor. This is only exactly correct if we can neglect the slight difference in frequency between the incident and scattered radiation. Within this approximation, antisymmetric components in the Raman tensor can be introduced only by magnetic fields. Since most semiconductors are nonmagnetic we can usually assume the Raman tensor in semiconductors to be symmetric. Additional requirements are often imposed on Raman tensors as a result of the symmetry of the vibrating medium and of the vibrational modes involved. The result of these symmetry requirements is that the scattered radiation vanishes for certain choices of the polarization of the incident and scattered light and scattering geometries. These so-called Raman selection rules are very useful for determining the symmetry of Raman-active phonons. Commonly, the experimental configuration is given in a compact notation as $\mathbf{k_i}(\mathbf{e_i}, \mathbf{e_S})\mathbf{k_S}$. This notation is also known as Porto's notation [64]. The first symbol refers to the direction of the propagation of the exciting radiation, while the last one refers to the direction of observation. The symbols in parentheses specify, from left to right, the polarization directions of the incident and scattered light. We use for our experiments backscattering configuration. The peculiarity of this configuration it that the incident and scattered light lie along the same direction, but in different senses. Therefore, using Porto's notation, if $\mathbf{k_i} = \mathbf{z}$ then $\mathbf{k_S} = -\mathbf{z}$. In the particular case that the polarization of the incident and scattered light are parallel, we have parallel ($||$) polarization. Otherwise, if the polarizations of the incident and scattered light are perpendicular to each other, it is named crossed ($\perp$) polarization.

The intensity of polarized Raman scattering intensity is given by Eq. 2.25. Taking the corresponding Raman tensors from Eq. 2.26 we can determine the selection rules for each mode. Two different backscattering configurations are considered: along [0001] and along [$11\bar{2}0$]. We denote as θ the angle formed by the polarization of the incoming light and the wurtzite c axis. For backscattering

along [0001] we obtain:

$$\begin{aligned} I^{\parallel}_{A_1(TO)} &\propto |a|^2, \\ I^{\parallel}_{E_2} &\propto d^2\cos^2 2\theta + d^2\sin^2 2\theta. \\ I^{\perp}_{E_2} &\propto d^2\sin^2 2\theta. \end{aligned} \tag{2.27}$$

And for backscattering configuration along $[11\overline{2}0]$ we have:

$$\begin{aligned} I^{\parallel}_{E_2} &\propto d^2\sin^4\theta, \\ I^{\parallel}_{E_1(TO)} &\propto e^2\sin^2 2\theta, \\ I^{\parallel}_{A_1(TO)} &\propto |a|^2\sin^4\theta + |c|^2\cos^4\theta + \frac{|a||c|}{2}\cos(\Delta\alpha)\sin^2 2\theta. \\ I^{\perp}_{E_2} &\propto \frac{d^2}{4}\sin^2 2\theta, \\ I^{\perp}_{E_1(TO)} &\propto e^2\left(\sin^2\theta - \cos^2\theta\right)^2, \\ I^{\perp}_{A_1(TO)} &\propto \left(\frac{|a|^2}{4} + \frac{|c|^2}{4} + \frac{|a||c|}{2}\cos(\Delta\alpha)\right)\sin^2 2\theta. \end{aligned} \tag{2.28}$$

Other combinations are said to be symmetrically forbidden since the corresponding scattering intensity is zero, $I = 0$. For the forbidden configurations the modes will not appear in the spectra unless a mechanism exists, such as internal reflection due to defects and interfaces, that may cause the forbidden scattering. Notice that it is possible to determine the values of $\Delta\alpha$ by a detailed study of the $A_1(TO)$ scattering intensity. Values of $\Delta\alpha = \pi/2$ have been reported in Ref. [65]. Table 2.3 summarizes the selection rules for different scattering geometries for Raman-active modes in the WZ structure.

Configuration	Mode
$x(y,y)\overline{x}$	$A_1(TO)$, E_2
$x(z,z)\overline{x}$	$A_1(TO)$
$x(z,y)\overline{x}$	$E_1(TO)$
$x(y,z)y$	$E_1(TO)$, $E_1(LO)$
$x(y,y)z$	E_2
$z(y,x)\overline{z}$	E_2
$z(y,y)\overline{z}$	$A_1(LO)$, E_2

Table 2.3: Raman configurations of allowed modes in hexagonal nitrides. Taken from [28]

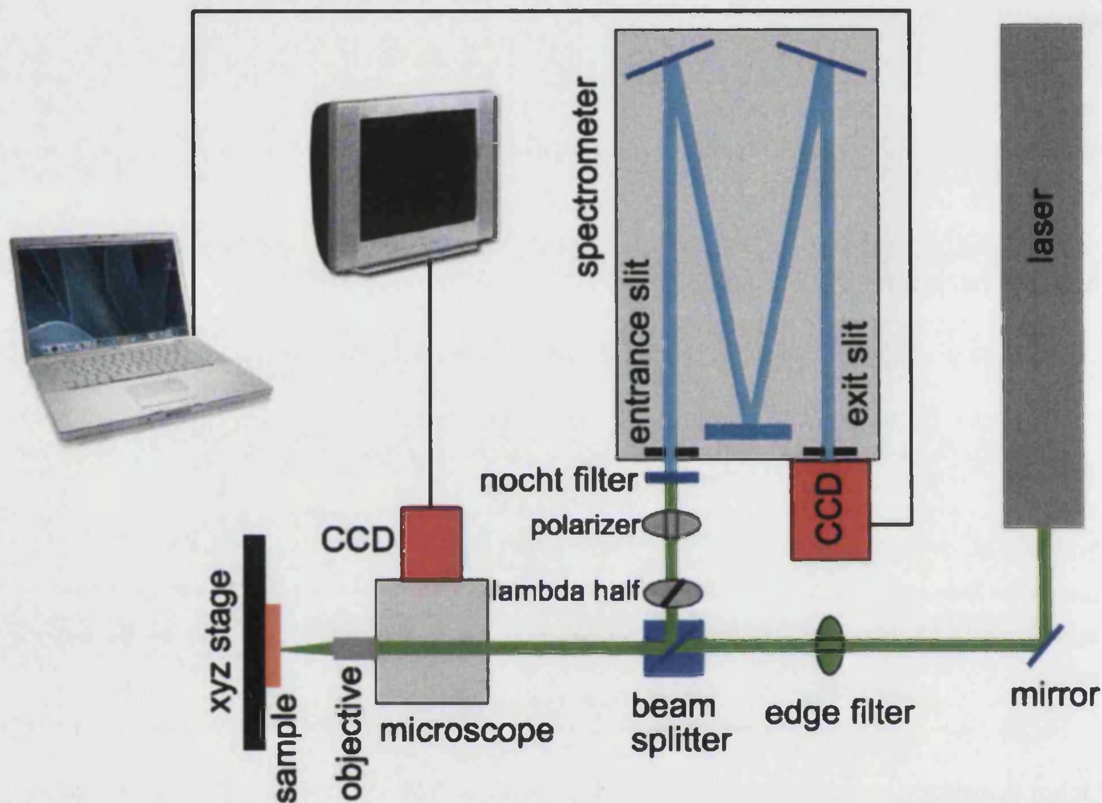

Figure 2.15: Schematic diagram of the setup used for Raman experiments.

2.4.2 Micro Raman Scattering setup

The different parts of the Raman setup used for the experiments of this work are shown in Fig. 2.15.
The sample is placed on a mechanical stage which can move along the three spacial directions by steps of 0.1 μm. The laser used as excitation source is a continuous wave Ar^+ laser Coherent model SBRC-DBW-20/4P. The laser wavelength used for our Raman experiments is at 514.53 nm with an output power of several mW. Due to the orientation of the Brewster's windows located in the cavity of the laser, the radiation is linearly polarized. The laser beam is driven through a filter in order to block the plasma lines. The laser is driven by mirrors to a confocal microscope equipped with a CCD camera JVC model TK-C701EG. The camera is used for localizing visually the laser spot on the surface of the sample. A variety of objectives can be used, normally a 100× or 40× for our experiments. The backscattered light is collected again by the same objective and driven to the entrance slit of the spectrometer. An optional $\lambda/2$ sheet and a polarizer can by

used at this step for polarization measurements (see section 2.4.1). A notch filter at the wavelength of the excitation source is placed in front of the spectrometer to avoid the elastically scattered light to enter the spectrometer. The spectrometer used is a Jobin Yvon model T64000. The light enters directly into the spectrometer stage equiped with a grating of 1800 groves/mm. After dispersion, the light is detected by a CCD camera Jobin Yvon model CCD-3000V refrigerated by liquid N. The monochromator slit is arranged so that the system has a spectral resolution around 0.5 cm^{-1}.

2.5 Atomic Force Microscopy

Scanning Probe Microscopy (SPM) is a branch of microscopy that forms images of surfaces using a physical probe scanning a specimen. An image of the surface is obtained by mechanically moving the probe. SPM was founded with the invention of the scanning tunneling microscope in 1981 by Gerd Binnig and Heinrich Rohrer in 1981 at IBM Research - Zurich [66], a development that earned them the Nobel Prize for Physics in 1986. Some years later Binnig, Quate and Gerber invented the first AFM in 1986 [67]. Atomic force microscopy (AFM) is a very high-resolution type of scanning probe microscopy, with atomic demonstrated resolution. AFM has found applications at many important processes in nanotechnology: for the investigation of surface polishing and etching processes, the development of new etch resists, the assessment of oxidation and metallization processes, for measuring the electrical force at the surface (EFM)[1], surface potentials (KP-AFM)[2], obtain the surface capacitance (SCM)[3] or techniques involving tip-sample current flow using conducting cantilevers. In this section the principles of AFM for measuring by the most common configurations will be explained, as well as the modifications needed in order to perform electrical measurements.

2.5.1 Fundamentals of Atomic force microscopy

The fundamentals of force microscopies consist in the interaction between a sharp tip located at the end of a cantilever and a surface. An image of one of the tips used for AFM is shown in Fig. 2.16 as illustrative example. The Figure shows a SEM image of a typical cantilever fabricated by nanosensors [68]. The cantilever is

[1] Electrical Force Microscopy
[2] Kelvin Probe Atomic Force Microscopy
[3] Scanning Capacitance Microscopy

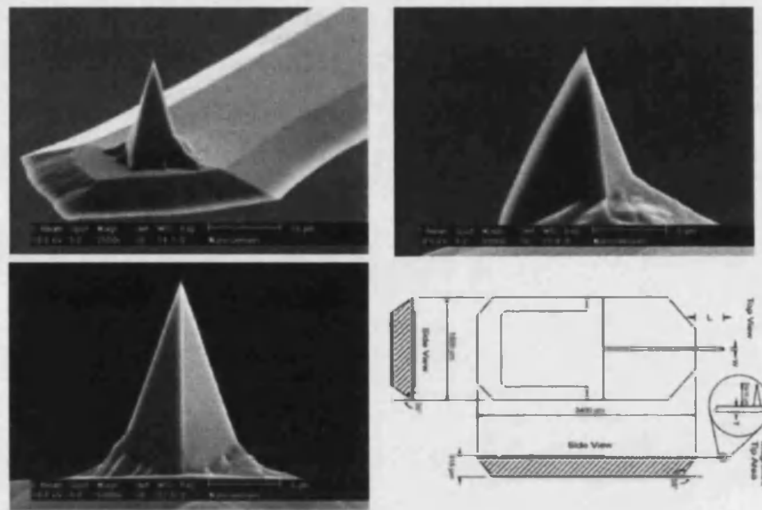

Figure 2.16: SEM images of a typical cantilever used for AFM measurements. A schematic diagrame of a whole chip is shown at the bottom right part of the figure. Images taken from [68].

often made of silicon or silicon nitride and it is characterized by the constant force that characterizes its bending. A second relevant characteristic of the tip is its radius, in the order of a few nanometers. The basic objective of these techniques is to obtain a topography image from the surface. For that purpose, the existence of a magnitude characteristic of the interaction between the probe and the surface is necessary. This magnitude changes very strongly with distance, and acts as a feedback, so that the electronic controller acts on the piezoelectric scanner where the sample is placed. It moves in the z direction for maintaining the constant distance (and in this way maintain a constant interaction) between the probe and the surface. The piezoelectric scatter acts along the x and y directions for scanning the sample surface. The schematic diagram of Fig. 2.17 represents the configuration of an AFM system. The deflection of the cantilever, caused by the probe-surface interaction, is measured using a laser spot reflected from the top surface of the cantilever onto a four quadrant photodiode.

There are two common imaging modes: the static (also called contact) mode and the dynamic (or non-contact) mode. In dynamic mode the cantilever vibrates during the surface scan. These two measurement modes will be described in the following sections.

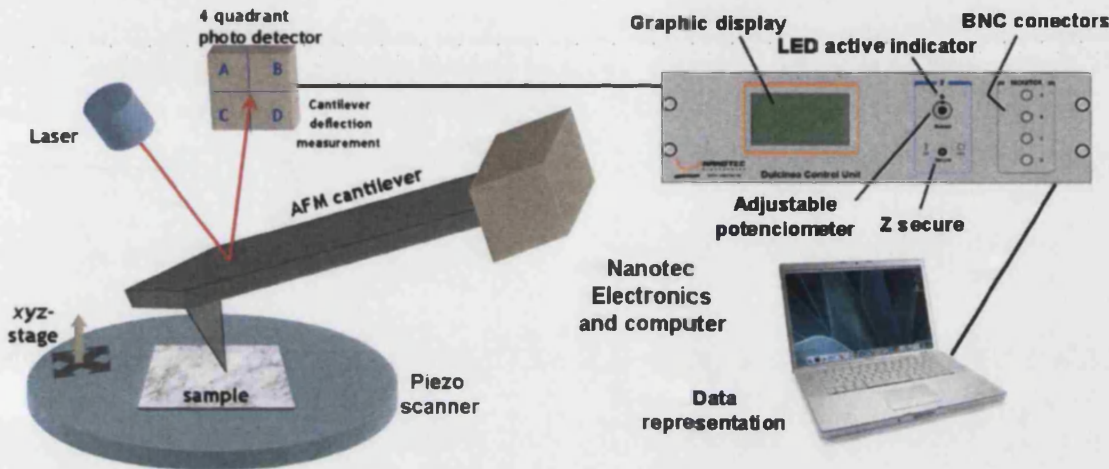

Figure 2.17: Schematic diagram of an Atomic force microscope. Images taken from the manual of nanotec [69].

Vertical and lateral resolution

A figure of merit of any microscopic technique is its resolution. An AFM generates three dimensional images of the sample surface. As a consequence two different, although not always independent, resolutions should be distinguished, *lateral* and *vertical*. Vertical resolution is limited by both noise from the detection system and thermal fluctuations of the cantilever. In general, the thermal noise of the cantilever is the largest source of noise. If the oscillation amplitude is measured with an optical deflection system the thermal noise is calculated by [70]:

$$z = \sqrt{\frac{4k_BT}{3k}} = \frac{0.074 \text{ nm}}{\sqrt{k}}, \tag{2.29}$$

where the cantilever force constant k is in N/m and $T = 295$ K. For a cantilever with a force constant of 40 N/m, the thermal fluctuations of the cantilever are below 1 Å.

On the other hand, for an isolated object the lateral resolution is determined entirely by the radius of the tip used to scan the surface. The measured topography is often rather inaccurately described as a convolution of the real surface and the tip shape. In the case of truncated islands, as explained in Fig. 2.18, it may be shown, using basic trigonometry, that the measured width is larger than the real width by an amount $\Delta\omega$ depending on the height of the pyramidal island and the radius of the tip:

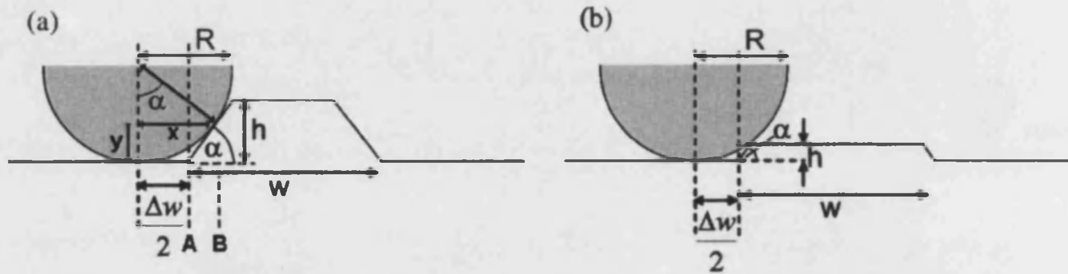

Figure 2.18: Schematic of the interaction of a hemispherical tip with a flat-topped nanoscale island for (a) $h > R(1 - \cos\alpha)$ and (b) $h < R(1 - \cos\alpha)$. Figure taken from [71].

$$\frac{\Delta\omega}{2} = \begin{cases} \sqrt{h(2R - h)} - h\cot\alpha & \text{for } h < R(1 - \cos\alpha), \\ R\tan(\alpha/2) & \text{for } h \geq R(1 - \cos\alpha). \end{cases} \quad (2.30)$$

It is important to stress the fact that the error in the width measurement depends not only on the shape of the tip but also on the shape of the object being imaged. This means that for an unknown tip shape imaging an unknown object, the process of recovering the real shape of the object from the image is in no case simple.

One should remember that the shape of the tip may also affect the measured data in the vertical direction. For instance, for an array of nanowires, the finite size of the tip may make it impossible for it to penetrate to the bottom of the nanostructures, resulting in an underestimation of the nanostructures height.

2.5.2 Surface topography measurements

Contact mode

In contact AFM mode, also known as repulsive mode, an AFM tip makes soft "physical contact" with the sample. The tip is attached to the end of a cantilever with a low spring constant, lower than the effective spring constant holding the atoms of the sample together. As the scanner gently traces the tip across the sample (or the sample under the tip), the contact force causes the cantilever to bend in order to accommodate changes in topography. In this scanning mode, the system uses the normal force suffered by the cantilever in its interaction with the sample surface as a feedback parameter to maintain constant the probe-surface distance. In order to examine this scenario in more detail, we will refer to the curve in Fig. 2.19 (van der Waals curve), that shows, from right to left, the variations

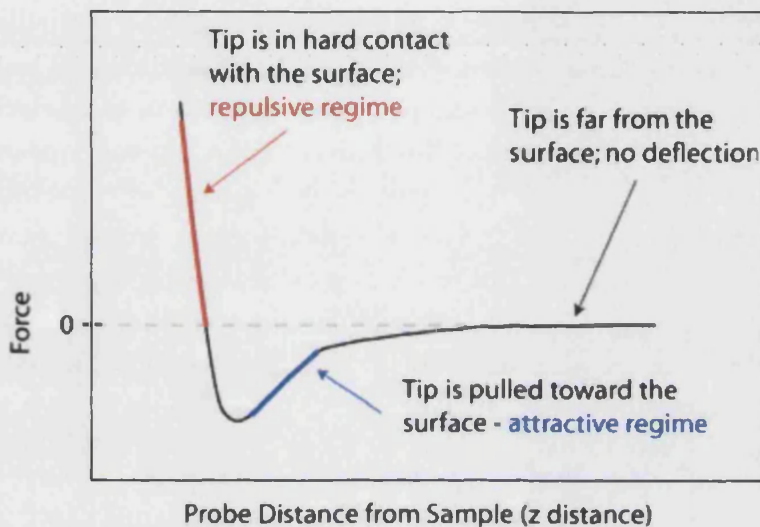

Figure 2.19: Interatomic force vs. distance curve.

of the tip-surface interaction force as the tip approaches the sample.
At the right part of the curve the atoms of the tip and the sample surface are separated by a large distance. Therefore, the tip-surface interaction is negligible. In a next step, as the atoms get closer to the surface, they are weakly attracted by the surface atoms (attractive regime). In AFM this means that when the cantilever pushes the tip against the sample, the cantilever bends rather than forcing the tip atoms closer to the sample atoms. This attraction increases until the atoms are so close together that their electron clouds begin to repel each other electrostatically. This electrostatic repulsion progressively weakens the attractive force as the interatomic separation continues to decrease. The force goes to zero when the distance between the atoms reaches a couple of Å. At this point, the total van der Waals force becomes repulsive, and it is said that the atoms of the tip and the surface are "in contact" (repulsive regime). Once the probe is "in feedback regime", the four quadrant photodiode can detect the cantilever deflection when moving along the xy plane. The electric signal in the four quadrants of the photodiode induced by the deflected laser beam is processed by the electronic components of the AFM in order to transform it into topographic data.

Dynamic mode

In spite of the demonstrated resolution, contact mode scanning presents several limitations. Among them, the role of lateral forces and frictions should be pointed out. Lateral forces can be large enough to move objects loosely placed on a smooth

surface or even to damage soft samples. These limitations pushed towards the development of the dynamic scanning modes [72], also known as tapping mode. In tapping mode, an oscillating voltage applied by a small piezoelectric element produces the oscillation of the cantilever at a fixed frequency, usually near its resonance frequency $\omega_{res} \approx \sqrt{k/m}$. Here, m is the mass of the cantilever which must be extremely small in order to be described by this simple equation. In this scanning mode, the oscillation amplitude is used as feedback parameter, since it decreases very quickly by the interaction of the tip with the sample. The system tries to keep constant the amplitude of the cantilever oscillation and in this way it reproduces as accurate as possible the scanned topography.

A thorough understanding of dynamic AFM operation requires solving the equation of motion of the cantilever under the influence of tip-surface forces. Some symmetry considerations allows approximating the cantilever by a one-dimensional object [73]:

$$EI\frac{\partial^4 \mathrm{w}(x,t)}{\partial x^4} + \mu\frac{\partial^2 \mathrm{w}}{\partial t^2} = F(x,t). \tag{2.31}$$

Here $\mathrm{w}(x,t)$ is the transverse displacement of the cantilever beam. E, I and μ are Young's modulus, moment of inertia and mass per unit of length of the cantilever, respectively. $F(x,t)$ is a term that contains all the forces per unit length acting on the tip. The above equation implicitly assumes that the tip is a massless object. In order to get some insight in the solution of Eq. 2.31, some simplifying assumptions can be considered. If we assume that the cantilever-tip ensemble can be described as a point-mass spring, then the tip motion can be approximately described by a non-linear, second-order differential equation [74, 75]:

$$m\ddot{z} + kz + \frac{m\omega_0}{Q}\dot{z} = F_{ts} + F_0\cos(\omega t), \tag{2.32}$$

where F_0 and ω are the amplitude and angular frequency of the driving force, respectively, and Q, ω_0 and k are the quality factor, angular resonance frequency and force constant of the cantilever. F_{ts} contains the tip-surface interaction forces. In the absence of F_{ts}, Eq. 2.32 describes the motion of a forced harmonic oscillator with damping.

Finally, it is important to note that in a damped harmonic oscillator the phase depends on the medium and the relationship between the excitation and resonance frequencies. These are the same factors that control the amplitude. Based on the analogy of our vibrating system with an harmonic oscillator,it seems reasonable to expect some sensitivity of the phase shift to surface properties, such as adhesion, elasticity and viscoelasticity.

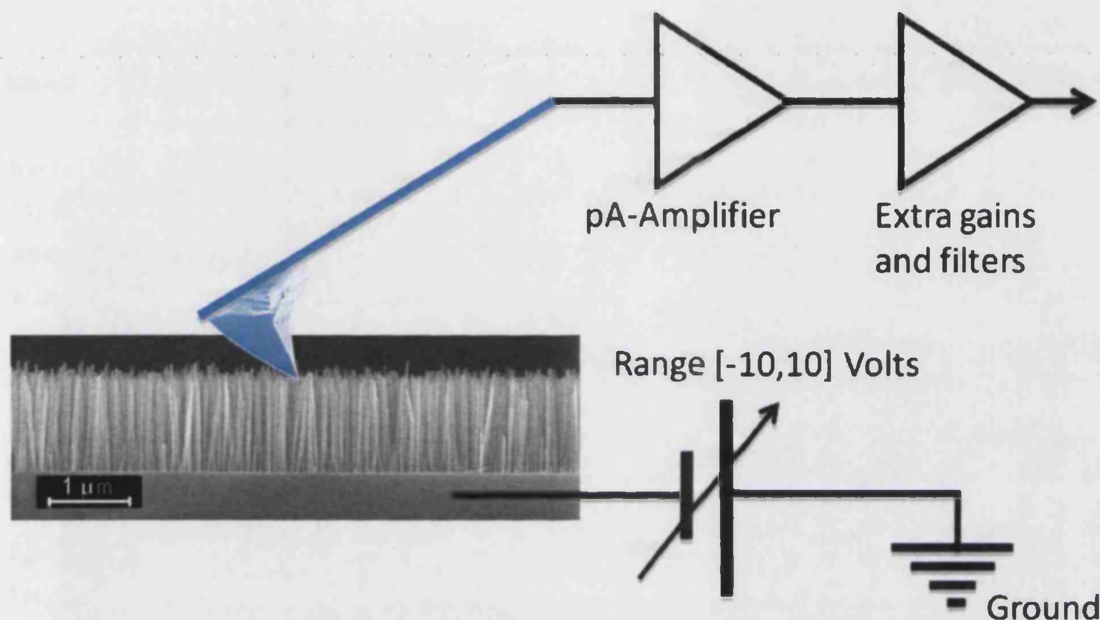

Figure 2.20: Sketch illustrating the setup for measuring electrical properties of NWrs as-grown.

2.5.3 Conductive measurements

Besides topographic applications, AFM is widely used in electrical research of semiconductors. In this section we will provide a qualitative explanation of electrical measurements performed with an AFM, namely conductive atomic force microscopy (CAFM). Besides a topographic profile of the surface, CAFM uses electrical current to reconstruct the electrical properties of the sample studied. For these kind of measurements a metal-coated tip (usually Pt/Ir, Au or Co/Cr) is used. By applying a potential to the tip, the current flows through the conducting sample. Usual AFM topography is acquired simultaneously with the current. This enables the correlation of the spatial features of the sample with their conductivity. CAFM can operate in two different modes: imaging and spectroscopic mode. In the conventional imaging mode, the tip is scanning over a small sample area, a voltage bias is applied to the sample and the electrons tunneling through the tip-surface are collected. In the spectroscopic mode the tip is stationary, while the voltage is being swept. This allows recording conventional current-voltage characteristics from tiny areas of the sample, and thereby extracting information on the local electronic properties. This last conductive mode is explained schematically in Fig. 2.20. This configuration is prepared to measure electrical properties in as-grown GaN nanowires. Figure 2.21 contains photographs corresponding to the real system used to carry out electrical measurements for this Thesis. The

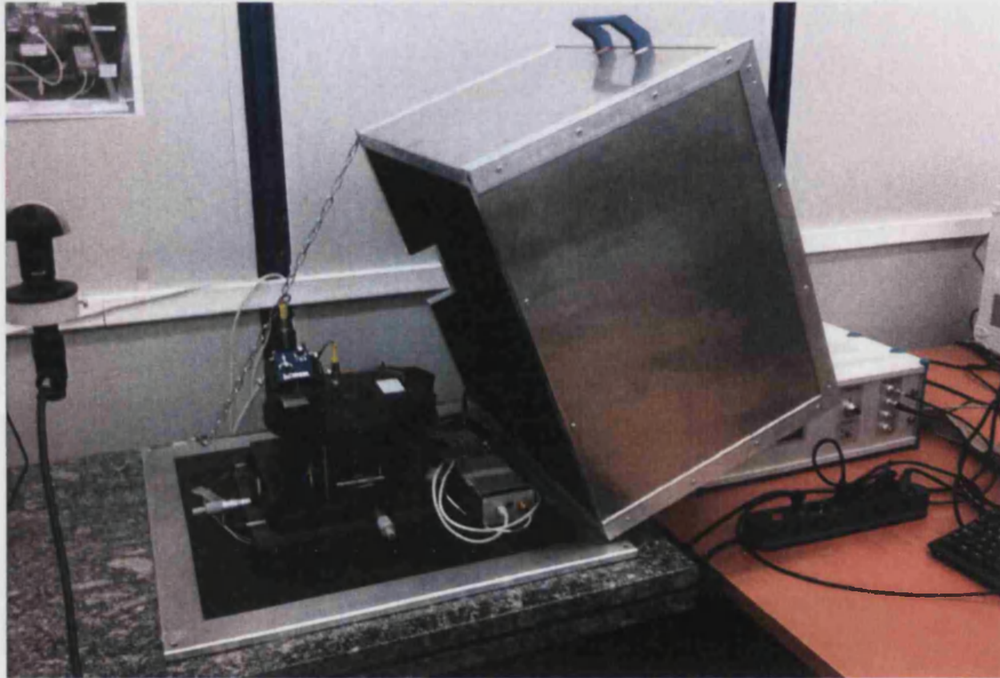

Figure 2.21: Photo of the atomic force microscope used to perform conductive measurements. The system was designed by nanotec and the dumping system and the Faraday cage by our owns.

system was made and designed by nanotec.

Plasma Assisted molecular beam epitaxy is the growth technique used to grow the samples studied in this Thesis. This Chapter is dedicated to describe the fundamentals of this growth technique. The following Sections show the characterization techniques employed in the analysis of the grown samples. Scanning electron microscopy has been used to characterize the morphology of the samples containing nanowires. The fundamental processes involved, together with the main parts of a scanning electron microscope are exposed. Photoluminescence is a useful technique for optical characterization. The fundamental physics involved in the photoluminescence process have been described, together with a real example of the photoluminescence emission from bulk GaN along a direction perpendicular to the wurtzite c-axis. Raman spectroscopy is a widely used technique to study structural and vibrational properties of semiconductors. The fundamentals of Raman spectroscopy have been given and the selection rules have been described for the different phonon modes of the wurtzite structure. Finally, the last technique explained here is Atomic Force Microscopy. This kind of microscope is used in order to characterize the surface morphology of a given sample. A description for its use for the electrical characterization of nanostructures is given.

Chapter 3

Characterization of non-polar GaN/AlN heterostructures

An investigation of the structural and optical properties of non polar GaN/AlN heterostructures is presented in this Chapter: *a*-plane quantum wells (*a*-QWs) and *a*-plane quantum dots (*a*-QDs). The strain state of the samples will be studied through changes in their phonon modes by means of Raman spectroscopy. We will then analyze the influence of strain on the electronic band structure of the different heterostructures. As we will see later, the photoluminescence emission will reveal strong confinement effects and the absence of QCSE. The polarization of the photoluminescence emitted along the growth direction will also be studied. Finally, we will make use of theoretical calculations to determine the influence of strain and confinement on the polarization of the emission.

3.1 Non-polar heterostructures

For different reasons that we will highlight in this introductory Section, in GaN optoelectronics activities in the area of non-polar and semipolar nitrides are rapidly expanding. More than a decade ago, the emission from the first GaN-based blue and green light emitting diodes (LEDs) was demonstrated and shortly thereafter the first violet laser diodes were realized by Ponce *et al.* [76]. Today, white LEDs are being widely commercialized and start to replace conventional light sources in everyday life. Mass-production of ultraviolet laser diodes for applications in optical storage devices, such as Blue-Ray and HD-DVDs, is ramping up as well. In order to continue this trend every percentage point increase in efficiency and total

light output is worth major efforts, because of the tremendous impact that LED-based illumination might have on the global market and energy saving. One of the physical problems hindering further advances in nitride emitters is the presence of large piezoelectric fields in these materials (see Sec. 1.1.2). The active regions of nitride LEDs or laser diodes are typically comprised of InGaN QWs which are under biaxial compressive stress due to the larger lattice constant of InGaN compared to GaN. Consequently, InGaN QWs grown along the crystallographic c-axis exhibit an internal piezoelectric field in the MV/cm range. The piezoelectric field also causes an undesired current-dependent red-shift of the emission due to the QCSE. A possible solution to overcome these problems is the growth of nitride heterostructures and QWs along crystallographic directions where the field associated to piezoelectric and spontaneous polarizations is small or zero. This is, for example, the case for a-plane or m-plane GaN. Waltereit and collaborators at the Paul Drude Institute in Berlin first demonstrated the absence of QCSE in m-plane GaN/AlGaN QWs grown on $LiAlO_2$ substrates [4]. As was pointed out by Park and Chuang [77], the piezoelectric polarization can be canceled out for certain oblique crystal directions, as it is shown schematically in Fig. 3.1 for the case of the polarization perpendicular to the growth plane in an In_xGa_{1-x}N layer pseudomorphically grown on GaN. In this Chapter we study and demonstrate the reduction of the QCSE in non-polar QWs and QDs. Additionally, we analyze the optical properties of non-polar heterostructures. We will see that the influence of the strain induced by the lattice mismatch between the different materials forming the heterostructure, together with confinement and shape influence in different ways their optical properties.

3.2 Characterization of a-plane GaN/AlN quantum wells

In this Section we present a study of the emission of a series of highly strained a-plane GaN/AlN QWs with increasing well thicknesses. Morphological features are determined by means of HR-TEM. The structural properties have been studied by a combination of HR-TEM, X-rays and RS, while the optical properties are addressed by PL. The emission along certain crystallographic directions allows us to study the selection rules for the corresponding optical transitions and compare them with those of the bulk material. In general, a change of the selection rules is observed as the QW width changes. This influences considerably the polarization of the emission. We will give an interpretation of the behavior studying the influ-

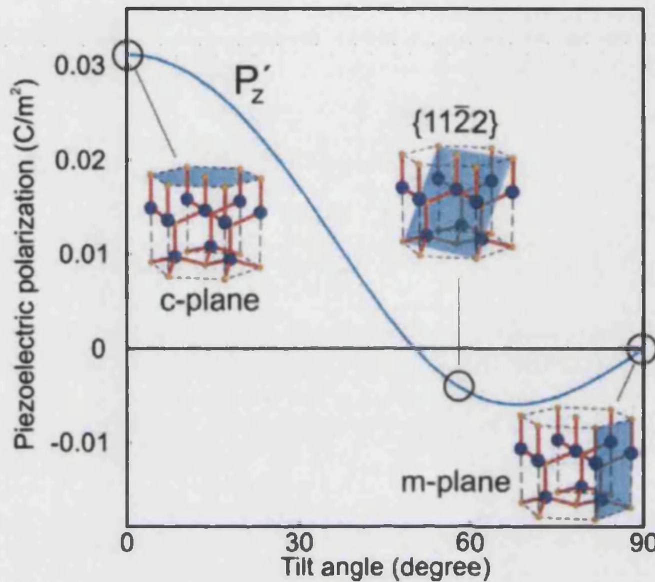

Figure 3.1: Piezoelectric polarization of an $In_xGa_{1-x}N$ quantum well surrounded by relaxed GaN barriers. The lattice planes of relevant polar, semipolar, and nonpolar orientations are shown as insets. The polarization P_z' refers to the plane perpendicular to the growth direction.

ence of strain and confinement on the optical transitions with the aid of theoretical calculations developed in the framework of an 8-band $\boldsymbol{k} \cdot \boldsymbol{p}$ model.

3.2.1 Description of the samples

These samples were grown by Dr. Sébastian Founta [78] at CEA (Grenoble). Four samples were grown by PA-MBE in the chamber described in Sec. 2.1. The substrate used was a commercial a-plane 6H-SiC polished by Novasic. The different crystal orientations are indicated in the sketch of Fig. 3.2. During growth, the RHEED diagram presented a streaky pattern characteristic of smooth $[11\bar{2}0]$ GaN and AlN surfaces [79]. The substrate temperature was fixed at 750°C. Metal-nitrogen ratio during growth was $\frac{\Phi_{III}}{\Phi_V} \approx 0.6$, namely under N-rich conditions. The growth sequence starts with a 50 nm AlN buffer layer in order to improve the crystalline quality of the QWs. Subsequently, a GaN QW of thickness d and a 10 nm thick AlN barrier were grown. This structure was repeated 5 times. Four samples with GaN QW thicknesses of $d = 2, 4, 8$ and 16 nm were grown. For simplicity, in the following we label these samples as QW2(S2447), QW4(S2444), QW8(S2489) and QW16(S2488). The number of each label refers to the well thickness d and the code in parenthesis is the grower's name of the samples.

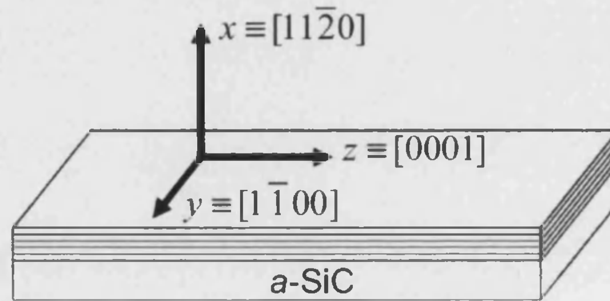

Figure 3.2: Sketch showing the orientation of the coordinates x, y, and z with respect to the crystallographic directions of the multiple QW samples.

3.2.2 Structural characterization

As a first step, RS experiments were performed to determine the orientation of the c axis into the samples using the selection rules for the phonon mode of SiC at frequency 765 cm^{-1}. Once the orientation of the WZ polar axis was determined, we verify the RS selection rules. The selection rules for the modes corresponding to GaN and AlN are very well fulfilled in all the samples. This fact allows us to assign the symmetry of the various modes for GaN and AlN. As a representative example, Fig. 3.3 shows the RS spectra from sample QW2. The spectra are taken in backscattering geometry and three different polarization configurations. In configuration $x(z,z)\bar{x}$ only the mode A_1(TO) is allowed, while in $x(yy)\bar{x}$ additionally mode E_{2h} is also allowed. On the other hand, in configuration $x(zy)\bar{x}$ only modes E_1(TO) are permitted. However, in this last configuration, as well as in $x(yy)\bar{x}$, some forbidden peaks are observed, although with a weak intensity. This partial breakdown of the selection rules can be explained by a small misalignment of the WZ c-axis with the polarization of the incoming light.

The peaks of interest have been fitted by Lorentzian functions for all the samples. The result is shown in green. The frequency of the modes has been plotted in Fig. 3.4 as a function of QW thickness. In all the graphs, the dashed line represents the frequency of the corresponding phonon mode in bulk (relaxed) material (see values en Table 1.7). The graphs on the left column present the modes attributed to GaN. They are strongly shifted towards higher energies circa 30 cm^{-1} with respect to the reference values. This shift can be attributed to the compressive in-plane strain in the GaN layers due to the AlN and/or the SiC substrate. In addition, as d increases there is a small shift of the modes to lower frequencies, that is, toward their relaxed values. This trend is in concordance with a progressive relaxation of strain as the thickness of the QWs increases. Regarding the phonon

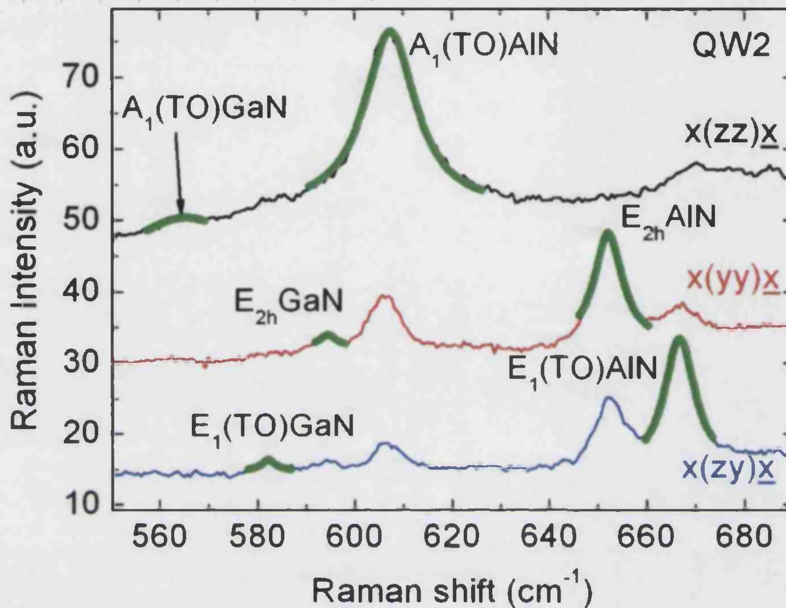

Figure 3.3: RS spectra of sample QW2 in various configurations. The green lines represent the Lorentzian fittings performed for each mode.

modes related with AlN, corresponding to the graphs on the right column, the signal is shifted around 5 cm^{-1} to lower frequencies with respect to their reference values. Separate modes corresponding to the AlN barriers (shown with empty circles) and buffer could only be resolved for sample QW16. In this case, it can be seen that the barriers experience a larger tensile strain than the buffer layer, evidenced by a larger red-shift, of around 10 cm^{-1}, of the phonon modes.

We use the shift of the modes (see Sec. 1.3.2) to calculate the components of the strain tensor along the principal crystallographic directions. For this calculation we have chosen the E_{2h} and $A_1(TO)$ phonon modes. This choice is justified by the analysis of the relative values of the GaN deformation potentials (see Table 1.8), that originates a smaller uncertainty in the determination of strain than other pairs of modes. The frequency shift suffered by the modes is related by the phonon deformation potential [26] through Eq. 1.16 and Eq. 1.17. To separate the in-plane strain components from the out of plane ones we assume that the heterostructure grows stress free along the direction $[11\bar{2}0]$ (biaxial approximation), which leads to Eq. 1.9. This assumptions are supported by HR-TEM measurements performed in samples QW2 and QW16. In this way, the values of the three diagonal strain tensor components can be obtained separately. The strain values derived from

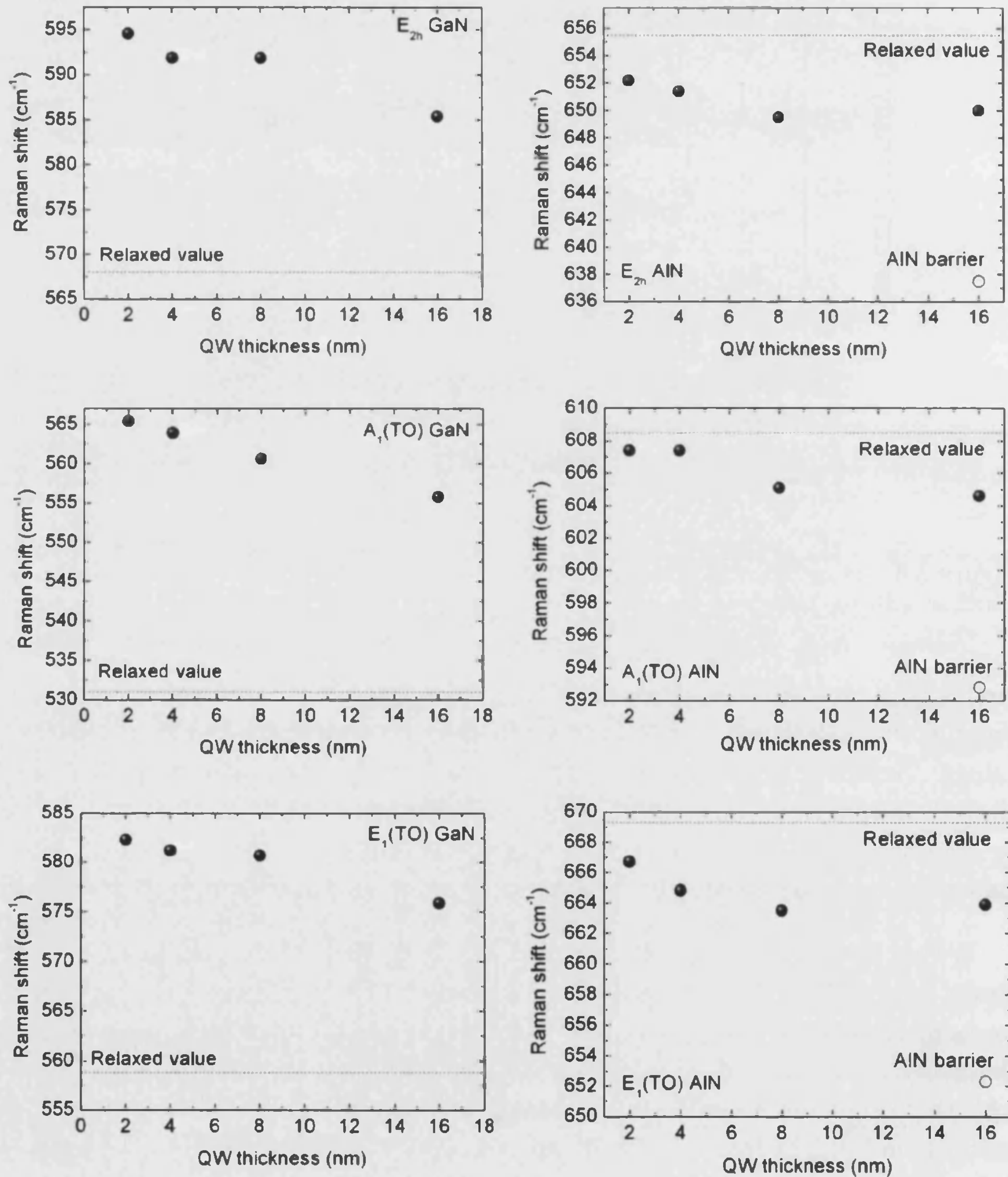

Figure 3.4: Frequency modes for GaN (left column) and AlN (right column). The dashed line represent the value of the frequency of the mode in the case of relaxed materials.

the analysis of the RS experiments are classified in Table 3.1 for the whole series. As we could expect from the blue-shift of the modes assigned to GaN, in-plane strain values (ε_{yy} and ε_{zz}) have a negative sign indicating a compressive strain as defined by Eq. 1.7. It is important to stand out the large in-plane strain anisotropy observed for all the samples. Sample QW16 presents a considerably smaller compression along the y axis, which results in a larger in-plane anisotropy. The value of ε_{xx} is also shown. It corresponds to an expansion of the lattice along the growth axis following that decreases slightly with increasing QW thickness. Samples QW2 and QW16 have also been studied by TEM along both $[1\bar{1}00]$ and

QW thickness (nm)	$\varepsilon_{yy}(\%)$	$\varepsilon_{xx}(\%)$	$\varepsilon_{zz}(\%)$
2	-1.8	1.4	-2.4
4	-1.2	1.1	-2.5
8	-1.9	1.2	-1.9
16	-0.7	0.8	-1.9

Table 3.1: Values of the three diagonal components of the Raman tensor calculated through the shift suffered by the Raman modes of GaN and applying the biaxial approximation.

[0001] zone axes. This analysis was carried out by Dr. Catherine Bougerol from CEA (Grenoble). Low magnification images from both samples taken along [0001] zone axis have revealed the anisotropic morphology of the QWs, which appear wavy, with undulations starting from the first AlN/GaN interface. Due to the absence of correlation in the rugosity of the successive AlN layers, the width of the QWs varies, up to 20%. The upper image in Fig. 3.5 shows low magnification TEM images of sample QW16. We can appreciate the substrate at the bottom, the AlN buffer on top of it and finally the 5 GaN/AlN periods. Additionally, HR-TEM images were taken along both zone axes and analyzed with the geometrical phase analysis (GPA) method in order to get the values of the lattice parameters c, a_x, and a_y as well as their change with position. Figure 3.5 shows in its bottom part the HRTEM images taken along the [0001] zone axis and the corresponding map of a_x for samples QW2 [(a) and (b)] and QW16 [(c) and (d)]. Analysis of the (0002) reflection did not show any change of the c parameter across the whole heterostructure, i.e., it remains constant from the SiC substrate through the whole sample. From this analysis the lattice parameter along the c axis is calculated to be $c_{GaN} = c_{AlN} = 0.504$ nm, which is the value reported for $c/3$ of bulk SiC. Values of a_x and a_y were obtained from images taken along the [0001] zone axis that allowed the evaluation of the various strain tensor components. No significant difference was detected for a_y between AlN and GaN either, and the values were checked to satisfy the Poisson relation in Eq. 1.10. The corresponding values of the three strain components for GaN are listed in Table 3.2. These values

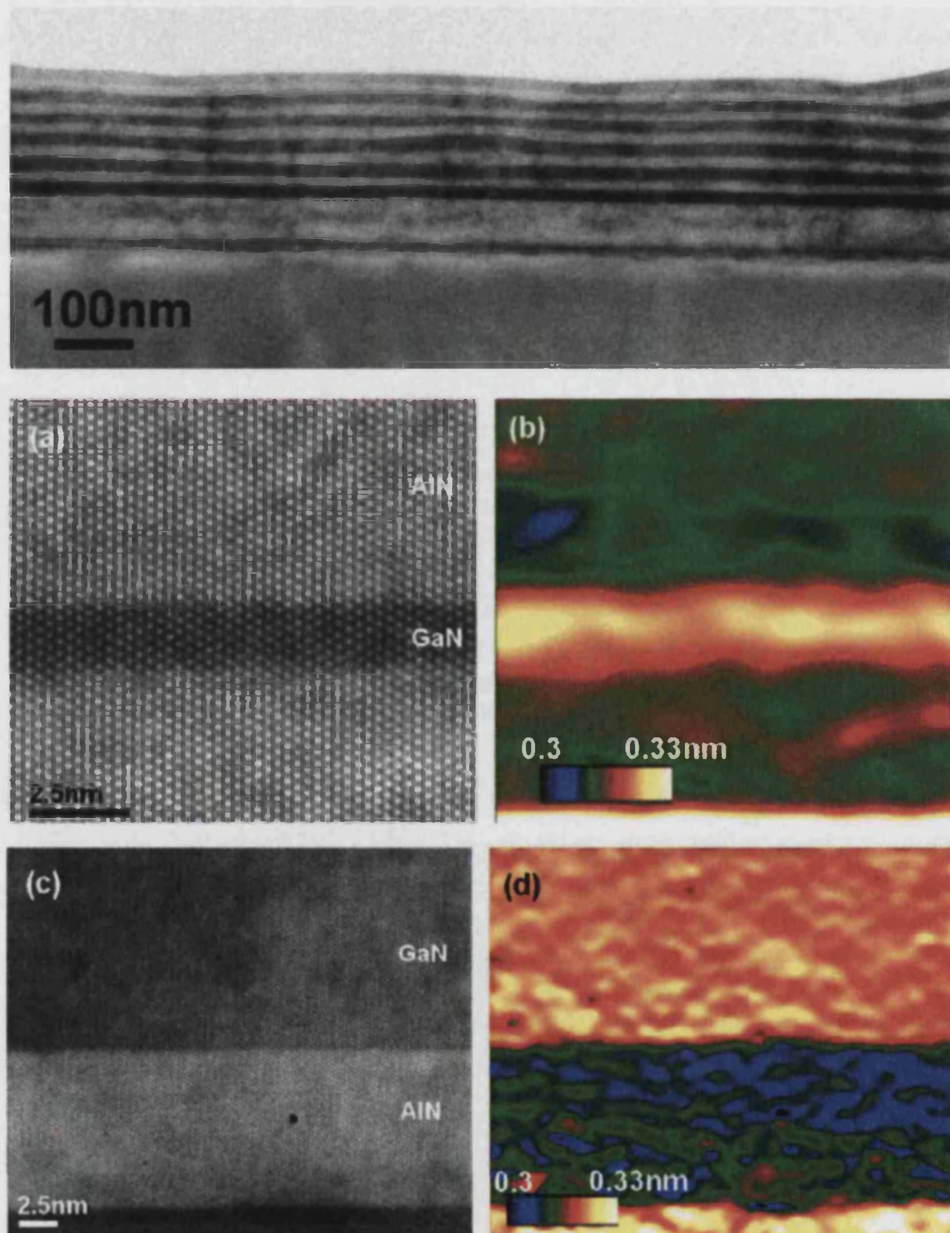

Figure 3.5: The upper image corresponds to the low-resolution TEM micrograph of sample QW16 along the [0001] zone axis. The square images at the bottom part show HRTEM micrographs taken along the [0001] zone axis and corresponding map of a_x obtained from GPA analysis.(a) and (b)correspond to QW2 and (c) and (d) to QW16.

were obtained with accuracy of 0.1%. Stands out the compressive in-plane strain components and the positive out-of-plane strain component, in agreement with RS measurements. Although there are some discrepancies on the quantitative value of ε_{yy} and ε_{zz} obtained by both techniques, the overall behavior is similar, specially in the stronger relaxation of QW16 along the y axis. About the fluctuation in the thickness of the QWs, GPA analysis indicates that the influence of QW thickness on these strain values is negligible.

QW thickness(nm)	$\varepsilon_{yy}(\%)$	$\varepsilon_{xx}(\%)$	$\varepsilon_{zz}(\%)$
2	-2.5	+1.6	-2.8
16	-0.6	+1.0	-2.8

Table 3.2: Strain values of samples QW2 and QW16 extracted from TEM measurements and GPA analysis.

In addition, XRD experiments were performed on the samples by Dr. Edit Bellet-Amalric. Acctually, conventional XRD analysis allows determining the in-plane lattice parameters a_y and c of the complete heterostructure. The results show that for all the samples the AlN buffer layer is strained by the SiC substrate, in agreement with TEM predictions. Along the y direction the QWs are partially compressed by the SiC substrate, resulting in a value of $\Delta a/a$ between -0.5% and -0.8%. Along the c axis the QW is expanded to the SiC value, with $\Delta c/c = +1.17\%$. This is consistent with TEM data for QW2 and QW16. It should be emphasized that the procedure developed for the calculation of strain values by means of RS is fully justified by TEM and XRD results where in-plane and out-of-plane lattice parameters are found to be consistently related through the Poisson's relationship.

Finally, the strain tensor components of the QWs have been computed by means of a simple model based on the elastic continuum theory. The model has been developed by my colleague Dr. Alejandro Molina. In this model, the multiple GaN/AlN periods are assumed to form a coherent freestanding multilayer, with the same in-plane lattice parameters throughout the whole structure. The possibility of a plastic relaxation has not been taken into account. By imposing the condition of minimum elastic energy under the above assumptions, the coherent in-plane lattice parameters and strain components of the planar GaN/AlN heterostructure can be obtained as a function of d. The total material thicknesses d_{GaN} and d_{AlN} used in the model are the same as in the structure studied experimentally, namely $d_{GaN} = 5 \times d$ and $d_{AlN} = 50$ nm $+5 \times 10$ nm.

Figure 7.16 shows the strain values for all the QW samples obtained by means the different techniques described above. The empty symbols represent the strain values obtain by means of RS. Values resulting from the combination of TEM/GPA

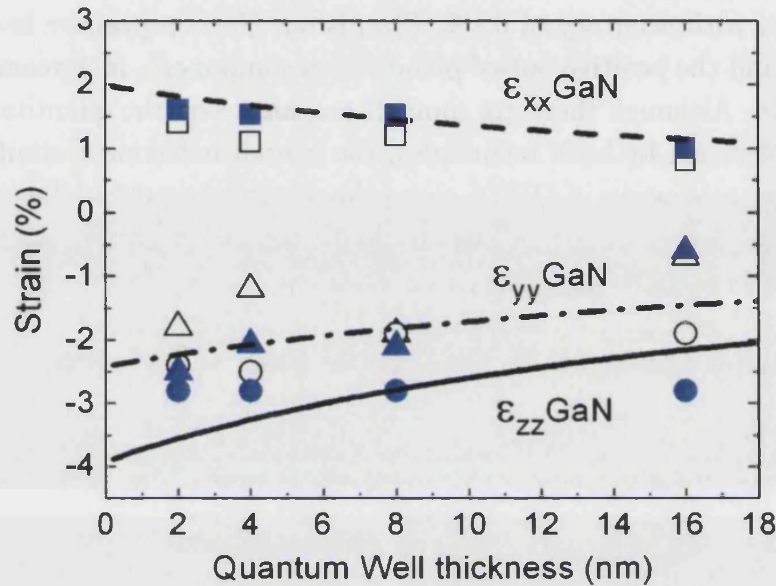

Figure 3.6: Comparison between experimental (full symbols for XRD/TEM, empty for Raman) and theoretical (lines) values of strain as a function of QW width. Squares show the expansion along the growth direction x while triangles and dots correspond to the in-plane compression along y and z.

and XRD are indicated by full symbols. Finally, the lines reproduce the theoretical calculations for the QW width varying from 0 to 18 nm. Circles and triangles correspond to the in-plane strain values, ε_{zz} and ε_{yy}, respectively. The out-of-plane ε_{xx} strain values are denoted by squares. The calculated strain values show that the GaN layers are strongly compressed along both in-plane directions z and y and tensile strained along x. The comparison with XRD/TEM results indicates that the relaxation of ε_{yy} and ε_{xx} approximately follows the elastic trend. However, the experimental results indicate that ε_{zz} remains constant at the value imposed by the SiC substrate, while in the results from the elastic theory ε_{zz} relaxes with increasing d in a way similar to ε_{yy}. This discrepancy is ascribed to the growth mode of a-plane AlN on SiC. The anisotropic relaxation observed experimentally may be understood to some extent by considering the high energy necessary for the activation of pyramidal slip systems along [0001], in $[11\bar{2}0]$ oriented AlN. In agreement with XRD/ TEM, RS data indicate a larger relaxation of the ε_{yy} component as the QW width increases. However, strain values obtained by RS underestimate the in-plane compression, especially along z. Finally, the elastic influence of the SiC substrate on the superlattice strain state has also been computed. The result shows that an inclusion of a SiC layer effectively decreases the value of ε_{zz} of the GaN well toward the GaN-SiC lattice mismatch (see Table 2.1). However, the ef-

fect of this layer on ε_{yy} is even larger since the lattice mismatch along y is as large as -3.4%, increasing the discrepancy between the results from the elastic theory and experiment.

3.2.3 Polarized photoluminescence emission

Low temperature photoluminescence measurements of the emission with polarization perpendicular ($E \perp c$) and parallel ($E \parallel c$) to the c-axis have been carried out by using the set up described in Sec. 2.3.2. The spectra were acquired with $k \perp c$, where k is the wavelength of the emitted light and it is parallel to the growth direction ($k \parallel a$). Figure 3.7 shows for QW2 (a), QW4 (b), QW8 (c) and QW16 (d) the spectra obtained for both polarization components. $E \perp c$ is plotted in black and $E \parallel c$ in red. These spectra have been taken from different spots on the sample's surface, that was found to be highly homogeneous. In order to compare the intensity between both polarization components, both spectra have been acquired under the same conditions. Additionally, the background signal has been subtracted in all the spectra with the aim of calculating the degree of polarization (DOP) of the emission, which is defined as:

$$DOP = \frac{I_{\perp} - I_{\parallel}}{I_{\perp} + I_{\parallel}}, \tag{3.1}$$

where $I_{\perp}$ and $I_{\parallel}$ correspond to the intensities of the emission polarized perpendicular and parallel to the c axis respectively, plotted in blue in the figures for all the samples.

We can observe that as the QW thickness increases, the energy of the emission red-shifts as a result of decreasing quantum confinement. Additionally, the energy is higher than the bulk GaN band gap (see Sec. 1.4.1) for all QW widths. This indicates a strong reduction or even the absence of QCSE. The energy shift suffered by the emission is shown in Fig. 3.8(a) together with the theoretical calculations of the lowest energy optical transition based on the $\mathbf{k} \cdot \mathbf{p}$ theory and effective mass approximation [80]. The experimental data lie below the theoretical calculations since the model does not take into account the exciton binding energy or a possible Stokes shift. Badcock *et al.* [81] reported that the combined effect of excitonic binding energies and Stokes shift lead to a shift in the range of 50 to 100 meV for a-plane GaN/$Al_{0.18}Ga_{0.82}N$ QWs. Although precise estimation of these effects is difficult to make in our case, we expect them to lie in the same range. Indeed, Fig. 3.8(a) illustrates that experimental results can be reasonably fitted by red-shifting the calculations by 100 meV. Further aspects are related with the full width at

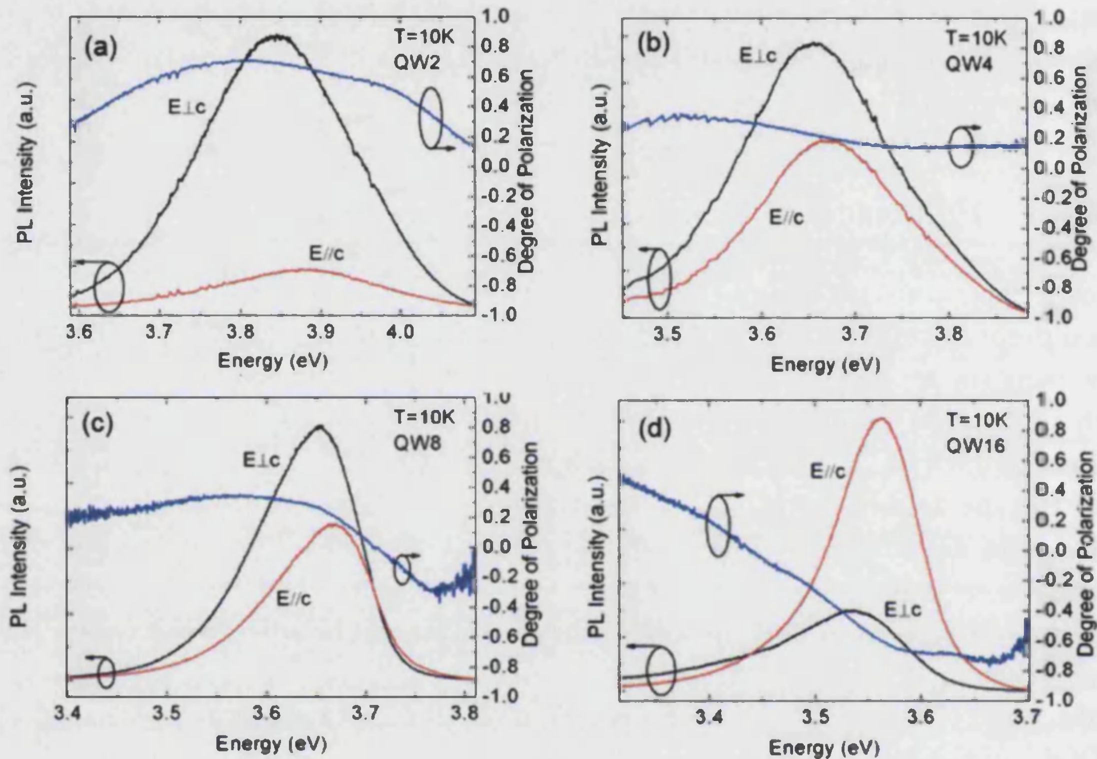

Figure 3.7: Polarized low temperature PL spectra from the whole set of a-plane QWs. Black and red lines represent the components of the polarization perpendicular ($E \perp c$) and parallel ($E \| c$) to the c-axis respectively. The DOP is calculated as a function of energy (blue line).

half maximum (FWHM) of the emission, plotted in Figure 3.8(b) as a function of the QW thickness. We observe that the FWHM of the emission peak decreases from 200 meV to 90 meV as the QW width increases. This trend is characteristic of inhomogeneous broadening due to fluctuations in QW width and strain, which are observed in the samples TEM analysis. In any case, as expected from the lack of internal electric field and the evidence of the reduction of the QCSE, the width is considerably smaller than that reported for 2 nm wide c-plane GaN/AlN QWs [82], which is around 350 meV.

Besides the characteristics described above, the most relevant feature of the spectra is related to the evolution of the DOP with QW width. The trend is, at first sight, quite unexpected, since an increase of the quantum well width from 2 nm to 16 nm reduces considerably the quantum confinement effects. Consequently, polarization values close to those found in bulk $\sim 100\%$ [83], could be intuitively foreseen. However, in the spectra we can observe that the emission of the 2 nm width QW is dominated by the component $E \perp c$, similarly as in bulk crystals. As the QW width increases, the relative intensity of the $E \parallel c$ polarization component

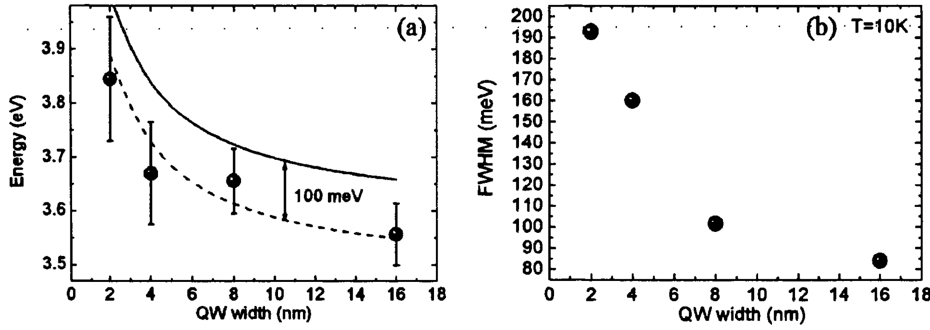

Figure 3.8: The graph on the left (a) represents the ennergy of the PL peak for all the samples (dots). The line shows the calculated energy of the first allowed optical transition. The dashed line is the result of the calculatios, red-shifted 100 meV.

increases, and for sample QW16 this component eventually dominates the emission. Besides, the component $E \parallel c$ is shifted between 15 and 25 meV to higher energies when compared to $E \perp c$. This shift may be an evidence of optical transitions involving deeper valence bands, populated by the use of relatively high excitation powers. In order to analyze in more detail the evolution of the DOP with QW width, we have assigned a mean degree of polarization to each sample. For this purpose we have evaluated the integrated intensity of the PL in both polarization configurations ($E \perp c$ and $E \parallel c$), measured at low temperature, and used Eq. 3.1. The values are shown in Table 3.3.

(%)	QW2	QW4	QW8	QW16
DOP	67.7±7	28.8±11	21.9±13	-31.8±3

Table 3.3: Degree of polarization of the emitted light from the whole set of samples. Note the inversion of sign for QW16.

We observe that the DOP decreases as the QW width increases, starting from large positive values (67.7% for the 2 nm QW) and showing a clear sign reversal (-31.8%) for the 16 nm well. Since the absolute intensities of the PL spectra may be influenced by the setup used in the measurements, and with the aim of verifying the reliability of our results, our colleague Dr. Julien Renard repeated the measurements in Grenoble with a different PL set up. The new set up consists in a 0.46 m spectrometer focal length, 600 grooves/mm gratings and a $\lambda/2$ plate. Small differences in the DOP were obtained in both measurements, which are taken into account in the uncertainties included in Table 3.3. Additionally, temperature-dependent PL measurements indicate that the DOP weakly depends

on temperature, decreasing around 10% at 200 K. The fact that the DOP remains almost constant in temperature is an indication that it is not significantly affected by localization that is likely to occur in QW structures at low temperature.

3.2.4 Theoretical description and interpretation

The electronic structure of the QW samples has been analyzed by means of an eight-band envelope function model computed by Dr. Jorge Budagosky, that includes the (Bir-Pikus) theory [14] to give account of the effect of strain. Quantum confinement is introduced through the envelope function approximation, taking into account a valence-band offset between GaN and AlN of VBO=0.5 eV (Ref. [84]). For computational convenience the multiple QW is treated as an infinitely periodic superlattice so that the envelope function can be expanded in plane waves. Luttinger-type parameters A_i and deformation potentials D_i are taken from References [85] and [1] respectively. From the calculated conduction and valence subband structures, we are particularly interested in the interband transition energies and wave functions at $(k_y, k_z) = (0,0)$. These wave functions are generally written as eight component spinors, $\Psi = \Sigma_j F_j |u_j\rangle$, where F_j are the envelope functions and $|u_j\rangle$ run over the eight Bloch functions used as a basis in the theoretical model, $|S,\sigma\rangle$, $|X,\sigma\rangle$, $|Y,\sigma\rangle$, $|Z,\sigma\rangle$, $\sigma = \uparrow, \downarrow$. The polarization-dependent oscillator strengths, *f*, are given by the following Equation:

$$f_\alpha = \left| \Sigma_{j,m} \left[\int_{-\infty}^{+\infty} F_j^{cv}(x) F_m^{vb} dx \right] \langle u_j | p_\alpha | u_m \rangle \right|^2 . \quad (3.2)$$

Here, the labels cv and vb refer to the lowest conduction band and highest valence-band confined states respectively and p_α is the momentum operator. As an important point, we would like to indicate that excitonic effects, not taken into account in the calculations, will change the optical transition energies, but they are not expected to modify significantly the oscillator strengths.

We turn now our attention to the effect of strain and confinement on the polarization of the optical transitions. We have discussed in Sec. 1.2 the character of the valence bands and the corresponding optical transitions for bulk GaN. In the unperturbed material the selection rules of the optical transitions predict that only the light emitted from transitions to the third valence band will be strongly polarized along the c-axis. However, we have already seen in Sec. 1.2.2 that both confinement and strain can influence on the electronic band structure. For analyzing the relative importance of these effects we have used the model presented above to compute the polarization components ($E \perp c$ and $E \parallel c$) of the oscillator

strength, f_y and (f_z) of the lowest-energy interband transition, (see Eq. 3.2), as a function of the in-plane strain for both bulk GaN and the 2 nm GaN/AlN quantum well sample. In the model, the in-plane strain components, ε_{yy} and ε_{zz}, are independently mapped from 0 to -4%, while ε_{xx} is obtained through Poisson's equation (see Sec. 1.1.3). The results are displayed in the form of color maps in Fig. 3.9. The component polarized perpendicular to z, (f_y), is represented in Figs. 3.9 (a) and (c), and that along z (f_z) in (b) and (d). Interestingly, bulk and QW oscillator strengths are almost identical provided that ε_{yy} <-0.5%, as it is the case in our samples. Consequently, the calculations indicate a negligible influence of confinement provided that strain in the QW is large enough. We have checked that, as expected, the similarity between the oscillator strength of the heterostructure and bulk GaN increases for thicker QWs. As pointed out by Yamaguchi [86] in the special case of isotropic in-plane strain, the small influence of confinement on the character of the bands can be attributed to the similarity of the valence-band Luttinger-type parameters A_4 and A_5 characteristic of GaN.

Once we can disregard the influence of quantum confinement on the electronic band structure of our QWs, we analyze the effect of strain on the oscillator strength, i.e., on the degree of polarization. From both components of the oscillator strength, (f_y) and (f_z), calculated for sample QW16, we computed the degree of polarization, $\mathrm{DOP}_{theoretic}$, plotted as a color map in Fig. 7.17. We have also plotted with empty circles the values of strain determined by TEM for the 2 nm and 16 nm thick QWs. The analysis of the figure indicates that the emission would be polarized along the c axis provided that the compression along z is large, while that along y is sufficiently small. As shown in Fig. 7.16, Raman, TEM, and XRD measurements reveal that these conditions are fulfilled only for the 16 nm QW. Consequently, the theoretical calculations predict a negative degree of polarization $\mathrm{DOP}_{theoretic} < 0$ (see Eq. 3.1) for the emission of this sample. On the contrary, the emission of thinner QWs, subject to larger compression along y, is predicted to be polarized perpendicular to the c axis, $\mathrm{DOP}_{theoretic} > 0$, as observed in the experiments. The contour lines $\mathrm{DOP}_{theoretic} = 0$, corresponding to unpolarized emission, are marked in white and separate the zone where the DOP is negative (red) from positive $\mathrm{DOP}_{theoretic}$ (blue). We can appreciate that the DOP sign reversal takes place smoothly, since the change from 0.8 to -0.8 covers a large range of strain. This ensures a gradual change in polarization as the strain in the QWs is relaxed, in very good accordance with PL experiments that indicate a slow change in the DOP as a function of QW thickness.

For a better comparison of our experimental PL results with the theoretical predictions we have plotted together in Fig. 3.11 the $\mathrm{DOP}_{theoretic}$ (full line) and the

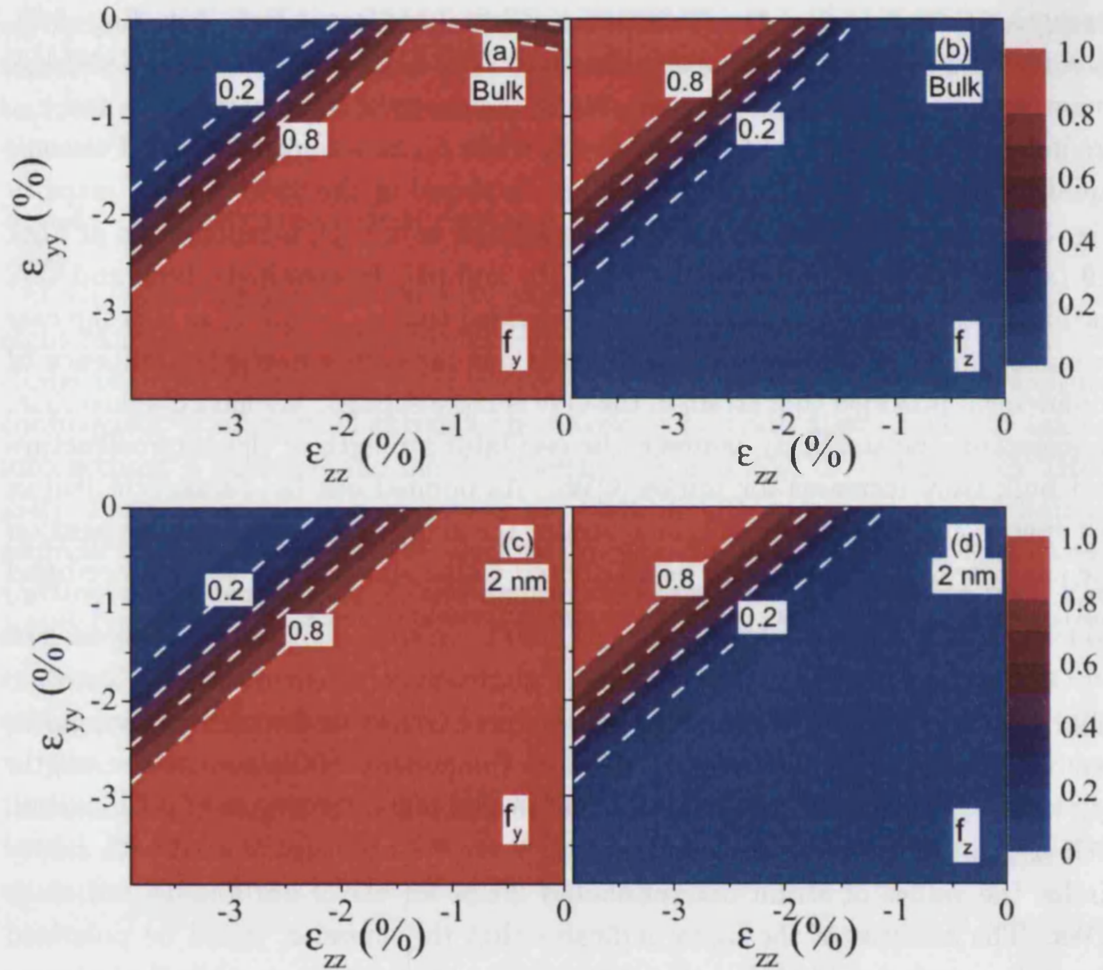

Figure 3.9: Oscillator strengths f_y (a) and (c)and f_z (b) and (d) mapped as a function of in-plane strain. The figures correspond to bulk GaN (top) and to the QW2 (bottom). Contour lines are plotted at intervals of 0.2.

experimental results (black spheres). In these calculations the QW width has been kept constant to 16 nm and strain values correspond to those determined by X-ray and TEM. As occurs in the experiment, the value of $\mathrm{DOP}_{theoretic}$ changes gradually from positive to negative values. The analysis of higher-energy optical transitions, specially relevant in the region of strain of sample QW16, (ε_{zz}=-2.8% and ε_{yy}=-0.6%) reveals an inversion of the DOP in agreement with the experimental results. Additionally, we also analyze the fundamental and first excited optical transitions. They present a dominant character of p_z and p_y respectively. As it can be observed in experimental results, theory shows a energetic separation of 12 meV between the emission energy of the polarization component $E \perp c$ and $E \parallel c$. This fact suggests the population of the second valence band by the relatively high excitation power

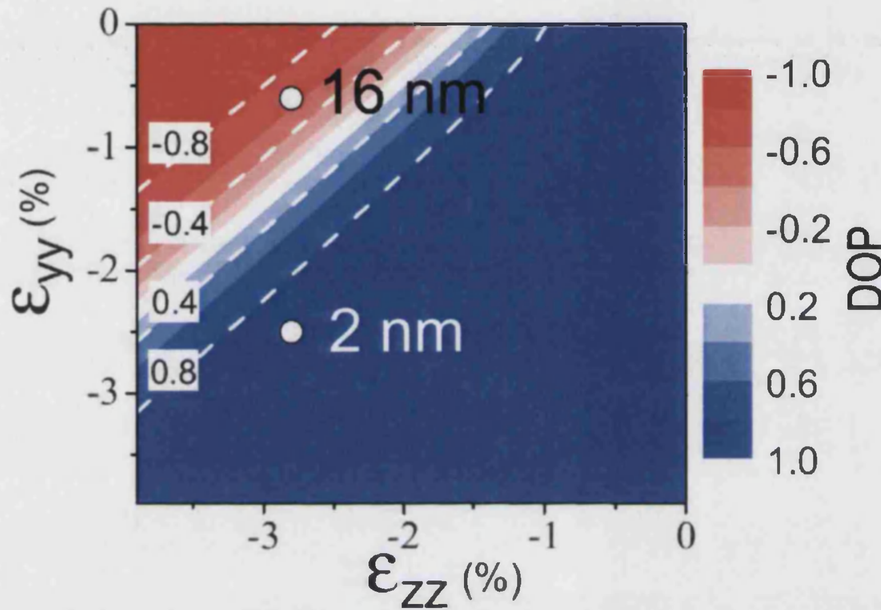

Figure 3.10: Calculated $(DOP)_{theoretic}$ mapped as a function of in-plane strain for a 16 nm GaN/AlN a-plane QW. The black ribbon marks $(DOP)_{theoretic} = 0$. The open circles correspond to the values of strain obtained by TEM for the 2 nm (lower point) and the 16 nm QWs (upper point).

used in our experiment. Finally, we would like to point out that the influence of the out-of-plane strain component, ε_{xx}, on the polarization characteristics is much smaller than that of ε_{yy} and ε_{zz}. Changes of 10% in the value of ε_{xx} resulted in variations of only 0.1% in the DOP.

In conclusion, we have studied the optical properties of the emission from a-plane GaN/AlN QWs. The emission energy shifts according with confinement. Regarding the polarization of the emitted light, we found a change in the degree of polarization as the QW width increases, decreasing its value and reversing its sign for the thickest QW. Calculations for the oscillator strength of the first optical transition for the main in-plane polarization components indicate a negligible influence of quantum confinement. However, the oscillator strengths and, consequently, the degree of polarization of the emission, are very sensitive to the values of strain along the in-plane directions. This dependence explains the characteristic evolution of the DOP as a function of QW thickness observed in our samples. In the next Section we present a similar study of the polarized emission from a-plane GaN/AlN quantum dots.

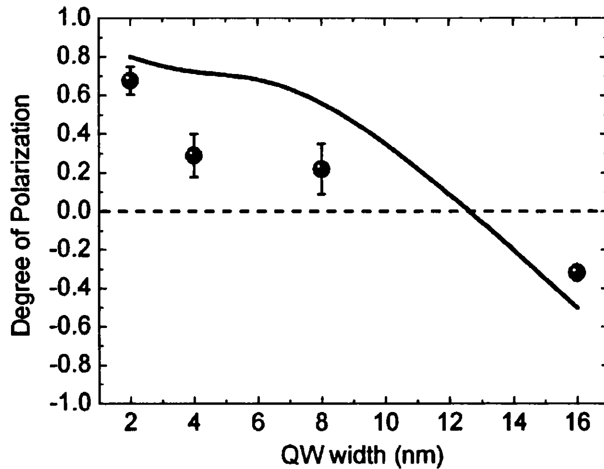

Figure 3.11: DOP vs QW width. Dots correspond to the experimental values. Full line corresponds to theoretical calculations.

3.3 Characterization of a-plane GaN/AlN quantum dots

In this Section we report an experimental and theoretical study of the polarization selection rules of the emission from four samples of a-plane GaN/AlN self-assembled quantum dots (QDs) with different structural characteristics. Time-integrated and time-resolved photoluminescence measurements have been performed in order to analyze their degree of polarization. It is found that in one of the samples the emission is predominantly polarized parallel to the wurtzite c axis, while in the others the emission is preferentially polarized perpendicular to the c axis. Theoretical calculations based on an 8-band $\boldsymbol{k}\cdot\boldsymbol{p}$ model are used to analyze the relative importance of strain, confinement along the growth direction and quantum dot shape on the polarization selection rules of the optical transitions.

3.3.1 Description of the samples

We have investigated 4 samples consisting of GaN/AlN QDs grown along the $[11\bar{2}0]$ WZ direction. All of them were grown by molecular beam epitaxy (MBE) on a commercial 500 μm thick a-plane 6H-SiC substrate polished by NOVASiC. For the first sample, labeled as D1 (s1826), the growth proceeded as follows: Prior

to GaN deposition, a 15 nm AlN buffer layer is grown. GaN grows in Ga-rich conditions at a 0.27 ML/s rate and at a substrate temperature of 700 °C. After the deposition of 2.7 monolayers of GaN, the SK transition takes place and the Ga flux is interrupted. The excess metal is then consumed by the nitrogen present in the chamber. Each QD layer is covered by a layer of 5.6 nm of AlN. This structure is repeated 18 times, except for the last QD layer, which is capped by 20 nm AlN. For morphological measurements, a second sample was grown under identical conditions without the last AlN layer. The growth sequence in sample D2 (s2283) starts with the deposition of a 7 nm AlN buffer layer on the SiC substrate. It is followed by a GaN/AlN quantum well superlattice consisting of 5 periods with 1 ML GaN and 13 MLs AlN. A second 7 nm AlN layer was then deposited on top of this superlattice. The aim of this QW-based buffer is to prevent possible structural defects or chemical impurities originating from the substrate surface from propagating through the subsequent layers[87]. On top of this buffer, a first GaN layer was grown under Ga-rich regime. After a deposition of about 3 GaN MLs, the RHEED pattern abruptly changed from streaky to spotty, revealing the formation of GaN QDs following the SK growth mode. Then, the GaN dot plane was covered by a 30 nm AlN layer, and a second GaN dot plane was deposited following the same procedure as for the first one. Sample D3 (s2287) is identical to D2 but the QD growth time increases in order to vary the size and density of the resulting QDs [88]. The last sample D4 (s2050) was grown on a 15 nm AlN buffer layer deposited on the SiC substrate. Growth temperature was kept at 750 °C and growth proceeded under Al-rich conditions. On this buffer, 3 GaN MLs were deposited to create self-assembled QDs. This layer of dots was covered with 3.8 nm AlN and the structure was repeated 150 times. As we will discuss next, the various samples present different morphologies, and this reflects in their optical characteristics.

3.3.2 Morphological characterization

AFM micrographs showing the surface of the set of samples containing a-plane QDs are presented in Fig. 3.12. From left to right the images correspond to D1, D2, D3 and D4. Images of D1 and D4 correspond to a scanning area of 1×1 μm^2, while those of D2 and D3 correspond to an scanning area of 0.5×0.5 μm^2. The average QD areal density is 1.2×10^{11}, 8.4×10^{10}, 1.6×10^{11} and 7×10^{10} QDs/cm^2 for samples D1 to D4, respectively. An evident increase in the density and height of dots in D3 with respect to D2 is observed, as expected by the increasing amount of GaN deposited during growth. An alignment of the dots along the $[1\bar{1}00]$ direction is

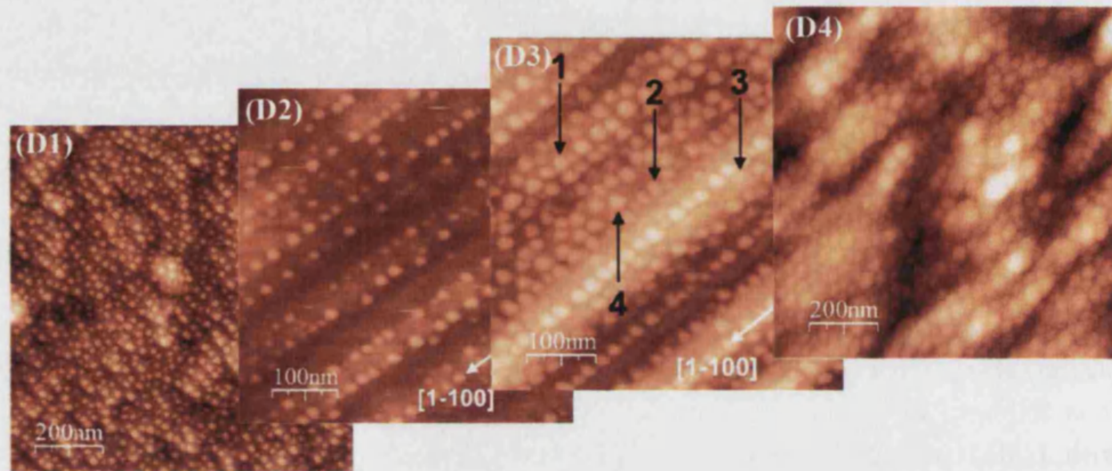

Figure 3.12: AFM micrographs of *a*-plane GaN QDs at the surface of the samples. From left to right D1, D2, D3 and D4. The scanning area for samples D1 and D4 corresponds to 1×1 μm^2, while for D2 and D3 to an scanning area of 0.5×0.5 μm^2 was swept.

observed on samples D1, D2 and D3. However, in sample D4 the dots are disposed randomly on the surface. An AFM study of the surface of an AlN buffer layer similar to the one present in samples D2 and D3 revealed a streaky morphology, consisting of ripples oriented along the $[1\bar{1}00]$ direction, with a typical periodicity of the same order of magnitude than that found in the QD lines. The authors propose two possible origin for this anisotropy: On the one hand, the anisotropy of the strain relaxation in the buffer that results from an in-plane anisotropy of the lattice mismatch between AlN and SiC. On the other, the presence of *c*-plane stacking faults propagating through the nitride layer, that create an anisotropy of the strain field at the surface of the buffer. This results in observed ripples and/or stacking faults that may act as nucleation centers. A detailed analysis of the origin of this alignment is given in Ref. [89].

In order to study the shape of the QDs, detailed morphology measurements by means of AFM were performed by Founta *et al.* [89] on samples D2 and D3. For sample D2 the shape of the QDs can be distinguished. They mostly appear squared or rectangular. The mean QD shape gives different dimensions for the in-plane directions perpendicular and parallel to the *c*-axis. The ratio between both directions results in 0.89 ± 0.14, with 80% of the dots having their side perpendicular to the *c*-axis larger than the parallel one. In sample D3 the edges of the QDs are more pronounced and the population has a wide variety of distinct shapes: squared, rectangular with the biggest side along the $[1\bar{1}00]$ direction, or trapezoidal. In Fig. 3.12, the images of sample D3 show the different shapes, labeled by arrows enumerated from 1 to 4. The dispersion of sizes in this sample

is wider than in the case of sample D2. An in-plane dimension ratio of 0.97 ± 0.23 is found after the analysis of the images. For samples D1 and D4 no exhaustive statistical analysis was carried out. Their mean dimensions have been obtained by measuring a couple of tens of QDs. For the whole series of *a*-plane QDs, we also determined the hight of the dots by means of AFM images. According with the resolution limitation of the AFM (see Sec. 2.5.1), we assign an uncertainty of 10% for the lateral dimensions and a 1% for their height. Table 3.4 compiles the mean dimensions of the QDs. The notation $\perp$ and $\|$ corresponds to perpendicular and parallel to the [0001] axis, respectively.

(nm)	D1	D4		D2	D3
Mean side $\|$	20	38.7		18.7	24.6
Mean side $\perp$	20	38.7		20.8	25.3
Mean height	2.7	1.1		1.6	2.6

Table 3.4: Mean size in nm calculated by means of AFM on the *a*-plane QDs from samples D1-D4. Only statistical analysis has been performed in samples D2 and D3. The notation $\|$ and $\perp$ correspond to parallel and perpendicular to the [0001] axis, respectively.

3.3.3 Structural characterization

Room temperature RS has been employed to analyze the strain state of the GaN QDs of D1 and D4. The small amount of GaN in samples D2 and D3 hinders the detection of the RS signal associated to the QD. Fig. 3.13 shows the RS spectra of D1 and D4 in various backscattering configurations. The fulfilment of the Raman selection rules found experimentally indicates the good crystalline quality of the investigated samples. In a first step of the RS analysis, we determine the *c*-axis direction along the in-plane orientations by using the signal from the peaks related to the SiC substrate and their selection rules. All the observed peaks have been fitted with Lorentzian functions. The frequencies and assignments of the Raman modes observed in the spectra are reported in the Table 3.5.

(cm^{-1})	D1 GaN	D1 AlN	D4 GaN	D4 AlN
E_{2h}	595.7	650.5	597.4	650.0
$A_1(TO)$	568.0	603.7	566.5	603.5
$E_1(TO)$	587.8	664.7	593.9	661.6

Table 3.5: Phonon frequencies corresponding to the modes observed in the Raman spectra acquired from samples D1 and D4.

The shift in frequency of the measured Raman modes with respect to the bulk strain-free values (see Table 1.7), is a manifestation of the strain state of the AlN

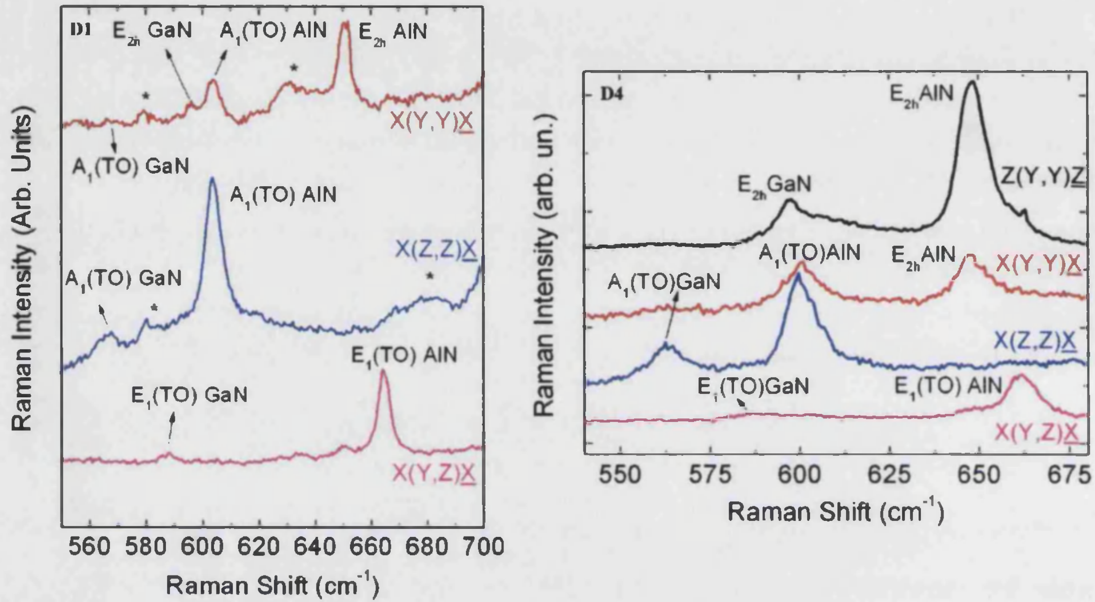

Figure 3.13: Raman spectra in different configurations for samples D1 (left) and D4 (right). The asterisks indicate peaks ascribed to the SiC substrate.

and the GaN dots. The measured shifts of the modes E_{2h}, $A_1(TO)$ and $E_1(TO)$ are classified in Table 3.6 for both samples. We observe a general blue shift up to 34.5 cm^{-1} for the peaks corresponding to GaN. Consequently, in the QDs compressive strain dominates(+ sign). The opposite occurs for AlN (− sign), where the peaks red shift up to 7.5 cm^{-1} with respect to the reference value.

(cm^{-1})	D1 GaN	D1 AlN	D4 GaN	D4 AlN
ΔE_{2h}	+28.0	-5.0	+29.8	-7.4
$\Delta A_1(TO)$	+34.5	-4.7	+34.7	-7.5
$\Delta E_1(TO)$	+30.2	-4.6	+35.1	-9.2

Table 3.6: Phonon frequency with respect to the reference falues for samples D1 and D4. The sign indicates the blue shift (+) and redshif (-) of the modes.

In order to obtain the three components of the strain tensor, we chose, as in the previously studied QWs, modes E_{2h} and $A_1(TO)$. As before, their frequency shift is related with the strain components through the deformation potential by Eqs. 1.16 and 1.17. If the stress along the growth direction x is assumed to be zero, it is possible to separate the three main strain components by using Eq. 1.9. This last hypothesis is not as straightforward as in QWs, but provides initial values for the principal tensor components in order to analyze the influence of strain on

their optical properties. The strain state of GaN and AlN in samples D1 and D4 is given in Table 3.7.

(%)	ε_{yy}	ε_{xx}	ε_{zz}
D1 GaN	-2.2	+1.5	-2.4
D4 GaN	-3.0	+1.7	-2.1
D1 AlN	-0.7	-0.3	+1.7
D4 AlN	-0.4	-0.3	+1.5

Table 3.7: Strain values of the samples D1 and D4 extracted from Raman measurements for GaN and AlN.

It is observed that the GaN QDs of sample D1 are highly compressed along both in-plane directions. The comparison with the biaxial strain for GaN grown on a-plane SiC ($\varepsilon_{yy} = -3.4\%$; $\varepsilon_{zz} = -2.8\%$; and $\varepsilon_{xx} = 2.0\%$) is similar, indicating that the strain is largely imposed by the chosen substrate. In the case of sample D4, Raman results indicate a larger relaxation of strain along the c-axis than in D1. This behavior can be attributed to the presence of misfit dislocations, as it has been observed previously in samples D2 and D3 by means of Medium Energy Ion Scattering (MEIS) [89]. It is important to stand out that the average value of ε_{yy}, ($\varepsilon_{yy} = -3.0\%$) obtained for this sample exceeds the lattice mismatch between GaN and AlN along that direction. We attribute this fact to the probable influence of the a-plane SiC substrate on the strain state of the heterostructures.

3.3.4 Polarized photoluminescence characterization

The setup described in Section 2.3.2 has been used to acquire the PL spectra polarized perpendicular and parallel to the WZ c-axis for the a-plane QDs. Both components are plotted in Fig. 3.14 in black (perpendicular) and red (parallel). We observe that the PL emission energy peaks above the bulk GaN band gap (3.506 eV) for all samples. As a matter of comparison, we would like to indicate that the PL emission from c-plane QDs is around 2.5 eV [32], much below the bulk GaN band gap. This is an indication of the absence or strong reduction of QCSE in our a-plane QDs. The emission energy from D1 to D4 is in the range of 3.6 to 4.1 eV. Actually, from the structural characteristics of the QDs shown in Table 3.4, we conclude that this energy is strongly determined by the height of the dots being 2.7 and 1.1 nm respectively. In this way, sample D3, with a mean QD height of 2.6 nm presents the lowest emission energy of the series. The largest emission energy corresponds to D2, (QD height of 1.6 nm). D1 and D3 do not follow this trend so well. We attribute this discrepancy to the uncertainties on the measured

height due to the absence of an exhaustive statistical analysis of the dimensions of the QDs in these two samples. Concerning the FWHM of the PL peak, it is well known that built-in electric fields in c-plane QDs amplify the inhomogeneous broadening due to dot size fluctuations [90] that can reach values up to 400 meV [32]. In our case, the reduction of QCSE narrows the width of the PL peaks. The FWHM of the emission ranges from 90 meV in sample D1 to 300 meV in sample D3, in correlation with the dispersion in QD sizes and shapes discussed above. In any case, the emission of a-plane QDs is still narrower than that characteristic of c-plane QDs.

The evolution of the photoluminescence spectra has been studied as a function of temperature and analyzed by means of a multi-Gaussian fit in order to obtain the characteristics of each PL peak and the relative contributions of the different recombination channels. As the temperature increases from 10 K to room temperature, a red-shift in the PL peak energy of 40 meV is observed. This shift is in agreement with a decrease in the GaN band gap [59] with increasing temperature.

Regarding the polarization of the emission, as in the case of a-plane QWs, the DOP has been calculated using Eq. 3.1 by integrating the area under the emission peak, polarized perpendicular and parallel to the c-axis. Table 3.8 lists the DOP of the calculated in this way from the four a-plane QDs samples. The emission of samples D1, D2 and D3 is preferentially polarized perpendicular to the c-axis, resulting in a positive DOP. The polarization of the emission from sample D4 is

(%)	D1	D2	D3	D4
DOP	68.4	84.7	88.7	-57.8

Table 3.8: Degree of polarization of the light emitted from samples D1 to D4.

considerably different. In this case the component parallel to the c-axis dominates. It is also interesting to highlight the fact that the parallel component is blue-shifted for samples D1 and D2 and amount of 22 and 25 meV respectively. However, in sample D3 this component of polarization is 21 meV red-shifted, while for sample D4 both components of polarization are at the same energy. This indicates that not only the oscillator strength, but also the energy of the lowest transitions is strongly affected by QD shape, size and strain. The DOP has been determined for all the samples as a function of temperature and it remains constant up to room temperature. In Figure 3.15(a) we can observe the evolution of the DOP (blue squares) as a function of temperature for sample D4 in a logarithmic scale. Black and red symbols represent the integrated intensity of the emission of both polarization components, $E \perp c$ and $E \parallel c$ respectively. From the evolution of

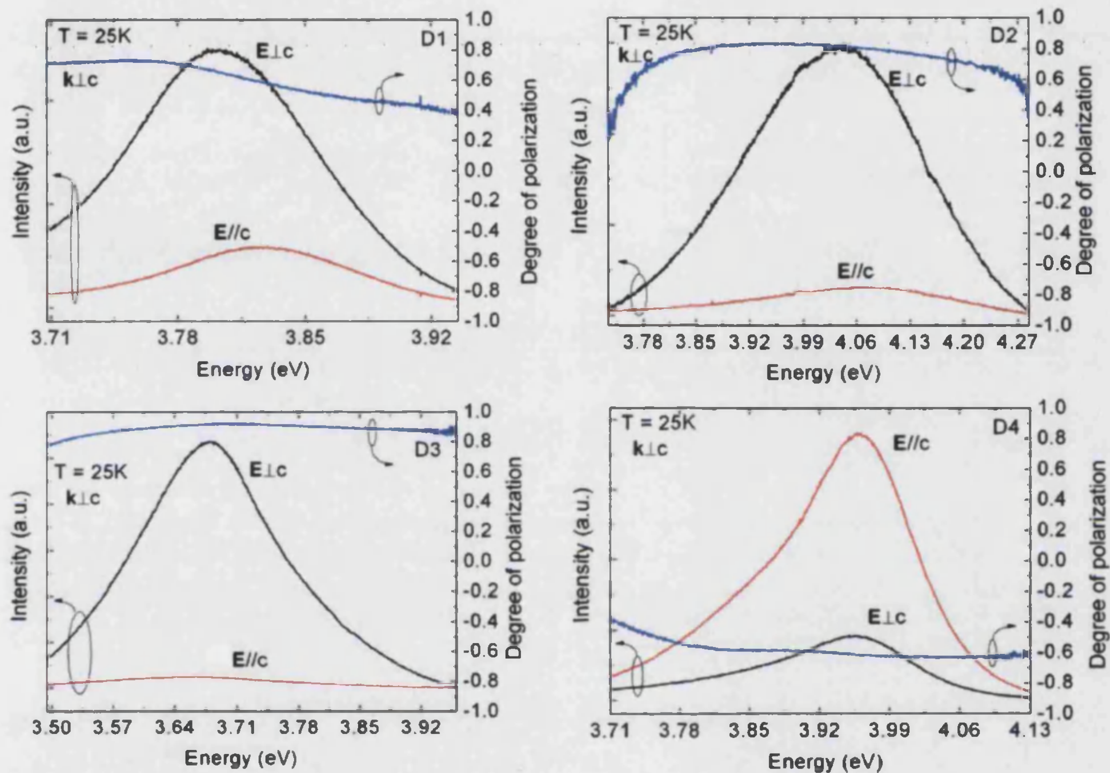

Figure 3.14: Polarized low temperature PL spectra from the whole set of a-plane QDs. Black and red lines represent the components of the polarization perpendicular ($E \perp c$) and parallel ($E \| c$) to the c-axis, respectively. The DOP is calculated for each emission energy and it is shown by the blue line.

the spectra with temperature it becomes clear that the intensity of the emission decreases only very slightly as the temperature increases. This is in contrast to the strong intensity decrease observed in the emission from bulk GaN. Actually, PL from bulk GaN is already very weak at 100 K, due to dominant non-radiative processes. We can estimate the internal quantum efficiency of the emission form our QD samples. Considering that at low temperatures all the recombination processes are radiative, we obtain for sample D4 an internal quantum efficiency of $\eta_{QDs} = 26\%$, while for bulk GaN its value is $\eta_{QDs} = 5\%$. The evolution with temperature of the emission of samples D1 to D3 is similar, indicating that in QDs most of the non radiative processes remain inactive up to room temperature.

Additionally to the time integrated PL experiments, we performed an analysis of sample D4 by means of time resolved PL. The evolution of the emission with time of both polarization components is shown in Fig. 3.15(b). $E \perp c$ and $E \parallel c$ are shown in black and red lines respectively, while the resulting DOP for each time is shown in blue. For this study, we used the set up described in Sec. 2.3.3.

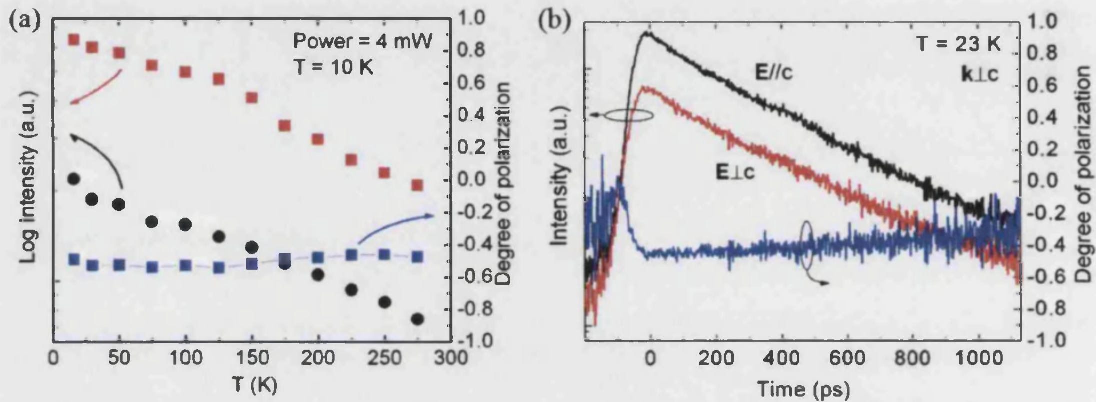

Figure 3.15: (a) Experimental DOP (in blue) obtained in the range of temperatures between 20 and 300 K using both polarization components of the emission: $E \perp c$ in black and $E \parallel c$ in red. (b) TRPL spectra of sample D4 for two polarization configurations: $E \perp c$ in black and $E \parallel c$ in red. The degree of polarization as a function of time has been included in blue(right scale). The emission was detected at 3.97 eV.

The signal was detected at the maximum energy of the emission, corresponding to 3.97 eV for both polarizations. Both PL decay curves can be fitted by a single exponential. This fact agrees with the hypotheses that only one transition is involved in the emission. From the fitting, we obtain a characteristic decay time of 300 ps for both polarization components, a value comparable with that of other non-polar QDs [88] and much smaller than that characteristic of c-plane QDs, in the order of ns [91]. The large value of the energy of PL emission together with the fast decay rate are strong indications of an important reduction of the internal electric field in this GaN/AlN a-plane QD superlattices. For this sample we find that the dominant $E \parallel c$ emission and consequently the negative DOP persists in time, decreasing only slightly after 800 ps, as can be observed in the Figure.

The analysis of the PL as a function of the excitation power allows the identification of the recombination processes involved in each PL peak and is presented in Fig. 3.16(a). The Figure shows three PL spectra at low temperature acquired with three different excitation powers, namely 100 μW, 1 mW and 5 mW. The shape of the PL peak and its energy remain constant, independent of excitation power. This is in agreement with a reduction of the internal electric field, as discussed above. We recall here that in c-QDs there is a blue shift of the emission as the excitation power increases due to the screening of the electric field by the photoexcited carriers [32]. The inset shows the integrated intensity as a function of excitation power, with logarithmic scale, fitted to the equation $\log I \propto n \log P$. Based in the model developed by Schmidt *et al.* [92], a value of n close to 1 identi-

fies the excitonic nature of the transition. Power dependence measurements were also performed as a function of temperature, ranging from 20 to 300 K. The Arrhenius plot corresponding to the three values of the excitation power is shown in Fig. 3.16(b). Again, the evolution of the intensity with temperature is independent of excitation power. Two different temperature regimes can be distinguished: at low temperatures, up to 66 K, the intensity remains almost constant. Above this value a very rapid quenching of the intensity is observed, indicating the dissociation of the excitonic complex involved in the emission. An analysis of Arrhenius plot has been carried out using the well-known thermal activation relation [93]:

$$I(T) = \frac{I_0}{1 + \tau_0 \Gamma^* e^{-\frac{E_a}{k_B T}}} \tag{3.3}$$

Here E_a represents the activation energy , τ_0 the life time of the involved transition while $1/\Gamma^*$ indicates the life time related to non radiative processes, which are more important at higher temperatures. I_0 is a normalization factor which is taken from the intensity of the emission at the lowest temperature. A detailed evaluation shows that one activation energy is sufficient for a satisfactory fit of the experimental data. We obtained an activation energy of 30 ± 3 meV at all excitation powers. The activation energy is related with the energy necessary to dissociate the complex involved in the radiative recombination. Therefore, an activation energy higher than the thermal energy at room temperature (25 meV) assures the survival of the complex up to room temperatures. This shows up in a measurable intensity at room temperature and an increase in quantum efficiency, as discussed in relation to Fig. 3.15(a). Taking into account that the binding energy of the exciton to the donor is expected to be smaller than 30 meV, the most probable process involved in the PL of sample D4 is the recombination of a free exciton related to the first valence band.

3.3.5 Theoretical description and interpretation

In order to get better insight into the mechanisms that influence the polarization of the PL emitted by these samples, we have made use of a theoretical model for the electronic structure of GaN QDs developed in the framework of an 8-band $\mathbf{k} \cdot \mathbf{p}$ Hamiltonian and the envelope function approximation. This relatively simple model represents the QD as a rectangular box with infinite barriers. Strain effects are considered through a Bir and Pikus-like Hamiltonian. The model provides insight into the effect of strain, confinement and QD dimensions on the orbital composition of the valence bands. More details about this theoretical model can

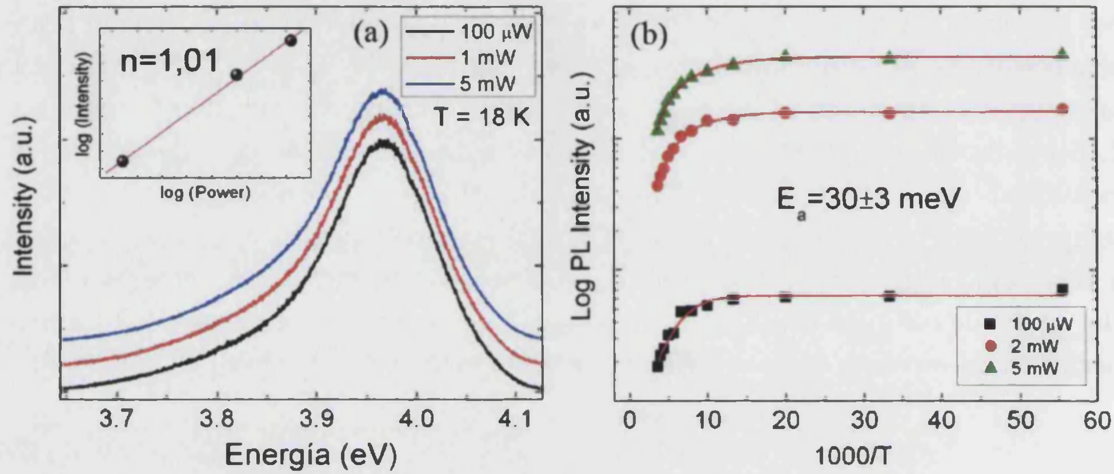

Figure 3.16: (a) Dependence of the low temperature PL spectra with excitation power. The spectra have been normalized and shifted for clarity. The inset shows the linear dependence between the intensity and the excitation power. (b) Arrhenius plot of the PL intensity versus temperature.

be found in the Doctoral Thesis of Dr. Jose Llorens [94]. For the analysis of the influence of strain, we use values in the range of those found experimentally and listed in Table 3.7. For the calculation of the DOP from the theoretical results, we have only taken into account the first electron-hole transition. No excitonic effects are considered.

We will analyze first the influence of strain. For the calculations, we have fixed the dimensions of the box to those of sample D4 (4 nm-separated boxes with base dimensions $Ly = Lz = 40$ nm and a height of $Lx = 1$ nm). Since this sample displays a negative DOP, we will center our discussion in its analysis. The values of the DOP obtained from the calculations are shown in the six graphs of Fig. 3.17 for different values of strain. In each pair of graphs one strain component is continuously swept, while the others are kept constant in the range of small (left) or high (right) compression. The first pair shows the variation of DOP with ε_{xx} (strain along the growth direction). We see that the DOP is different for both cases but, similarly as in a-QWs, the degree of polarization does not depend on this strain component both in the ranges of small (left) or strong (right) compression along y and z. For this reason, in the remaining graphs we have kept ε_{xx} constant to the experimental value (1.68%). The second pair of graphs represent the variation of the DOP with ε_{yy} for small (left) and strong (right) compression along z. In both figures we observe that the DOP degreases and changes sign as ε_{yy} relaxes towards zero. In the last pair of graphs we show the effect of varying ε_{zz}. On the left we consider the case of small compression along y, while on the right the

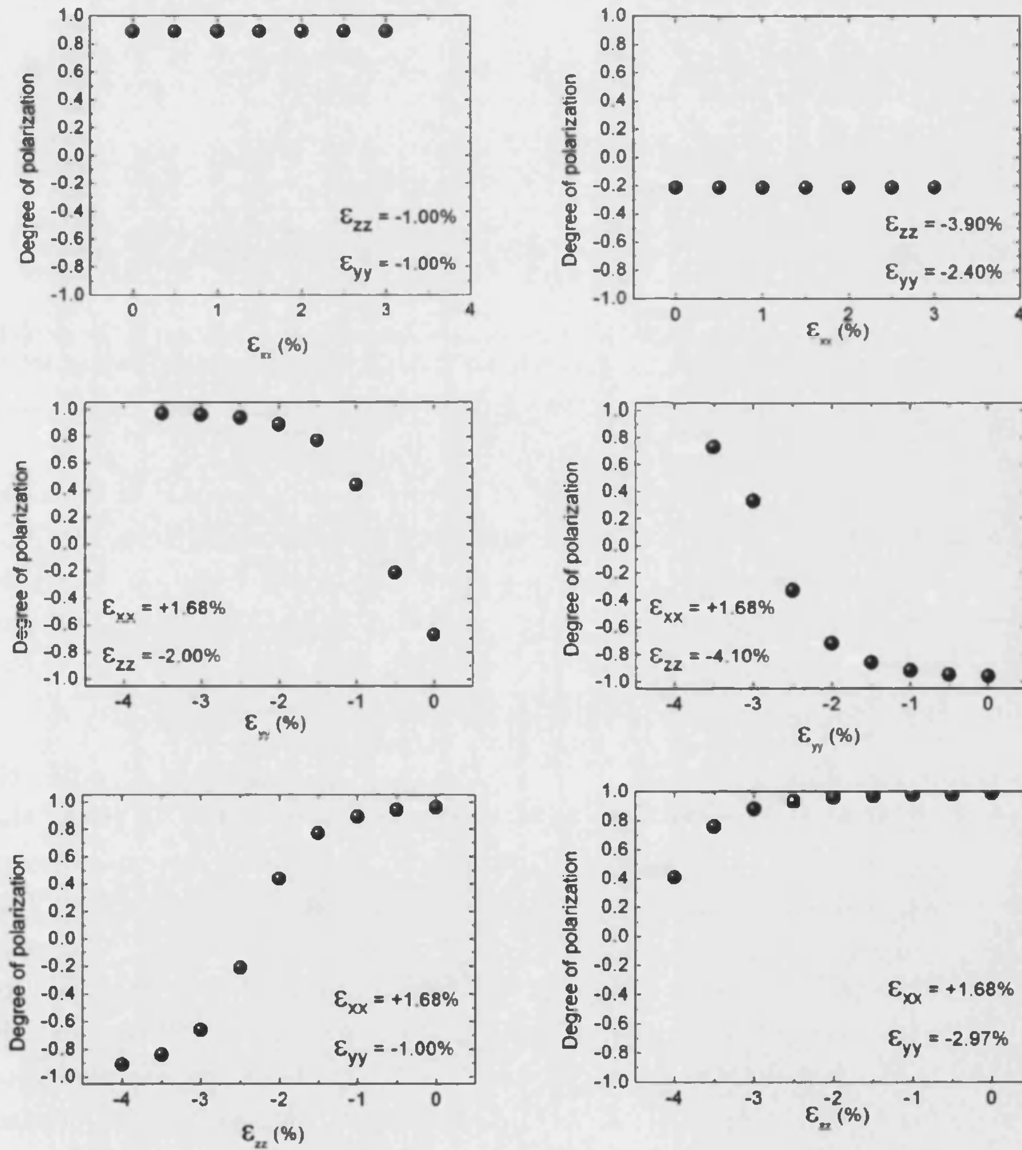

Figure 3.17: Evolution of the degree of polarization of the emission calculated for a GaN QD ($Ly = Lz = 40$ nm, $Lx = 1$ nm) as a function of strain. The values of strain considered are indicated in each graph.

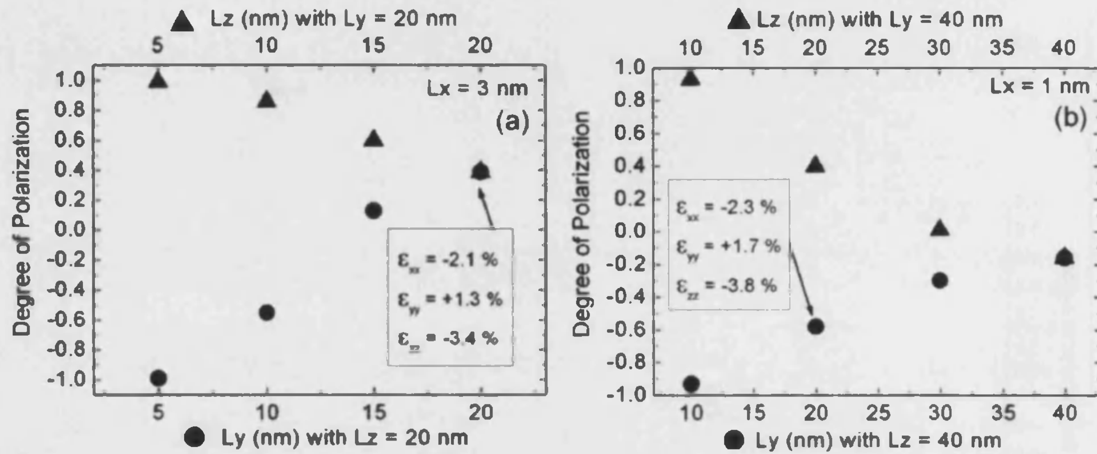

Figure 3.18: Degree of polarization of the emission from GaN QD as a function of the in-plane shape. On the left the parameters corresponds to samples D1 and on the right to sample D4. The values of the strain components are indicated in the inset of each graph.

compression is large. This time we observe an increase in the value of the DOP as ε_{zz} relaxes towards zero. Stands out the fact that in the graph on the right (strong compression along y) the DOP takes on only positive values. From the above considerations, it is clear that a negative value of the DOP can be obtained provided that the compression along z is large and that along y is small. These conclusions are similar to those obtained before for a-QWs.

Recalling that in sample D4 $\varepsilon_{zz} = -2.1\%$ and ε_{yy} is as large as -3%, the theoretical DOP resulting from our model would be close to 100%, in strong disagreement with experiment (-57.8%). This suggests that, either our experimental determination of strain is wrong, or that there might be other mechanisms that need to be considered to explain the observed negative polarization. Considering the fact that the tools necessary for the improvement of the determination of strain in our samples were not available, in the following we will consider the effect of QD shape on the value of the DOP. Actually, based on morphological studies performed on samples D2 and D3, Founta *et al.* established that a-plane GaN QDs present faceted trapezoidal shapes which should lead to rather asymmetric confinement potentials [79]. Therefore, it is relevant in this case to analyze the consequences of QD shape asymmetry on the DOP. Figure 3.18 shows the DOP calculated for QDs with different dimensions along $z = [0001]$ (L_z) or along $y = [1\bar{1}00]$ (L_z). In the calculations shown in the graph on the left (a) the height (L_x) of the box and the value of the strain components have been kept constant to those determined experimentally for sample D1. For comparison, the graph on the right (b) shows similar calculations, but this time using values representative

for sample D4. Full dots correspond to the variation of L_y, keeping L_z constant to 20 nm (bottom axis). Full triangles are the result of varying L_z, with $L_y = 20$ nm. It is observed that the shape asymmetry enhances the linear polarization of the QD emission along the largest side. For both sets of strain values a negative DOP is obtained under the condition of anisotropic lateral confinement. As well as for the simulation of D1 and D4, the experimental results are understood provided that the rectangular shape of the dot is oriented with the larger side parallel to the c-axis. In conclusion, according to simulations the DOP characteristic of sample D1 is influenced by the strain and the dominant squared shape of the dots. On the contrary, the polarization of the emission from D4 is strongly influenced by the anisotropic in-plane strain and the alignment of the longer QD side along the [0001] direction. In summary, both parameter: strain and lateral confinement can influence on the polarized emission.

Non-polar GaN/AlN QWs, and QDs grown along the *a* WZ direction have been analyzed. The structural properties have been obtained by means of RS, XRD and TEM. The anisotropy of the wurtzite structure along this direction results in polarized emission. Photoluminescence has been used in order to characterize the optical properties of the samples. Polarized polarization measurements reveal strong differences between the samples. By using a theoretical model, we discuss the different parameters that influence the polarization of the emission: strain, confinement and QD shape. For *a*-plane QWs it is shown that quantum confinement does not influence on the character of the optical transitions in the range of strain studied here. However, the influence of in-plane strain and its anisotropy is very important in order to understand the characteristics of the polarized emission of these samples. In the case of *a*-plane QDs the shape of the nanostructures turns out to be also an important factor.

Chapter 4

Growth and morphology of GaN nanowires

Plasma-assisted molecular beam epitaxy (PA-MBE) is particularly attractive for the growth of GaN NWrs due to the absence of catalysts, which are a potential source of impurity contamination [95]. The growth of GaN NWrs begins by the formation of nuclei to a critical size, called NWr precursors, followed with the continuous growth of the NWrs. However, the growth dynamics of GaN NWrs growth is still unclear. In this Chapter, we present a growth study of GaN NWrs with and without the use of an AlN buffer layer using Si(111) as substrate. In the last part of the Chapter we present an in-depth analysis about the morphologic features of GaN NWrs grown directly on Si(111), were we found a strong dependence of the radius, length and density of the wires on the substrate temperature during growth.

4.1 GaN nanowires in nanoscience

At the beginning of the previous Chapter we observed that non-polar heterostructures emerge up as a solution to improve the optical properties of devices based on nitride semiconductors. However, the substrates used for growing along non polar directions are notorious for their high density of threading dislocations and stacking faults. An alternative approach is facet-controlled growth on c-plane GaN. As GaN NWrs grown by PA-MBE are oriented along the c-axis, their lateral walls are perpendicular to the c-axis. More precisely, it has been established that the walls of hexagonally-shaped GaN NWs are $(1\bar{1}00)$ planes [96]. The lateral facets of GaN NWrs can hence act as dislocation and stacking fault free nanosubstrates for the

growth of non polar heterostructures. Besides this possibility, semiconductor NWrs are emerging as a powerful class of materials that, through controlled growth and organization, are opening up substantial opportunities for novel nanoscale photonic and electronic devices. These nanomaterials demonstrate new and enhanced functions crucial to many areas of technology. Central to realizing applications is the rational control of key NWr parameters, including morphology and size, crystalline quality, structure, and doping. These parameters determine, for example, electronic and optoelectronic properties critical to predictable device function. Significantly, semiconductor NWrs represent the nanomaterial system where these key parameters have been best controlled to date. First, an underlying conceptual framework has been developed to enable the growth of NWrs of virtually any uniform composition and structure, with the wide range of reported nanowires confirming these models. Second, the control over NWr growth has enabled the creation of a host of structures with different materials, including axial [97] and radial heterostructures [98], this last one grown along non-polar facets. And third, the control of p- and n-type doping is critical to almost any active device application [99], and has already been achieved in NWrs based on many material systems, including GaN. Henceforth, we will present in first place an investigation on the fundamental growth properties of GaN NWrs. We will analyze the influence of growth temperature on the morphology of GaN NWrs grown on Si(111). Following this study, we will also deal with the structural and optical properties of these NWrs. We will continue with the analysis of the optical and structural properties of axial and radial GaN/AlN heterostructures based on GaN NWrs. In the case of axial heterostructures, we will present an analysis of the vibrational properties of GaN nanodisks separated by AlN barriers. In the case of radial GaN/AlN heterostructures, also called core/shell NWr heterostructures, consisting of a GaN core surrounded by different thicknesses of an AlN shell, a thorough morphological, structural and optical analysis is presented. Of course, advances in the preparation of axial and radial NWr heterostructures with controlled characteristics will represent a substantial step forward in the development of nanoscale electronic and optoelectronic devices, crucial to future applications. Finally, in the last Chapter of this Thesis we will analyze the electronic properties of doped NWrs by means of atomic force microscopy.

4.2 Growth conditions of GaN nanowires by PA-MBE

Wagner and Ellis [100] described in 1964 the model, called vapor-liquid-solid (VLS), that described the growth mechanism for the formation of Si nanowhiskers starting from Si-Au eutectic droplets. Actually, it has been demonstrated that NWrs of the group III-nitride semiconductors can grow following the VLS mechanism using catalysts [101] under characteristic growth conditions. Here we will center our attention on the growth of GaN NWrs by PA-MBE without the use of any catalyst. The growth of group III-nitride NWr nanostructures is quite challenging as it often imposes a critical selection of the growth conditions to achieve both a high material quality and a homogeneous columnar morphology of the whole structure. The first reports about the growth of GaN NWrs by means of PA-MBE on Si(111) and sapphire substrates were given in 1998 by Sánchez-García *et al.* [102] and by Yoshizawa *et al.* [103].

In order to specify the growth conditions for GaN NWrs, it is important to describe first the optimal conditions required for the growth of compact 2D layers. Calleja *et al.* [104] performed a study of the growth rate of GaN as a function of Ga flux, for a given active nitrogen amount at three different growth temperatures. It was found that for low Ga fluxes, the GaN growth rate increases continuously with Ga flux. The region of growth parameters for which this behavior holds defines the N-rich regime in which the growth rate depends only on the amount of Ga supplied. A further increase of the Ga flux eventually saturates the growth rate, that reaches a maximum value. The saturation point represents an effective stoichiometry, where the effective III-V ratio is equal to unity. This effective III-V ratio does not refer to the ratio between the arriving Ga and N atoms fluxes, but to that between the incorporated Ga and nitrogen elements. The difference between the two ratios depends obviously on the growth temperature that modifies the metal thermal desorption. Therefore, an increase of the growth temperature requires a higher Ga flux to saturate the growth rate, since the Ga desorption rate increases with temperature. Finally, the use higher Ga fluxes beyond the stoichiometry point leads to the formation of Ga droplets on the surface, representative of a Ga-rich growth regime.

Additionally, Calleja *et al.* [104] report the achievement of various interesting morphologies by changing the Ga flux during a single growth process. Actually, two dimensional and nanocolumnar morphology have been observed at conditions of high and low Ga fluxes, respectively. In particular, a nanocolumnar morphology is achieved if, starting from stoichiometric conditions at a given temperature and

a fixed active nitrogen amount, the Ga flux is gradually reduced. Following this process, the Authors found a morphology sequence that started with a compact flat layer, leaded to a compact rough layer for smaller Ga fluxes, to coalesced NWrs if the Ga flux was farther reduced and, finally, to isolated NWrs for very low Ga fluxes. Within the nanocolumnar regime (high N-rich regime) that normally yields high density/small diameter NWrs, an increase of the Ga flux will lead to a rapid and homogeneous nanocolumnar coalescence. In a parallel way, a higher growth temperature will enhance not only Ga desorption, but also Ga adatom surface diffusion.

In summary, the nanocolumnar growth regime needs excess nitrogen, but the actual NWrs morphology and its evolution with III-V ratio depends strongly on the specific growth temperature. In order to improve the formation of nanocolumns, a high growth temperature is needed, which enhances Ga diffusion. Since the Ga flux is determined by Ga cell temperature, the Ga cell used for the growth of our samples has been calibrated by measuring the growth rate of a 2D GaN layer as a function of Ga cell temperature. Growth rate is expressed in ML/s, where ML denotes one monolayer and is equivalent to 2.5 nm for GaN WZ structure along the c-axis. For calibration, several GaN 2D layer were grown. The resulting calibration curve shows a linear dependence of growth rate with temperature and it is shown in Figure 4.1. The horizontal line determines the maximum growth rate limited by the nitrogen flux. The vertical one, situated at 980 °C, points out the temperature at which the system reaches the stoichiometric growth conditions. The Figure indicates that, under the conditions determined by the MBE reactor used in our experiments, whatever a Ga cell temperature in the range below 980 °C would ensure an N/Ga ratio smaller than 1.

Several studies have allowed establishing a model for the different growth steps involved in NWr formation. We will describe here the results obtained by O. Landré and coworkers [105]. Later, we will use the conclusions of this model in order to interpret the morphological features observed in the NWrs of our samples. The Authors studied the mechanism of nucleation and growth of GaN NWrs grown on Si(111) with a thin AlN buffer layer using different values of the Ga flux. With this purpose, they grew several samples using different Ga cell temperatures, namely 870°C, 875°C and 880°C. 4.2. The samples were analyzed in-situ during growth by means of X-ray diffraction in grazing incidence. The measurements were performed at the ESRF in Grenoble, using an MBE chamber on-line with the synchrotron X-ray beam. The representation of the integrated intensity of $(30\bar{3}0)$ GaN diffraction peak in the reciprocal space is shown in Fig. 4.2 as a function of time for three values of the Ga flux (symbols ▼, □ and ◇ in order

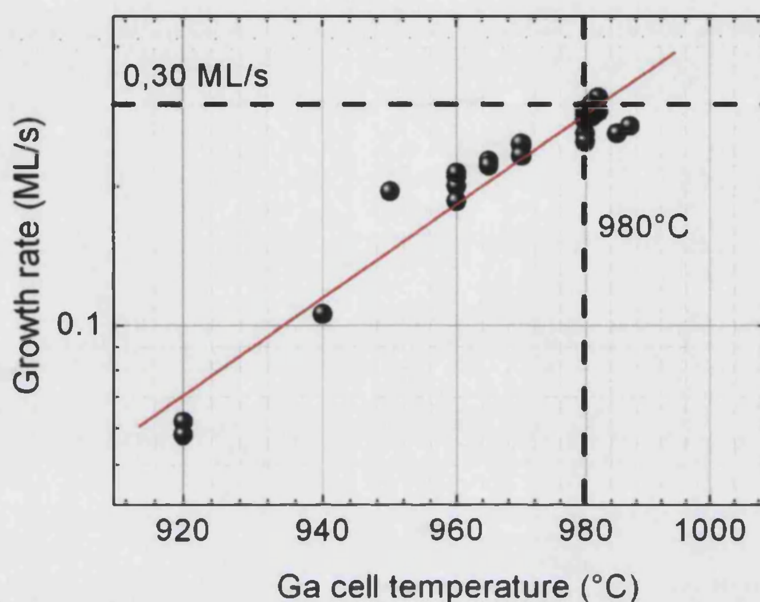

Figure 4.1: Experimental relation between growth rate and Ga cell temperature. The crossing point of the two dashed lines represents growth in stoichiometric conditions.

of increasing Ga cell temperature). The evolution of the intensity is similar for all values of the Ga flux, and can be divided into three regions, corresponding to three growth regimes. The first regime, where the measured intensity is zero, corresponds to the duration of the deposition of a GaN 2D layer, lattice matched to the AlN buffer layer. In this conditions the GaN layer is characterized by the same in-plane lattice parameter as AlN, and hence it cannot be detected by X-ray diffraction in the region corresponding to GaN. The second regime corresponds to a quick, supralinear, increase of the intensity as a function of time. The duration of this regime corresponds to the time needed for the formation of the islands that act as precursors for NWr formation. Consonni *et al.* [106] also reported a similar behavior for the formation of precursor islands. They conclude that precursors have to reach a critical size before turning into NWrs. Indeed, it has been previously demonstrated that NWr 3D precursors grown on Si(111) covered by a thin AlN buffer layer are plastically relaxed, consistent with the observation by meas of HRTEM of misfit dislocations at the interface between the 3D precursor and the thin AlN buffer layer [105, 107]. After the plastic relaxation, these islands are commonly called precursors of the NWrs. Finally, a third regime corresponding to the linear increase of intensity is identified and related to the continuous growth of the NWrs.

Consonni *et al.* [107] perform a similar study of NWr growth as a function of

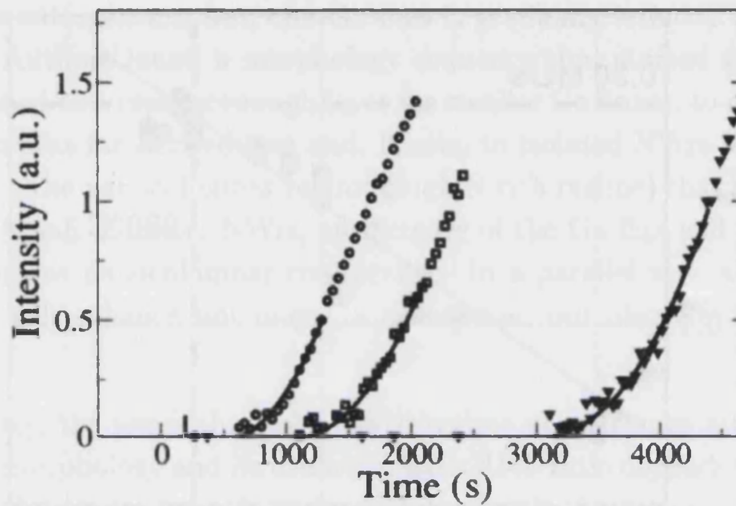

Figure 4.2: Integrated intensity of $(30\bar{3}0)$ GaN diffraction peaks as a function of time for three Ga fluxes corresponding to three different Ga cell temperatures, namely 870°C (▼), 875°C (□) and 880°C (◊). Image taken from [105].

temperature. Since the results of both works are similar, we conclude that as far as nucleation is concerned, Ga flux and growth temperature play a similar role during NWr growth. Based on these results, in the following we investigate the growth and morphology of GaN NWrs as a function of temperature.

4.2.1 Effective temperature and its related NWr density

We have seen above that high substrate temperature and low III/V ratios are the necessary conditions for NWr growth. In this Section we will investigate the effect of substrate temperature on NWr growth. In order to ensure the reproducibility of the growth temperature, we use a method based on the analysis of the reflection high energy electron diffraction (RHEED) pattern from the 7×7 Si(111) reconstructed surface. It is well known that this pattern appears above 700°C [108] and disappears at 860°C [109]. The left image of the Figure 4.3 contains a typical RHEED pattern from Si(111) substrate at high temperature. Two superposed patterns can be distinguished: that composed by the brightest vertical lines reveals the presence of a 2D layer; the second pattern is formed by the vertical lines in between those of the 2D layer, corresponding to the 7 × 7 surface reconstruction of Si(111). For the analysis of the picture, we center our attention in the intensity of the red area in the image, corresponding only to the 7 × 7 reconstruction pattern. Next, the surface of the substrate is exposed to 10 seconds of Ga flux and this intensity is represented as a function of time (right part of Figure 4.3).

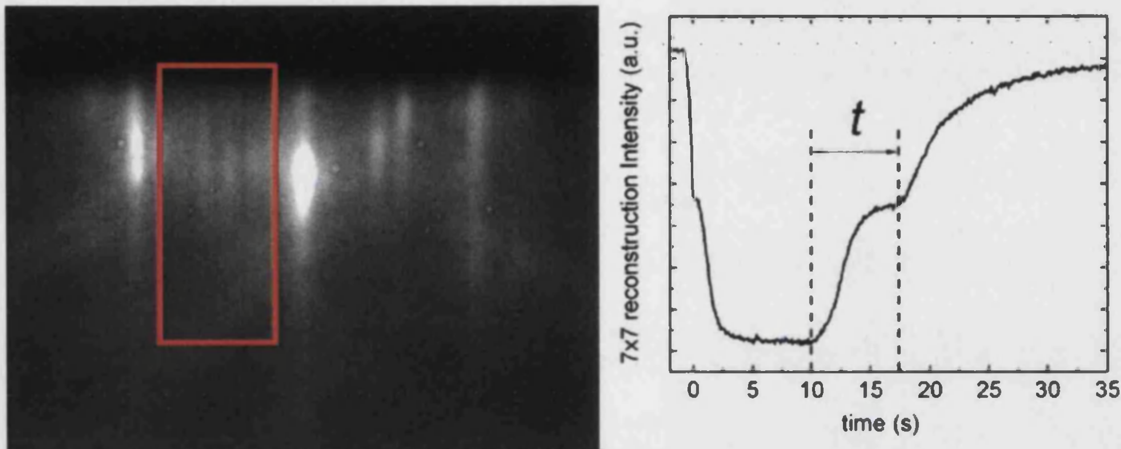

Figure 4.3: Left: characteristic RHEED pattern of the 7×7 surface reconstruction of Si(111). Right: The graph represents the intensity of the 7×7 reconstruction pattern collected from the red square area.

The intensity of the RHEED pattern shows two definite and reproducible steps, marked by vertical dashed lines in the graph of the Figure. They correspond to a transient time related to Ga desorption. This characteristic leads to a reproducible relationship between the Ga desorption time and the temperature indicated by the thermocouple in mechanical contact with the rear face of the Si wafer. In order to determine the effective substrate temperature, a further correction has to be applied to the temperature data. This correction is necessary due to the fact that the thermocouple measurement is biased by direct thermal radiation from the heater filament. It consists of a temperature shift, determined by the observation of the appearance/disappearance of the 7×7 reconstruction, which takes place at 860°C [109]. This procedure provided a relationship between the Ga desorption transient and the effective surface temperature, shown in Figure 4.4. Note the logarithmic scale in the Ga desorption time axis.

Since GaN NWrs were first grwon in 1998 [102], several research groups have studied the nucleation process [44, 105, 107, 110, 111], analyzing the first steps of the NWr formation and the NWrs morphology as a function of different parameters, like Ga flux or growth temperature [112–114]. However, the understanding of NWrs structural evolution as a function of temperature and III-V ratio is still not complete. In order to get more insight into the influence of substrate temperature in the morphology of GaN/AlN NWrs, 2 inches Si(111) substrates used to grow the samples are placed on a heater into the growth chamber. The design of the heater originates a temperature gradient of the order of 40 °C between the edge and the middle of the wafer. The temperature is higher at the center of the substrate

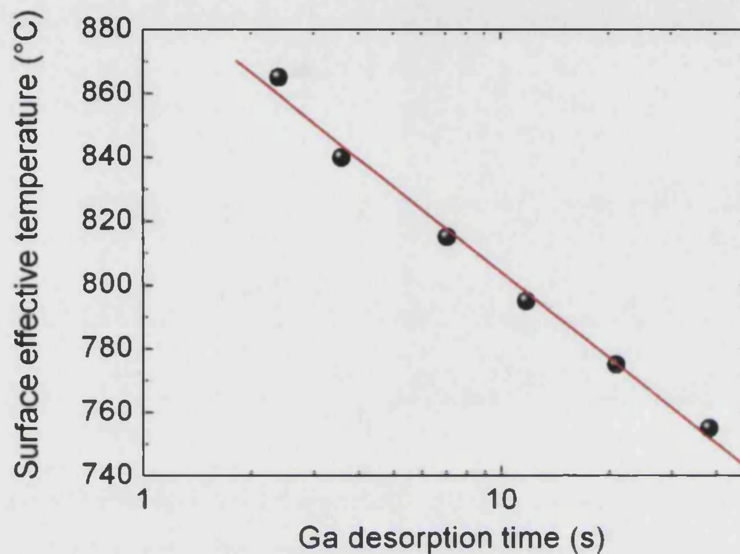

Figure 4.4: Relation between effective surface temperature and Ga desorption time. Note that the scale related to the Ga desorption time is logarithmic.

and decreases towards the edge. For the detailed calibration of the temperature, several samples, cut into small pieces, so that the temperature was uniform in the whole substrate, were grown at different temperatures in the range of 770 °C and 810°C. For each sample, we determine the NWr density by means of SEM micrographs. This study provides a relation between growth temperature and density or, equivalently, NWr coverage. The coverage is the area occupied by GaN NWrs with respect to the total area, and can be easily determined from top-view SEM images. Knowing the NWr coverage of any sample grown under the same conditions of Ga/N flux and growth time as the reference samples, we can determine its growth temperature. The relation between GaN NWr coverage and surface effective temperature is shown in Figure 4.5. The trend shows that the coverage decreases very quickly between 780 and 805 °C and falls down to zero above 805°C. This behavior is in agreement with the rapid increase of the decomposition rate of GaN above 800°C, reported by Grandjean and coworkers [115], which hinders the formation of NWrs above this temperature.

We present in the following the growth conditions of GaN NWrs grown on Si(111) with and without the use of an AlN buffer layer. We will see that the temperature gradient is only relevant when the NWr growth is performed directly on Si(111), and we will study the morphological changes observed in these NWrs as a function of substrate temperature.

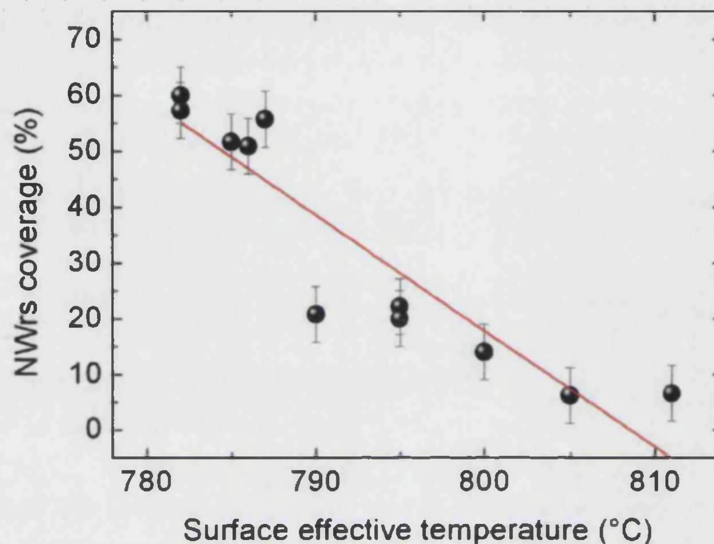

Figure 4.5: Relation between GaN coverage and effective growth temperature. The red line represents a linear fit to the data.

4.2.2 Growth of GaN nanowires using an AlN buffer layer

In this Section we describe the growth conditions of GaN NWrs grown on 2 inches Si(111) substrates using a AlN thin buffer layer. For future electrical characterization, the substrates chosen were highly n-doped. GaN NWrs were grown by using radio frequency PA-MBE. N-rich atmosphere was established by selecting a Ga cell temperature of 925°C. The substrates were degreased before being passivated by hydrofluoric acid (HF) at 5% for 2 min. Next, they were thermally outgassed until the 7×7 surface reconstruction indicating a clean Si(111) surface appeared. The sample was grown using a surface effective temperature of 820 °C at the wafer center. Before the deposition of GaN, a thin AlN buffer 2D layer was grown. In the case of GaN NWrs it has been demonstrated that the AlN buffer layer improves the alignment of the NWrs [44]. A coincidence relationship between AlN and Si(111) lattice and the wetting of the substrate's surface allows the deposited AlN to grow in 2D mode, as evidenced by the appearance of a streaky RHEED pattern after the growth of this layer. For the deposition of the buffer layer, Al flux is left on during the time equivalent to the growth of 2 nm of AlN. After the deposition of this AlN buffer layer, the Ga cell is opened. Under these same growth conditions we find that, after 3 minutes deposition, the RHEED pattern changes from streaky to slightly spotty. This pattern transition indicates the change of phase from 2D

layer to 3D islands, as has been previously observed for instance in the growth of GaN/AlN QDs [116]. This transition of GaN on the AlN buffer layer is described in more detail in Sec. 2.1.1. These islands are expected to be preferential sites for further GaN NWrs growth due to strain minimization. Thus, the islands could act as a material collector and become NWr seeds. The growth time was 14 hours and 23 minutes and the RHEED pattern at the end of the growth is shown in Fig. 2.5. This sample has been labeled as N1340.

The structural features of these GaN NWrs are shown in the SEM images of Fig 2.7, both in cross section and top view. The NWrs present an average diameter and length of 50 nm and 1 μm respectively. These morphological features indicate that the deposited material preferentially participates to the vertical growth, with a lateral incorporation of only 5%. As can be observed in the SEM images, the NWrs are very well aligned. This fact can also be concluded by the analysis of the RHEED pattern shown in Fig. 2.5. Between the bright spots there are shiny lines of weak intensity. These lines have their origin on the weak reflections of the electron beam on the sides of the NWrs. The good alignment of the NWrs was expected due to the presence of the AlN buffer layer, as commented before. On the other hand, structural studies of the AlN buffer layer indicate that it grows totally relaxed, but containing a high density of dislocations. In addition, AlN buffer layers normally exhibit a marked granular structure. The influence of the AlN buffer layer on the GaN NWr growth has been studied in detail by Sekiguchi *et al.* [117]. The Authors have demonstrated that both density and morphology of NWrs grown on an AlN buffer layer deposited on sapphire were strongly dependent on the thickness of the AlN buffer. In the case of a thick AlN buffer layer (8.2 nm), the nucleation of GaN NWrs was almost totally suppressed. This effect is ascribed to a significant increase in size of AlN grains. Moreover, for increasing thickness of the AlN buffer, the standard formation of GaN QDs can be eventually observed, characterized by an elastic strain relaxation of GaN through 3D islanding, further followed by QD coalescence and growth of a rough GaN layer for increasing amount of deposited GaN. If we consider that the typical grain size on the AlN surface is around 50-100 nm, comparable to the typical NW diameter, it can be suggested that the plastic strain relaxation might be optimal when the GaN nucleus size matches the AlN grain size. As a matter of fact, it has been found that the final density of GaN NWrs could be correlated to the grain size of the AlN buffer layer [105].

With the aim of studying in more detail the intrinsic NWr nucleation mechanisms with and without AlN buffer layer, we present in the next Sections the growth and analysis of the morphological features of GaN NWrs that arise by the

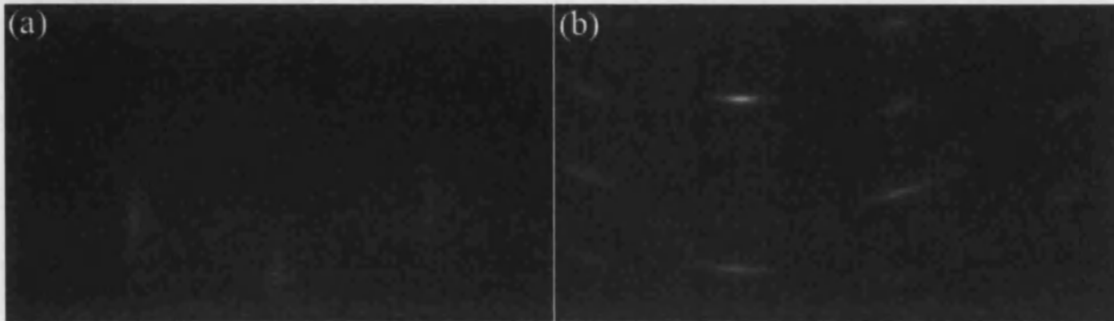

Figure 4.6: (a) RHEED pattern after 3 minutes GaN deposition on Si(111). (b) RHEED pattern after 13 hours growth. A characteristic pattern of a 3D structure overlapping a faint ringlike pattern can be observed.

absence of AlN buffer layer. Finally, they will be compared with those exposed above.

4.2.3 Growth of GaN nanowires directly on Si(111)

The main goal for growing GaN NWrs directly on Si(111) is the possibility of integrating NWrs properties with the electronic technology based on silicon. In particular, the electronic characteristics of doped NWrs can be determined without the need of separating them from the substrate, providing the Si substrate used for growth is adequately doped [118]. The sample described in this Subsection is labeled as N1405. Similar to the previous samples, the substrate used was a 2 inches n-doped Si(111) wafer. Following the same substrate cleaning procedure, a growth temperature of 820°C is fixed, and the growth proceeded under the same N-rich conditions used in the previous Section, but depositing GaN directly on the substrate. Once the deposition of GaN has started, we find that the RHEED pattern gradually evolves from a streaky to a spotty pattern after 3 minutes growth, as can be observed in Fig. 4.6(a), indicating the formation of 3D islands. After 13 hours GaN deposition the RHEED pattern was recorded and shown in Fig. 4.6(b). Overlapped to the spotty pattern we can observe a second one with a faint ringlike shape. This ringlike pattern is characteristic of NWrs tilted with respect to the normal direction of the substrate, as has been previously observed in GaN NWrs grown on Si(111) without AlN buffer layer [44].

After growth, the wafer presented a particular appearance. Its color was not homogeneous, as in sample N1340, but changed gradually along the radius. A schematic diagram of the wafer characteristics is shown in Fig. 4.7. Close to the wafer edge the sample presents a milky color, while towards the center it changes

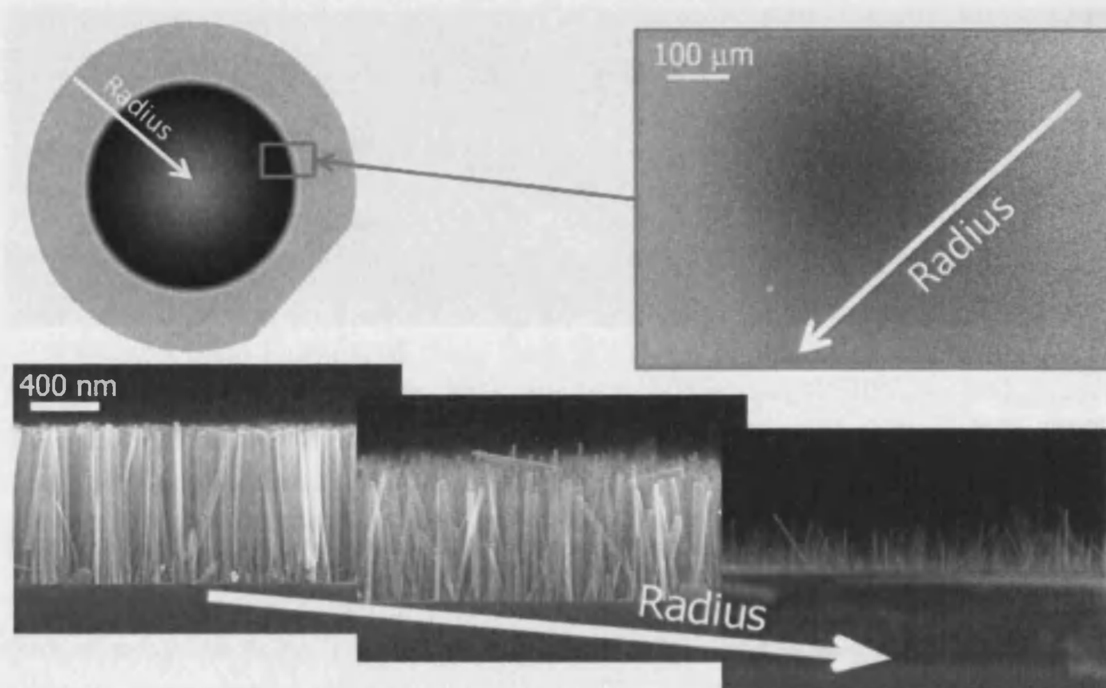

Figure 4.7: Top left: schematic diagram of the wafer and top view of the selected area. Bottom: SEM images in cross section. The sequence of the images from left to right follows the radius of the wafer from the edge to the center.

from milky to black. The wafer was cleaved along its radius in order to study its structural characteristics by SEM as a function of position along the wafer radius. Taking into account the temperature gradient that exists along the radius, it is important to remember that the different points along the radius correspond to different temperatures, increasing towards the center of the wafer. At the bottom of Figure 4.7 we show three characteristic SEM images taken at three different positions along the radius of the wafer. The images are ordered starting from the edge of the wafer (left) towards the center (right). The images reveal a slight misorientation of the NWrs with respect to the growth direction, as indicated by the RHEED pattern. This misalignment increases towards the wafer center. We observe as well a gradual decrease in density from the edge towards the center of the wafer, related to the increase of the temperature. Together with the decrease in NWr density, a decrease in the average NWrs length is also observed. Besides these morphological characteristics, a dispersion in NWr length is also apparent, as well as a decrease in the mean diameter of the NWrs. All of these features differ strongly from those presented by GaN NWrs grown with AlN buffer layer, indicating that when the growth takes place directly on Si, the influence of the temperature gradient on the morphology of the NWrs is much stronger.

In the next Section we present a statistical analysis of the morphology of the NWrs as a function of growth temperature.

4.3 Nucleation and morphology of GaN NWrs grown directly on Si(111)

The direct relation between the position along the radius of the wafer and the growth temperature has been obtained by taking SEM images in steps of 1 mm along the wafer edge. A previous step to establish this relation, the coverage has been calculated by using the SEM micrographs as a function of position along the radius wafer (see Fig. 4.5). Therefore, the relation between temperature and distance from the wafer edge is able to be calculated and it is shown in Fig. 4.8. All the temperatures comprised in the first 12 mm from the wafer edge are between 770 and 810°C, that is, compatible with NWr growth. However, if we move farther towards the wafer center the temperature increases towards 820 °C at the center, and no NWrs were found. Again, this behavior is in agreement with the study of Grandjean *et al.* [115], indicating the fast decomposition of GaN above 800°C. We used the sequence of SEM pictures for the study of the morphological characteristics of the NWrs and the Precursors. Representative examples of the images are shown in Figures 4.9 and 4.10 for NWrs and Precursors respectively.

Figure 4.9 shows the SEM images for the NWrs sample taken from the edge towards the center of the wafer, that is, increasing temperature, from the top to the bottom of the Figure. One can easily appreciate that the NWrs density decreases as the temperature increases. Moreover, changes in diameter and length can be as well observed, decreasing towards higher temperatures. Likewise, the dispersion of the length of the NWrs also presents a strong variability as a function of growth temperature. The SEM images corresponding to smaller growth temperatures reveal that the sample consists of longer wires, larger diameters and there is a small dispersion of their lengths. In the case of higher growth temperatures the wires are shorter, their mean diameter is smaller and a much larger dispersion of their lengths is observed.

In order to understand these morphological changes from the first growth steps we have grown and analyzed a second sample. This sample is grown under the same conditions but with a growth time limited to 20 min. Given the small growth time, this sample consist mainly of 3D islands and is referred to as Precursors sample. The characteristics of this sample are shown in Figure 4.10. The images taken in cross section correspond to the low temperature region (left) and the high

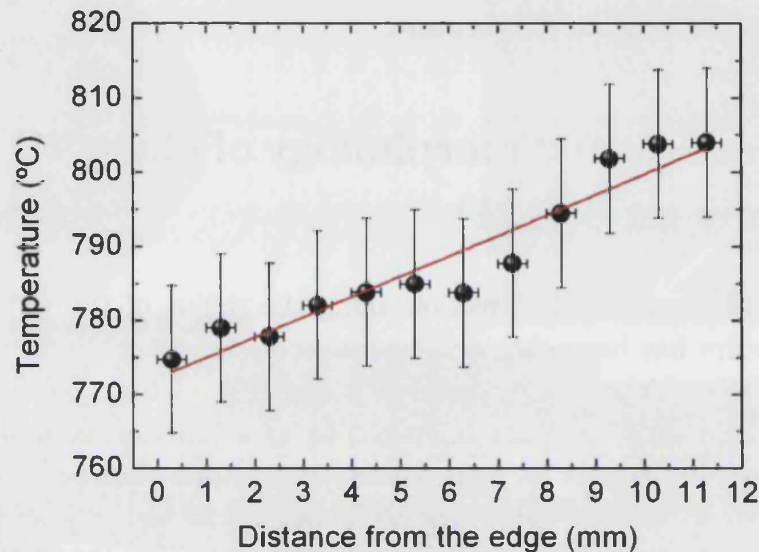

Figure 4.8: Relation between surface temperature and position along the wafer radius.

temperature region (right). As in the previous sample, SEM images are ordered from top (low temperature) to bottom (high temperature). From the cross section images we conclude that, during the growth time of 20 minutes and in the first 12 mm from the wafer edge, the GaN material nucleates in the form of 3D islands. Indeed, the analysis of cross section SEM images taken near the wafer edge (low temperature region) shows that the onset of continuous NWr growth on top of the 3D islands has already started. Interestingly, the variation of the diameter of the 3D islands constituting the precursors along the wafer edge is very different than that found for NWrs. It seems to remain constant along the whole wafer radius. For a quantitative description of these variation concerning both the NWrs and the Precursor samples, a complete statistical analysis must be performed.

We have performed a detailed statistical analysis of the diameter, length and length dispersion of NWs. In this analysis images with less than 20 wires have been excluded (they are not statistically significant) and coalesced wires were counted as one. Figure 6.4.1 shows the density of NWrs and Precursors as a function surface effective temperature. The NWrs and Precursor density decreases as the temperature increases. The difference observed in density between the NWrs and Precursor sample is ascribed to their different growth time. While NWrs have been growing during 3 hours, the growth of Precursor sample was stopped after 20 minutes. As a consequence of a non-negligible lateral growth of NWrs, in this growth time some of the NWrs coalesce, giving place to a reduction of the density,

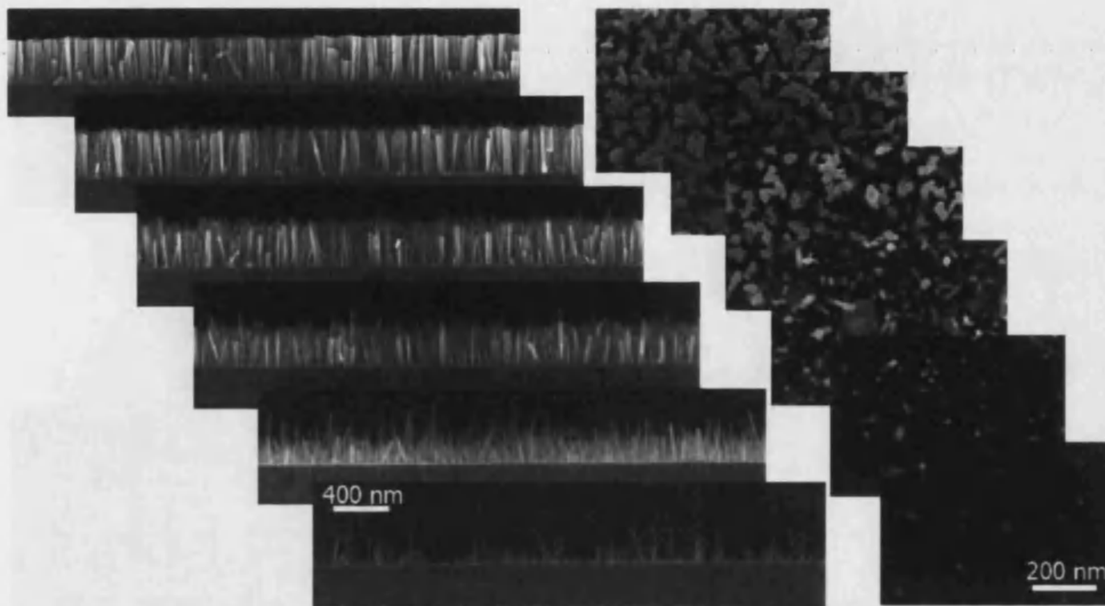

Figure 4.9: Cascade of SEM images taken at determined positions along the wafer radius in cross section (left) and top view (right). From top to bottom the growth temperature increases.

since coalesced NWrs are counted as one. Besides this difference, in NWrs sample we observe a rapid decrease of density above a temperature around 795 °C, while this change is observed for the Precursor sample above 785 °C. This decrease is related with the high Ga desorption rate that takes place at high temperatures. The differences observed between both samples is related, as before, to the growth time: the longer growth time of the NWr sample increases the probability of nucleation at higher temperatures.

The diameter of the NWrs has also been analyzed. Figure 4.12(a) shows the evolution of the mean diameter versus surface effective temperature along the radius of the wafer. Black spheres correspond to the mean diameter of NWrs and blue triangles to that of the precursors. The dashed lines are guides for the eye. The mean diameter of the NWrs increases linearly as the temperature decreases, emphasizing the fact that the lateral growth is not negligible at low temperatures due to the low Ga diffusion length, as expected from the density analysis. This feature is also in agreement with the fact that at low temperature a decrease of the Ga desorption rate is observed. Ga atoms cannot reach the top of the NWrs because of their low kinetic energy, incorporating at the lateral side of the NWrs and increasing the nanowire diameter. At higher temperatures the mean diameter reaches a value of $\approx$ 12 nm. As indicated before, the mean diameter extracted from the Precursor sample shows a much different behavior. It remains almost

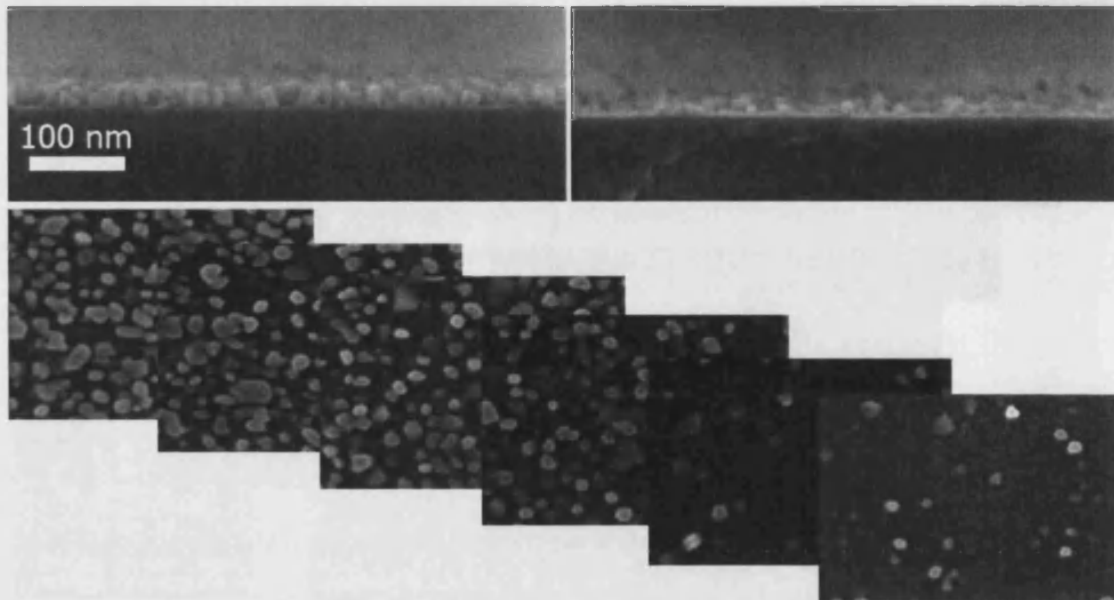

Figure 4.10: SEM images of Precursors sample. The upper images (cross section) were taken from the low temperature (on the left) and the high temperature region (on the right) of the wafer. The cascade shows the top view images increasing temperature from top to bottom.

constant at $\approx$ 12 nm, increasing slightly below 780°C. This increase that takes place for low growth temperatures is ascribed to an enhancement of the lateral growth. We have pointed out before that at low temperatures NWrs have already started to form, so that GaN can incorporate in their lateral facets, increasing its diameter with respect to that of the precursor island. From this behavior we can extract two conclusions. In the first place, before the onset of NWr formation the precursor islands reach a critical size of $\approx$ 12 nm, which is independent of temperature. This indicates that the critical size is not governed by nucleation kinetics. The size of the precursor islands is in agreement with the results reported by Consonni *et al.* [106]. Furtmayr and coworkers [119] propose that the critical size of the islands is governed by relaxation mechanisms related with the misfit lattice parameters between GaN and the substrate. Landré and coworkers [105] reach the same conclusion for NWrs grown on Si with the use of an AlN buffer layer. Figure 4.12(b) shows the diameter dispersion as a function of temperature. For the Precursors sample, the diameter dispersion remains almost constant at 4 nm for the whole range of temperatures, in accordance with the constant value of the diameter. The dispersion increases slightly for lower temperatures due to the enhanced lateral growth. In the case of the NWrs sample the diameter dispersion increases from 6 to 14 nm as the temperature decreases. This is also related with the enhanced lateral growth at low temperatures. It is important to stand out

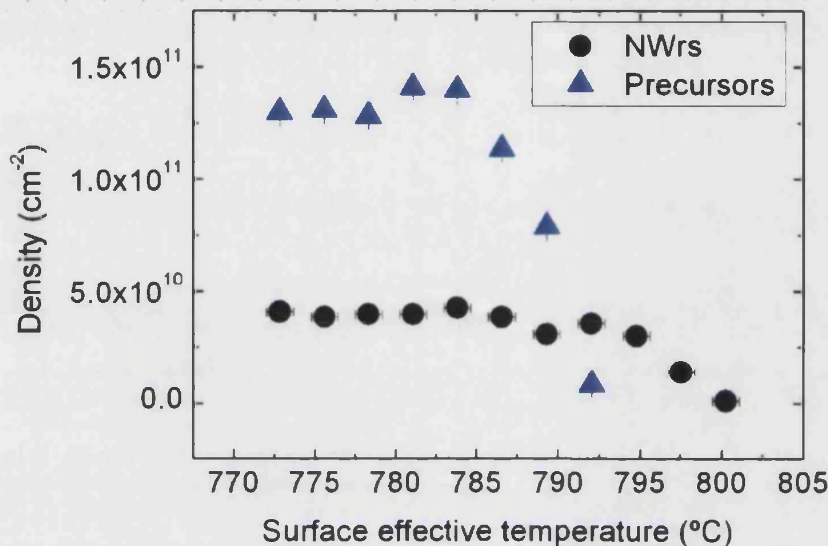

Figure 4.11: Density of NWrs and Precursors as a function of surface effective temperature. The size of the symbols represents the experimental uncertainties.

that the dispersion in NWr diameter converges to that of the Precursor islands for high temperatures, and is therefore limited by Ga desorption.

Regarding the length of the NWrs, a similar statistical analysis than that performed for their diameter is shown in Figure 7.18. In this case only the NWrs sample has been studied. The Figure shows the mean length of the NWrs (black circles) and their length dispersion (red triangles) as a function of surface effective temperature. At lower substrate temperature, up to 790°C, the NWrs present a longer mean length with low length dispersion, as expected from the SEM images shown in Fig. 4.9. Above this temperature, the NWrs present a much shorter mean length and the dispersion of length strongly increases, giving place to a combination of NWrs with different heights. Note that the uncertainties in the NWrs length from the region of high temperature are larger than those determined for the region at low temperature. This is related with the small number of NWrs in the SEM images taken at higher temperature. These characteristics lead to the hypothesis that at low temperatures all the precursors will reach their critical size after the same growth time, starting the growth of NWrs almost at the same time and resulting in NWrs of very similar length. On the contrary, at higher temperatures, which correspond to slow nucleation conditions, several families of precursors may grow at very different times, giving place to NWrs of different lengths.

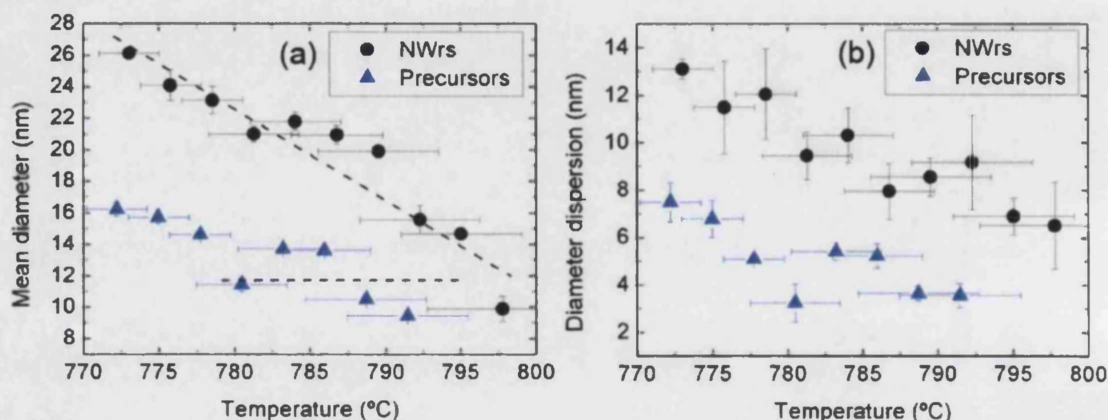

Figure 4.12: (a) Mean diameter and (b) diameter dispersion of the NWrs sample (black spheres) and of the Precursors sample (blue triangles) as a function of temperature.

In order to support our hypothesis, we will analyze from our data the growth time dispersion, defined as the time elapsed between the formation of the first and the last precursor island at a given temperature. This time is related to the dispersion in the NWr length: precursors formed early during the growth process give rise to long NWrs, while those formed at a later time give rise to shorter ones. In order to calculate the growth time dispersion, we need first to determine the NWr growth velocity at each temperature. This is obtained by dividing the mean NWr length at that temperature by the total growth time. The growth time dispersion is then obtained by dividing the length dispersion by the growth velocity. The growth time dispersion presents a linear trend as a function of mean length as it can be observed in Figure. 4.14.

This evolution is related to the gradient in temperature along the wafer radius (see Fig. 4.8). The region of larger NWr length is marked with a light shadowed area while the region of high temperature is darker and corresponds to NWrs with shorter mean length. We found that in the low temperature region the growth time dispersion is very small, only of a few minutes. Consequently, in this region all precursors nucleate almost at the same time. The opposite case is obtained in the high temperature region, where we find a very large growth dispersion time, about 150 minutes. This indicates that 150 minutes after formation of the first precursors, there are still precursors being formed. Taking into account that the total growth time is 180 minutes, this study indicates that in the high temperature region precursors are being formed almost during the whole growth process. Consequently, our results, together with those of previous works, support the hypothesis that at low temperature the 3D islands that constitute the precursors of

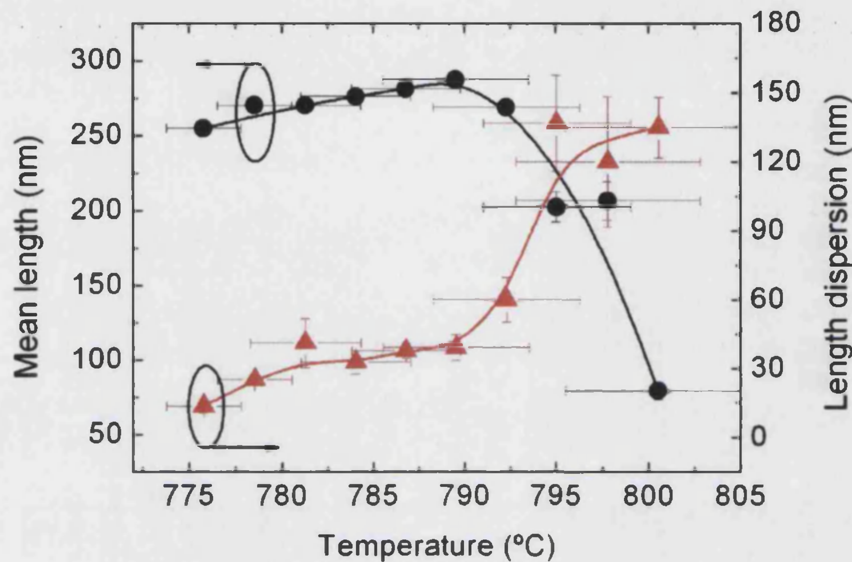

Figure 4.13: Mean length of the NWrs sample (black circles) together with their length dispersion (red triangles) as a function of surface effective temperature.

the NWs will reach their critical size at the same time, relaxing plastically, and giving place to the continuous growth of NWrs, resulting in NWrs with similar height. Additionally, we experimentally find that the critical size of these islands corresponds to about 12 nm. On the contrary, a long nucleation time is needed at higher growth temperatures. The formation of precursors will take place at very different times, during the whole growth duration. The possible formation of different families at very different times enhances the probability of growth of wires with different lengths, presenting a much larger dispersion at high temperatures than those grown at lower temperatures.

As a final remark, we would like to indicate that the possible elaboration of light emitting diodes (LEDs) based on InGaN/GaN or AlGaN/GaN has been demonstrated recently, emitting both in the visible [96] and the ultraviolet [99] range. Compared to the standard 2D LEDs, additional difficulties specific to NWrs arrays are faced: for instance, processing of NWrs LED structures requires a planarization step, in order to optimize the upper electrode. This step is expected to be greatly eased if the height distribution of NWrs is narrow enough. As we have shown in this Section, this is possible with a precise control of growth process. Our results indicate that for GaN NWrs low temperature growth decreases the NWrs length dispersion, simplifying the manufacturing process of devices based on NWr arrays.

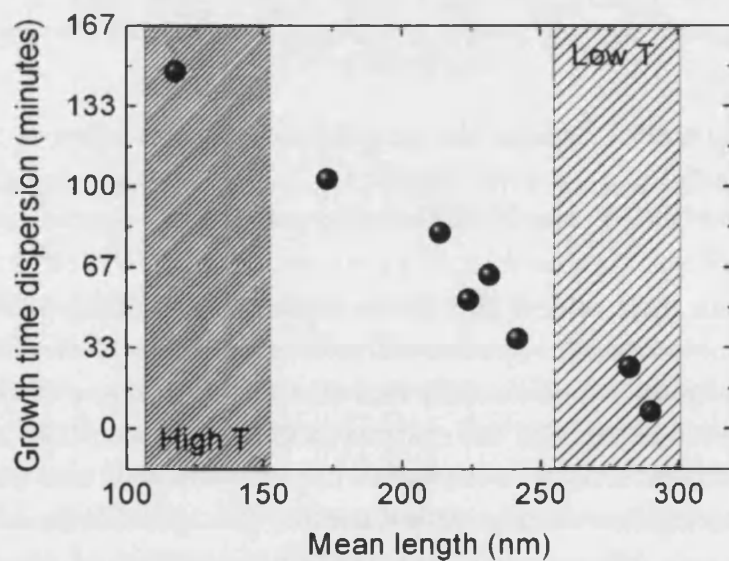

Figure 4.14: Dispersion of the growth time in minutes as a function of the mean length of the NWrs in nm.

In this Chapter we have shown the growth condition characteristics for the formation of NWrs. GaN NWrs samples grown on Si(111), both with and without AlN buffer layer, have been grown and analyzed. In particular, the growth of GaN NWrs directly on Si(111) has been investigated as a function of growth temperature. Growth temperature influences the morphology and density of the NWrs. We conclude that at low temperature all the NWrs start to grow at the same time and a low dispersion in their length is found. On the contrary, at higher growth temperature the formation of precursor islands takes place during the whole growth duration, giving rise to different NWrs families with different length.

Chapter 5

Vibrational and optical characterization of GaN nanowires

In Chapter 1 it has been shown that intense theoretical and experimental research efforts have been devoted to the understanding of the structural and optical properties of semiconductors belonging to the group III-nitrides. Important parameters such as the electronic band gap, free-exciton binding energy, effective masses, impurity ionization energies, etc. have been studied [1]. The development of strain free high quality GaN NWrs with a very low impurity concentration and dislocation density enables the accurate study of the parameters related to GaN material with nanocolumnar shape, which are slightly different from those found for homoepitaxial GaN layers due to the high surface/volume ratio. This Chapter incorporates a comparison of the structural properties of bulk GaN and GaN NWrs. Taking into account the importance of the surface to volume ratio in these nanostructures and considering that this ratio changes with diameter, the last part of this Chapter includes a study of the structural and optical characterization for NWrs with different diameter.

5.1 Vibrational properties of GaN nanowires

We will begin our study with the analysis of the vibrational properties of GaN nanowires. Typical Raman spectra of an ensemble of GaN NWrs are shown in Fig. 5.1 in different polarization configurations taken in backscattering configuration at room temperature. The NWrs grow predominantly perpendicular to the silicon substrate, with the Nwr axis parallel to the WZ crystal c-axis. In backscattering configuration with $z(-,-)\overline{z}$ geometry, z is parallel to the c-axis, and the selection

rules for the wurtzite structure predict the appearance of E_{2h} and $A_1(LO)$ Raman lines in the spectra (see Sec. 2.4.1). These peaks are clearly identified besides the strong signal from the Si substrate that starts to rise on the left side of the spectrum. The modes $A_1(TO)$ and $E_1(TO)$ are also visible, although these modes are forbidden in this polarization configuration. We attribute this breakdown of the selection rules due to the multiple reflections of the light at the lateral sides of the NWrs. Tilted NWrs can also contribute to the intensity of these modes. Additionally, GaN belongs to a system where long-range electrostatic forces predominate over short-range ones. This can be easily understood from the fact that the TO-LO splitting (180-200 cm^{-1}) is much larger than the A_1-E_1 splitting (7-30 cm^{-1}). In these conditions, the mixing of A_1 and E_1 modes may easily occur when the incident or the scattered radiation are not strictly parallel or perpendicular to the optical axes [26]. Since the wurtzite nitrides are uniaxial crystals, purely transverse or longitudinal phonons with A_1 or E_1 symmetry can be observed only when the phonon propagation direction is strictly parallel or perpendicular to the crystal axis. For an intermediate propagation direction, therefore, mixing of A_1 and E_1 modes occurs, yielding to quasi-TO and quasi-LO modes. In other geometrical configurations, such as $x(z,y)\overline{x}$ or $x(z,z)\overline{x}$, the modes $A_1(TO)$ and $E_1(TO)$ are expected. In this configuration we observe that modes E_{2h} and $A_1(LO)$ also appear although they are forbidden. As a consequence, their relative intensity with respect to the allowed modes decreases considerably. Besides the expected phonon modes from bulk GaN, we found a structure around 700 cm^{-1} attributed to surface optical modes. In order to analyze the Raman peaks, they have been fitted to Lorentzian functions. The frequency of the different phonon modes and the corresponding line widths (FWHM) are summarized in Table 5.1. They present small differences with those reported in Table 1.7, specially concerning modes E_{2h} and $A_1(LO)$. As commented before, a possible misalignment of the excitation light with respect to the c-axis may be responsible of small changes in the frequency of the polar modes, increasing the value of the $A_1(LO)$ mode towards that of the $E_1(LO)$ mode. However, as can be observed with more detail in Fig. 5.2, the mode $A_1(LO)$ appears at the same frequency for all the scattering configurations studied here. This fact indicates that the red shift may have a different origin. As has been explained in Sec. 1.3.3, polar modes may couple with free electrons present in the sample, giving rise to phonon-plasmon coupled modes which frequency increases with increasing electron density. A blue shift of almost 4 cm^{-1} from the 734 cm^{-1} reference value would correspond to an electron concentration of $2 \cdot 10^{17}$ cm^{-3}.

The E_{2h} mode is about 1 cm^{-1} red shifted with respect bulk GaN. This shift has already been observed in GaN NWrs grown on Si(111) and Si(100) [120]. Its

(cm^{-1})	E_{2h}	$A_1(TO)$	$E_1(TO)$	$A_1(LO)$	SO1	SO2
Frequency	566.3	531.2	557.2	737.9	690.4	708.3
FWHM	3.2	4.6	4.1	9.8	36	22

Table 5.1: Phonon frequencies and the corresponding line width in cm^{-1} of free standing as grown GaN NWrs with wurtzite structures at the Γ point.

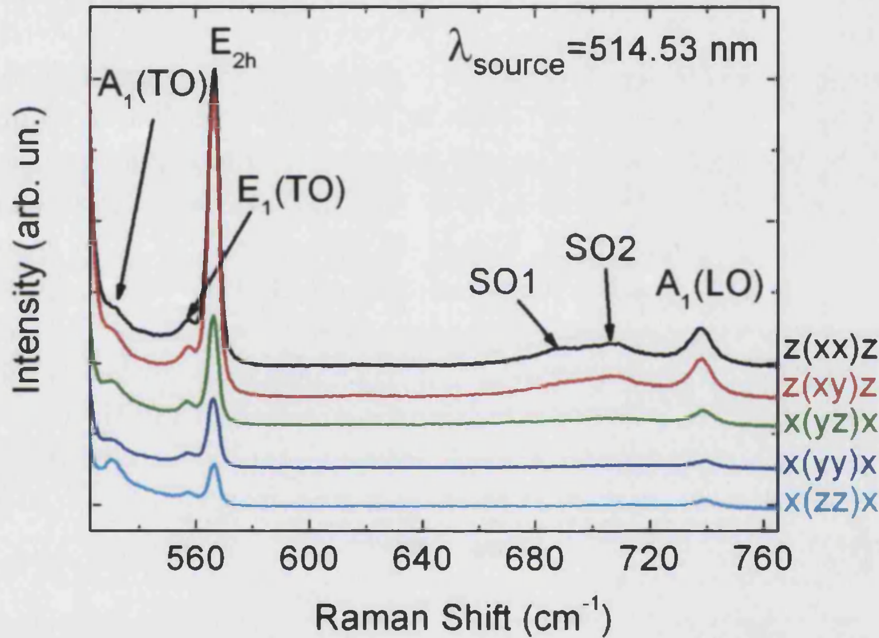

Figure 5.1: Raman spectra of free standing GaN NWrs in different polarization configurations.

origin is not clear, but may be related with the increased surface to volume ratio of the NWrs. However, it is well known that the existence of different boundary conditions for the atomic states at the surface with respect to bulk give rise to local electric and polarization forces that can influence in the propagation of optical phonons [121]. A red-shift due to the local heating of the NWrs by the excitation laser is excluded, since the shift does not depend on laser power. Besides these small shifts, we would like to remark that the small value of the FWHM of the E_{2h} mode, about 3.2 cm^{-1}, proves the high crystal quality of the nanowires. This value is to be compared with the ~ 5 cm^{-1} FWHM characteristic of high quality bulk GaN samples [21].

Of course, the most interesting Raman feature found in GaN NWrs compared with bulk GaN is the mode observed around 700 cm^{-1}. This feature will be analyzed more extensively in the next Section.

5.1.1 Surface optical modes

Surface optical modes are associated with vibrations of the surface atoms which amplitude decays rapidly when moving away from the surface. They always arise at frequencies between those of the LO and TO phonons. Several works have reported the presence these modes in nanostructures of different materials [121–128]. However, there are very few reports available concerning nanostructured III-nitride systems. In a recent study, Hsiao *et al.* [129] reported on a SO phonon at 708.7 cm^{-1} in a single 1D GaN nanowire, observed as a broad, hump-like feature. In addition, GaN nanopillars of diameter ~50 nm ares reported to show a SO phonon mode at ~716 cm^{-1} [127]. Finally, Bhattacharya *et al.* [125] reported SO modes at 633 and 678 cm^{-1} in GaN nanoribbons. SO modes can be sustained at interfaces between materials characterized by different values of the dielectric function. Previous works indicate that this mode may be activated by a breaking of the translational symmetry of the surface potential, which in the case of NWrs can be ascribed to the presence of roughness, sawtooth faceting on the nanowire sidewall or to diameter variations along the nanowire length. Surface related modes in polar materials are also called Fröhlich modes.

In the case of GaN, calculations based on the macroscopic dielectric theory indicate that SO modes are allowed in the frequency window between the $E_1(TO)$ and $A_1(LO)$ phonon modes [130]. In the Raman spectra of the sample characterized here (N1076), we observe the SO mode as a broad emission at a frequency below the $A_1(LO)$. Two peaks can be observed in the range of frequencies between 655 and 725 cm^{-1} in Fig. 5.2, better resolved in the spectrum in configuration $z(x,x)\overline{z}$. The frequency at the peaks and the FWHM are indicated in the last two columns of Table 5.1. As expected, their frequency is comprised between those of the modes $E_1(TO)$ and $A_1(LO)$.

The frequency of the SO modes depends on the dielectric constant of the materials at the surface and the shape of the surface. Consequently, it will vary with the dielectric constant of the medium surrounding the wires as well as with the radius of the wire [122]. Taking profit of the morphological characteristics of the samples studied in Chapter 4, we will present in the last Section of this Chapter a detailed study of the variation of the SO modes with NWrs coverage, that can be represented, within the dielectric continuum approximation, as variations in the mean dielectric constant of the material surrounding the nanowires.

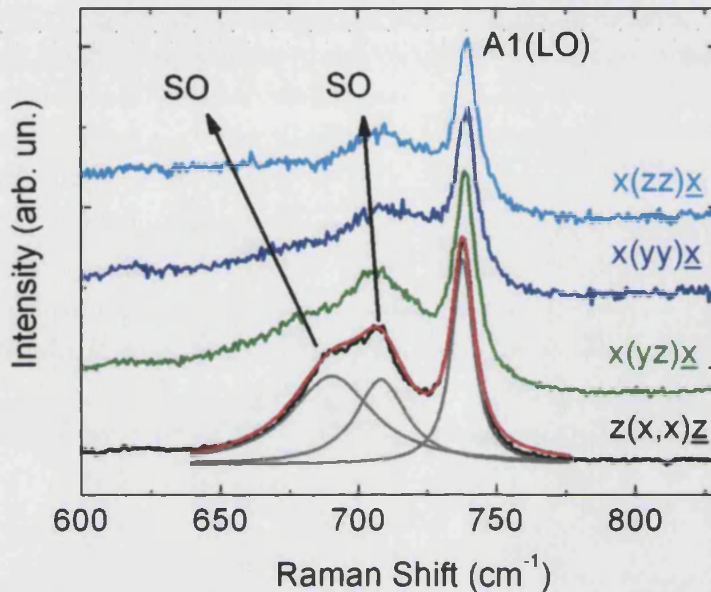

Figure 5.2: Raman spectra in different polarization configurations corresponding to the region of Optical Surface modes. The spectrum in configuration $z(x,x)\bar{z}$ has been fitted with three Lorentzian functions. Two SO modes can be resolved in the range of frequency between 690 and 710 cm^{-1}.

5.2 PL emission properties of GaN nanowires

The emission properties of bulk GaN and its heterostructures have been intensively studied during the last years. The near-band gap low temperature photoluminescence spectrum of the undoped material consists of a number of peaks arising from the recombination of free and bound excitons. Since the energy, relative intensities, and line widths of the emission peaks are strongly influenced by the residual strain, crystalline defects, and uncontrolled impurity incorporation, the interpretation of the spectra in heteroepitaxial GaN layers is rather difficult and often leads to confusing conclusions. With the availability of high quality free standing bare GaN NWrs, accurate studies of the different emission peaks and the identification of new ones related to quantum confinement and surface effects can be detected. All the experiments reported in this Section have been performed with the wave vector of the emitted light **k** parallel to the c-axis of the WZ crystal. In these conditions excitons with a dipole momentum perpendicular to the c axis are probed. In wurtzite GaN, however, the complex valence band structure and spin-exchange interaction results in five optically active free exciton states, which obey different selection rules [17]. When the light wave vector **k** is perpendicular to the c axis of the crystal, the 12-fold degenerated ground exciton state in wurtzite

GaN is completely split by the crystal field, spin-orbit, and spin-exchange interactions. Among the 12 exciton states only five are optically active: the three states with Γ_5 symmetry (allowed for the $E \perp c$ polarization) and the two states with Γ_1 symmetry (allowed for the $E \parallel c$ polarization). Due to their strong coupling with photons all dipole-allowed excitons form mixed exciton-polariton states, and the exciton recombination process becomes a propagation of polariton waves to the crystal surface and transmission outside as photons, rather than the transition from the exciton state to the photon state and subsequent photon propagation. In this case the emission line width does not reflect the inherent lifetime broadening of the free excitons. The emission peaks are usually quite broad and their line shape (not exactly symmetric) is determined by the spectral dependence of the density of states, group velocity, and transmission coefficient of the different polariton branches. In contrast, when excitons are bound to a donor or an acceptor the wave function of the complex is strongly localized and sharp emission lines are observed. Because the oscillator strength of a bound exciton is proportional to the oscillator strength of the free exciton from which it is derived, the same selection rules are expected to hold for bound and free excitons.

We will start comparing the low temperature PL emission from two samples containing bare GaN NWrs grown on Si(111) with an AlN buffer layer. Figure 7.20 shows PL spectra at low temperature from samples 1076 and 1025 with different columnar structures. Sample 1076 present a much higher NWr density (2.36×10^9 NWrs/cm^2) compared with sample 1025 (3.38×10^8 NWrs/cm^2), as can be observed in the SEM images exposed in the Figure. Sample 1076 contains NWrs of $\sim$ 3.5 μm long and an average diameter of 50 nm. On the other hand, sample 1025 presents shorter wires, of the order of 500 nm long and 40 nm diameter. The PL spectra of both samples present a strong and narrow excitonic emissions at 3.469 eV associated to the recombination of the D^0X_A complex. This peak has a FWHM of 4 meV, comparable with that reported in the literature [120, 131], indicating the good crystalline quality of the nanostructures. In addition, in the region of energy corresponding to the GaN band edge emission, PL spectra show a shoulder identified as the recombination of the free exciton X_A at 3.475 eV. The assignment that we have made is based on the thermal and excitation power dependencies of the PL lines which are discussed below. At the low energy side of the band edge, there are three characteristic emission peaks more, present in both samples: an emission at 3.449 eV, a broad emission at 3.415 eV and a weak peak at 3.354 eV. The yellow band emission, associated to nitrogen vacancies and other defects, is absent in both samples, which corroborates the high crystalline quality of the NWrs.

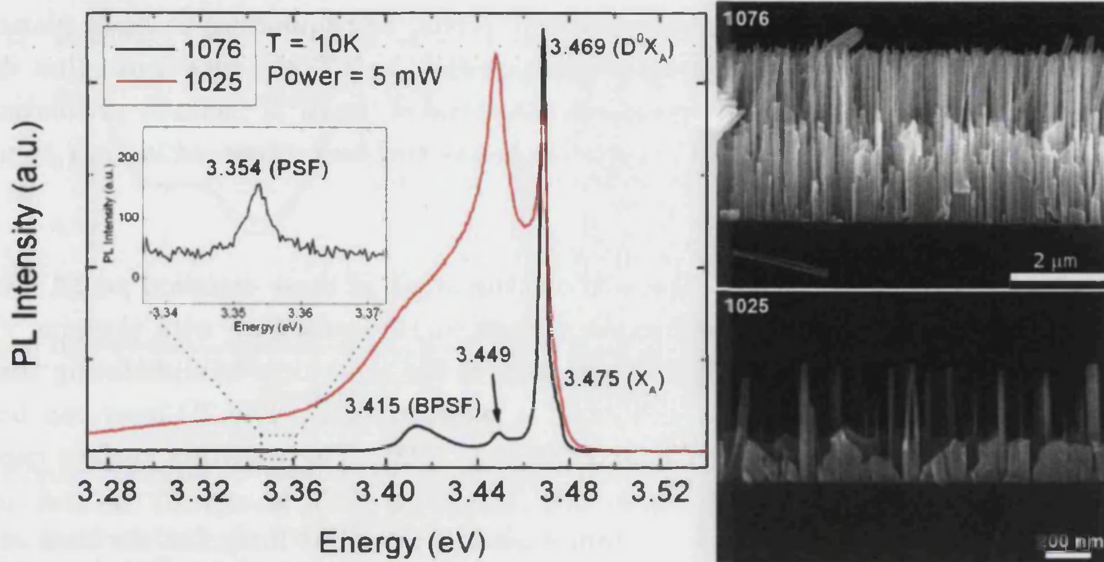

Figure 5.3: Photoluminescence spectra from sample N1076 with high density and long GaN NWrs and, from sample N1025 with low density and shorter GaN NWrs. Both spectra were acquired with the same excitation power and temperature. Representative SEM images from each sample are shown on the right part of the Figure.

In the spectrum of sample N1076, with a longer and higher density of NWrs, we can observe that the intensity of the emission close to 3.45 eV represents the 5% of the intensity corresponding to the D^0X_A emission. However, in sample 1025 this relative intensity is as high as 120% that of the donor bound exciton emission. This feature has been observed in previous works [95, 131, 132]. Taking into account the different NWrs density in both samples, this effect suggests that at low density the extraction of light related with this emission is be more efficient. Consequently, this emission could be related to the lateral sides of the NWrs. This emission will be studied more deeply as a function NWr density in the following Sections, where it will be shown that the ration $3.45/D^0X_A$ increases as the NWr density decreases. The broad peak at 3.41 eV is present in both samples. Actually, when the column density is small the band edge emission becomes weaker, rendering the peak at 3.41 eV dominant. the emission of this peak varies with the sample from 3.40 to 3.42 eV, and has also been observed in compact GaN layers, both grown along the WZ c-axis [133] and along the a-direction [83]. It becomes dominant in columnar GaN with very short columns, as occurs in sample 1025. This effect suggests that the emission is associated to the bottom part of the columns and is enhanced in sample 1025, since the excitation light can reach better the base of the NWrs due to their low density and the short length. By comparison with other works [134–136], we conclude that the emission around 3.41 eV is originated

atthe dislocations formed at the base of the NWrs, corresponding to basal plane staking faults (BPSF). Regarding the emission close to 3.32 eV, we suggest that it is related to the formation of dislocations at the end of the BPSF, namely prismatic stacking faults (PSF). This board emission has as well been observed in GaN thin films [134].

In order to prove our hypotheses about the origin of these emission peaks, we glided the surface of sample 1025 over a clean Si(111) substrate with the aim of dispersing the NWrs on the Si substrate and, at the same time of eliminating the NWrs, keeping the GaN 2D layer formed in between them. The 2D layer can be appreciated in the bottom SEM image of Fig. 7.20. The resulting surface can be seen in the SEM images of Figure 5.4. The upper SEM images correspond to the NWrs sample after the gliding process, while the SEM image at the bottom shows the dispersed NWrs on the Si(111) substrate. Through this procedure the NWrs are eliminated from the original sample and transferred to the Si substrate. Only the 2D GaN layer, together with the bottom part of the NWrs, remains. The graph on the Figure shows the PL spectra taken from different spots of the cleaned sample (blue), and those taken from the dispersed GaN NWrs (red). In first place, we observe that the peak corresponding to the D^0X_A emission broadens to 7 meV. This broadening is often observed in dispersed NWrs when compared to the as-grown samples [137, 138], and is ascribed to the interaction of the NWr with the surface used for the deposition. Regarding the emission below the D^0X_A transition, it can be observed that the peak at 3.45 eV dominates the spectra in dispersed NWrs. At the same time, the band edge emission becomes weaker. On the contrary, the emission at 3.45 eV completely vanishes in the spectra acquired from the cleaned sample 1025. This fact supports our hypothesis that the emission comes from the NWrs and not from the GaN 2D layer at the bottom of the wires. Additionally, the current analysis shows that the emission at 3.41 eV originates at the disordered GaN column/substrate interface. The spectra in Fig. 5.4 show that the emission at 3.41 eV, characteristic of BPSF, almost disappears in the dispersed NWr sample, supporting the fact that this emission comes from the bottom part of the NWrs. On the contrary, this emission becomes stronger in the spectra corresponding to the remaining GaN 2D layer. From these results we conclude that the upper volume of the NWrs is dislocation free, and that they are located at the bottom. It is also expected that in the 2D layer several dislocations are formed, giving place to a PL broad emission in the low energy ranges. Finally, the emission corresponding to the PSF in the energy range of 3.32 eV weakly appears in the red spectra, while in the blue ones a strong and broad emission in this energy region dominates the spectra. As discussed before, this is an indication of

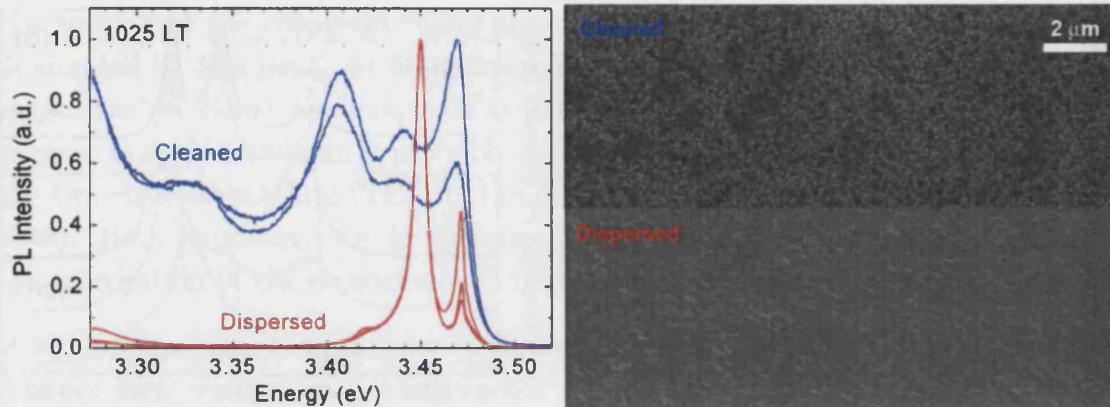

Figure 5.4: Low temperature PL spectra taken from dispersed NWrs on clean Si(111) of sample 1025 in red. The spectra in blue are obtained from the remaining 2D layer in sample 1025. SEM images from both the NWrs dispersed on the Si substrate and the remaining "cleaned" surface of sample 1025 are shown.

the very good crystalline quality of the NWrs, and the formation of a large variety of dislocations in the 2D layer and first stage of nucleation in the bottom part of the NWrs.

5.2.1 Temperature dependence

The question concerning the thermal evolution of the PL peaks is shown in Fig. 5.5. In order to distinguish between the optically active free exciton states polarized measurements have been performed to analyze their emission selection rules. The characteristics of the emission of bulk GaN in the $k \perp c$ geometry have been reported by Paskov *et al.* [17] using the cleaved sample edge of bulk GaN. The Figure shows the PL spectra taken for $E \perp c$ (a) and $E \parallel c$ (b) polarization in the temperature range between 10 and 160 K. These experiments are carried out, as before, with the light wave vector perpendicular to the c-axis. The spectra have been normalized to the most intense peak and shifted for clarity. The dashed lines are guides for the eyes. The well-resolved emission peaks in both polarizations allow us to reveal excitonic states with different symmetry and to distinguish between the extrinsic and intrinsic emissions.

In the case of the $E \perp c$ configuration, the low-temperature spectrum reveals the five characteristic peaks studied above. A sharp line at 3.469 eV and its shoulder on the high energy side at 3.475 eV are assigned to the D^0X_A excitonic complex and the A exciton respectively. The extrinsic nature of the peak D^0X_A is verified by its faster quenching with temperature compared to the exciton related emis-

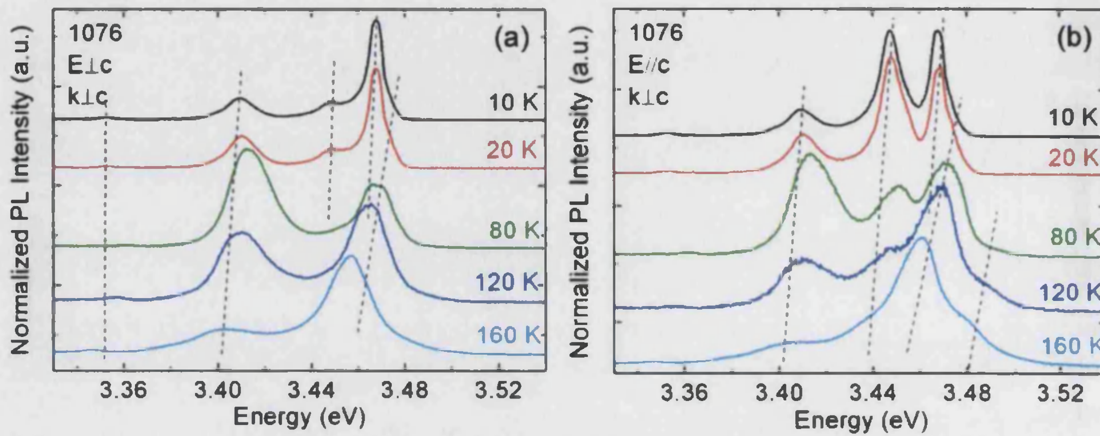

Figure 5.5: PL spectra of the components of polarization $E \perp c$ (a) and $E \parallel c$ (b) in the range of temperature between 10 and 160 K. The spectra were acquired with the wavevector of the light perpendicular to the NWr direction, $k \perp c$. The dashed lines are guides for the eyes.

sion. As the temperature increases, a new shoulder at around 3.48 eV appears. This peak is associated with the emission from the B exciton recombination, which is more pronounced in the $E \parallel c$ polarization. This is consistent with the optical selection rules for the B exciton. We also note that due to the small energy difference between the A and B excitons the two emission bands are slightly overlapped. The close vicinity of the two first upper valence bands has been observed in several works, compiled in Table 2.2. In the case of $E \parallel c$ polarization, quite different PL spectra are obtained. The low-temperature spectrum is dominated by the D^0X_B emission at 3.468 eV. The peak appears at the same energy as in the $E \perp c$ polarization, which is not surprising having in mind that the Γ_1 and Γ_5 states of the B exciton are almost degenerated at zero strain. Although the A exciton is dipole forbidden for the $E \parallel c$ configuration, the emission peak of the D^0X_A complex can contribute at low temperatures implying some relaxation of the selection rules, most probably due to a small misalignment from the $k \perp c$ geometry or multiply reflections of the excitation laser with the NWrs surface. The dominant peak D^0X_B in this configuration at low temperature is attributed to the recombination of the B exciton, according with its emission selection rules. At temperatures above 80 K the complex D^0X_B quenches, and at the same time it allows resolving the peak associated to the X_B exciton as a weak emission in the high energy side of the D^0X_B complex. Such a structure of the X_B peak persists up to room temperature and then the higher energy peak is taken over by the broad emission labeled X_C, originated from the C exciton. One more transition at 3.45 eV is characteristic for GaN NWrs as we have already demonstrated in the previous Section. For an assignment of this peak, we turn our attention to

the spectra of the dispersed NWrs shown in red in Fig. 5.4. The spectrum is dominated by this peak. At higher energies, the peak corresponding to the D^0X_A is also visible. Some Authors, such as Brandt *et al.* [131] and Corfdir *et al.* [132], suggest that this emission is probably produced by impurities at the surface or by the two-electron satellite (TES) of the dominant donor bound to exciton, respectively. Both hypothesis are in agreement with the low density of impurities and the segregation of Ga vacancies or O implantation close to the surface.

The temperature dependence of the fundamental band gap widths of semiconductors with wide band gap represents a basic material-specific property which is of considerable experimental as well as theoretical interest. It is known from experimental results that the band gap widths of many materials decrease monotonically with increasing temperature [59, 139, 140]. We present here the study of the temperature dependence of the optical properties of as-grown GaN NWrs. In general, in photoluminescence experiments where the excitation density is sufficiently low that only recombination occurs from ground states, in the temperature dependence spectrum can be resolved the different transitions. Figure 5.6 shows the temperature dependence of the emission energy for several of the peaks characteristic of GaN NWrs. The energy of the optical transitions remain almost constant up to 120 K. Above this temperature the energy starts to decrease due to the GaN band gap shrinkage and following the evolution commonly indicated in the literature, namely, the empirical and semi-empirical function of $E_g(T)$ proposed by Varshni [141] and Viña *et al.* [142]. The variation observed in the energy gap in the range of temperatures between 10 and 300 K is about 65 meV for the excitonic complexes, while for the emission corresponding to the D^0X_A complex is around 75 meV. A similar variation has been recently observed in GaN epilayers [143] with different intrinsic n-doping levels.

In order to get insight into the thermal redistribution of the excitons, we studied the temperature dependence of the integrated intensity of those emission peaks that can be fitted in a wide range of temperature. The Arrhenius plot of the integrated intensity as a function of temperature is shown in Fig. 5.7 for the emission corresponding to X_A, D^0X_A and the peak assigned to the two electron satellite (TES). The experimental data are analyzed by the well-known relation for the thermal quenching of the PL intensity (Equation 3.3), where several non radiative processes with thermal activation energies E_a can be included [93]. In this case we describe the quenching of the recombination processes plotted in the graph by taking into account only one non radiative process. In the case of D^0X_A, in configuration $E \parallel c$, the detrapping of the excitons from the donors occurs for a thermal activation energy of 11 ± 1 meV. This value is in a good

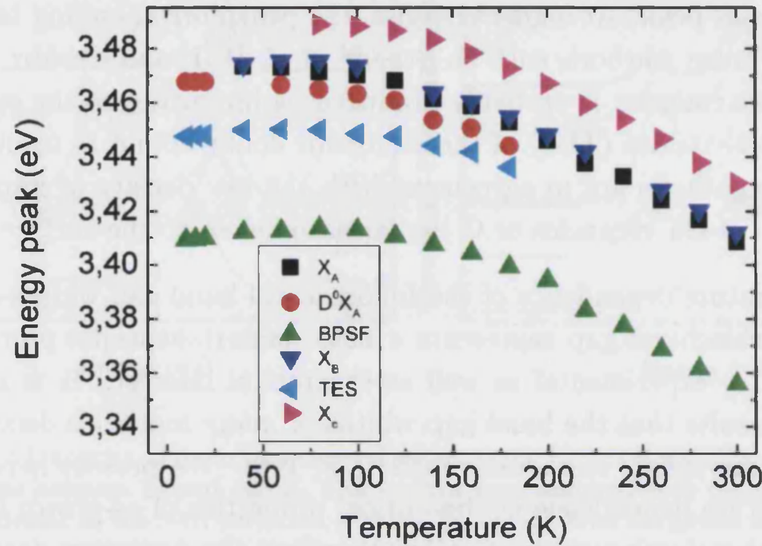

Figure 5.6: Evolution of the peak energy of the different emissions with temperature.

agreement with the measured optical intensity at low temperature (see spectra in Fig. 5.5). This non radiative process becomes important at higher temperature and can be attributed to the ionization of the donors or to a simultaneous exciton delocalization and exciton dissociation [144]. The thermal quenching of the A exciton is also satisfactorily explained with a single non radiative process with activation energy of 30 ± 2 meV. This process reflects the exciton dissociation. We can obtain the energy gap of GaN by the addition of the emission energy of the A exciton (3.469 eV) and the activation energy related with the dissociation of the exciton. The result, 3.499 eV, is in good agreement with values reported in the literature [55] for very good quality GaN layers grown on HVPE GaN substrates. The last emission studied as a function of temperature is the peak labeled as TES. As well as in the other cases, the evolution with temperature of the energy of this emission has been fitted with a single process. The obtained activation energy is of 14 ± 3 eV, of the same order than the activation energy for the D^0X_A complex. This result agrees with the fact that the TES is an excited state of the D^0X. Concerning the peak related to free exciton recombination, it is found that at higher temperatures the intensity of X_B quenches with the same thermal activation energy as X_A. This is not surprising because the exciton binding energies of the A and B excitons are almost the same. The best fit of the experimental data yields an activation energy of 23 ± 6 meV, which implies that the quenching is mainly due to the exciton dissociation. Finally, due to

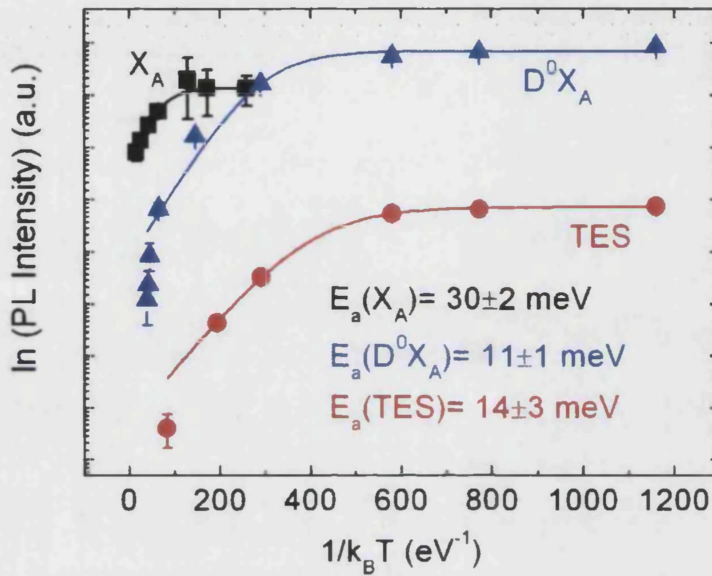

Figure 5.7: Arrhenius plots of the integrated intensities versus $1/k_BT$ for the peak assigned to the free exciton A, the neutral donor bound exciton transition and the two electron satellite peak. The solid curves represent the theoretical fits using Eq. 3.3 using only one activation energy.

thermalization of the electrons excited to the third valence band (labeled CH in bulk), an increase in the intensity of the X_C emission is also observed above T=80 K. Soon this emission becomes unresolved because of its increasing broadening at high temperatures. Therefore, in our experiment it has not been possible to make a reliable Arrhenius representation for this excitonic emission.

5.2.2 Polarization of the emission

In previous Sections, we have presented the PL emission for polarization components $E \perp c$ and $E \parallel c$, obtained in the experimental configuration where $k \perp c$. An analysis of the polarized emission as a function of temperature was also performed. Here, we will discuss in more detail the polarization characteristics of the emission of GaN NWrs, comparing the relative intensity of the emission related to both polarizations. Figure 5.8 shows the polarized PL measurements at low temperature for $E \perp c$ and $E \parallel c$ in the geometrical configuration $k \perp c$. The peaks assigned to the D^0X_A and the D^0X_B complexes in the spectra polarized along $E \perp c$ and $E \parallel c$ are observed. A shift of 3 meV between these to peaks can be resolved. The peak corresponding to the perpendicular configuration ($E \perp c$) presents a higher PL intensity compared with the transition D^0X_B.

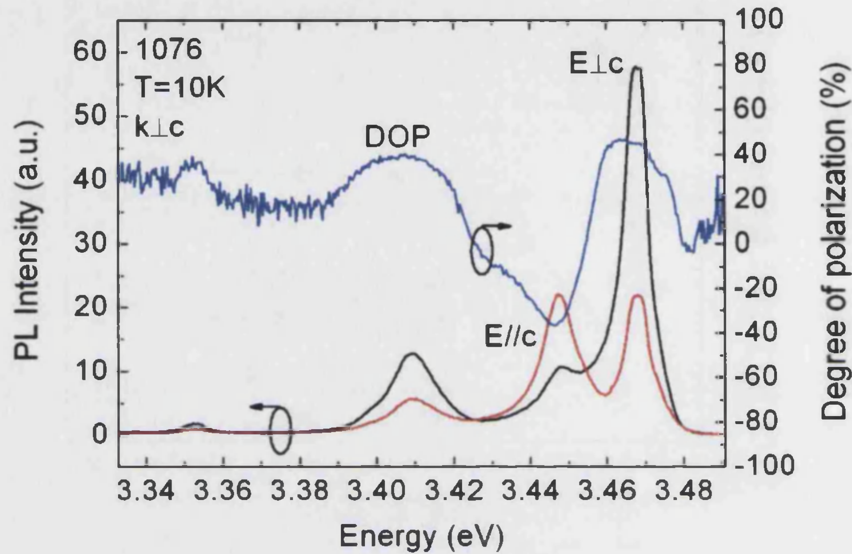

Figure 5.8: Low temperature PL spectra in configuration $E \perp c$ (black line) and $E \parallel c$ (red line). The blue lien represents the DOP calculated for each emission energy.

Similar results have also been reported for other semiconductor nanowires with WZ structure, such as CdSe [145]. The degree of polarization has been calculated using the Eq. 3.1 for each emission energy and it is shown in blue (right axis). We can observe that the value of the DOP is positive, that is, the emission is preferentially polarized perpendicular to the c-axis, for all the peaks except for the TES emission. The selection rules of optically active excitonic emissions are well fulfilled in the spectra.

The DOP of the different emission peaks from GaN NWrs has been determined as a function of temperature. The spectra have been fitted by multi Lorentzian functions in order to obtain the relative intensity of each emission studied in Section 5.2. Equation 3.1 has been used and the results are plotted in Figure 5.9 versus temperature. As a matter of reference, the dashed line represents an unpolarized emission. Taking into account the similar polarization characteristics of the complexes D^0X_A and X_A, we have summed up the integrated intensity of both peaks. In the Figure we represent the evolution of their DOP with only one set of points (black points). We can see that as the temperature increases the polarization gradually is lost. Regarding the absence of the emission related to exciton B, we should remember that the small energy difference between A and B excitons in GaN renders the resolution of both excitons very difficult. Additionally, as the temperature increases the band filling and thermalization of the carriers hinder

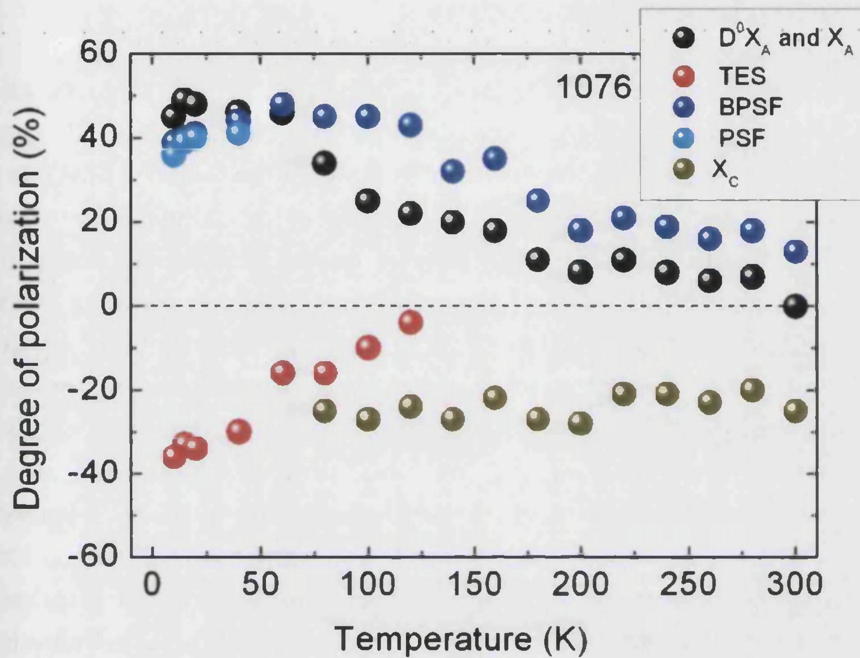

Figure 5.9: DOP calculated from the integrated intensity for each transition as a function of temperature. The dashed line represents the unpolarized emission.

the detection of both excitons. For a more rigorous analysis, a spectral deconvolution of contributions from A and B excitons might be necessary, but this resulted in very imprecise numbers. Concerning the emission assigned to BPSF, its DOP presents a similar behaviour as as the excitonic complexes, with a positive value at low temperatures that decreases gradually as the temperature increases towards room temperature. The DOP related with the emission from PSF can only be determined at temperature smaller than 50 K, and follows a similar trend. Coming back to the analysis of the polarization of the TES emission, its DOP starts with a value of -40% at low temperatures and losses its polarization in the rage of temperature between 10 and 120 K. This is in accordance with the fast quenching suffered by the TES emission. Finally, for temperatures above 80 K, it is possible to observe the emission related to the C. This is due to the thermal filling of the bands favored by the increase of temperature. Its DOP remains constant up to room temperature, as expected from the polarization selection rules for bulk GaN.

5.2.3 Power dependence study

The optical emission properties of sample 1076 have been investigated as a function of excitation power. Figure 5.10 shows the low temperature PL spectra for five values of the excitation power in the range of 0.2 to 5 mW. The five characteristic peaks of the emission from GaN NWrs appear in the whole range of power excitation. After the analysis of the spectra by means of a multi-Gaussian fitting, we can determine that the energy of the excitonic emissions remains constant independent of excitation power. However, the emission from the BPSF blue-shifts 6 meV as the excitation power increases. Actually, the dislocations associated to basal plane stacking faults behave as quantum wells grown along the c-axis in what concerns its optical properties. The 6 meV shift can be understood as a screening of the internal electric field due to the photoexcited carriers. Regarding the FWHM, the width of the peaks remains almost constant with increasing excitation power. Actually, it increases only 3 meV for most transitions, a number consistent with the increase in the density of photoexcited carriers. The behavior of the emission associated to BPSF is, however, quite different. It an increment of its FWHM four times larger than the rest of the peaks (12 meV). This broadening is easily understood by the filling of high energy states when excited at high power. Since BPSF can be found at the base of the NWrs, their PL signal increases if the NWrs density is small or for high excitation power. A study of the PL emission as a function of excitation power also allows the identification of the recombination processes involved in the emission. Schmidt *et al.* [92] present a theoretical study based on the power dependence of the near band edge photoluminescence of different III-V semiconductors. They conclude that the power dependence of the luminescence lines can be describe by an $I \propto P^n$ when the P is varied a range of less than two orders of magnitude, where I is the luminescence intensity, P is the excitation power and n is a coefficient. For excitation with energy larger than the band gap of the material, the coefficient n is generally $1 < n < 2$ for free and bound excitonic emissions. In the case of $n < 1$ the recombination corresponds to free to bound and donor acceptor pair complexes.

In Figure 5.11 we plot the low temperature PL integrated intensity of each peak as a function of the excitation power in logarithmic scale for two different power ranges. In the low power range, between 0.6 and 14 μW, only one emission peak is observed. The corresponding experimental points are shown at the left side of the graph, in red. The fitting of the data to the function $\log I \propto n \log P$ gives a factor $n = 1.12$, a number between 1 and two, in accordance with the excitonic character of the complex D^0X_A. This assignment is therefore in agreement with our previous study. The rest of the peaks can be observed if we increment the

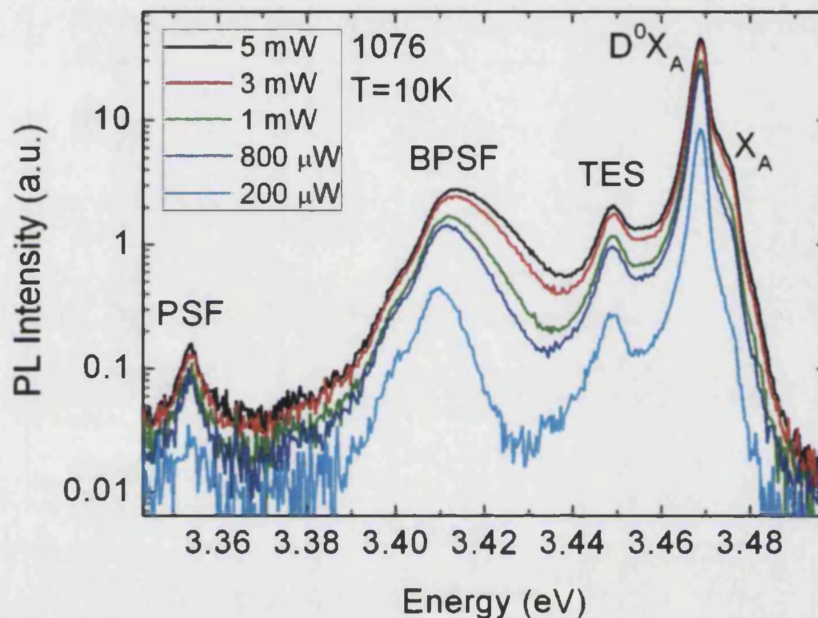

Figure 5.10: Low temperature PL spectra of sample 1076 as a function of excitation power. The intensity is represented in logarithmical scale.

excitation power to the range 0.2 to 5 mW. A similar fitting performed to the D^0X_A emission gives a much smaller coefficient, $n = 0.56$, suggesting the saturation of the donor impurities for excitation powers larger than of 14 μW. Nevertheless, the power dependence of the peak attributed to free exciton recombination, X_A, is characterized by a coefficient $n = 1.48$, confirming its excitonic origin. The coefficient that characterizes the emission assigned to the TES is $n = 0.66$, similar as that of the complex D^0X_A in the saturated range, suggesting a relation between the two complexes. This emission is, however, not observed at lower values of the excitation power. Finally, we would like to point out that the peaks associated to emissions related to BPSF and PSF have been observed in bulk GaN [135] and a-plane GaN layers [134]. The power evolution of these two peaks is characterized by a coefficient n equal to 0.74 and 0.29 respectively. These coefficients rule out the excitonic origin of these emissions. As proposed by Schmidt *et al.*, a coefficient $n <$ 1 could arise from free to bound recombination or donor acceptor pair complexes. However, the donor acceptor pair transitions in this nanostructures would be very unlikely due to their low density of donors and acceptors, supported by the rapid saturation of the donors and the absence of the acceptor peak in the PL emission. On the other hand, our assignment is consistent with reports in the literature,

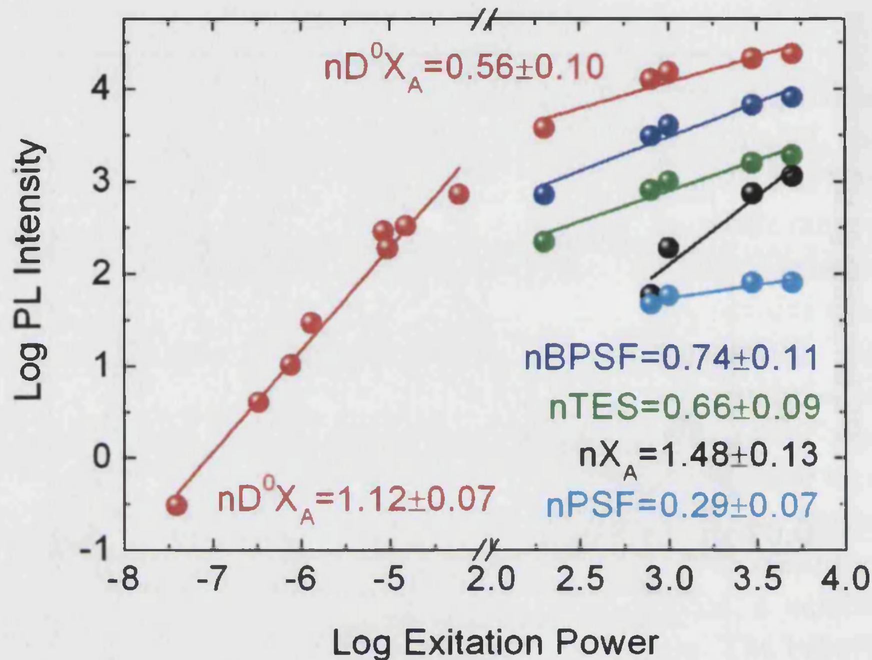

Figure 5.11: Representation of the relation $logI \propto nlogP$. The brake in the axis of the excitation power separates the low and high excitation power regions.

where these transitions have been attributed to excitons bound to planar defects such as stacking faults [138]. The nature of these peaks is also consistent with the fact that excitons bound to planar defects are generally not as easily saturable as excitons bound to point defects [146].

5.3 Effect of density on the optical properties GaN nanowires

In this section, we present study by means of RS about the surface optical (SO) modes of GaN NWrs as a function of density of GaN and the surrounding air (coverage). The results are related with the coverage extracted from SEM pictures. Additionally, the PL evolution as a function of density is also presented.

5.3.1 Sample description and Raman Scattering

The GaN NWrs studied in this Section correspond to sample 1405. Its growth conditions were described in Sec. 4.2.3. In the morphological studies performed

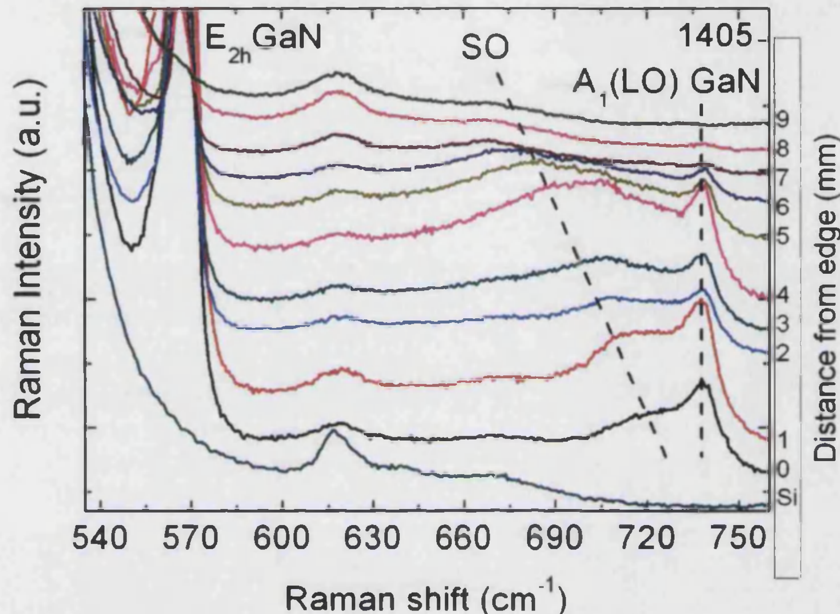

Figure 5.12: Room temperature RS spectra taken from the edge to the center of the wafer with steps of one millimeter. The dashed lines are a guide for the eyes to follow the SO frequency shift. A Raman spectrum of Si is included at the bottom as reference. The SEM images can be used to visualize the changes in morphology of the NWrs along the wafer radius.

on this sample, we observed a gradual change in the NWrs density as a function of position along the wafer radius (see Sec. 4.3). μ-RS spectra at room temperature taken in backscattering configuration along the radius of the Si wafer, one spectrum each millimeter, are sequenced in Figure 5.12. The position 0 represent the edge of the wafer. The spectra have been vertically shifted for clarity. On the right part of the Figure we have included three SEM micrographs representing the morphology of the NWrs at characteristic positions along the wafer. A reference Si spectrum is included at the bottom for comparison. On the left, it can be observed the intense emission of the E_{2h} mode about the frequency of its relaxed value. In addition, the $A_1(LO)$ emission is also observed around 730 cm^{-1}. On its low frequency side, a broad shoulder is observed, assigned, as before, to SO phonon modes. As the NWrs density decreases, the frequency of the $A_1(LO)$ mode remains constant, while that of the prominent shoulder red shifts as the laser spot moves towards the center of the wafer. The dashed lines on the graph can be used as a guide for the eyes.

The information extracted from the Raman spectra related to the E_{2h} mode is summarized in Figure 5.13. Within the spectrometer resolution of 0.5 cm^{-1} the energy of the E_{2h} mode is almost constant and characteristic of relaxed NWrs.

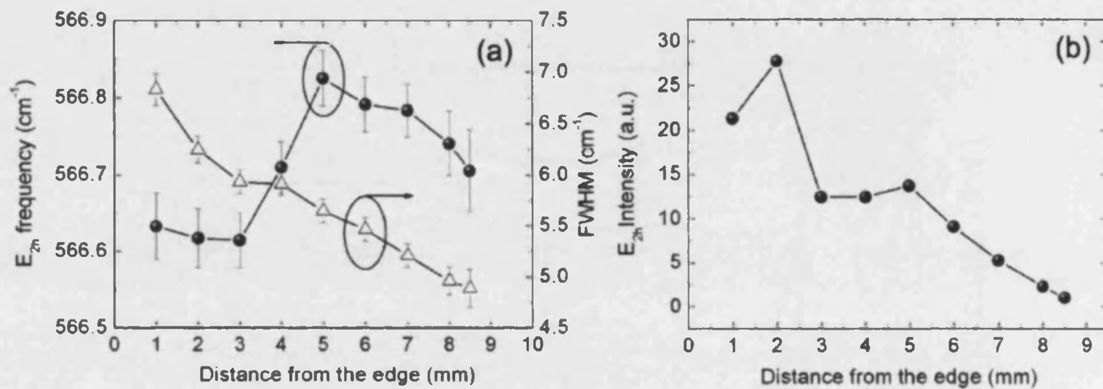

Figure 5.13: (a) Raman shift of the E_{2h} mode (spheres) and its FWHM (triangles) as a function of the position along the wafer radius. (b) Evolution of the integrated intensity of the E_{2h} mode.

Interestingly, the width of the mode decreases considerably with decreasing density, indicating the further improvement of the crystalline quality of the NWrs towards the wafer center [Fig. 5.13(a)]. This fact is in agreement with the disappearance of collapsed NWrs as the NWr density decreases. Furthermore, the intensity of the mode correlates very well with the amount of GaN, decreasing as the spectra is taken closer to the center of the wafer, as can be seen in Fig. 5.13(b). We should keep in mind however that small changes in laser focus and multiple scattering of light at the NWr lateral facets may influence the Raman intensity to some extend, specially in the high density region.

Besides the E_{2h} mode, we observe the $A_1(LO)$ mode at 738.4 cm^{-1}. It appears blue-shifted about 4 cm^{-1} with respect to its relaxed value (see Table 1.7). As it has been explained in Sec. 1.3.3, this mode is sensitive both to strain and the phonon-plasmon coupling. Since this kind of nanostructures are strain free, the energy shift suffered by the A_1(LO) mode indicates the existence of free carriers. The Equation 1.20 relates the frequency shift of the $A_1(LO)$ mode with the free electron density. By using the upper branch of the Graph 1.6, we obtain a free carrier concentration of $2 \cdot 10^{17}$ cm^{-3}. This value is in good agreement with electron an density of $\sim 1.1 \cdot 10^{17}$ cm^{-3} measured by Hall effect in unintentionally n-type doped GaN films [147]. Finally, in the next Section we analyze the evolution of SO modes as a function of density.

5.3.2 Surface optical phonon modes as a function of NWrs density

The frequency of the SO phonon modes depends strongly on the dielectric properties of the materials involved. Since the wurtzite structure of GaN has an optical axis along c, its dielectric tensor has two different components, one corresponding to the optical axis and one perpendicular to it. Based on Loudon's uniaxial crystal model, these components can be written as:

$$\varepsilon_z(\omega) = \varepsilon_\infty \frac{\omega^2 - \omega^2_{A_1(LO)}}{\omega^2 - \omega^2_{A_1(TO)}} \text{ and } \varepsilon_\perp(\omega) = \varepsilon_\infty \frac{\omega^2 - \omega^2_{E_1(LO)}}{\omega^2 - \omega^2_{E_1(TO)}}. \quad (5.1)$$

In these expressions the frequency of the polar phonon modes are taken from Table 1.7. The high frequency dielectric constant of GaN, ε_∞, is taken to be isotropic and equal to 5.35 [148].

The dipolar interaction between NWrs can be very well described within the Maxwell-Garnet approach [149]. This model describes the optical properties of the NWr-air system by an effective dielectric function that depends on NWr coverage [123], and is given as:

$$\begin{aligned} \varepsilon_z^{eff}(\omega) &= (1-c)\varepsilon_m - c\varepsilon_z(\omega) = 0 \quad (5.2) \\ \varepsilon_\perp^{eff}(\omega) &= \varepsilon_\perp(\omega)\frac{(1+c)\varepsilon_\perp + (1-c)\varepsilon_m}{(1-c)\varepsilon_\perp + (1+c)\varepsilon_m}. \end{aligned}$$

Here c represents the NWr coverage or relative NW/air fraction in the sample and ε_m is the dielectric constant of the surrounding medium, in our case air ($\varepsilon_m = 1$).

In uniaxial crystals, ordinary and extraordinary excitations exist, which depend on the angle θ between the wave vector of the exciting light and the wurtzite c-axis. The Raman intensity of the ordinary phonons is proportional to $\mathrm{Im}\,[\varepsilon_\perp^{eff}(\omega)]$, while that of extraordinary phonons is proportional to $\mathrm{Im}[-1/(\varepsilon_z^{eff}(\omega)\cos^2\theta + \varepsilon_\perp^{eff}(\omega)\sin^2\theta)]$. The ordinary excitations give rise to two peaks in the Raman spectra, but only $\omega_{E_1(TO)}$ has a large enough intensity to be observed. Additionally, the extraordinary part of the Raman scattering gives rise to two peaks that depend on the angle of incidence θ. These two peaks are the ones observed in the Raman spectrum of Fig. 5.2 and labeled as SO. In the simple case of normal incidence, the frequencies related to these vibrational modes have been plotted as a function of coverage in Figure 7.19 with blue dashed line. Surface phonon modes related to longitudinal modes are labeled SO_1, while those related with transversal modes are labeled SO_2. Additionally, the frequency of $A_1(LO)$ mode, at 738 cm^{-1}, has also

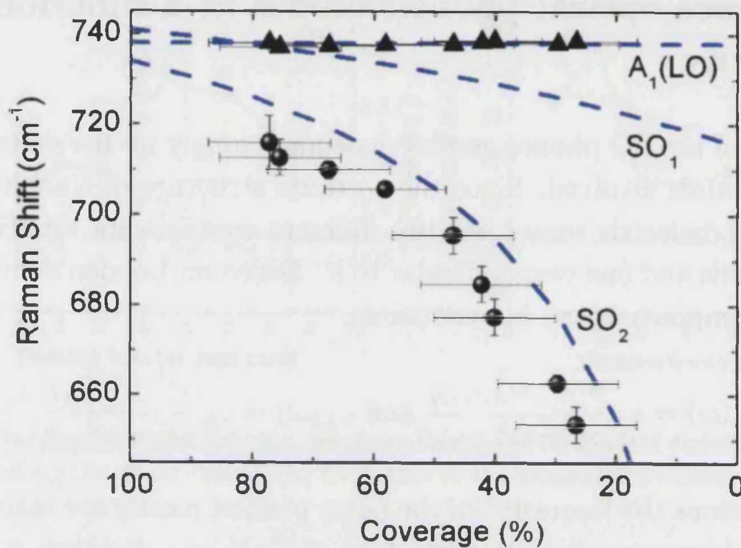

Figure 5.14: Frequency of the SO modes together with the A_1(LO) as a function of coverage as determined by SEM images (black spheres) and theory (dashed lines).

been plotted. The results indicate that the frequency of the SO_1 mode decreases only slightly as the coverage decreases from 100% to 0%, with a total shift of the order of 20 cm^{-1}. The shift of the SO_2 mode is much larger, of the order of 60 cm^{-1}.

From the SEM images taken along the wafer radius we can determine the NWr coverage. Figure 5.15 shows, with triangles, the variation of coverage in percentage of GaN along the radius of the wafer. With black spheres we have also plotted the experimental frequency of the SO modes. The results correspond with good agreement with the theoretical calculations.

The information contained in this Figure allows us to plot the experimental SO frequencies in Fig. 7.19 (black spheres), together with the theoretical results. It is clear that, while SO_1 cannot be resolved in the spectra, the SO data follow very closely the theoretical curve for SO_2. The small discrepancy may be due to the finite size of NWrs, which is not taken into account in within the Maxwell-Garnett approximation.

5.3.3 PL analysis and discussion

Photoluminescence experiments at low temperature have been performed on this same sample (N1405). The laser was focussed onto a diameter spot of 50 μm and

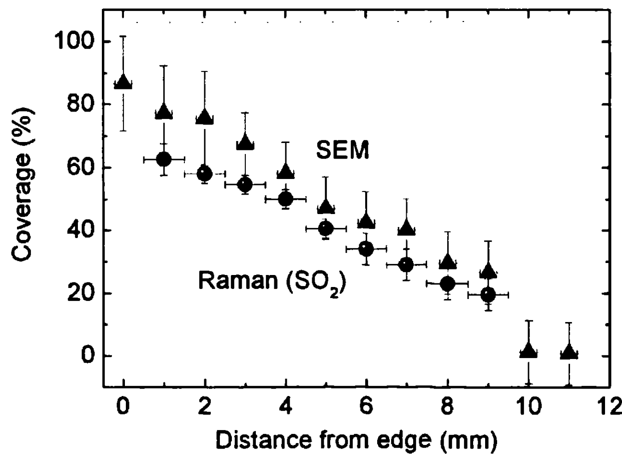

Figure 5.15: Coverage of GaN NWrs along the radius of the wafer.

the excitation power was kept constant to 1.7 μW. In the same way than Raman spectra, each PL spectrum was acquired along the radius of the wafer at millimeter steps, covering from 0 mm (edge) to 13 mm. The results are plotted in Figure 5.16. All the spectra have been normalized by the acquisition time and shifted for clarity. It can be observed that the D^0X_A emission dominates in intensity in all the spectra. The shoulder related to the X_A emission can be observed on the high energy side. The emission assigned to TES is also observed in all the spectra. In the region near the edge, we can also see a weak and broad emission around 3.40 eV. The intensity of this emission increases from the high to the low NWr density region. We believe that this emission is related to BPSF.

The analysis of the spectra shows a very small blue shift of the D^0X_A emission energy in the order of 1 meV as the density of NWrs decreases, a shift which is below the resolution of our experimental system. This shift can be better observed in Figure 5.17(a). Even though the diameter of the NWrs decreases towards the center of the wafer, reaching values of 10 nm in the region of highest growth temperature (see Figure 4.12), considering that the Bohr radius of the exciton in GaN is in the order of 2.8 nm [150], we do not expect any shift of the bands due to confinement. It can be observed in the spectra of Fig. 5.16, however, that the intensity of the D^0X_A decreases with respect to that of the free exciton as the density decreases. This is related to the fact that at higher growth temperature the desorption of the donors increases and therefore the amount of impurities decreases. As a result of this change in relative intensity, the D^0X_A seems to

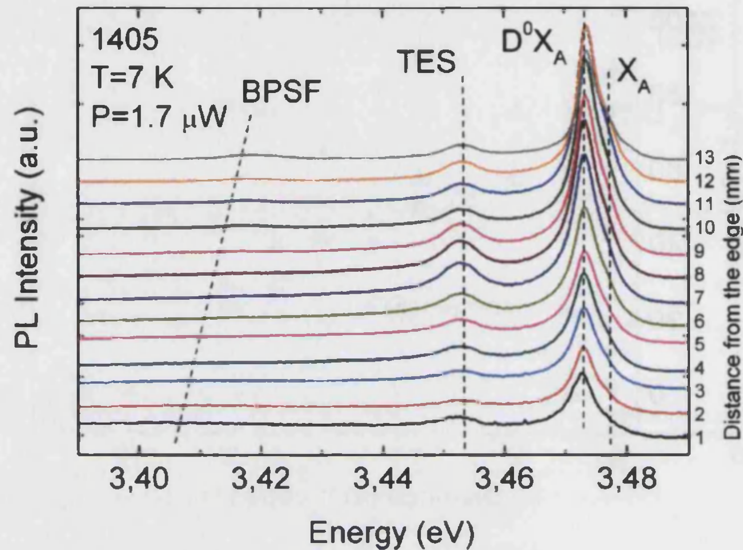

Figure 5.16: PL spectra acquired from different positions along the wafer radius, from the edge (0) to the center (13) with steps of one millimeter. The dashed lines are a guide for the eyes to follow the trend of the different emissions. Note that the intensity axis is logarithmic.

shift to higher energies by 1 meV. In the same graph, we have plotted (triangles) the evolution of the FWHM of this emission along the wafer radius. A small decrease, of the order of 2 meV, is observed in the low density region. Similarly as in the Raman spectra discussed previously, we ascribe this decrease to the absence of coalesced NWrs, with the consequent improvement in NWr material quality. The intensity of the peak assigned to D^0X_A and TES emission are plotted in Fig. 5.17(b) with red squares and blue triangles respectively, together with the intensity ratio TES/D^0X_A plotted with black spheres. We can see that the PL intensity related to D^0X_A emission increases by a factor 7 when by moving from the high density area, at the edge, to the low density region, about 10 mm from the edge. Beyond 10 mm, the intensity starts to decrease until it vanishes due to the absence of NWrs. This behavior is striking, since we would expect the PL intensity to be proportional to the amount of material present in the sample. We can explain it considering several factors, both geometrical and optical. First, in the low density zone the excitation laser illuminates the whole NWr length, while in the high energy region the penetration of light is limited by absorption. Second, we also expect a better light extraction in the low density region. Besides this, SEM analysis revels that in this region the tilt of the NWrs increases. Both effects contribute to an increase of the emission from the NWr facets reaching the

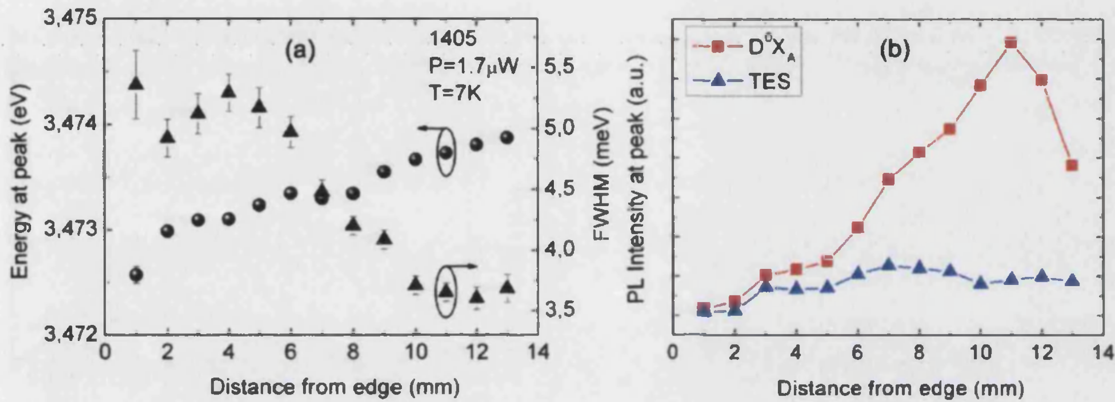

Figure 5.17: (a) Emission energy of the D^0X_A as a function of the position along the wafer radius, together with its FWHM. (b) Evolution of the intensity of the D^0X_A and TES emissions versus de position of the wafer.

detector. Additionally, an small increase in material quality can also contribute to the intensity, as indicated by the decrease in FWHM of the D^0X_A emission.

TRPL characterization has been performed on the this sample with a setup similar to that presented in Sec. 2.3.3 but using a streak camera as detector. We study now in detail the recombination dynamics of the emission corresponding to TES, D^0X_A and X_A in the low and high density regions, taken at 5 mm and 11 mm from the edge of the wafer respectively. All emissions are characterized by subnanoseconds decay times. In Figure 5.18 we represent the corresponding TRPL. We have fitted the spectra with a single exponential decay. In the high NWrs density region, Fig. 5.18(a), the decay times obtained for for TES, D^0X_A and X_A are 472 ps, 267 ps and 195 ps respectively. These values are similar to those reported before by other groups [132]. The longer decay time characteristic of the TES emission is tentatively ascribed to an enhanced localization, expected for processes located at the NWr surface. Paskov *et al.* [52] observed as well slower decay times for TES emission than for the D^0X_A line. They attributed this unexpected behavior to the possibility of different sites for the donor, where the respective dynamics of TES and D^0X_A lines could be different. Furthermore, in Ref. [137] the authors have shown that the decay time of the luminescence is strongly related to the NWr diameters. Actually, they found a linear relation between the decay time and NWr diameter. For NWrs with diameter close to 250 nm the decay time remains in the ps region, while it can reach values close to 3 ns in NWrs with a diameter of 1 μm. These values compare well with GaN NWrs from our high density region, where the sample present NWrs with large diameter and a larger coalescence degree. On the other hand, the fitted decay times for TES, D^0X_A

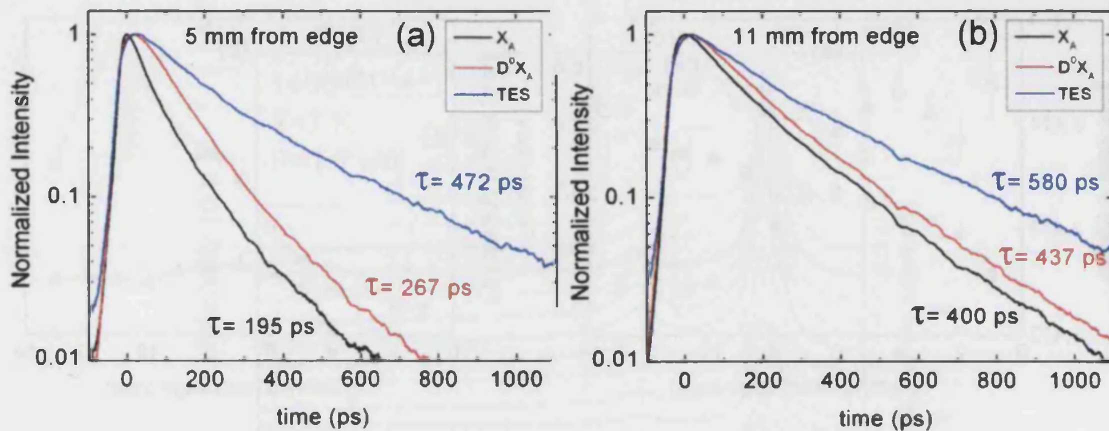

Figure 5.18: TRPL spectra for the three recombinations taken at 5 (a) and 11 mm (b) from the wafer edge. The curves have been fitted by a single exponential decay.

and X_A recombination at 11 mm from the edge (low density region) are found to be 580, 437 and 400 ps respectively. These times are larger than those found in the high density regions. Based on the studies performed by Schlager *et al.* [137] and considering that the NWr diameter is smaller in this region, we would expect the opposite behavior. However, additional considerations have to be taken into account in our sample. Actually, we expect that the influence of NWr density on the recombination dynamics would be very important. As shown before concerning SO Raman modes, a change of NWr coverage can be optically represented as a change in the effective dielectric function of the material surrounding the NWr. Ab initio calculations performed by Diarra *et al.* [151] have pointed out an increase of the donor activation energy with the dielectric contrast between the NWr and the surrounding medium. The decrease of the effective dielectric function that takes place at the low density region could then explain an increase in recombination time. The detailed study of this dependence will be performed in future studies.

Photoluminescence and Raman spectroscopy were used to investigate the optical properties of bare GaN NWrs. Raman spectra exhibit a very intense and narrow E_{2h} phonon peak at 566.3 cm^{-1}, providing evidence for the strain free nature and high crystal quality of the NWrs. Emission related to surface optical phonon modes has been resolved in the low energy side of the A_1(LO) mode. Concerning photoluminescence, very narrow and well resolved spectral excitonic structures have been observed in the PL spectra. Five characteristic PL emission peaks of GaN NWrs have been identified. A sample containing GaN NWrs with varying density, diameter and length has been studied in order to analyze the evolution of the SO modes with NWr coverage. A dielectric continuum model based on the Maxwell-Garnett approximation has been used to calculate the frequency of the SO modes. From the two modes predicted by theory, only the SO(2) mode is observed, showing a strong dependence on NWr coverage. The data suggests an enhancement of the crystalline quality of the GaN NWrs towards the low density region, due to a decrease in the number of coalesced NWrs. In this region the intensity of the PL emission increases, a feature that has been related to a better light extraction and NWr illumination.

Chapter 6

GaN/AlN heterostructures grown in GaN nanowires

In order to use NWrs as active material for optoelectronic applications, the combination of different materials and the formation of heterostructures becomes necessary as an interesting tool that allows the tuning of the material characteristics through quantum confinement. In this Chapter we present an investigation of the structural and optical properties of axial and radial GaN/AlN NWrs heterostructures. The strain characteristics of GaN axial insertions with different thicknesses grown between AlN barriers were characterized by a combination of HR-TEM, RS and PL, and the values of the strain tensor components obtained have been compared with the results of a theoretical model. On the other hand, the growth conditions and structural properties of AlN/GaN core-shell (radial) NWrs heterostructures have been studied using a combination of HR-TEM, resonant X-Ray diffraction, RS and PL. With this respect we present a study of the NWrs as a function of AlN shell thickness and as a function of NWrs density.

6.1 Nanowires based heterostructures

We discussed in Section 1.4 that the optical properties of III-nitride polar heterostructures are influenced by the presence of an internal electric field built-up along the c-axis. This statement also holds in the case of NWrs heterostructures. Two possible cases are studied in this Chapter: axial and radial heterostructures. An axial heterostructure is obtained when the normal direction of the interfaces between the different materials is parallel to the NWr growth axis. In the radial (or core/shell) configuration, the normal to the interfaces is perpendicular to the

growth direction. In the growth technique used here (PA-MBE), the growth direction corresponds always to the WZ c-axis. It has been recently shown that the PL from axial GaN insertions in AlN NWrs exhibits a marked red-shift, as indicative of the QCSE associated with the presence of an internal electric field [152]. Although the piezoelectric component tends to vanish for thick GaN insertions, due to the elastic strain relaxation resulting from the NWr free lateral surface, it is expected that the optical properties of such insertions will still be dominated by the presence of the field related to the spontaneous polarization. Consequently, the resulting oscillator strength will decrease. Along these lines, it has been also shown that for InGaN/GaN QWs in NWrs the QCSE is strongly reduced compared to two dimensional QWs emitting in the same spectral region [153]. Analysis of InGaN/GaN NWrs LEDs structures led to similar conclusions [154], the reduction of the QCSE being attributed in both cases to a reduction in the piezoelectric polarization in the NWrs [155]. GaN/AlGaN quantum discs in nanowires have also been studied. Time resolved data also showed that the optical properties of thick GaN insertions exhibited an oscillator strength reduction assigned to the presence of an internal electric field [155, 156]. The above considerations and results have naturally nurtured the interest in core/shell heterostructures, with the aim of growing non polar nitride NW heterostructures on the lateral m-planes of the NWrs. This opens the way to the growth of non polar radial heterostructures while also raising the issue of strain relaxation in GaN/AlN core/shell heterostructures through. The formation of dislocations beyond a given critical thickness has been recently addressed from a theoretical point of view [157]. The study of radial heterostructures is of special relevance, since even during growth of axial GaN insertions in AlN NWrs, it has been found that the formation of an AlN shell could not be avoided [111]. Furthermore, it has been recently demonstrated that the growth of this AlN shell was associated with the formation of misfit dislocations, due to the peculiar shape of the GaN insertions which leads to an AlN shell thickness locally larger than the critical one [44]. More generally, the issue of the critical thickness in GaN/AlN, GaN/$Al_xGa_{1-x}N$ and $In_xGa_{1-x}N$/GaN core/shell NWrs heterostructures is a crucial point from both basic and applied perspectives, in the context of realizing efficient non polar LEDs in the visible and UV range.

6.2 GaN/AlN quantum disks: axial heterostructures

It has been shown that growth of III-nitride NWrs is governed by diffusion of metallic species along the side of the NWr before incorporation on their top [158]. This leads to a very large vertical to lateral growth ratio of about 32 in the case of GaN NWrs [44]. However, due to the reduced diffusion length of Al compared to Ga and to its enhanced probability of incorporation on the NWrs sides, the formation of GaN/AlN NWrs axial heterostructures is accompanied by the growth of a thin AlN shell around the GaN insertions [153, 156]. This experimental feature raises the issue of strain relaxation in GaN/AlN core/shell heterostructures through dislocation formation beyond a given critical thickness.

6.2.1 Description of the samples

Samples were grown catalyst-free on Si(111) by radio frequency PA-MBE under an N-rich atmosphere following a similar procedure as in the previous Chapters. The select growth temperature is of 820oC. A thin two-dimensional AlN buffer layer was grown on the Si substrate prior to GaN deposition in order to improve NWr orientation [44]. The samples consisted of a base of standard GaN NWrs, between 500 and 700 nm long. After the growth of the NWrs, several tens of nanometers of AlN were deposited under N-rich conditions. Insertions of GaN were grown on top of the AlN section using the same experimental conditions as for the GaN NWrs. The thickness of the GaN insertions was proportional to the deposition time. They were covered by an upper AlN barrier of 12 nm and the operation was repeated several times. Two samples with different thicknesses of GaN insertions were studied. The one with 1 nm width quantum disks is labeled as I1(N0747) and the other, containing 2.5 nm thick insertions, is labeled I2.5(N0737). The labels in parenthesis correspond to their original names.

6.2.2 Structural analysis and Raman experiments

The samples were first analyzed by means of SEM. Figure 6.1 shows a representative example of the morphology of the GaN/AlN axial insertions grown on GaN NWrs. Several regions can be identified in the image. We can observe the GaN NWrs base sticking out from the bottom. The rest of the base is embedded in a AlN 2D layer formed during the AlN barriers growth, which is due to the low

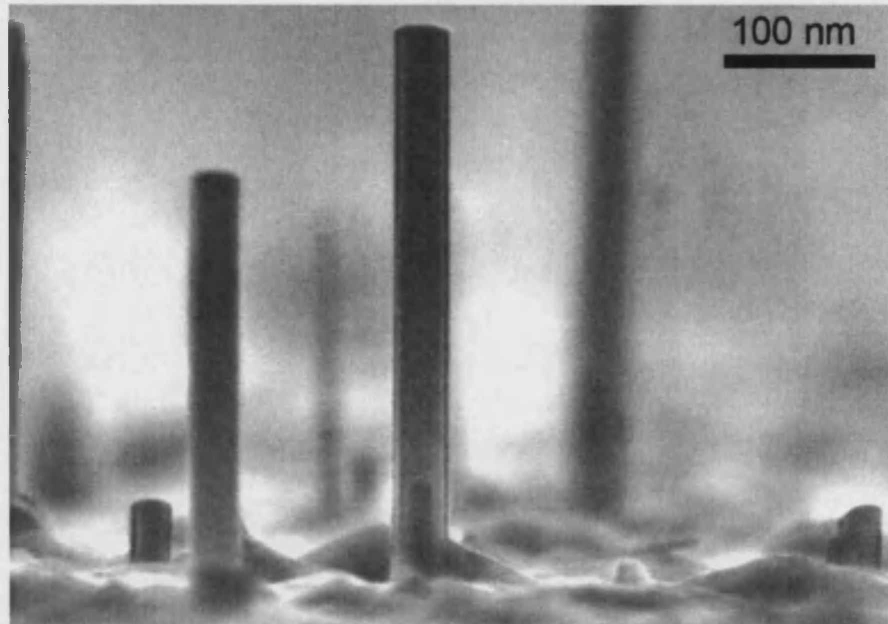

Figure 6.1: SEM images of a representative GaN/AlN axial quantum disk grown on a GaN NWrs base.

mobility of Al atoms. In the upper part of the NWrs we can appreciate the GaN insertions (dark contrast) in between the AlN barriers, with brighter contrast. Additionally, although the resolution of the SEM images is not enough to resolve the atomic planes, it is possible to appreciate a lateral GaN/AlN layer that forms on the NWrs facets. In this kind of subsequently axial insertions, it is observed a slight widening of the GaN insertion from the first to the last. This morphological effect comes from the fact of the increase of the AlN shell thickness due to the low Al diffusion length each time that the AlN barrier is grown.

The microstructure of samples I1 and I2.5 was analyzed by Dr. Catherine Bougerol at CEA, Grenoble, by using a Jeol 4000EX HRTEM operated at 400 kV. The nanowires were scrapped off the substrate and sonicated in ethanol. They were then dispersed on a Cu microscope grid covered with a carbon film. Off-axis high resolution images, i.e. tilted from the main $[11\bar{2}0]$ zone axis, of the top part of the nanowires were recorded. Images of samples with quantum disks of different thicknesses are given in Figure 6.2. The part (a) of the Figure corresponds sample I2.5. The successive GaN inclusions can be seen, appearing in dark. They are all similar, with dimensions of 30 nm in diameter and 2.5 nm in height. The insertions are separated by regular AlN barriers of 12 nm thick. The direction of the WZ c-axis is also shown. The presence of a thin AlN shell around the NWr can also be observed. A HR-TEM image from sample I1 is shown in part (b) of

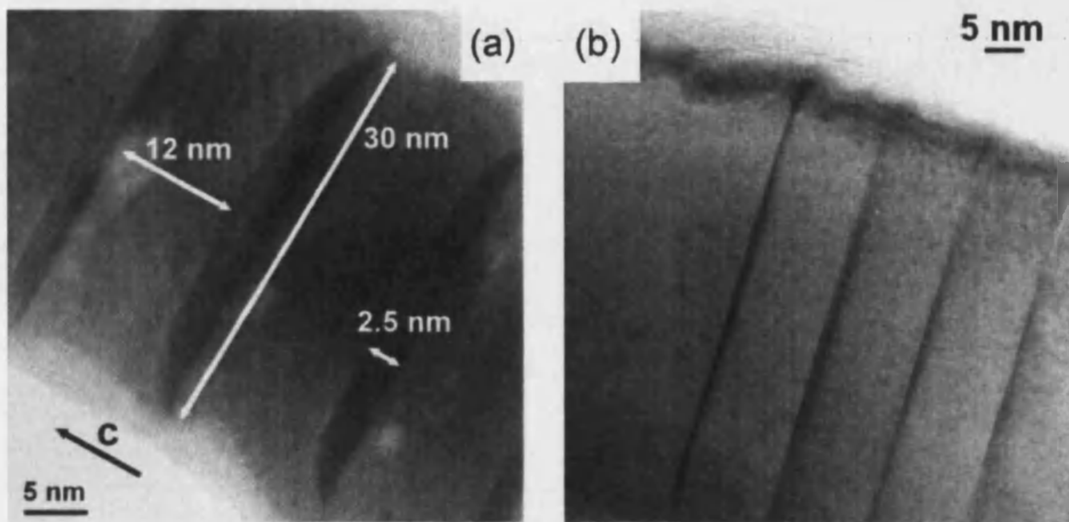

Figure 6.2: Off axis high resolution electron microscopy images of samples I2.5 (a) and I1 (b).

the Figure. This sample presents the same morphology than the previous one, but with insertions of 1 nm thick.

Raman measurements on these two samples have been performed in a backscattering configuration along the growth direction. The samples were found to be homogeneous, since the spectra displayed no significant changes when taken from different spots. Figure 7.21 shows the measurements performed on one of these spots. The relevant Raman peaks appear around 570 cm^{-1} and 650 cm^{-1} and have been attributed to the E_{2h} modes of GaN and AlN present in the NWrs, respectively. The spectrum of sample I2.5 resembles that of the reference GaN NWrs, shown with a dashed line in the bottom part of the graph, due to its large GaN content. It displays a very intense peak at 566.7 cm^{-1}, the wavelength expected for relaxed GaN, as shown in Chapter 5. As regards I1, the careful subtraction of the Si reference spectrum (dotted line) shows two weak peaks in the GaN spectral region, assigned to $E_{2h}(1)$ at 570.3 cm^{-1} and $E_{2h}(2)$ at 580.2 cm^{-1}. This part of the spectrum is shown in the inset of the graph, together with a Lorentzian fitting, shadowed in black. Both peaks are slightly blue-shifted with respect to the reference, indicating the compression of the GaN material in this sample. As for the AlN spectral region, the E_{2h} mode appears at 653.0 cm^{-1} and 648.1 cm^{-1} for samples I1 and I2.5, respectively, that is, red shifted with respect to the reference value (see Table 1.7). This indicates a small tensile strain in the material, which is larger for I2.5. The asterisks in the graph indicates signal arising from the Si substrate. We have seen in Section 1.3.2 that the deformation potential approximation relates the Raman shift relative to the relaxed value ω_0 with the strain

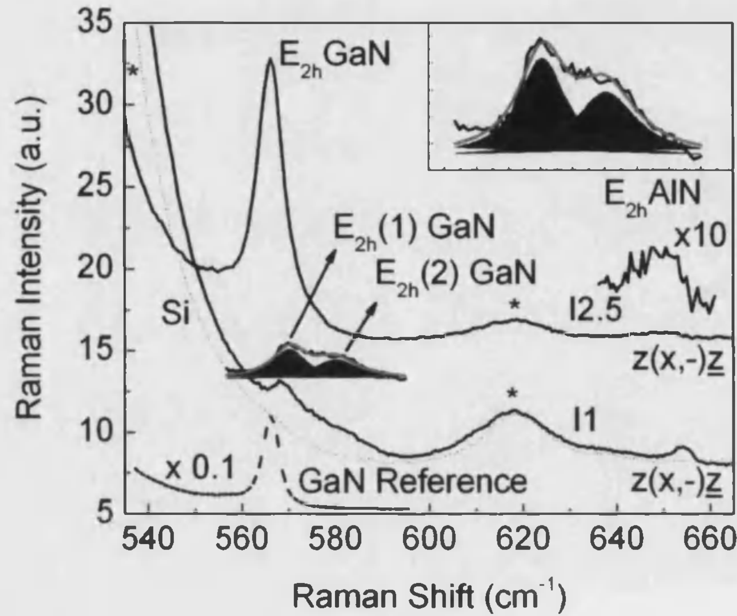

Figure 6.3: Room temperature μ-RS spectra of samples I1 and I2.5. The fitted peaks corresponding to E_{2h} mode from I1 after the substraction of the Si reference are shown in the inset. The spectral region of the AlN E_{2h} mode of sample I2.5 has been amplified for a better view. GaN NWrs and Si reference spectra are plotted with dashed and dotted lines respectively.

tensor components through the phonon deformation potentials a and b classified in Table 1.8. Together with the biaxial approximation of Eq. 1.8 this equation allows the determination of ε_{xx} and ε_{zz}, that is, the tensor components with respect to relaxed materials. The elastic constants have been taken from Table 1.5. For I1, the axial strain values ε_{zz} corresponding to peaks $E_{2h}(1)$ and $E_{2h}(2)$ are 0.12% and 0.60% respectively. This large difference suggests that peaks (1) and (2) originate from scattering by different regions of the nanowires: their GaN base would correspond to peak (1), while the GaN insertions, embedded in AlN and showing a larger axial dilatation, would correspond to peak (2). As commented before, the E_{2h} mode of GaN in I2.5 corresponds to a completely relaxed material and has been attributed to scattering from the base of the NWr. The signal from the GaN insertions, much weaker, cannot be resolved. In any case, the fact that tensile strain is larger in the AlN insertions of I2.5 (ε_{xx} = 0.56%, ε_{zz} = -0.32%), than in those of I1 (ε_{xx} = 0.30%, ε_{zz} = -0.17%) leads us to conclude that the GaN disks of I2.5 undergo a larger relaxation than in I1.

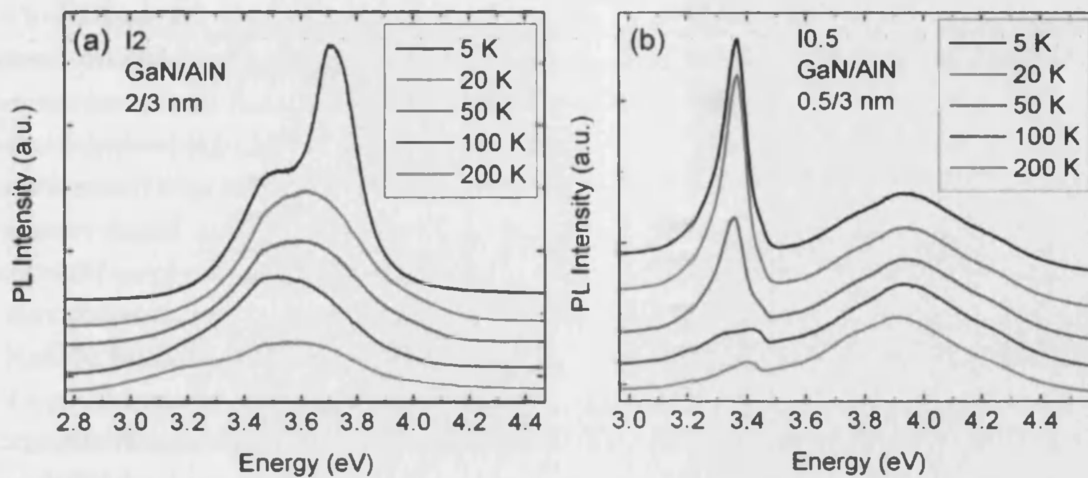

Figure 6.4: PL spectra in the range of temperature between 5 and 200 K for samples with 2 nm insertions (a) and 0.5 nm insertion thick (b). The spectra have been shifted for clarity.

6.2.3 PL emission from GaN/AlN axial insertions

In this Section, we present the optical properties of GaN/AlN axial insertions in GaN NWrs. The samples studied have been grown under similar growth conditions than those shown in the previous sample RS. The sample are labeled as I2(N1356) and I0.5(N1394). The first contains 50 periods of 2 nm thick GaN insertions while the quantum disks of I0.5 are 0.5 nm wide in 70 periods. In both samples the quantum disk are separated by 3 nm thick AlN barriers. These NWrs present the same morphology than those of samples I1 and I2.5 studied by SEM, i.e., than those shown in Fig. 6.1. Generally, in comparison with the auto-ensembled GaN/AlN QDs studied in Chapter 3, these quantum disks do not have wetting layer. Other interesting aspect to be mentioned is the strong reduction of the QCSE due to the small height of these quantum disks.

Figure 6.4 presents the PL spectra as a function of temperature from both samples, I2 and I0.5. The optical excitation and detection are made along the longitudinal direction of the wires. In contrast with what we discussed before for QDs, the intrinsic absence of wetting layer for the insertions embedded in the NWrs suggests that the excitation occurs directly in the excited states of the insertion. In addition, it is relevant to compare the dimension of these insertions with the exciton Bohr radius in GaN. This value corresponds to 2.8 nm [150], much larger than the NWrs height. The carriers will hence be strongly confined along the axial direction, while it is expected that the confinement in the radial direction will be weak. For both samples, the spectra at low temperature show two principal

features. One at higher energy compared with the other around 3.7 and 3.9 eV for I2 and I0.5 respectively. In both cases, it is attributed to the emission from the GaN insertions due to the suffered blue shift. This blue shift of the energy is caused by the confinement into the insertions. The large FWHM of this emission is consistent with the height dispersion of the disks. The insertion height fluctuation might arise from the growth competition among neighboring NWrs which results in different vertical growth rates for different NWrs. Regarding the lower energy emission, we assign it in sample I2 to that from bulk GaN at low temperature around 3.5 eV. It is supposed that this signal comes from the large amount of GaN localized at the base of the NWrs. On the contrary, sample I0.5 presents much freaky feature at lower energy. This emission is found about 3.3 eV and it can not be attributed to the same origin. We will consider first this emission is red shifted with respect to the near band edge of bulk GaN. Additionally, it has to be reminded that this sample (I0.5) contains 70 GaN/AlN periods, and in consequence a higher AlN relative content than the other sample. As a consequence of the high AlN content, its GaN base is completely embedded by an AlN 2D layer. Also the AlN thickness at the lateral facets of the NWrs increases. Indeed, we did not observe such an intense emission at energies below the GaN band gap from standard GaN NWrs, as can be seen in Fig. 7.20. In any case, the origin of this emission will be studied later in relation with the PL of core/shell GaN/AlN heterostructures.

Concerning the temperature behavior, we observe a quenching of the lower energy emission probably related with the thermalization of the complex as the temperature increases and the activation of nonradiative channels such as impurities or defects. However, in the temperature range under study between 5 and 200 K, one can see that the emission at higher energy in sample I2 also quenches while for I0.5 the intensity at higher energy remains almost constant. In sample I2 the quenching could be also attributed to the thermal dissociation of the D^0X_A due to the height of the disks. On the other hand, because of a strong confinement is present in the insertions of sample I0.5 the complexes remain active.

6.2.4 Theoretical support and discussion

The strain in GaN/AlN NWrs was computed by Dr. Yann-Michel Niquet at the CEA using a nearest neighbor valence force field based on Keating's model [159]. We considered [0001] oriented GaN NWrs with hexagonal cross section with a radius R ~15 nm and $[1\bar{1}00]$ facets. The GaN insertion was modeled as a slice of a sphere. The elastic energy of the NWrs was minimized assuming coherent growth, i.e., with no dislocation formation [160]. The atomic columns were projected into

a $(1\bar{1}00)$ plane and the deformation ε_{zz} was computed from the average column positions using a finite difference scheme. As expected, the GaN insertions grow under in-plane compressive strain due to the AlN barriers and therefore tend to be dilated along the c-axis ($\varepsilon_{zz} > 0\%$) despite the AlN shell [161]. Strain appears to be maximum at the basis of the GaN insertion. The decrease of ε_{zz} toward the upper edge of the insertion results from strain relaxation and from the increase of the AlN content in each projected atomic column. For comparison with Raman data the mean strain values in the GaN insertions have been obtained. The axial dilation is slightly larger in I1 ($\varepsilon_{zz} = 0.61\%$) than in I2.5 ($\varepsilon_{zz} = 0.59\%$) as expected from the smaller height of the insertion in I1, which limits in-plane relaxation. Similar differences between the two samples are found for the in-plane strain ($\varepsilon_{xx} = 0.03\%$ for both I1 and I2.5). These values compare very well with those obtained experimentally for I1 ($\varepsilon_{xx} = -1.1\%$, $\varepsilon_{zz} = 0.6\%$), although the Raman data show a somewhat larger relaxation. The comparison is very good taking into account that the biaxial relation only holds approximately in the columnar geometry. In the case of sample I2.5, the discrepancies between experimental results and atomistic calculations could be explained by the presence of a relaxation mechanism not taken into account in the calculations, such as the formation of dislocations.

Actually, the appearance of dislocations in nanowires has been theoretically predicted in either axial [152], or radial heterostructures [157], depending on the lattice mismatch, NWr radius and disk height (axial), or core radius and shell thickness (radial). As regards sample I2.5, HRTEM images show dislocations at the GaN/AlN interface, as illustrated in Figure 7.22. Image (a) shows three successive inclusions. From this image, one can see that the dislocations occur at the same position along the oblique side of the three inclusions, corresponding to the same AlN shell thickness, namely about 3 nm. This is in qualitative agreement with what has been predicted [157] and observed [162] for coaxial NWrs heterostructures. A single dislocation has been magnified and shown in the part (b) of the Figure. From here we determine that the dislocation is produced by the insertion of an extra (0002) plane. It has to be emphasized that the situation is different in the case of I1. More precisely, we propose that the dislocations shown in Fig. 7.22 are related to both the rounded shape of the GaN insertions and to the AlN capping process. The rounded shape of GaN insertions is a general feature observed by several groups [111, 158]. Although the reason for such a shape is not clear at this stage, it is probably related to the rounded shape of AlN itself. The AlN thickness of the AlN/GaN core/shell structure resulting from the lateral growth of AlN with capping GaN insertions continuously increases when moving from the base to the top of the GaN insertion, eventually reaching the critical thickness for AlN plastic

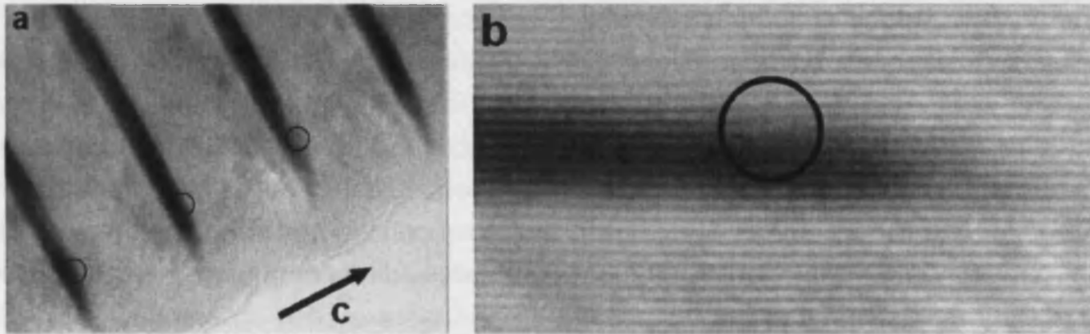

Figure 6.5: (a) Off axis HRTEM of sample I2.5 showing dislocations at the AlN/GaN interface for three successive inclusions. (b) Enlargement showing the insertion of an extra (0002) plane in AlN.

strain relaxation, which is of the order of a few nanometers [157]. This is the case experimentally observed for sample I2.5 (see Fig. 7.22(a)), whereas in the case of sample I1, the thickness of GaN insertions and the size of their rounded part are small enough (see Fig. 6.2(b)) to prevent the occurrence of AlN plastic relaxation when capping them.

6.3 Core/shell GaN/AlN NWrs heterostructures: Their properties as a function of shell thickness

In the previous Section we have observed the appearance of dislocations as a result of plastic relaxation due to the lateral growth of AlN on GaN NWrs. A critical thickness about 3 nm was found. In this Section we study the structural and optical properties of core/shell GaN/AlN NWrs varying their shell thickness. We use a combination of RS, XRD, PL and HRTEM to characterize their optical and structural properties. As before, the results are supported by theoretical calculations in the framework of an atomistic valence force field approach. It will be shown that the value of the strain and the relaxation mechanisms strongly depend on the homogeneity of the AlN shell surrounding the GaN core.

6.3.1 Description of the samples

A set of samples containing core/shell GaN/AlN NWrs with different shell thicknesses were grown by PA-MBE. The substrate used was Si(111). The growth temperature was 820 °C for all the samples. A thin AlN buffer layer was grown

prior to GaN deposition. These GaN NWrs constitute the cores of the core/shell heterostructures. Their typical length is 500 nm and the mean diameter is about 40 nm. Next, AlN was deposited. Simultaneously to the axial AlN formation, an AlN shell grow around the GaN core, due to the significant lateral growth of AlN assigned to the limited diffusion of Al on the NWrs facets [158, 163–165]. By changing the Al flux exposition time, several samples were grown varying the shell nominal thickness in the range of 0.5 to 15 nm.

6.3.2 Morphological analysis and Raman measurements

The morphological characteristics of the core/shell GaN/AlN NWrs heterostructures has been analyzed by means of scanning electron microscopy in transmission mode (STEM). NWrs were dispersed on a Cu microscope grid covered with a holey carbon film. Figure 6.6 shows STEM images of a representative GaN/AlN core/shell NWr. It can be seen that the AlN shell covers almost the whole NWr, presenting a much effective growth along the axial direction. The red arrow on the left indicates the GaN core. The lateral AlN capping constituting the shell of the GaN core is marked with red dashed lines. The AlN cap on the upper part of the NWr is labeled by a second red arrow with two arrowheads. In the images we can appreciate the different thickness of the AlN cap compared with the lateral shell. It has actually been checked that in our experimental conditions, the ratio between the axial and lateral growth rates of AlN (ν_a/ν_l) was about 15/1. The effective AlN shell thicknesses were assessed by HRTEM analysis of a significant number of as-grown NWrs (about ten in each case). It was found that for a given sample, the average shell thickness satisfactorily matches the nominal one. The shell thickness distribution around the average value was estimated to be of the order of 20% of the nominal value, taking into account the inhomogeneities of the AlN shell on a given NWrs as well as the fluctuations of the AlN shell thickness between different NWrs.

A general view of the core/shell NWrs samples in cross section is shown in Figure 6.7. The NWrs present an average length between 600 and 700 nm, as can be observed in Fig. 6.7(a). The NWrs are bend, in contrast to bare GaN NWrs used as reference, which are straight (see Fig. 2.7). This is an indication of the influence of the AlN shell on the morphology of the GaN core. The observation of about 20 NWrs by means of STEM revealed that bent GaN NWrs often exhibit an asymmetrical AlN shell. This is the particular case shown in Fig. 6.7(b). On the contrary, perfectly straight NWrs exhibit a symmetrical shell, as can be seen in the representative NWr shown in Fig. 6.7(c).

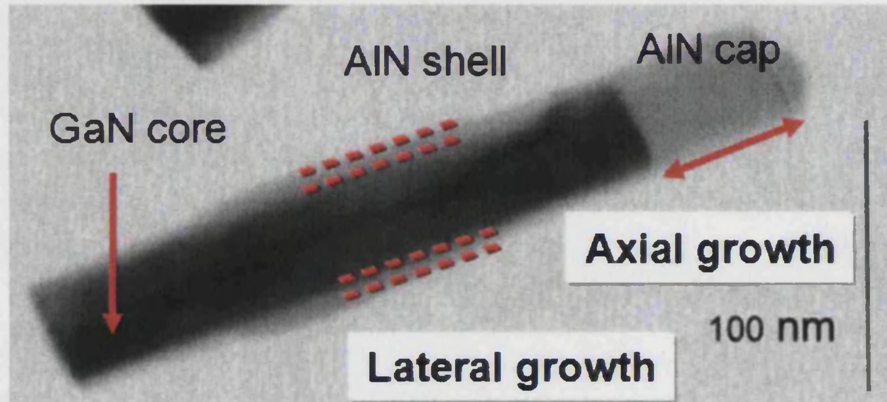

Figure 6.6: SEM images in transmission mode of a single core/shell NWr. The GaN core, the lateral AlN shell and the AlN cap on the upper part of the NWr are indicated by red signals.

μ-Raman measurements were performed at room temperature in backscattering configuration along the NWr axis. The dimensions of the laser spot focused on the samples was around 1 μm^2 and the incident power density was kept in the 10^5 W/cm^2 range to avoid heating the sample. The analysis of the Raman signal from different spots on the samples indicated that they were homogeneous. Figure 6.8 shows the evolution of the frequency of the E_{2h} mode assigned to GaN as a function of shell thickness. The frequency of this mode from a plain GaN NWr sample (566.3 cm^1) is taken as reference. It is well known that the frequency of the E_{2h} mode is only sensitive to strain, so the changes in frequency are correlated with strain changes in the core material [23]. It is observed that the frequency strongly blue shifts as the AlN thickness increases until 3 nm, as a consequence of the increasing compression of the core by the shell. However, for shell thicknesses above 3 nm, this trend changes abruptly and the frequency shift of the mode remains almost constant at 571 cm^{-1}. This fact evidences the existence of a process that relaxes the structure, related with the deposition of the AlN shell, that we will discuss later.

In the measured Raman spectra the mode $A_1(LO)$ is also observed. This mode is sensitive both to strain and the free charge density, due to the phonon-plasmon coupling, as explained in Sec. 1.3.3. Its frequency is observed between 739 and 740 cm^{-1} for the whole range of AlN shell thicknesses studied. In order to obtain the displacement in frequency related to the phonon-plasmon coupling, the strain induced Raman shift has been subtracted. Making use of the L^+ branch in Fig. 1.6 we can estimate the free electron density in the NWrs. It remains almost constant around 10^{17} cm^{-3}. comparable with the free electron density of intrinsic GaN NWrs (Section 5.3.1).

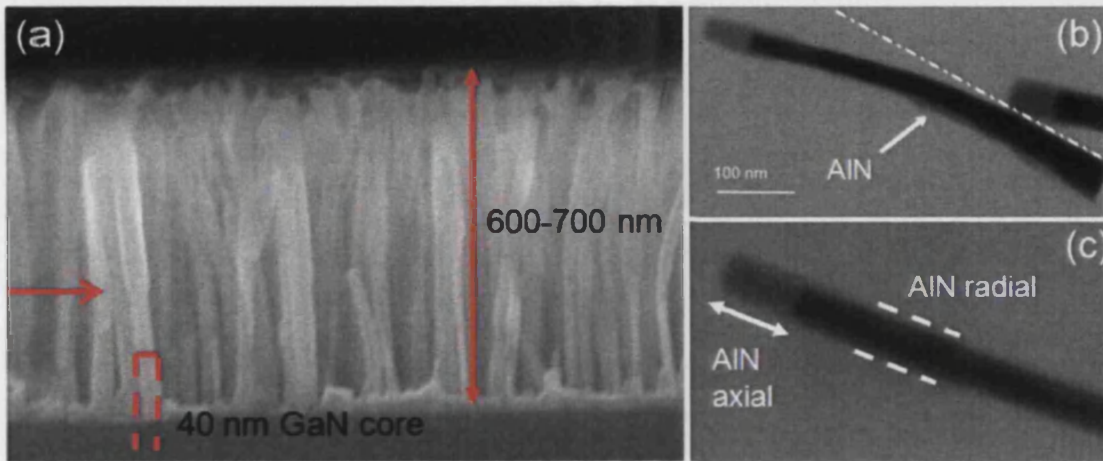

Figure 6.7: On the left (a) a SEM image in cross section of a representative GaN/AlN core/shell NWrs heterostructure. On the right, STEM images of a core/shell NWr with (b) an asymmetrical shell and (c) a symmetrical shell. A step on one side of the GaN core is clearly visible in the case of the asymmetrical shell.

6.3.3 PL emission characteristics

The core/shell GaN/AlN NWr heterostructures have been characterized by means of PL measurements in order to study their optical characteristics. The low temperature PL spectra of four core-shell samples with increasing AlN shell are shown in Figure 6.4.2, together with the spectrum of a GaN NWr sample (sample 1076), included for comparison. The peaks around 3.44 eV characteristic of bare GaN NWrs vanish after the deposition of the AlN shell, and the overall PL intensity decreases dramatically. Please, pay attention to scale in the Intensity axis, which changes for the reference sample. At the same time, increasing the AlN shell thickness produces a remarkable broadening of the emission. Additionally, the emission energy varies with shell thickness. In the case of the sample with 0.75 nm AlN shell, a broad emission around 3.2 eV appears, that it is not observed in other samples. This emission will be study in the next Section for a sample with a nominal constant shell thickness as a function of density. This emission has been observed in PL experiments on AlN, and is assigned to O inclusions or Al vacancies [166, 167].

Figure 6.10(a) shows the integrated intensity of the whole spectrum as a function of the AlN shell thickness. Considering the logarithmic scale, the quenching suffered by the emission after the deposition of AlN is very strong, and the intensity decreases with increasing AlN shell thickness. This trend will be investigated in more detail in the next Section. On the other hand, as expected from the spec-

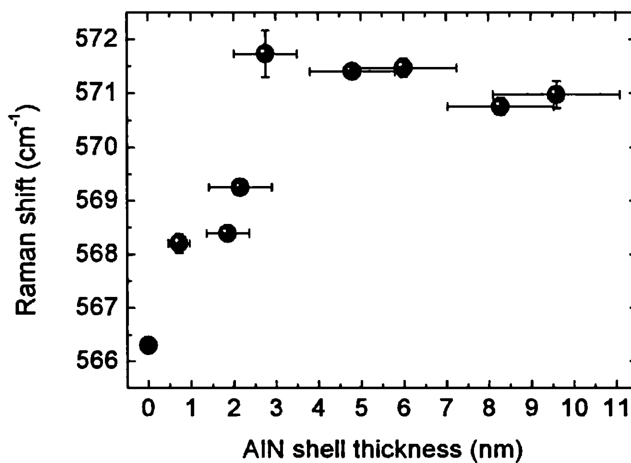

Figure 6.8: Raman shift of the E_{2h} mode of GaN as a function of the AlN shell thickness.

tra shown in Fig. 6.4.2, the FWHM corresponding to D^0X_A increases as the AlN shell thickness increases. This behavior is shown in Fig. 6.10(b). A rapid increase of the broadening, from few meV to 100 meV, is observed during the deposition of the first 4 nm AlN. Beyond this AlN thickness, the FWHM remains almost constant. This behavior suggests that the formation of defects takes place during the deposition of the first few nanometers of AlN.

The PL emission has been also investigated as a function of temperature in the range from 10 K to room temperature. The integrated intensity of the whole spectra has been represented as a function of temperature in an Arrhenius plot. The evolution of the intensity is well reproduced by using the thermal activation equation, 3.3, taking into account two activation processes. The activation energies (E_a) related to each process are plotted in Fig. 6.11 as a function of AlN shell thickness. In Reference [168], the Authors explore the electrical properties of GaN NWrs in the context of dielectric confinement, as manifested through changes in the impurity activation energy. Two dielectric configurations are considered: bare NWrs in the air and a similar device fully embedded in SiO2. Their study suggests two distinct conduction channels in GaN nanowires. One conduction channel is associated to a large activation energy related to processes on the NWr surface. The other conduction channel shows relatively smaller activation energies and almost no variation with the NWr radius. This last one is attributed by processes

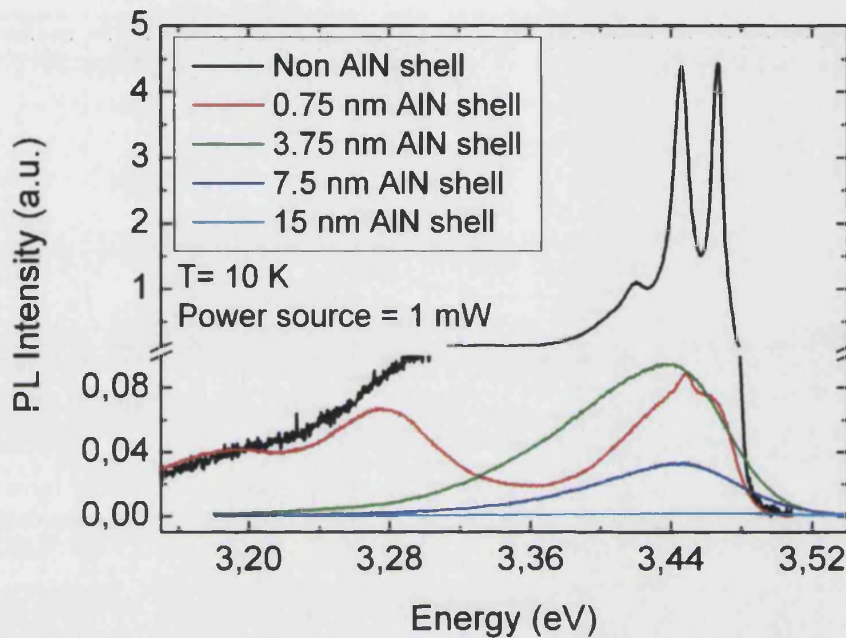

Figure 6.9: Low temperature PL spectra from four core/shell GaN/AlN GaN NWrs heterostructures. The shell thickness ranges from 0.75 to 15 nm. The low temperature PL emission from bare GaN NWrs is also added for comparison.

into the NWrs. In our GaN/AlN NWrs it is found also two activation energies in the order of those found in the study. Figure 6.11 shows both, E_a1 and E_a2, activation energies as a function of shell width. E_a1 denotes the highest activation energy, around 40 meV, and is plotted with black spheres. E_a2 corresponds to the lowest activation energy, in the range of 5 meV, tagged with empty circles. Regarding E_a1, it decreases from 60 to 20 meV until 4 nm AlN capping. After that, it increases from 20 to 40 meV and remains almost constant for the rest of the series. The lower activation energy, E_a2, remains almost at the same value and seems to be independent of the AlN shell thickness. Considering the evolution of the activation energies with shell thickness, it is reasonable to ascribe E_a1 to optical processes that take place at the interface and seems to be influenced by the AlN shell. On the contrary, E_a2 suggests to be related with processes into the GaN core, since its energy value seems to be independent of the shell.

6.3.4 Theoretical modeling and discussion

With the purpose of understanding the evolution of strain with shell thickness, we have made use of an atomistic valence force field model adapted for WZ materials.

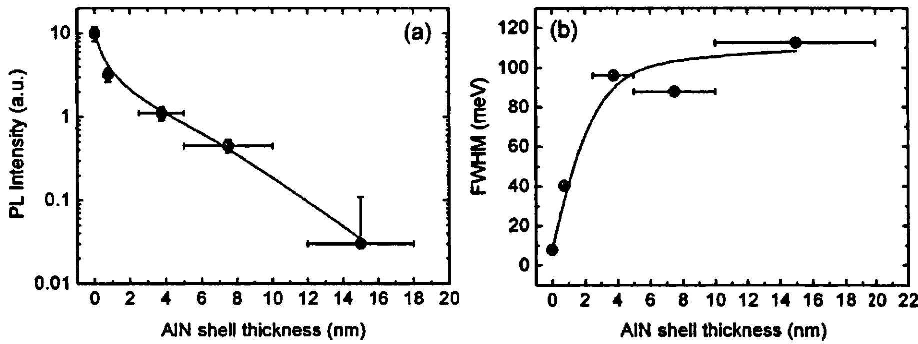

Figure 6.10: Representative low temperature measurements of the integrated intensity of the whole spectrum (a) and FWHM (b) of the emission as a function of AlN shell thickness. The lines are guides for the eyes.

The calculation has been performed in the research group of Grenoble by Camacho *et al.* [169]. The model is similar to that described before for axial heterostructures. Based on Raman Scattering results we apply the approximation of $\varepsilon_{xx} = \varepsilon_{yy} = 0$, due to the small values of in-plane strain values compared with ε_{zz}. As expected from experimental results, the calculation suggests that the axial strain ε_{zz} is very homogeneous in both the core and shell, and takes on much larger values (10 times larger) than the in-plane strain ε_{xx}. The result from the simulation for a core radius of 10 nm is plotted in Figure 6.12 as a function of shell thickness, together with the strain components calculated from our RS measurements and X-ray analysis performed at the European Synchrotron Research Facility (ESRF), Grenoble, by Prof. Hubert Renevier. Dots show the values of strain obtained by RS and triangles that from X-ray diffraction. The empty symbols refer to the in-plan strain components and the full symbols to ε_{zz}. It is found that the GaN core is compressed by the AlN shell until ε_{zz} reaches a value around -0.6%, at a shell thickness of ~3 nm. Both RS and X-ray results are in satisfactory agreement. This rapid increase in the GaN strain is also in qualitative agreement with theoretical calculations. However, while theoretical results show a continuous increase of strain for shells thicker than 3 nm, the experimental values remain almost constant, suggesting a change in the relaxation process of the GaN core for thick AlN shells.

With the purpose of clarifying the disagreement between experiment and theory, my colleague Karine Hestroffer (CEA, Grenoble) has studied by means of HRTEM several NWrs having an asymmetrical shell. Limiting the analysis to NWrs with a core diameter of 20 nm, which corresponds to the mean diameter of

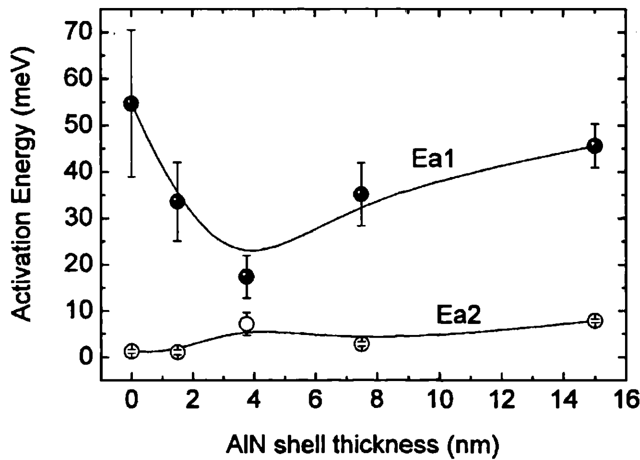

Figure 6.11: Activation energies extracted taking into account the intensity of the whole spectrum. Two processes have been considered for the fit. The lines are guides for the eyes.

the NWrs of the sample, we obtain a value of ε_{zz} very close to those obtained by RS and X-ray diffraction ($\sim -0.9\%$. This value is represented by a star in Figure 6.12. On the other hand, straight NWrs with a symmetrical AlN shell, like the one illustrated in Figure 6.7 (c), have been as well analyzed by the GPA technique. In this case both the core and the shell present the same c lattice parameter. The corresponding value for ε_{zz} is plotted in the Figure with blue squares, and follows very closely the theoretical results. This analysis leads us to the conclusion that the discrepancies between the data reported in Fig. 6.12 by the different techniques might be related to the fact that RS and X-ray diffraction are techniques that analyze the properties of the NWrs ensemble, and most of the NWrs are characterized by an asymmetric shell. On the other hand, HRTEM results correspond usually to NWrs with a symmetrical shell, being therefore close to ideal NWrs similar to the ones considered for the calculations, but not necessarily representative of the majority of the NWrs. Actually, dislocations were observed on HRTEM images of NWrs with an asymmetrical shell, and located at the GaN/AlN interface on the thin shell side. The dislocation consists of the introduction of an extra (0002) plane in the shell, as can be observed in Figure 6.13.

The above results have established that the asymmetry in the AlN shell plays a determining role in the structural properties of the core/shell NWrs. When the shell grows homogeneously, the system responds elastically, which results in a large out-of-plane strain within the GaN core. This strain increases as a function of the

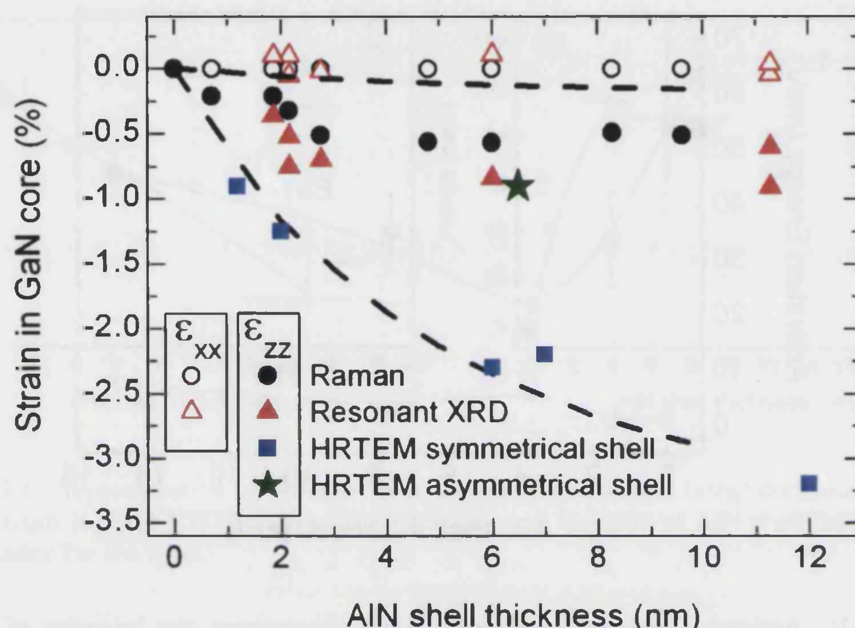

Figure 6.12: In-plane (empty symbols) and axial (full symbols) strain within the GaN core. The circles and triangles are respectively related to Raman and resonant XRD data. Note that the empty circles depict the approximation $\varepsilon_{xx} \sim 0\%$. The squares were obtained from HRTEM data for wires with a symmetrical shell, the star for a wire with an asymmetrical shell. The dashed lines correspond to the calculations performed for a core radius of 10 nm. Uncertainties in the AlN shell thickness of the order of 20% of the nominal values are not displayed in the form of error bars for clarity.

shell thickness without plastic relaxation and in the absence of significant in-plane strain. Actually, the extrapolation of the results of [157] for a 10 nm radius GaN core and an AlN shell actually suggests that plastic relaxation would occur even for a shell as thin as 1 nm through the introduction of line dislocations. This is not what we observe experimentally. Actually, our results indicate that, as soon as the AlN shell becomes asymmetrical, a strain gradient appears in the shell, eventually inducing the bending of the GaN core until the formation of edge dislocations (extra c-plane) in the AlN shell, as evidenced by HRTEM. This hypothesis raises the question of the origin of the AlN shell inhomogeneity. Asymmetry in the lateral growth of AlN on GaN has been previously observed by Tchernycheva *et al.* [170] and attributed to the NWrs environment, i.e., to the proximity of neighboring NWrs as well as to the angle between the NWrs and the substrate. Alternatively, the AlN asymmetry could originate from pure geometrical effects due to the angle of about 20°C between the axis of the Al cell and the normal to the substrate [171]. The Al atoms actually have a short diffusion length and would therefore preferentially reach one side of the wire and be incorporated there

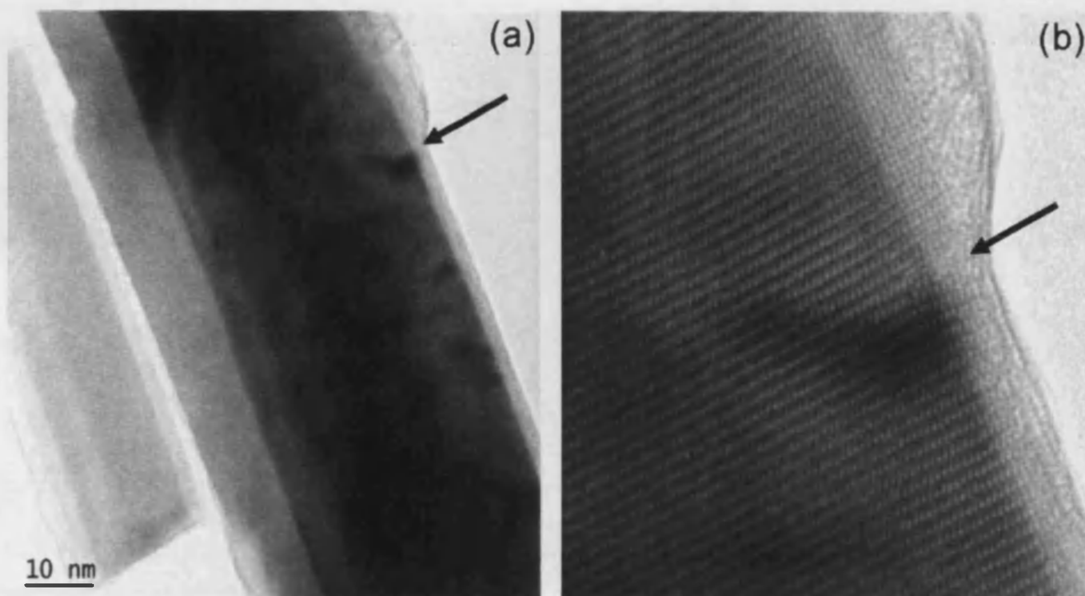

Figure 6.13: (a) HRTEM image of a wire with an asymmetrical shell. (b) Magnification of the edge dislocation (extra c-plane) found on the thinner shell side.

without diffusing to the opposite facet. The substrate was however rotating with a speed of about 5 revolutions per minute during NWrs growth, which discards simple geometrical effects as the origin for the large asymmetry that is often observed. More likely, the inhomogeneity of the AlN shell could be assigned to the presence of steps at the base of the GaN NWrs, as seen in Figure 6.7 (b). The presence of such steps has also been previously reported by Park *et al.* [172]. It is well known that steps are preferential incorporation sites. In accordance with this idea, SEM in transmission mode and HRTEM analysis of a statistically significant number of NWrs have revealed that inhomogeneous thickening of the AlN shell is most often associated with such a step at the base of the GaN NWrs. As a consequence of the asymmetrical growth of the AlN shell, shear strain is expected to build up in the GaN core. Such strain would result in the bending of the NWrs and would eventually lead to the plastic relaxation of the AlN shell, consistent with the observation of dislocations. In such a framework, the change of regime around a shell thickness of about 3 nm put in evidence by both XRD and RS experiments may be interpreted as the amount of AlN above which shear-strained GaN/AlN heterostructures can easily relax by the formation of dislocations in AlN. By contrast, for a homogeneous AlN shell, no plastic relaxation is observed up to a shell thickness of at least 12 nm, which was the upper value explored in the present study.

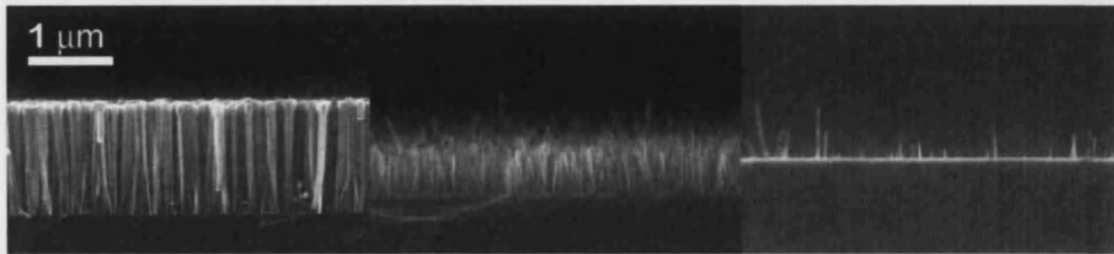

Figure 6.14: SEM images in cross section of core/shell GaN/AlN NWrs heterostructures corresponding to sample N1443. From left to right the images are acquired from the edge to the center of the wafer.

6.4 Core/shell GaN/AlN NWrs heterostructures as a function of density

Taking profit of the strong variation of GaN NWrs density when grown directly on Si(111) (see Sec. 5.3), we present in this Section a study of the properties of core/shell GaN/AlN NWrs heterostructures as a function of density. To analyze the structural properties, the sample has been studied by means of SEM, TEM and RS. The results are completed with the optical analysis by means of PL spectroscopy.

The sample consists in GaN NWrs grown directly on Si(111) under the same growth and time conditions than those used in Section 4.2.3. For the growth of the shell, we calibrate the aperture time of the Al cell in order to obtain a nominal shell of 5.5 nm thickness. During the growth, the substrate was kept in rotation in order to enhance the homogeneity of the shell. SEM pictures in cross section at different positions along the radius of the wafer, shown in Figure 6.14, allow to appreciate the morphology of the NWrs. The Figure shows three representative SEM images taken from the edge to the center of the sample ordered from left to right. We can confirm that as well as the density, the length and diameter follow the same trend of the NWrs studied in Chapter 4. Related with the shell, in the high density region, the shadow effect seems to be relevant. As a consequence, NWrs present a thicker shell in their upper part. Towards the center of the wafer, the NWrs density decreases and the shell becomes more uniform along the whole NWr. Additionally, the low NWr density allows the Al atoms to reach the substrate. Due to the low diffusion length of Al atoms, it gives place to a 2D AlN layer. This sample has been labeled as N1443.

6.4.1 Raman scattering analysis

μ-RS spectra in backscattering configuration have been obtained at room temperature on sample N1443 along the NWr axis. A sequence of spectra were obtained placing the laser spot at different positions along the wafer radius from the edge towards the center in millimeter steps. The results are plotted in Figure 6.15. The spectra have been normalized to the acquisition time and shifted for clarity. In the low energy range, the E_{2h} mode of the GaN core is observed around 566 cm^{-1}. The E_{2h} mode associated to the AlN shell can also be seen in the Raman spectra. This mode does not evolve significantly as a function of position, with a frequency close to its relaxed value of 655.5 cm^{-1}. However, the FWHM of the peak decreases from 10 to 4 cm^{-1} as the density decreases, indicating a considerable improvement of the crystalline quality of the AlN deposited. Regarding the polar mode $A_1(LO)$, its frequency is blue shifted with respect to its relaxed frequency at 738 cm^{-1}. As indicated before, both strain and phonon-plasmon coupling can influence this value. Additionally, in the spectra we observed a small deep at 743 cm^{-1}. This is typical of the so called Fano resonance that indicates a coupling of discrete modes with a continuum of states. Fano interference in Raman scattering has been extensively studied in highly doped bulk Si samples by Belitsky *et al.* [173] and Arya *et al.* [174]. It results in an asymmetric line shape of the first order phonon Raman peak, following the relation [175]:

$$I(\omega) \propto \frac{(q+\epsilon)^2}{1+\epsilon^2}, \text{ with } \epsilon = \frac{\omega - \omega_0}{\Gamma}. \tag{6.1}$$

Here ω is the scattered photon energy, ω_0 and Γ are respectively the resonance frequency and the width of the peak. The influence of Fano scattering on the Raman spectra is determined by the parameter q, the asymmetry parameter. In the case of bulk Si [175], it has been found that $1/q$ is proportional to the free carrier concentration. The curve becomes Lorenzian for $q \to \infty$ and the asymmetry increases as the value gets smaller. In Fig. 6.15 the asymmetry becomes very clear at the high frequency side of the $A_1(LO)$ mode. We have not attempted here to develop a model for the observed Fano resonance, which will be the scope of farther studies.

We center now our attention on the phonon mode E_{2h} of the GaN core. We represent in Figure 6.16(a) its Raman shift, as a function of position along the radius of the wafer (decreasing NWr density). We have included in the plot the Raman shift of the same mode obtained from sample N1405. This sample is used as reference, since it has been grown under the same conditions but with no AlN

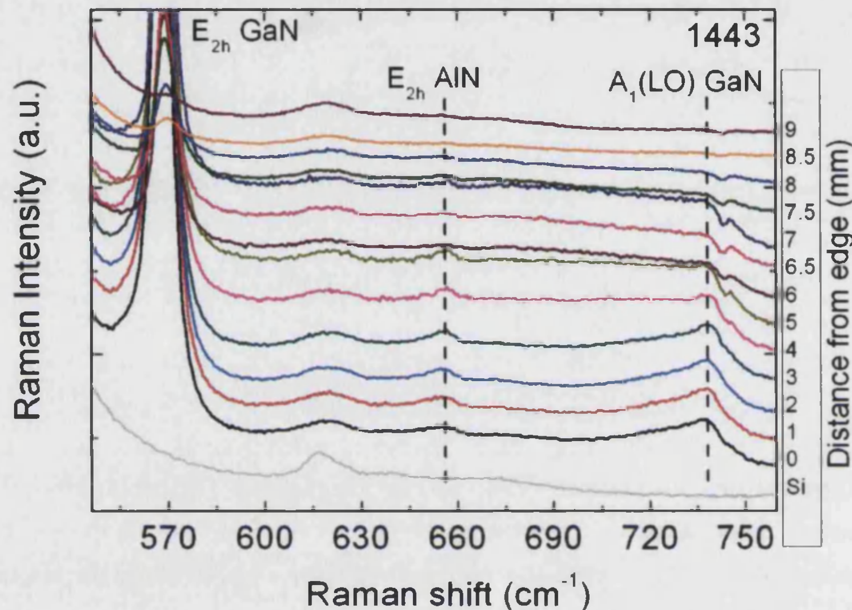

Figure 6.15: Raman spectra taken in steps of 1 mm from the edge to the center of the wafer. A Si spectrum is plotted at the bottom for comparison. The dashed lines are a guide for the eyes to follow the behavior of the modes E_{2h} of the AlN shell and the $A_1(LO)$ mode corresponding to the GaN core.

shell. The frequency of the mode from the reference sample (N1405) remains constant around 566 cm^{-1} for all the positions, the value corresponding to relaxed GaN. On the contrary, as we move the spot of the laser towards the wafer center the E_{2h} frequency from sample N1443 blue shifts about 3 cm^{-1}. We attribute this behavior to the compressive strain along the NWrs axis that the GaN core suffers under the increasingly homogeneous AlN shell. At the right part of the Figure we represent the evolution of the intensity of the GaN E_{2h} mode, together to its FWHM. According with the density trend along the radius of the wafer shown in Fig. for bare GaN NWrs, the intensity remains constant along the fist 3 mm from the edge. Beyond this point the intensity decreases as the NWrs density decreases. The FWHM remains almost constant around 7 cm^{-1} indicating the good crystalline quality of the GaN core along the whole substrate.

The strain component along the WZ c-axis has been estimated through the PDP relation by applying the approximation $\varepsilon_{xx} = \varepsilon_{yy} = 0$. The strain component ε_{zz} is represented in Figure 6.17 as a function of position along the wafer radius. It can be seen that until we reach a position at 6 mm from the edge the component of strain ε_{zz} remains almost constant, close to its relaxed value. This fact can be

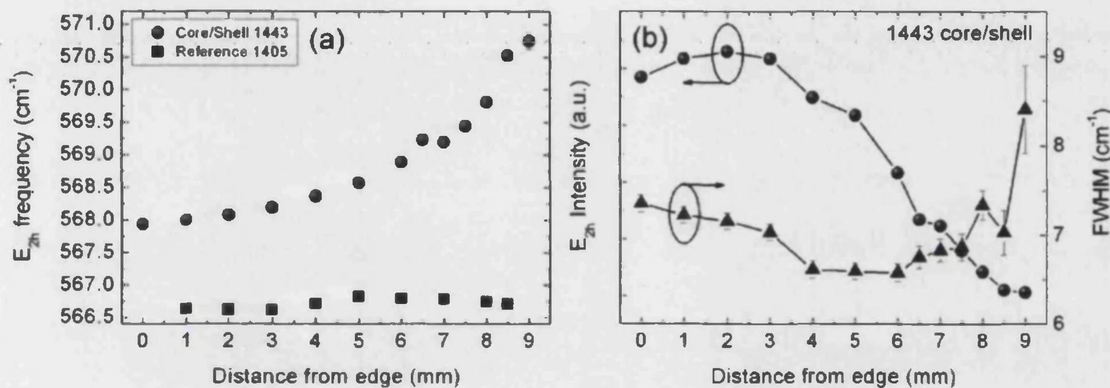

Figure 6.16: (a) Comparison between the frequency of the E_{2h} mode of GaN from the reference sample N1405 (squares) and the core/shell heterostructures NWrs sample N1443 (spheres) as a function of position along the Si(111) wafer. (b) Integrated intensity of the E_{2h} mode together with the evolution of its FWHM.

correlated with the inhomogeneous shell and the appearance of plastic relaxation processes, as it has been determined in the previous Section. Closer to the wafer center the value of strain increases, reaching -0.5% at 9 mm from the edge. This region is highlighted shadow in the Figure. 6.17. This increase in the compressive strain along the NWrs axis might be attributed to the homogeneous shell growth, as it has been determine in the previous epigraph by HRTEM analysis. By taking into account these considerations, we suggest that a reduction of plastic relaxation in the AlN shell takes place as the NWr density decreases. In this sense, a reduction of shadow effects can be determinant to obtain homogeneous AlN shells. In order to find more indications that support this hypothesis, we perform a PL and HRTEM analysis for different positions along the wafer radius. The results are discussed in the following Section.

6.4.2 PL characterization

Low temperature PL spectra have been taken in configuration $k \parallel c$ from different spots along the wafer radius. Figure 6.18 presents representative spectra of the evolution of the PL emission with position from the edge, indicated in millimeters in the labels. The spectra taken at 1 mm from the edge is dominated by a strong emission at low energy around 3.25 eV labeled as Peak1 in the Figure. Additionally, we can observe a broad and intense emission in the range of energy between 3.27 y 3.34 eV. The GaN band edge emission can be weakly detected at 3.47 eV. The emission assigned to the TES transition, around 3.45 eV is not detected in the spectra. Additionally, two narrow peaks can be distinguished: one at 3.44 eV

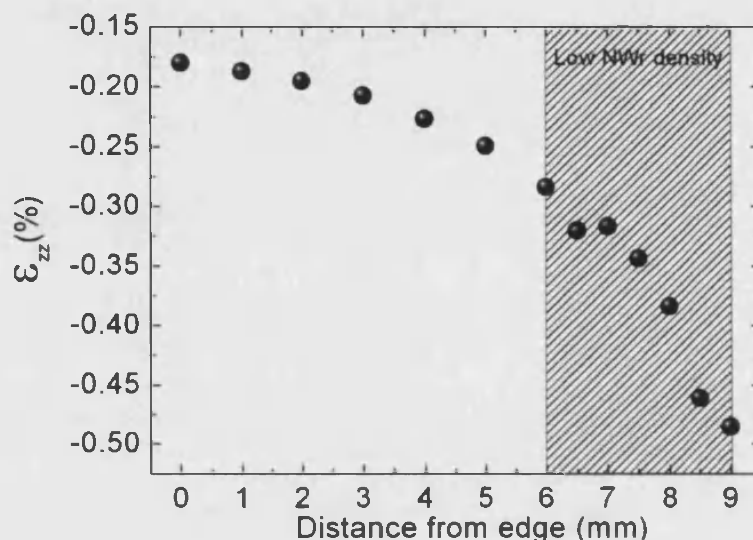

Figure 6.17: Evolution of the strain component ε_{zz} of the GaN core as a function of position along the radius of the wafer.

and the other at 3.53 eV. They are assigned to resonant Raman scattering from LO modes. Due to the limited resolution of the setup (3 meV), it is not clear if the signal corresponds to the $A_1(LO)$ or $E_1(LO)$ modes, with energies of 91 and 92 meV respectively. However, the observed energy agrees better with that of the $E_1(LO)$ mode. Although the mode $E_1(LO)$ should be forbidden in the configuration $z(-,-)\overline{z}$, this emission can be explained by multiple reflections and the better extraction of light through the NWrs facets. Following the sequence of spectra towards the center of the wafer, a strong change in the emission characteristics can be observed. The spectrum taken in the high density region (wafer edge) is dominated by emission at low energy, and that corresponding to the GaN band edge emission, near to 3.47 eV, is almost vanished. As the spot moves towards the low NWr density area, the low energy PL emission quenches, while the intensity from the band edge emission increases considerably. Actually, a sudden change takes place in the region between 4 and 5 mm. At this point the low energy emission disappears almost completely while the intensity of the band edge emission strongly increases, despite the decrease in NWr density. As shown before, SEM micrographs indicate the absence of coalesced NWrs beyond this point. We have already demonstrated in the previous Section the presence of dislocation in core/shell GaN/AlN NWrs with inhomogeneous shells. Due to shadow effects, we expect to have a predominance of inhomogeneous shell coverage in the high density

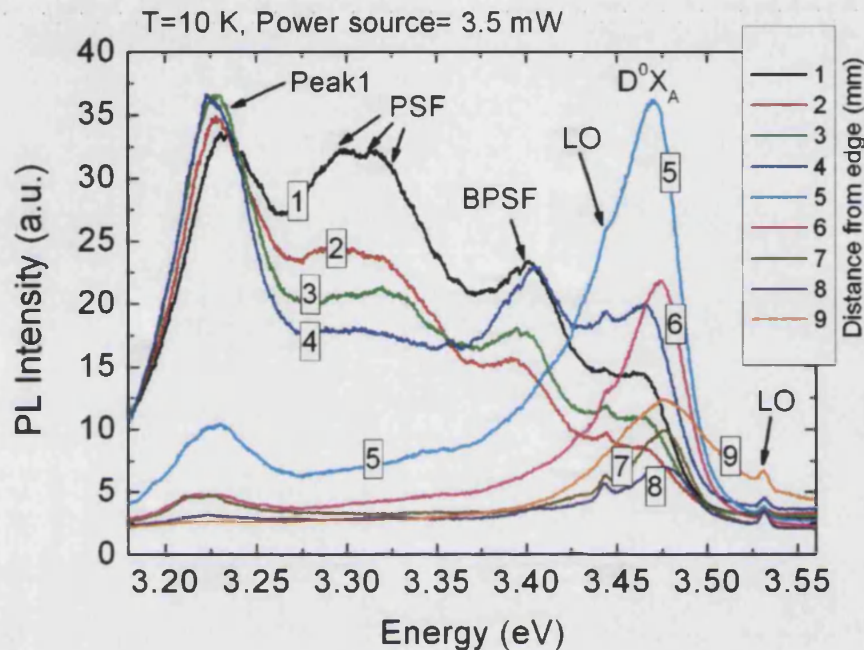

Figure 6.18: Characteristic low temperature PL spectra obtained along the radius of the wafer with steps of 1 mm. The spectra are labeled with a number corresponding to the distance in mm from the edge.

part of the sample (1 to 5 mm). Beyond this point, however, shadow effects are minimized due to the low NWr density. This behaviour is in agreement with the increasing compression of the GaN core observed by Raman scattering, and the decrease in FWHM of the mode related to AlN. We expect as well that homogeneous shells will have a better crystalline quality. Hence, the emission at 3.20 eV can be tentatively attributed defects in the AlN shell, such as dislocations induced by a plastic relaxation processes. Actually, the emission from bulk AlN presents a broad feature at this energy [166, 167]. The Authors relate this emission with inclusions of Oxygen atoms and/or vacancies of Aluminium. These kind of defects can trap the carriers and act as recombination centers. This emission has been also observed in the core/shell series studied in the previous Section (see the sample with 0.75 AlN shell thickness in Fig.), supporting the hypothesis of the quenching from the GaN band edge emission due to the formation of dislocation at the AlN shell when the shell is inhomogeneous.

We center now our attention on the emission from the GaN band edge. Due to its large broadening, it has not been possible to fit the spectra with Gaussian functions. Instead, to follow the evolution of the emission with position we have

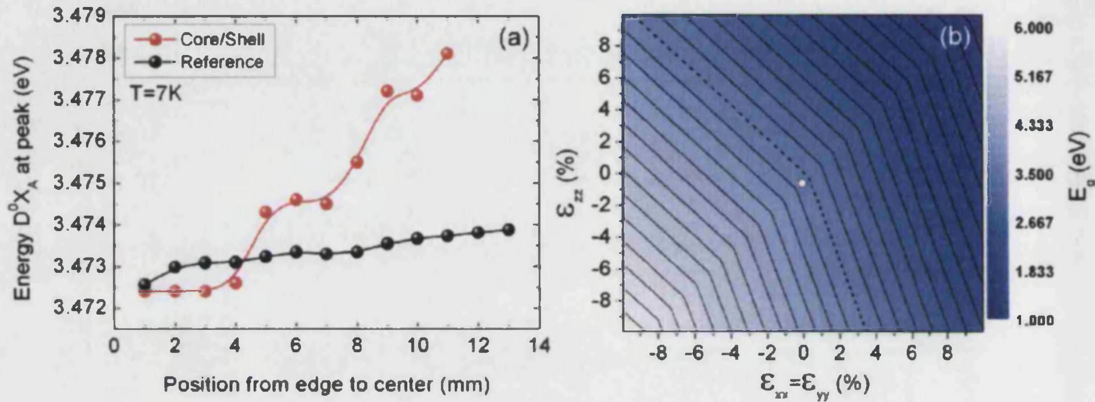

Figure 6.19: (a) Energy of the D_0X_A emission peak from the reference sample N1405 and that of core/shell NWrs (N1443) as a function of position. (b) Calculation of the first electronic transition as a function of strain.

determined the peak energy and intensity of the D_0X_A transition. The energy is plotted in Figure 6.19 (a) with red spheres, together with that from the reference sample (N1405), as a function of the distance from the edge of the wafer. The energy of the D_0X_A peak remains almost constant for the reference sample. However, in the case of the core/shell sample it blue-shifts 4 meV in a distance of 12 mm. This shift is ascribed to the influence of the strain, induced by the AlN shell, on the electronic transitions of the GaN core. In order to prove if this assumption is reasonable, my colleague Dr. Jorge Budagosky [16] performed a set of calculations to establish the influence of strain on the electronic bands of bulk GaN. This simulation is performed in the framework of the $\mathbf{k} \cdot \mathbf{p}$ theory, using an 8×8 Hamiltonian, as was done in Sec 1.2. Given the symmetry of the NWr, the in-plane strain was considered to be isotropic in the calculations ($\varepsilon_{xx} = \varepsilon_{yy}$). The energy of the first electronic transition across the band gap has been plotted in a color map is shown in 6.19 (b). Although the calculation does not take into account the binding energy of the complex D_0X_A, the evolution of the recombination energy of this excitonic complex with strain is expected to be similar to that of the first electronic transition. In the figure, the energy scale is represented by grades of blue. The white point represents the maximum value of strain reached by the core/shell NWrs, as determined by Raman scattering: $\varepsilon_{zz} = -0.5\%$ and $\varepsilon_{xx} = \varepsilon_{yy} = 0\%$, which corresponds to the low-density region (11 mm from the edge). The band energy corresponding to these strain values is that of 3.56 eV, far above the one observed experimentally. The energy difference can be explained because of the absence of dislocations not taken into account in the theoretical model.

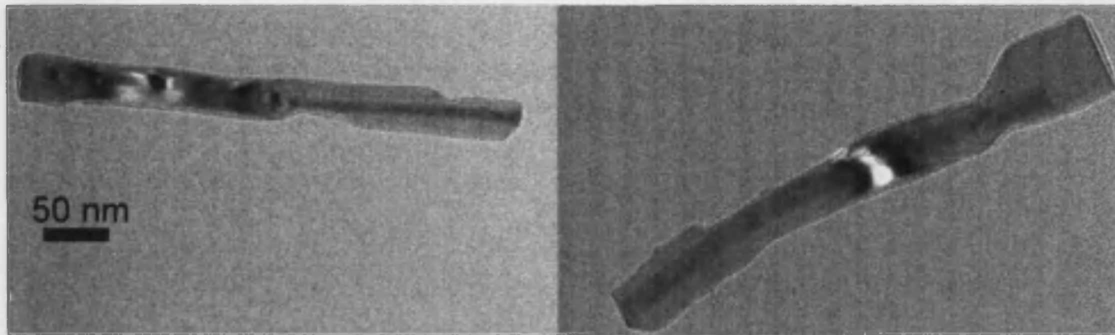

Figure 6.20: TEM images of GaN/AlN core/shell NWrs from the high density region.

6.4.3 HRTEM analysis and discussion

HRTEM measurements on this sample were performed by my colleague Dr. Said Agouram, from the University of Valencia. As we have determined from SEM images, NWrs in this sample, N1443, present a variable morphology along the wafer radius. In order to analyze these differences in more detail, we extracted NWrs from two regions of the sample for HRTEM analysis: the high density region, that is, between the edge and 5 mm towards the wafer center, and the low density region, (from 5 mm onwards). NWrs from both regions were mechanically dispersed on a Cu grid with a C film. In the high density region, we found NWrs with an core diameters in the range between 10-90 nm, and lengths of the order of 900-1000 nm. Representative NWrs are shown in Figure 6.20. An important characteristic reveled by HRTEM images is that the NWr is covered by the AlN shell from top to bottom, although its thickness is highly inhomogeneous due to shadow effects. The images show the larger axial to radial growth velocity ratio, with the formation of an AlN cap at the top. Large variations of the height of the upper AlN cap in the range 30-100 nm are observed. If we consider an axial/radial growth velocity of 15/1, we obtain a mean AlN shell thickness that ranges roughly from 4 to 7 nm, with a deviation of 1.5 nm around the nominal shell thickness of 5.5 nm. This shell is, however, very inhomogeneous. The thickest side is about 15 nm and the thinnest side in the order of 3 nm.

Several dislocations were found in the NWrs representative of this high density region. As a representative example, we present in Figure 6.21 several dislocation found in the zone shadowed with a red square. For the treatment of the images, they were processed by applying the Fourier transform to select only the interesting frequencies related with the oriented planes. The images of the processed zones are shown as insets in the images at the corresponding place where the dislocations are. It is easy to observe the absence of one plane forming a dislocation in the

AlN shell. The points where the dislocations were found are indicated by numbers. Surprisingly, several dislocations were found in places close to the bottom part of the NWrs where the AlN coverage remains constant.

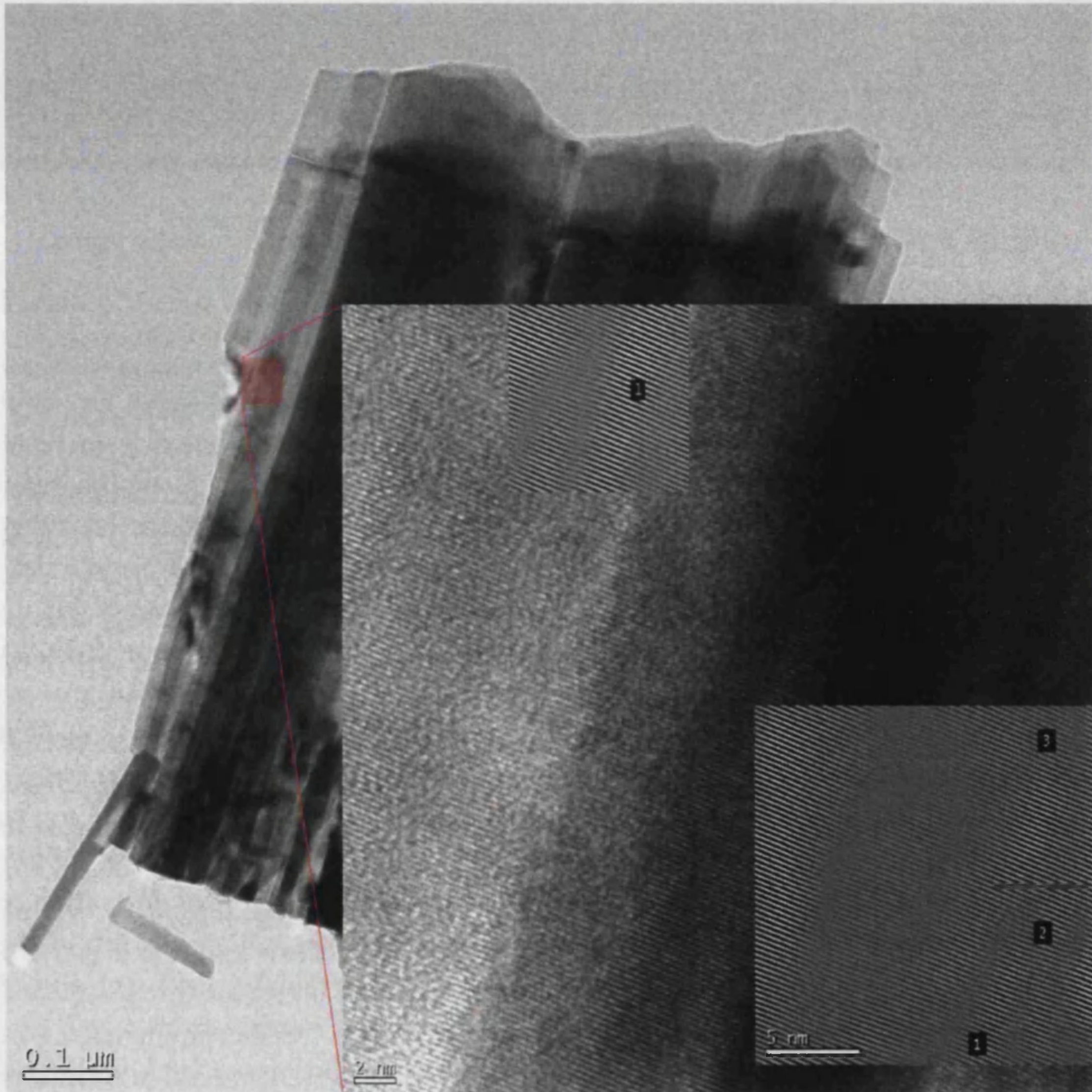

Figure 6.21: TEM images of core/shell GaN/AlN NWrs from the high density region. The red square marks the region where dislocations were found.

The NWrs from the low density region present a clearly different morphology. As determined by SEM, they have smaller mean diameter and they are shorter compared with those from the high density zone, as can be appreciated in Figure 6.22. The average core diameter is in the range of 10-20 nm and the average core length is observed in the range of 200-400 nm. The height of the AlN cap ranges

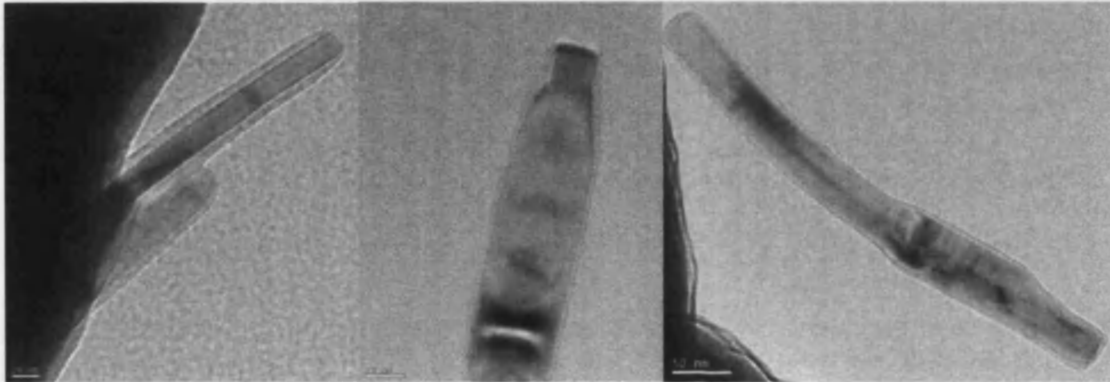

Figure 6.22: TEM images of NWrs from the low density region.

in this case from 60 to 100 nm, giving similar values as in the high density region. This is expected considering a constant Al flux for the whole wafer. The main difference with respect to the wires found in the high density region is that when the density is low many of the NWrs are covered by an homogeneous shell, in the order of 7 nm thickness. However, some of the NWrs found present well an inhomogeneous shell, with its thickest side of the order of 20 nm and the thinnest in the order of 3 nm. This effect might be attributed to the fact that many NWrs in this low density region are tilted with respect to the substrate normal direction. Similarly as in the high density zone, we searched for dislocations in the AlN shell. After the investigation of more than 10 NWrs, we found only one dislocation, located, as expected from previous studies, in a place where the AlN shell presents a big step. Although no statistics has been carried out by means of HRTEM, the smaller number of dislocations found indicate that the higher homogeneity of the shell might be a determinant condition for avoiding the formation of dislocation in the AlN shell.

In summary, a core/shell GaN/AlN NWrs heterostructures have been investigated as a function of density. A nominal AlN shell thickness of 5.5 nm has been grown. It has been found in RS measurements a blue shift in the energy of the E_{2h} mode of GaN as the density decreases, indicating a large compressive strain of the GaN core. Probably due to the reduction of plastic relaxation processes with decreasing the NWr density. The PL analysis consists in several spectra taken as a function of NWr density. From the spectra acquired from the high density region we observed a very intense emission around 3.2 eV together with a quenching of the GaN band edge emission. As the NWr density decreases the intensity of the emission at low energy gradually decreases and the intensity of the emitted light from the GaN band edge strongly increases. Base on previous studies on core/shell

GaN/AlN NWrs, we launch the hypothesis that due to the shadow effects, in the high density region the shell should be more inhomogeneous giving place to plastic relaxation processes. Therefore, we perform an study by means of HRTEM in order to demonstrate the existence of dislocations. In the high density region, the NWrs present a very inhomogeneous shell and we found several dislocations although the shell cover the whole length of the NWrs. Contrary to this, after the inspection of a tenth of NWrs from the low density region, we observe a considerable reduction of the number of dislocations. Additionally, in this region the shell is homogeneous, supporting the fact that AlN shell grows avoiding the plastic relaxation processes.

In this Chapter, we have investigated the structural and optical properties of axial and radial GaN/AlN nanowires heterostructures. Thick axial insertions present evidence of plastic relaxation. Dislocations at a constant distance of 3 nm from the surface are found by TEM analysis. Regarding the radial heterostructures, the optical and structural properties from core/shell GaN/AlN heterostructures have been investigated as a function of shell thickness. The homogeneity of the shell is the most relevant parameter for the improvement of the structural characteristics of the NWrs. A study of radial core/shell heterostructures varying diameter and density of the core, is performed. The NWrs at the low density zone are under axial strain, while those at the high energy region are almost relaxed. This is ascribed to plastic relaxation mediated by dislocations in the AlN shell that occur when the shell is inhomogeneous and presents several steps. A decrease in the number of dislocations is observed as the NWr density decreases. This is in accordance with the blue shift of the GaN E_{2h} phonon mode observed by Raman scattering. A blue shift observed in the D^0X_A excitonic complex is also observed. Both effects reflect the increasing strain of the GaN core in the low density region.

Chapter 7

Silicon doped GaN nanowires

GaN nanowires have been extensively studied because of their excellent properties, such as high thermal conductivity, high mobility and large volume/surface ratio, making them an excellent material for UV emitters, detectors and optoelectronic applications. In order to take advantage of these possibilities, n- or p-type doping are necessary for the use of NWrs in devices. It is well known that the doping concentration in a NWr system may vary from NWr to NWr, and it is difficult to evaluate the exact amount of carriers present in the system. In this Chapter, the structural and optical properties of GaN NWrs are investigated as a function of the nominal Si content. Additionally, we relate the growth conditions with the resulting electrical properties of Si-doped GaN NWrs considered one by one by means of Conductive Atomic Force Microscopy.

7.1 Growth parameters and description of the samples

Si doped GaN NWrs have been grown with different doping concentration. As in previous samples, the substrate used was a 2 inches n-type highly doped Si(111) wafer, and no AlN buffer was used. The effective growth temperature at the center of the wafer was fixed to 820°C and 10 minutes after the Ga deposition the temperature was increased by 10°C. By this procedure, it is possible to reduce the coalescence of NWrs and assure the homogeneity of the doping along the whole NWr. Growth was performed during 14 hours and different amounts of Si were used. The Si cell temperature was varied between 850 and 1000°C in order to change the Si doping of the different samples. The samples have been labeled

as Si850(N1357), Si875(N1418), Si900(N1393), Si950(N1379) and Si1000(N1395). The number in the label refers to the Si cell temperature used during the growth and the number in parenthesis corresponds to the grower's name.

7.2 Morphological and structural properties

The morphology of the samples has been studied by means of SEM micrographs. As we have explained in Chapter 4, the morphological features of the NWrs strongly depend on the growth temperature, i.e., on the distance from the wafer edge. In order to compare the morphology of the NWrs in samples with different Si doping, SEM images were taken at a fixed distance from the edge of the wafer for all the samples. Figure 7.1 shows both cross section (left column) and top view (right column) SEM micrographs of samples Si850, Si875 and Si900, ordered from top to bottom. We would like to point out that the scale bar is different for each image. These samples present a distribution of regular nanocolumns with hexagonal cross section. The average length and diameter of the NWrs are in the order of 1.5 μm and 50 nm respectively.

In contrast, the NWrs of the other two samples, Si950 and Si1000, present unusual features in their morphology. We attribute these changes to their high Si content. Figure 7.2 presents SEM images of these two samples in cross section (left column) and top view (right column). Sample Si950 presents a "baseball bat" shape with the thin section at the base of the NWrs. However, no coalescence of NWrs has been observed by SEM analysis and the NWr surface is pretty smooth. The average length and diameter are about 1 μm and 150 nm respectively, indicating an enhancement of the lateral growth when compared with the previous samples. Sample Si1000 presents a very rough surface, probably induced by the even higher density of Si atoms used during growth. These NWrs have lost the hexagonal cross section characteristic of wurtzite GaN NWrs, as can be appreciated in Figure 7.2. The NWrs present a higher coalescence degree compared with the rest of the samples of the whole series, even for points of the sample far away from the edge, which correspond to a higher growth temperature. An average length of 1 μm and a diameter around 500 nm is observed in the NWrs of sample Si1000. Larger diameters accompanied with a reduction of the NWr length have been already observed by the influence of Si doping during growth in GaN nanorods [119]. The morphological characteristics of this NWrs would suggest a noticeable substitution of Ga atoms instead of Si ones in the crystalline lattice.

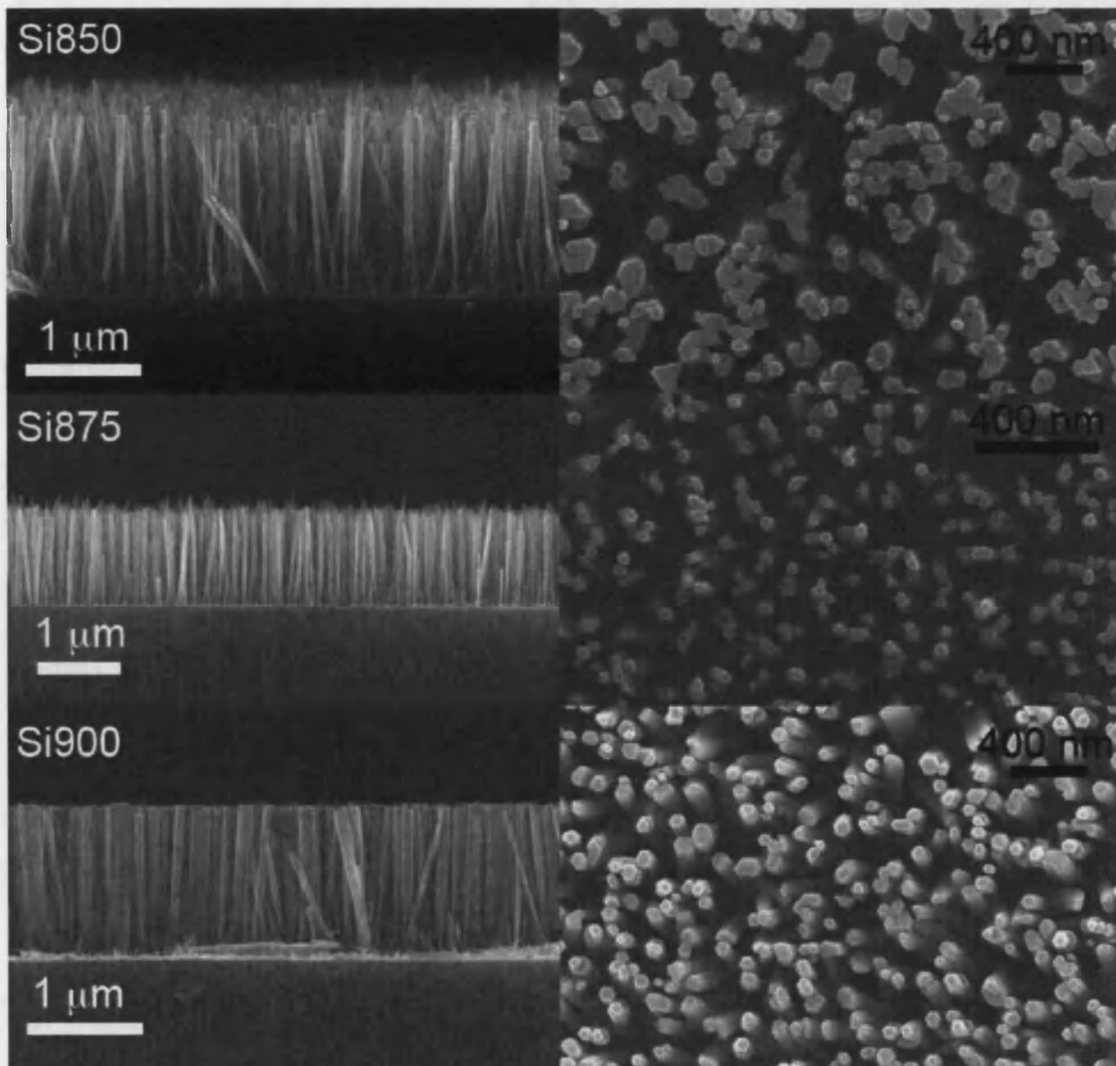

Figure 7.1: SEM images both in cross section and top view of Si doped GaN NWrs. The Si cell temperature employed for these samples was in the range from 850 to 900 °C.

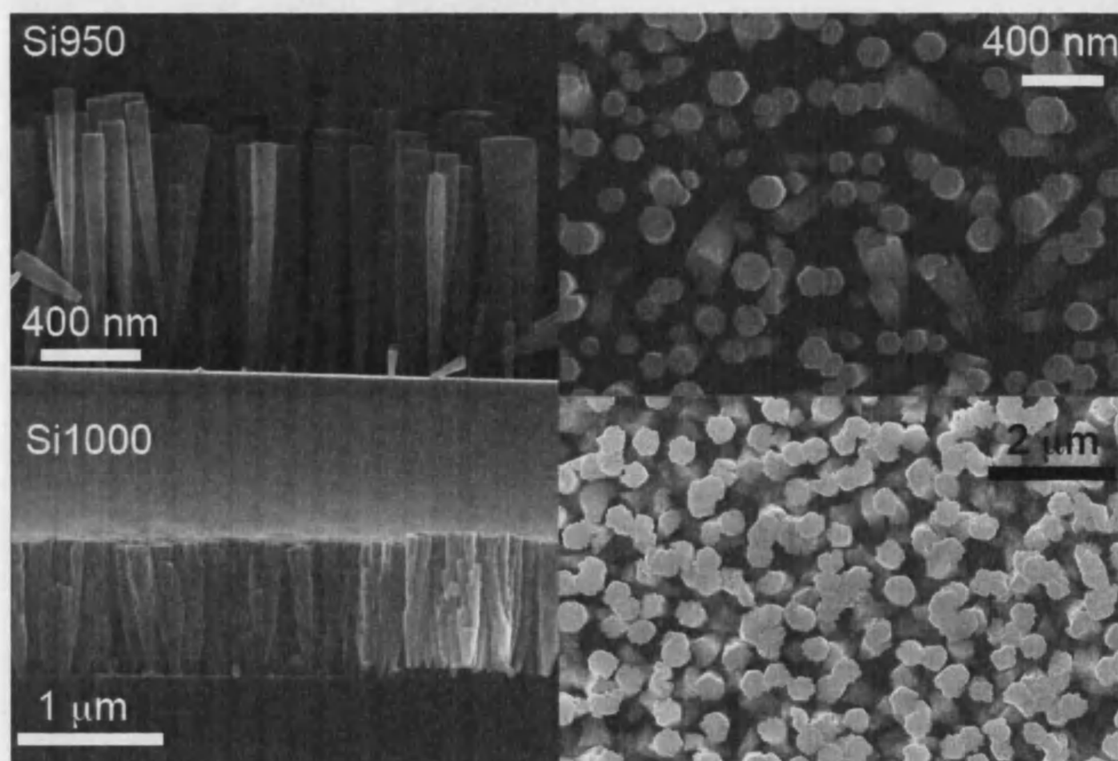

Figure 7.2: SEM images both in cross section and top view of the samples with the highest Si doping. The Si cell temperature employed for these samples was 950 and 1000°C. Note the different scale.

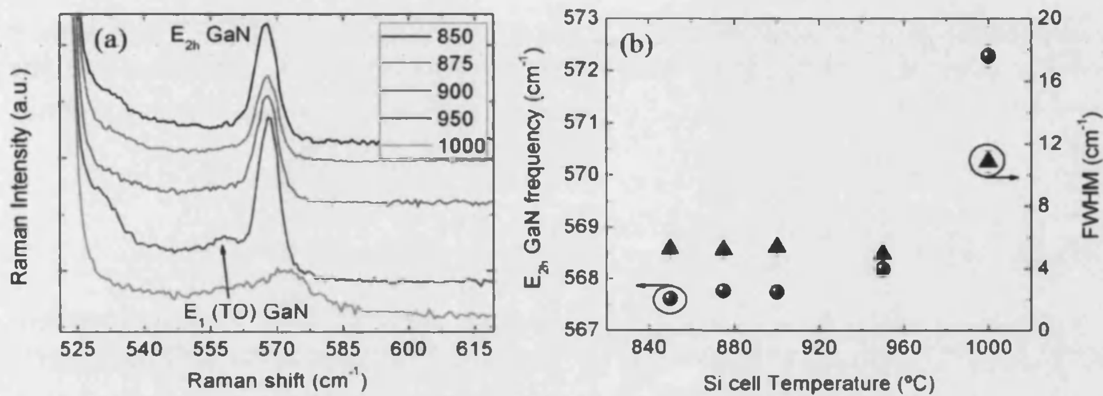

Figure 7.3: (a) Raman spectra of the Si doped NWr series. Line colors refer to the different samples. (b) Raman shift of the E_{2h} mode together with its FWHM.

The structural properties of Si doped GaN NWrs have been studied by means of μ-RS at room temperature. The samples were illuminated along the NWr axis and the light was collected in a backscattering geometry as described in Sec. 2.4.2. The region of the samples selected for the experiment was at the same distance from the edge as the SEM picture shown before, between 6 and 7 mm from the wafer edge. The Raman spectra are shown in Figure 7.3(a). We observe the tail of the Si Raman signal, that peaks at a frequency of 520 cm^{-1}. Around 570 cm^{-1} we find the E_{2h} phonon mode of GaN. Additionally to this peak, samples Si950 and Si1000 present a shoulder at ≈ 558 cm^{-1} attributed to the $E_1(TO)$ mode. The emission of this mode is forbidden in our Raman backscattering configuration $(z(-,-)\bar{z})$, but it may be allowed due to the multiple light reflections on the lateral NWr facets and the NWr top, very irregular in these samples. The peak frequency and FWHM of the E_{2h} mode are represented in Fig. 7.3(b) as a functions of Si cell temperature. The frequency of the mode remains almost constant for the lowest Si cell temperatures, and increases quite abruptly (5cm^{-1}) for Si1000. The FWHM of the mode follows the same trend, remaining nearly constant at 4 cm^{-1} for the whole series, except for the Si1000 sample, for which it increases to 11 cm^{-1}. The influence os Si doping on the frequency of the phonons of GaN NWr has been investigated before, and a negligible influence has been reported [176, 177]. However, the blue shift in frequency and line broadening of the E_{2h} mode for sample Si1000 is clear. We attribute these changes to the high coalescence degree of the NWrs of this sample, together with the morphology changes observed in the SEM micrographs.

In the frequency region corresponding to the $A_1(LO)$ mode, around 734 cm^{-1}, there is no evidence of any Raman peak. The absence of the $A_1(LO)$ mode can

be attributed to the damping of the phonon-plasmon resonance. Besides this, a possible inhomogeneity in the Si doping of different NWrs may contribute to the broadening of this mode making, decreasing its intensity below the detection limit.

7.3 Carrier recombination

The PL of Si doped GaN NWrs has been investigated using the PL setup described in Chapter 2. Figure 7.23 shows the low temperature PL spectra of Si850, Si875, Si900 and Si950. Sample Si1000 has been excluded, since its PL emission is below our detection limit at the excitation power of 90 μW. The spectra have been acquired at the same distance from the edge than SEM images and RS spectra for comparison. A spectrum from undoped GaN NWrs is shown in gray as reference. In addition to the characteristic emission lines in this reference sample, we observe several new features related to Si donors. The spectrum of Si850 (black line) presents two broad emission bands between 3.1 and 3.3 eV, characteristic of donor-acceptor pair (DAP) transitions. Once Si donors are incorporated in the NWrs, they enhance the probability of pairing with intrinsic acceptors. Due to the weak intensity from PSF emission, we discard them as origin of the lines. The intensity of these emission bands depends on the spot of the sample illuminated, change that is related to a variation of the doping level in the NWrs. Sample Si875, with higher Si content, shows a decrease in intensity of the DAP transitions. This is ascribed to the partial compensation of the acceptor states with increasing doping. This emission peak is attributed to the formation of a new donor level $D-VB$ below the D^0X_A optical transition, associated to Si ($Si-VB$). Increasing the Si content, as it is de case of Si900 (green spectrum), the emission related to the DAP transition disappears due to the total compensation of intrinsic acceptors by the electrons of the Si atoms. On the other hand, the $Si-VB$ transition appears blue shifted at 3.433 eV. This shift is ascribed to an increase of the Fermi energy towards de CB. This emission has been already observed in moderately Si doped GaN NWrs [177]. However, in this reference the authors attributed this peak to the emission related to BPSF. Sample Si950 presents much different optical properties, in accordance with its different morphology. We point out the absence of the peaks related to the DAP transition. Besides this, a blue shift of the emission energy and a large broadening of the peak is observed.

The emission corresponding to the D^0X_A transition has been determined from the spectra for the different samples and is plotted in Figure 7.5. The graph on the left (a) shows the emission energy from samples Si850, Si875 and Si900. It remains almost constant around the band edge emission of undoped GaN NWrs

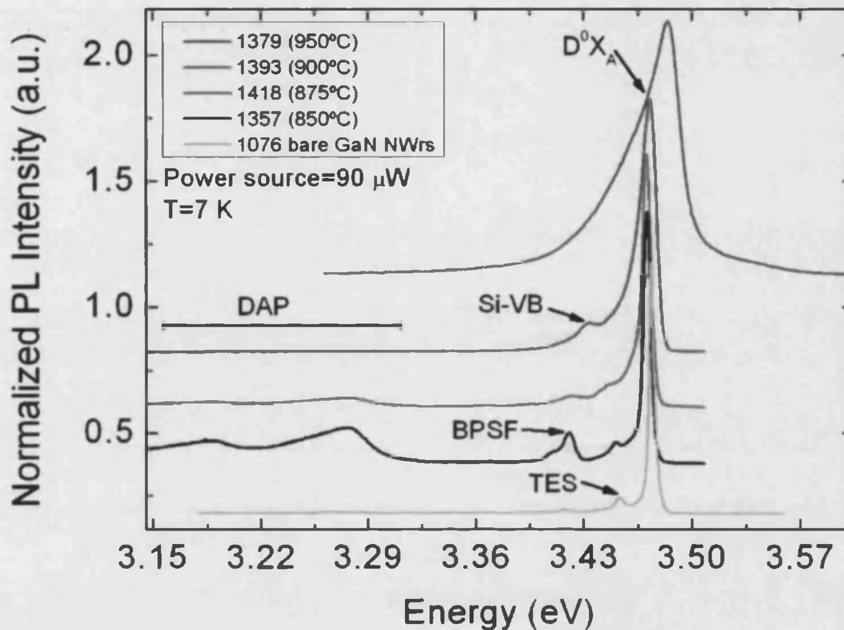

Figure 7.4: Low temperature PL spectra from Si doped GaN NWrs. PL from bare GaN NWrs is shown with dashed line for reference. The spectrum from sample Si1000 is not included since this sample does not emit at 90 μW.

(3.472 eV). However, the energy of this peak shows a remarkable increase for sample Si950. This effect is ascribed to the broadening of the Si level and its overlap with the conduction band, together with the filling of the conduction band by the electrons of the donors (Burstein-Moss shift). In accordance with the effect of doping, the FWHM increases from 7 meV to 42 meV for sample Si950. The intensity at this peak is plotted in Fig. 7.5(b). The intensity corresponding to the samples with the lowest Si content remains at the level for the undoped GaN NWr sample, increasing by a factor 12 for samples Si900 and Si950. The relatively low intensity at low doping concentrations is attributed to the presence of non radiative channels [178]. Actually, the lifetime of the non radiative channels is determined by the non equilibrium density of minority carriers (holes) and the density of traps participating in the recombination. The ratio of radiative to non radiative recombination processes is determined by the donor density divided by the trap density. If the trap density is independent of doping, the number of radiative transitions will increase with doping. Thus, a higher emission efficiency is expected as the Si doping increases. This increase in efficiency has been also observed experimentally in n-type bulk GaN. The results presented here show that in our GaN NWrs the average density of non radiative channels does not depend strongly on doping concentrations except for sample Si1000, containing the highest

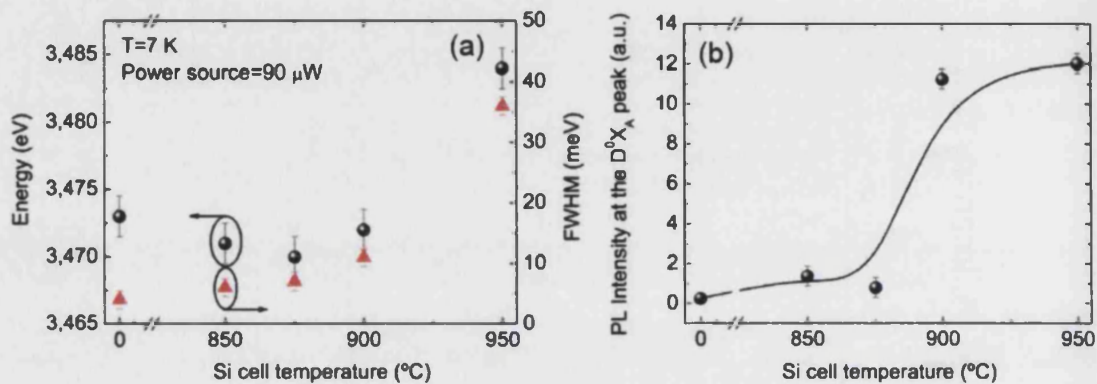

Figure 7.5: (a) Emission energy and FWHM of the band edge emission as a function of Si cell temperature, shown with black spheres and red triangles respectively. (b) Intensity at the peak of transition D^0X_A as a function of Si cell temperature. The line is a guide for the eye.

Si content, in agreement with analysis presented above.

7.4 Electrical properties

The electrical properties of Si doped GaN NWrs with different Si doping have been investigated be means of a conductive AFM. The configuration of the experiment is shown in Fig. 2.20. For these experiments we first check the reliability of our measurements by using AFM tips coated with Pt, Au and Co. Two different materials have been used as references, in order to check the integrity of the tip before and after the measurements: a gold film and graphene layers dispersed on gold. In both cases we obtain IV curves showing a clear Ohmic behavior, independently on the coated tip used. We have selected a Pt coated tip to perform the electrical measurements on the Si doped NWrs, this coating is stronger, that is, it is better preserved under friction with the sample's surface. Prior to the acquisition of the IV curves of the NWrs, it is necessary to obtain an AFM picture of the NWrs top, in order to determine their distribution and select the appropriate NWrs for the electrical studies. With this purpose we scan an area in tapping mode (non contact mode) in order to avoid the damage of the NWrs and the tip. As a representative example of the result of this procedure, Figure 7.24 shows the 2×2 μm^2 AFM image of sample Si950. The hexagonal shape of the NWrs top can be clearly distinguished. From the image, it is possible to select a single NWr and place the AFM tip on top of it, using contact mode.

At this point, it is very important to be sure that the tip is in intimate contact with the NWr. For this purpose, we represent in real time, by means of an oscillo-

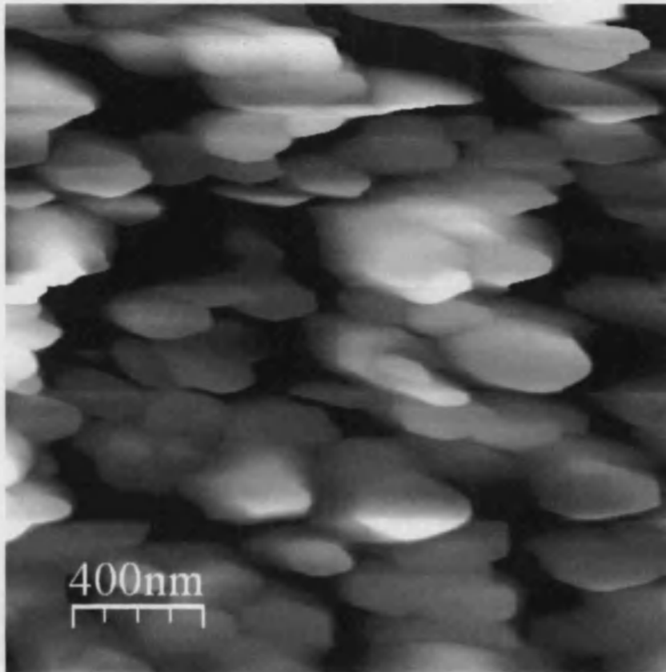

Figure 7.6: 2×2 μm^2 AFM image of the top part of the NWrs sample. The hexagonal shape of the NWrs section can be distinguished. Black color represents the absence of material.

scope, the signal corresponding to the Normal Force experienced by the cantilever versus the sample-tip distance. Figure 7.7(a) shows typical FZ curves corresponding to the situations when the sample approaches the tip (in black) and coming back to its original position (in red). During approach the Normal Force on the cantilever is zero until tip and sample interact. At that point, and depending on the tip and sample materials, the tip is slightly attracted towards the surface. Next the Normal Force starts to increase. In backwards direction, when tip and sample start to separate, the Normal Force decreases. The tip does not loose contact to the surface at the same point as during the approach, but it continues in contact until the Normal force overcomes the adhesion force. At that point the tip escapes from the attraction of the surface, it looses contact and the Normal Force becomes zero again. By analyzing the characteristics of the FZ curve, we can extract information on the properties of the tip-surface contact. In order to select an appropriated Normal Force for the acquisition of I-V curves we determine three regimes in the FZ curve. These regions are labeled in Figure 7.7(a) as 1, 2 and 3. Performing the I-V experiments with the Normal Force in region 3 we reproduce the conditions recommended by Pérez-García *et al.* [179]. In this work, performed on highly oriented pyrolytic graphite, the authors demonstrate that the current starts to flow through the Pt-graphite nanocontact when the normal force

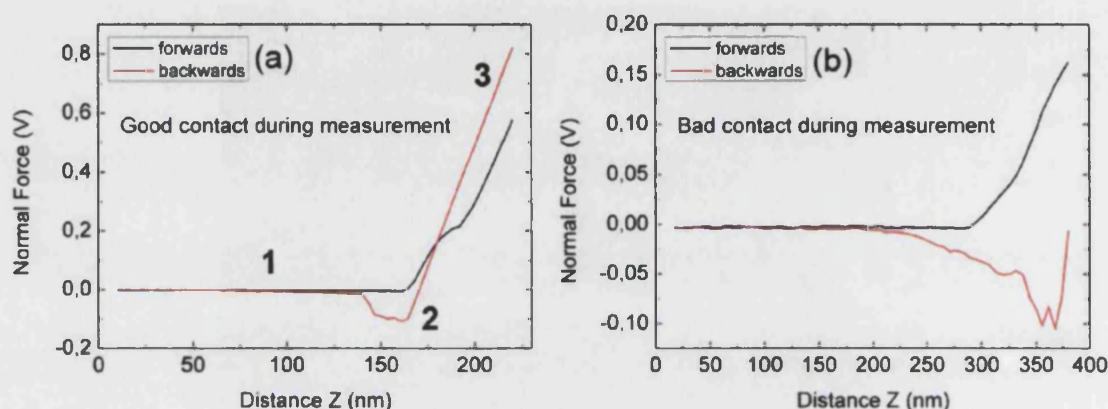

Figure 7.7: (a) Normal Force versus displacement of the sample towards (in black) the tip and back, away from it (red line). (b) The same curve but corresponding to the breaking of the NWr due to the pressure of the tip.

increases after the minimum of the FZ curve (region 2). A complete conducting and symmetric I-V cycle is obtained for both reverse and forward bias voltages when the experiment is performed with a Normal Force in region 3. Therefore, this region is the one recommended for I-V measurements. In the case of very low loading forces, during the very first stages of tip-sample contact formation (region 2), the I-V curves present a nonlinear trend in logarithmic scale. In consequence, a series resistance effect [180] is observed and they are discarded from the analysis. As an example of a bad tip-NWr contact, Figure 7.7(b) shows the case of the breaking of a single NWr due to the applied Normal Force. Observe that at the relative tip-NWr distance of 380 nm the FZ curve does not come back (red) over the same line followed in the forward direction (black). This points out the fact that the NWr under study has broken under the force of the tip. Controlling the FZ curve in this way we can acquire the I-V curves under a good and reproducible Schottky tip(metal)-NWr(semiconductor) contact.

A statistical analysis of the I-V curves is carried out by repeating the experiment under similar Force conditions in about 20 NWrs in each of the samples studied. Variations between the I-V of NWrs belonging to the the same sample have been observed, possibly due to small differences in their Si content, while several measurements performed on the same NWr give very reproducible results. In any case, the differences in the I-V characteristics between the different samples are much larger than between NWrs of the same sample. Figure 7.25 shows the I-V curves representative of the different samples. Most of the curves present I-V characteristics typical of Schottky contacts and related to the different Si content of the samples. Only sample Si1000, with the highest Si content, presents an

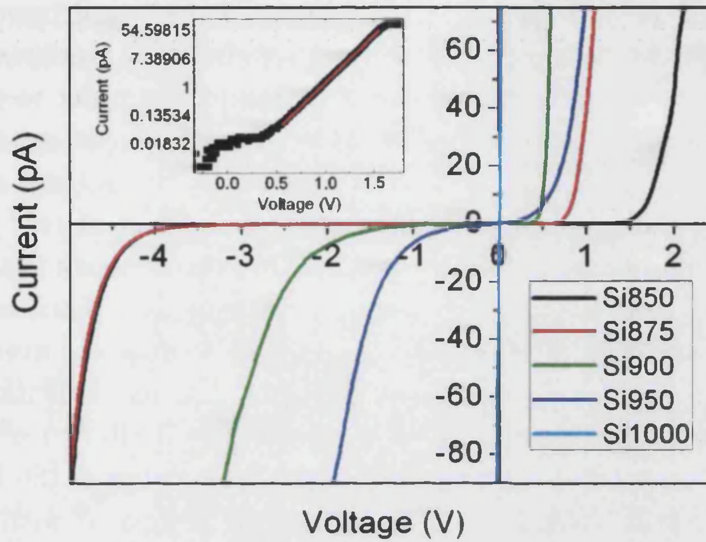

Figure 7.8: Representative IV curves from Si doped GaN NWrs. Notice how the Schottky behavior becomes Ohmic in the sample with highest Si content (Si1000). The inset shows an IV curve in logarithmic scale (black points). The red line fits the linear region to Equation.

ohmic contact. As the Si content of the samples increases, we observe a decrease in the absolute value of the breakdown voltage in reverse bias. At the same time, in forward bias the voltage at which the current starts to flow decreases. This behavior corresponds to a decrease in the slope of the IV curve in a logarithmic plot, shown in the inset of Fig. 7.25. The change from Schottky to Ohmic metal contact in the I-V curves between samples Si950 and Si1000 can be a signature of the degeneration of the Fermi level with the conduction band due to increasing Si doping.

The 20 I-V curves obtained from each sample have been represented in logarithmic scale, in a similar way as shown in the inset of Fig. 7.25. In this representation, the absence of series resistance effect is verified . Moreover, we can nicely fit the linear region of the logarithmic plot by the exponential law characteristic of the thermionic emission diffusion theory (see Sec. 1.5.2):

$$I = I_0 \left[\exp\left(\frac{qV}{\eta kT} \right) - 1 \right]. \tag{7.1}$$

For the fitting, values of I_0 and the ideality factor (η) are obtained. Values of the ideality factor in the range between 2 and 15 are found, depending of the sample and the investigated NWr. The large variation of η is influenced by uncontrolled mechanisms, such as NWr damage, indention of the tip in the NWrs and variation

in the metal-semiconductor contact properties. The electrical properties of each sample are represented by a value of I_0 obtained as the linear average of the currents representative of all the NWrs studied in that sample. In order to determine the corresponding current density J_0, we need the value of the contact area of the tip with the NWr top. Under similar experimental conditions as those used here, the Authors of Ref. [179] determined for a circular contact area of (πr^2) the influence of the indented area on the current behavior. They demonstrate that for values of r above a $r = 1.5$ nm the current behavior is reproducible. Since we are working only in region 3 (see Fig. 7.7(a)), and taking into account the average radius of our coated tip (about $r = 10$ nm), we estimate that our indentation radius is around $r = 4$ nm. The resulting contact area is $A = 5 \cdot 10^{-13}$ cm^2. As a check, we calculate the area corresponding to the maximum radius of the tip (~ 10 nm) and the final electrical results only change by 8% compared with our previous estimation. Once $J_0 = I_0/A$ is calculated, by using the Equation 7.5, exposed above, we can determine the experimental value of J_0 for each sample. According to the thermionic emission diffusion theory, J_0 is given by:

$$J_0 = A^{**}T^2 \exp\left(-\frac{q\phi_{Bn}}{kT}\right). \tag{7.2}$$

Here, A^{**} is the reduced effective Richardson constant taken here as 24 A/cm^2K^2 [180], T the lattice temperature (300 K), q the electron charge (1.602×10^{-19} C) and k the Boltzmann constant. From the experimental value of J_0 we obtain the value of $q\phi_{Bn}$ for each sample. In turn, this potential energy barrier can be decomposed into three contributions: $q\phi_0$, a characteristic potential associated to the metal contact (Pt-GaN); $q\phi_n$, the potential associated to the n-type doping level of the semiconductor; and $q\Delta\phi$, the image force barrier lowering potential. The average current density J_0, together with its uncertainty, from the fit of Eq. 7.6 are listed in Table 7.1 for each sample.

(A/cm^2)	J_0	$\varepsilon(J_0)$
Si850	4×10^{-6}	1×10^{-6}
Si875	1.1×10^{-3}	0.8×10^{-3}
Si900	5×10^{-3}	3×10^{-3}
Si950	0.59	0.15

Table 7.1: Average current density J_0 in A/cm^2 with its dispersion error extracted from the set of IV curves.

In contrast to the previous samples, for Si1000 the Schottky theory does not apply since it presents an ohmic behavior. For the description of its theoretical

properties we use therefore the ohmic theory described in Sec. 1.5.3 in order to obtain the equivalent resistance R_c. With this purpose, we calculated the slope of the I-V curve, which corresponds to the ohmic resistance (Eq. 1.32). The average value of the equivalent resistance experimentally obtained is $R_c = 537.63 \pm 9.25\ M\Omega$. It is related to the microscopic parameters of the wire as:

$$R_c = \frac{k}{A^{**}Tq} \exp\left(\frac{q\phi_{Bn}}{kT}\right). \tag{7.3}$$

From this equation we can obtain the values of the Schottky barrier height $q\phi_{Bn}$ for this sample. The values obtained for the different samples are listed in Table 7.2. All the values obtained are smaller than that corresponding to a macroscopic Pt contact with GaN, which is 1.1 eV [180]. Additionally, we observe that, as expected, the Schottky barrier decreases down to a value of $q\phi_{Bn} = 0.393$ eV as the Si content increases. Beyond this value, the barrier estimated for the NWrs with highest Si content inverts its sign, evidencing the fact that for this sample the Fermi level is contained in the conduction band.

(eV)	$q\phi_{Bn}$
Si850	0.702
Si875	0.556
Si900	0.515
Si950	0.393
Si1000	-0.128

Table 7.2: Average Schottky barrier $q\phi_{Bn}$ for the Pt-Si:GaN contact.

As aforementioned, the barrier height can be decomposed into three contributions: $q\phi_{Bn} = q\phi_0 + q\phi_n - q\Delta\phi$. In order to relate the donor impurity concentration N_D with the barrier height, we assume that in the depletion region (see Fig. 7.13 in Chapter 1) the electronic temperature is equal to the lattice temperature, i.e., the condition $\frac{E_C - E_D}{kT} \ll \frac{N_c}{8N_D}$ is fulfilled. The activation energy $(E_C - E_D)$ reported for Si donors in GaN ranges between 12 meV [181] and 30 meV [182], and may depend on doping. A value of 12 meV is representative for the doping levels achieved in our samples [183]. N_c is the effective density of states in the conduction band, that at room temperature takes the value of $2.24 \cdot 10^{18}$ cm^{-3}. For non degenerated samples, that is, for samples with low Si doping fulfilling the condition $N_D < 10^{18}$ cm^{-3}, the contribution $q\phi_n$ can be substituted by $kT \ln(N_c/N_D)$. Samples with higher free carrier concentration are supposed to have their Fermi level degenerated with the conduction band due to the broadening of the density of states and therefore the overlap of the Si levels with the conduction band. In this regime, by using the

Fermi-Dirac statistics the resulting $q\phi_n$ can be expressed as $(3\pi^2 N_D)^{2/3}\hbar^2/2m_e^*$. Finally, the image force barrier lowering $q\Delta\phi$ is taken from Eq. 1.26. We have to notice that the image force lowering contribution depends on the selected $q\phi_0$ and also on the N_D. Taking into account all these considerations, the Schottky barrier can be expressed by the following system of Equations:

$$\begin{aligned} q\phi_{Bn} &= q\phi_0 + kT\ln(N_c/N_D) - q\left[\frac{q^2 N_D q\phi_0}{8\pi^2\varepsilon_s^3}\right]^{1/4} \quad \text{Non degenerated} \\ q\phi_{Bn} &= q\phi_0 - \frac{(3\pi^2 N_D)^{2/3}\hbar^2}{2m_e^*} - q\left[\frac{q^2 N_D q\phi_0}{8\pi^2\varepsilon_s^3}\right]^{1/4} \quad \text{Degenerated} \end{aligned} \tag{7.4}$$

Here, m_e^* is taken as $0.511\cdot10^6\ eV/c^2$ and the Planck constant is $\hbar = 6.582\cdot10^{-16}\ eV\cdot s$. We have considered a temperature of 300 K, similarly as in the experiments. The dielectric constant for GaN is considered isotropic and is given by as 5.35 [148]. The values of the variables of this system have been plotted in Figure 7.26 for $q\phi_0 = 0.3, 0.4, 0.5, 0.6$ and 0.7 eV using different colored symbols. The curves corresponding to the non degenerate case have been plotted in the Figure in the range from 10^{15} to 10^{19} cm^{-3} so that they overlap with those corresponding to the degenerated cases. However, we have to keep in mind that the non degenerate equation can be only applied for concentrations up to 10^{18} cm^{-3}. For values of N_D above 10^{18} cm^{-3} the curves represented are obtained by means of the Equation corresponding to the degenerated case. The curves are limited by horizontal lines that correspond to the experimental range in which $q\phi_{Bn}$ is comprised. Additionally, the value of N_D must be also limited into a range determined by the undoped GaN and the value of the free electron concentration of sample Si1000. We take as low limit the value of $4\cdot10^{16}$ cm^{-3}, that corresponds to the value of the carrier concentration in non-intentionally doped bulk GaN determined by Hall measurements [184]. However, the determination of the upper limit is not so easy. Taking into account the SEM analysis performed on this particular sample (see the bottom images in Fig. 7.2), we recall that the average NWr diameter is 500 nm. Moreover, a very pronounced roughness in the NWrs surface is observed, attributed to the presence of Si atoms covering the complete NWr volume, as result of the high Si content. Consequently, the distribution of the carrier flux along the wire is not clear. Considering that the metal-semiconductor contact in this sample has an ohmic behavior, it is reasonable to consider that current transport takes place through the whole section of the NWr. This is in agreement with previous studies on the photoconductivity of n-doped GaN NWrs performed as a functions of the NWr diameter [185]. The Authors determine that, above a critical diameter, of the order of 40 nm for lightly doped NWrs, the thickness of the depletion region

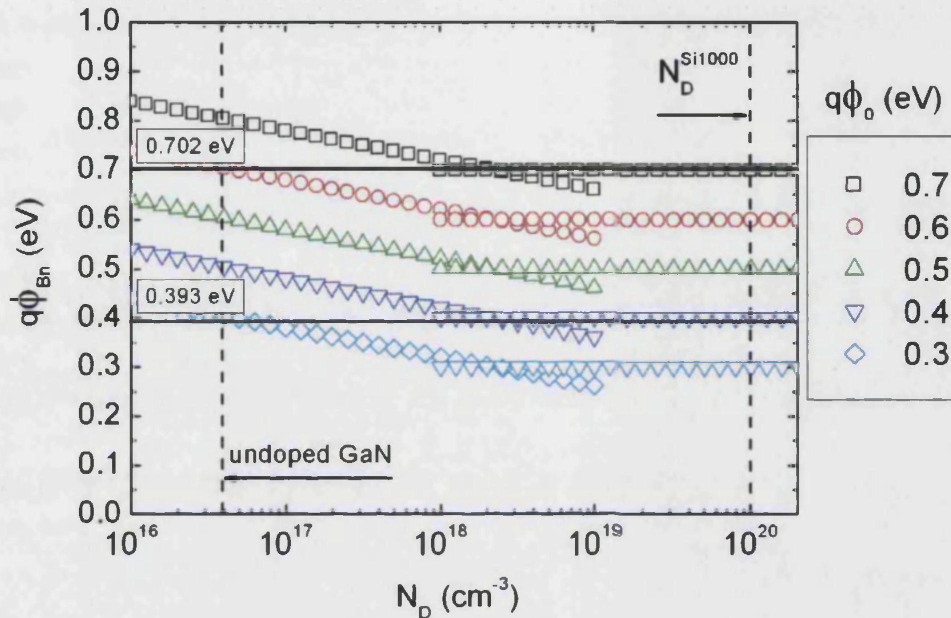

Figure 7.9: Schottky barrier $q\phi_{Bn}$ as a function of electron concentration N_D. Note the logarithmic scale in the horizontal axis. The color of the symbols determines the value of $q\phi_0$. The dashed vertical lines represent the values between the unintentionally doped bulk GaN and doping found for sample Si1000.

located at the NWr lateral surface tends to zero for increasing doping. Taking into account these considerations, from the I-V curve of sample Si1000, we calculate the resistivity $\rho = R_c SL$, where S and L correspond to the NWr area and length respectively, and are given by $1.9 \cdot 10^{-9}$ cm^2 and 10^{-4} cm. The free electron concentration is finally obtained through the Equation $N_D^{Si1000} = (\rho q \mu_e)^{-1}$, where μ_e is the mobility of the electrons in GaN and is taken as 440 cm^2·V^{-1}·s^{-1} [186]. The value estimated for N_D^{Si1000} is represented with a vertical dashed line in the Figure and corresponds to 10^{20} cm^{-3}. Since this is the sample with the highest Si doping, all the possible values for N_D for the other samples must be below this one.

Although the average value of $q\phi_0$ cannot be accurately determined, we can observe that only the curves in the range of $q\phi_0 = [0.4, 0.6]$ eV cover the whole range of doping limited by the experimental $q\phi_{Bn}$ (horizontal lines). This allows us to limit the value of $q\phi_0$ in this range. Taking into account this limitation, we estimate the carrier concentration for a representative value of $q\phi_0 = 0.5$ eV. Considering that at room temperature all the silicon donors are ionized, we obtain an estimation of the doping concentration of our samples, that is listed in Table 7.3.

(cm^{-3})	N_D
Si850	$5 \cdot 10^{16}$
Si875	$3 \cdot 10^{17}$
Si900	$2 \cdot 10^{18}$
Si950	$2 \cdot 10^{18} - 10^{20}$
Si1000	10^{20}

Table 7.3: Estimated values of N_D for the whole series of Si doped GaN NWrs.

Even if there are several limitations in this estimation, the obtained values for the Schottky barrier are in agreement with those obtained for a Pt Schottky contact on non-intentionally doped bulk GaN. Furthermore, we observe a decrease of the barrier as the Si content increases, in agreement with expressions 7.6 and 7.7. For a more accurate determination of the electron density in the NWrs, I-V measurements as a function of temperature or under illumination are necessary.

In this Chapter we present the growth parameters of a set of GaN NWrs with different Si doping. SEM micrographs reveal morphological changes in the NWrs with the highest Si content. A structural analysis by means of RS also indicates structural changes in this sample, ascribed to the coalescence of the NWrs. The PL spectra shows the emission peaks characteristic of GaN NWrs. Additionally, emission associated to donor-acceptor pair transitions are observed for the lowest Si doping levels. The emission energy of the main PL peak blue shifts as the Si content increases. This behavior is accompanied by a considerable increase of the broadening of the peak. CAFM measurements show the I-V characteristics of the NWrs of each sample. Only the sample with highest Si doping shows an ohmic contact. The I-V curves of the other samples present a Schottky behavior. From the curves we have estimated the value of the Schottky barrier, which are in accordance with the values reported for the Schottky barrier between Pt-non intentionally doped bulk GaN and the value of the Fermi level in sample Si1000. We use the change in the Schottky barrier to estimate an average electron concentration of each sample.

Conclusions

In this Thesis we have studied the optical, structural and electrical properties of GaN nanostructures. In order to understand the physical properties of these nanostructures, and the basic principles of the experimental techniques used, in the first Chapter we have described the properties of III-Nitride semiconductors with wurtzite crystalline structure, more specifically GaN and AlN. The second Chapter contains the description of the characterization techniques used in this study.

The following chapters perform the growth and characterization of the different samples. In the following we enumerate the main conclusions of our work.

- Concerning a-plane GaN/AlN QW superlattices, studied in Chapter 3, we find that the polarization of their PL emission changes with QW width. Actually, the degree of polarization decreases from values close to those of bulk GaN for the thinnest QW to negative values for the thickest one. This behavior is ascribed to the effect of strain on the electronic bands of GaN. Actually, theoretical calculations indicate that, while confinement effects do not contribute significantly to the degree of polarization of PL in these samples, the strain state of GaN is determinant. In accordance with the experimental determination of strain performed by a combination of techniques (namely Raman scattering, X-ray diffraction and TEM), the emission will be predominantly polarized along the c-axis (negative degree of polarization) if the compression of the GaN QW is strong along the z direction and partially relaxed along the in-plane axis perpendicular to z (y direction). Strain along the growth direction x follows closely the Poisson relation.

  Similar conclusions relating the polarization of the emission and strain are obtained with regard to a-plane GaN/AlN QD superlattices, although in this case QD shape also plays an important role. Actually, the result of the calculations indicate that the emission is predominantly polarized along the longer side of the QD. This means that when the longer side of the QD is

parallel to the c-axis, the degree of polarization will be negative, as observed in one of the samples.

- The conditions needed for the growth of GaN NWrs on Si(111) by PA-MBE are given Chapter 4. The morphological characteristics of NWrs grown without the use of an AlN buffer layer, that is, directly on Si(111), depend strongly on temperature. A study of their characteristics in the temperature range from 770 to 810°C. The density, diameter and length of the NWrs decrease as the growth temperature increases. Besides this, the length dispersion of NWrs is larger in the high temperature region than in the low one. Actually, the diameter of the NWrs converges in the high temperature region to the diameter of the Precursor islands, that is almost independent of temperature. The increased NWr diameter observed in the low temperature region is ascribed to a non-negligible lateral growth due to a decrease in Ga diffusion length.

  Finally, the increased dispersion in NWr length at high temperature is related to the nucleation process: at low temperature all the precursor islands nucleate almost at the same time, while at low temperature nucleation takes place along the whole NWr growth process. Calculations of the growth time dispersion of the NWr in the high temperature region, that is, the time related to the growth of NWr with different lengths, indicates that 130 minutes after the start of the growth process there are still precursor islands forming. This time is to be compared with the total growth time of 180 min.

- The structural and optical properties of GaN nanowires are studied in Chapter 5. Concerning its vibrational modes, we observe a two new peaks around 700 cm^{-1} ascribed to surface optical phonon modes. Their frequency decreases with decreasing NWr density. This characteristic can be understood within the Maxwell-Garnett approximation, that describes the optical properties of the NWrs by means of an effective dielectric constant. The two peaks observed are related to the extraordinary part of the effective dielectric constant, that depends on NWr coverage. The agreement between theory and experiment is very good, specially considering that there are no free parameters in the theoretical description.

  Concerning the PL emission of the NWrs, several peaks related to X_A, D^0X_A, TES (two electron satellite) and stacking faults are identified. PL experiments performed on dispersed NWrs and on a sample from which the NWrs have been eliminated, locate the origin of the stacking faults related emission at the bottom of the NWrs. On the other hand, the emission ascribed to

TES, polarized parallel to the NWrs axis, is shown to arise from the lateral facets of the NWrs.

- In Chapter 6, we tackle with the morphology, optical and structural properties of GaN/AlN axial (disks) and radial (core/shell) NWr heterostructures.

  Concerning axial nanostructures, RS measurements allow the determination of the strain state of the GaN constituting the disks. We have found that the material relaxes when the disk is thick enough, due to the formation of dislocations at the GaN/AlN lateral interface. These dislocations have been observed by means of HR-TEM, and appear at for a lateral AlN thickness of around 3 nm.

  Core/shell GaN/AlN heterostructures have been studied as a function of the shell thickness. We used a combination of RS, X-ray diffraction, HR-TEM and ab-initio calculations in order to characterize the dependence of strain with AlN shell thickness. We conclude that compression along the growth axis is the most important contribution to strain. Apart from this, most of the nanowires are bent by the influence of an inhomogeneous AlN shell. In these NWrs strain is partially relaxed by the formation of dislocations that are located predominantly at steps in the AlN shell. NWrs which remain straight are characterized by a much more homogeneous shell, and are characterized by higher compression, following the theoretical predictions.

  We have also investigated the properties of core/shell NWrs as a function of NWr density. Besides an increase in the compression of the NWrs as the density decreases,the most relevant feature is related to their optical emission. PL spectra of the high density region are very wide, with intense emission bands related to defects. In the low density region the presents a totally inverted behavior. It is observed how the defect band disappears and a strong band edge emission dominates the spectrum. This behavior can be understood by the analysis of TEM micrographs, that reveal a very inhomogeneous AlN shell in NWrs from the high density region, with presence of dislocations. TEM images taken from the low density region present NWrs with a much homogeneous shell and a smaller dislocation density.

- In the last Chapter a series of Si doped GaN NWrs has been studied. The morphology of the NWrs in the two samples with higher Si content changes, with a larger amount of coalesced NWrs. Two emission bands ascribed to donor acceptor pair recombination have been identified. These transitions quench as the Si content of the NWrs increases. At the same time, the

band-edge emission blue shifts and widens considerably, due to band filling effects.

The electrical characterization of the NWrs has been performed by means of conductive AFM measurements. The formation behavior of the contact between the Pt coated tip and the NWr top has been analyzed for different values of the normal force. Concerning the NWr I-V characteristics, only the sample with the highest doping level presents an ohmic contact. In the rest of the samples the contact is of the Schottky type. From the I-V characteristics we estimate the Schottky barrier height, that decreases from 0.7 to -0.1 eV as the Si content of the NWrs increases. From these results, approximate values of the electron concentration of the NWrs are derived.

Resumen en español

En esta Sección, se presenta un resumen en español del contenido total de la Tesis. El Resumen se encuentra dividido en Secciones correspondientes a los distintos Capítulos y el número total de páginas del Resumen corresponde al 10% del número total de páginas del contenido de la Tesis.

Introducción

Desde hace casi veinte años, los semiconductores del grupo III-V han experimentado un fuerte desarrollo, tanto en la calidad del material como en las aplicaciones comerciales. Los compuestos III-V están formados por Al, Ga e In como componentes del grupo III y nitrógeno como componente del grupo V. Los semiconductores de este grupo presentan una banda prohibida directa entre 0,63 eV para el InN, 3,5 eV para el GaN y 6,3 eV en el caso del AlN [1]. Por lo tanto, con la formación de aleaciones ternarias es posible cubrir la espectro electromagnético desde el infrarrojo al ultravioleta, como se puede observar en el esquema de la Figura 7.10. Este tipo de semiconductores cristaliza en varias estructuras diferentes, pero la más estable es la fase wurtzita. Esta estructura presenta una anisotropía inherente que permite que los nitruros se puedan utilizar como detectores de polarización en el rango UV. De los diferentes métodos comúnmente utilizados para el crecimiento de semiconductores III-N, en esta Tesis se ha utilizado el crecimiendo por epitaxia de haces moleculares (MBE).

A pesar de la profunda investigación y el esfuerzo realizado hasta ahora, en el sistema de materiales III-N, todavía hay muchos campos abiertos a la investigación, especialmente en torno a las propiedades de las nanoestructuras basadas en estos materiales. Por ejemplo, los parámetros que controlan las características de las emisiones, tales como la deformación de la estructura cristalina, el tamaño, la forma, la orientación o el dopaje, no han sido estudiados en profundidad. Esta Tesis tiene como objetivo analizar algunos de ellos.

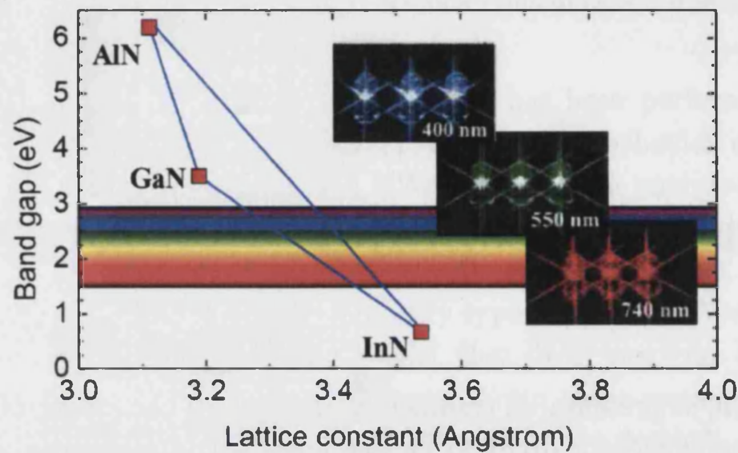

Figure 7.10: Energía de la banda prohibida en función de la constante de red a para semiconductores III-N. Imagen tomada de [3].

Propiedades fundamentales del grupo de semiconductores III-N y del contacto metal-semiconductor

La estructura cristalina WZ tiene una celda unidad hexagonal como la que se muestra en la Figura ??. Las esferas amarillas representan los átomos de Ga y las de color gris los átomos de N. Las direcciones cristalográficas correspondientes a los ejes c, a y m se muestran en la parte de la derecha. La secuencia de apilamiento de los átomos es ABA a lo largo de la dirección [0001] y también está indicada.

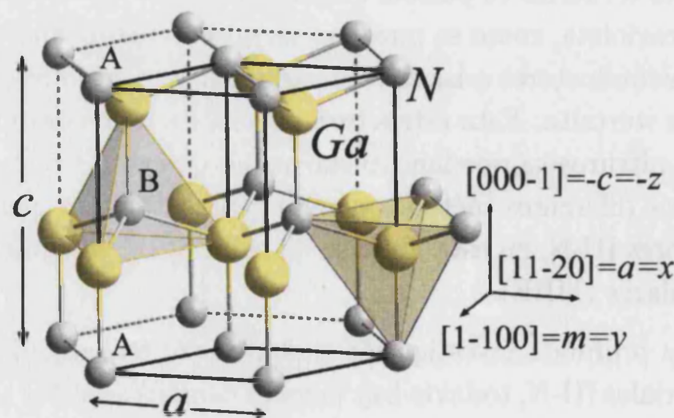

Figure 7.11: Esquema de la estructura wurtzita con sus diferentes parámetros de red y direcciones.

Los cristales compuestos no centro simétricos presentan dos secuencias difer-

entes de las capas atómicas. Para los compuestos binarios con estructura wurtzita, tales como GaN, la secuencia de las capas atómicas del Ga y el N se invierten a lo largo de las direcciones [0001] y [000$\bar{1}$]. Como consecuencia, se observa una polaridad cristalográfica a lo largo de este eje. Las superficies correspondientes, perpendiculares a [0001] y [000$\bar{1}$] se denominan de cara-Ga y cara-N, respectivamente. Además, la estructura WZ de los nitruros III-V presenta una simetría compatible con la existencia de polarización espontánea. Adicionalmente, cuando la estructura cristalina cambia por una tensión aplicada, da lugar a una polarización piezoeléctrica. Por lo tanto, la polarización macroscópica es la contribución de estos dos factores. En el caso de las heteroestructuras, el cambio de esta polarización a través de las interfases entre distintos materiales es la causante de una acumulación de carga que genera fuertes campos electricos internos. Estos campos influyen negativamente en las propiedades ópticas de la materia mediante la aparición del efecto Stark de confinamiento cuántido [33]. El efecto Stark provoca la separación espacial entre electrones y huecos. Esta separación tiene como consecuencia una disminución de la superposición de las respectivas funciones de onda, y en consecuencia una disminución de las recombinaciones radiativas, disminuyendo así su eficiencia óptica. Además, debido al cambio en el perfil de potencial de confinamiento, la energía de las transiciones ópticas también disminuye.

La estructura de bandas de los semiconductores III-V se puede describir mediante la aproximación de la masa efectiva a lo largo de las diferentes direcciones en el espacio del vector de ondas **k**. Para la descripción de las bandas, se han tenido en cuenta los cálculos realizados por Chuang *et al.* [14]. Conjuntamente, se ha representado el efecto de la deformación de la red cristalina sobre las bandas electrónicas, simulando una compresión biaxial. En la Figura 7.12 se muestran las bandas electrónicas para el GaN masivo tanto sin deformar (bandas grises) como para una deformación biaxial compresiva a lo largo de la dirección (0001) (a) y la dirección (11$\bar{2}$0) (b).

Además de las propiedades electrónicas, se han presentado las propiedades vibracionales del GaN y el AlN. Los modos normales de vibración de los átomos de un cristal, denominados fonones, son casi en su totalidad los responsables de las propiedades térmicas de los materiales. A través de ellos, se puede extraer mucha información sobre la estructura cristalina. Un cristal tiene un gran número de fonones. Cada uno se caracteriza por un vector de onda $\overrightarrow{q}$ en la primera zona de Brillouin (BZ). Las frecuencias relacionadas, $\omega(q)$, se obtienen por 3N funciones de $\overrightarrow{q}$, donde N es el número de átomos por celda unidad. Esto se traduce en tres ramas acústicas, en las cuales $\omega(0) = 0$. El resto, 3N-3 ramas, nueve en nuestro caso, corresponden a los modos ópticos, con $\omega(0) \neq 0$. El analisis de las frecuencias

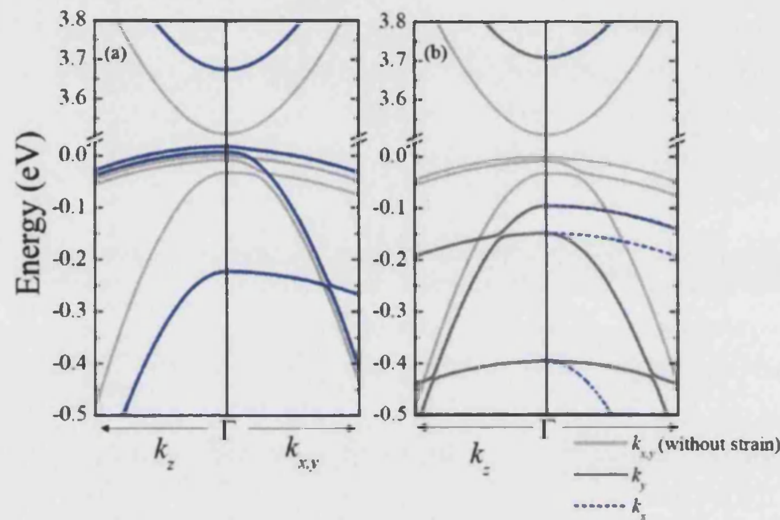

Figure 7.12: (a) Estructura de bandas bajo una compresión biaxial en el plano (0001) (blue line). (b) Lo mismo bajo una compresión biaxial en el plano (11$\bar{2}$0). Bandas sin deformar en gris claro. Figura extraída de [16].

de vibración de los diferentes modos nos permite estudiar, mediante los potenciales de deformación de los fonones, el estado de deformación de la estructura.

Para el analisis eléctrico de nanohilos de GaN dopados con Si, se ha presentado un resumen de la teoría Schottky. Cuando se forma un contacto metal-semiconductor, se produce una barrera en la intercara entre ambos materiales. Un esquema de las bandas electrónicas en contacto se muestra en la Figura 7.13. Cuando un metal y un semiconductor están en contacto, la carga comienza a fluir desde el semiconductor al metal hasta que se establece el equilibrio térmico. En esta situación, el nivel de Fermi en ambos lados se iguala. En relación con el nivel de Fermi en el metal, el nivel de Fermi del semiconductor se ha reducido en una cantidad igual a la diferencia entre las funciones de trabajo de ambos materiales. La función de trabajo se expresa mediante $q\phi_m$ para el metal, y es igual a $q(\chi+\phi_n)$ para el semiconductor, donde $q\chi$ es la afinidad electrónica medida desde la base de la banda de conducción E_C al nivel de vacío, y $q\phi_n$ es la diferencia de energía entre E_C y el nivel de Fermi. La diferencia de potencial entre las dos funciones de trabajo $q\phi_m - (\chi + \phi_n)$ representa el potencial de contacto.

Con esta recopilación de propiedades y teorías sobre los materiales formados por compuestos semiconductores de GaN y AlN iniciamos una investigación sobre las propiedades ópticas, estructurales y eléctricas de heteroestructuras crecidas a lo largo de direcciones no polares de la wurtzita, nanohilos de GaN, heterostructuras axiales y radiales de GaN/AlN basadas en nanohilos y nanohilos de GaN dopados

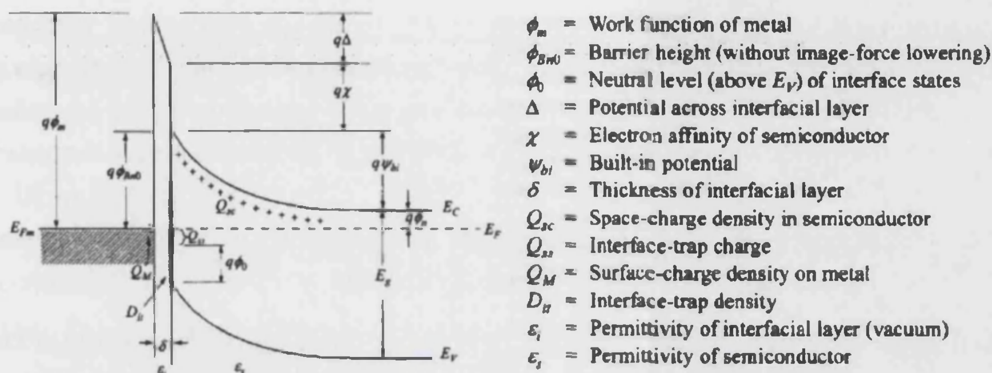

Figure 7.13: Diagrama de energías de un contacto metal semiconductor tipo n. Imagen extraida de [37].

con Si.

Crecimiento y técnicas de caracterización

El crecimiento epitaxial por deposición de átomos de diferentes especies en un sustrato cristalino es el usado para el crecimiento de las muestras estudiadas en este trabajo, llamado también MBE. El sustrato se selecciona de acuerdo a sus parámetros y orientaciones cristalográficas. Los haces moleculares son producidos por el calentamiento de la fuentes elementales en células de efusión. En el caso de nitruros, las células de efusión de sólidos por lo general se llenan de metales del grupo III, así como con Mg o Si para los dopados tipo p y n, respectivamente. El flujo del metal es posible controlarlo con el ajuste de la temperatura de la célula. Cada célula está equipada con un obturador, que responde en fracciones de segundo. El movimiento rápido del obturador permite cambiar el material casi al instante. De esta manera, es posible crecer heteroestructuras con intercaras abruptas. La fuente de nitrogeno se proporciona con un generador de plasma. La composición y la morfología de la estructura depende, principalmente, de las tasas de flujo de los elementos constitutivos y la temperatura del substrato. La tasa de crecimiento es típicamente varios cientos de nanómetros por hora.

La primera técnica de carácterización que se describe es el microscopio de barrido electrónico. Un haz de electrones es termodinámicamente emitido por un filamento de tungsteno sometido a altas temperaturas. El tungsteno es elegido porque tiene el punto de fusión más alto y la menor presión de vapor de todos los metales. El haz de electrones se puede ajustar en un rango de energía de 0,5 a 40 keV y se centra en la muestra por una lente formada por varios condensador en un

spot con un diámetro entre 0,4 y 5 nm. Estos electrones se denominan primarios. Cuando los electrones primarios interactuan con la muestra, pierden energía por la absorción y la dispersión dentro de un volumen en forma de gota, además de arrancar electrones del material analizado. Los electrones extraidos del material se denominan secundarios y son atraidos por placas expuestas a un potencial. La cantidad de electrones atraidos determina la intensidad transformada en fotones que luego se traduce digitalmente en imágenes.

La luz emitida por las nanoestructuras es analizada por Fotoluminiscencia (PL), que es una técnica no destructiva que se pueden utilizar para analizar las propiedades intrínsecas y extrínsecas de los semiconductores. Como fotoluminiscencia se entiende la radiación emitida por un material después de la excitación por una onda electromagnética de energía superior a la banda prohibida del semiconductor. Información general sobre las propiedades ópticas de los material puede ser obtenida mediante el análisis de espectros de PL como función de diferentes parámetros, tales como la temperatura, la excitación de la energía, la intensidad de la excitación, el campo magnético, etc. Los principales procesos involucradosla fotoluminiscencia se observan en el Figura 7.14: Excitación, termalización y recombinación; además de la densidad de estados de electrones y huecos.

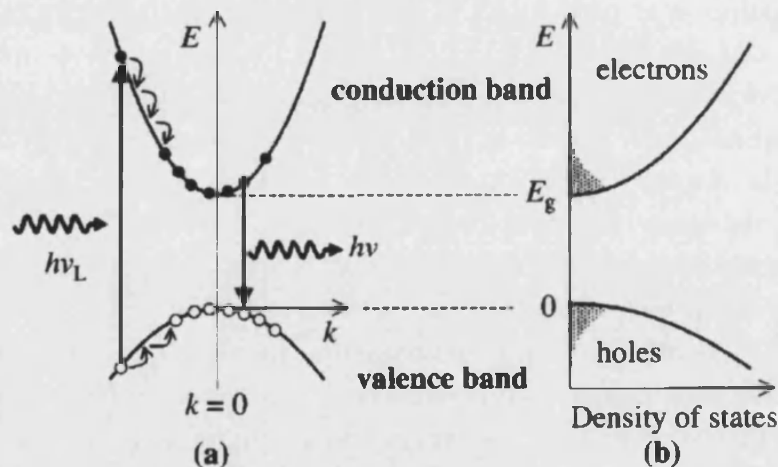

Figure 7.14: Principales procesos involucrados en la fotoluminiscencia: Excitación, termalización y recombinación (a). Densidad de estados de electrones y huecos (b). Imágen obtenida de [49].

Aunque la mayoría de la luz que viaja a través de un medio es transmitida o absorbida después de las leyes estándares de la reflexión y la refracción, una fracción se dispersa en todas direcciones por falta de homogeneidad dentro del medio. Inhomogeneidades estáticas como dislocaciones en un cristal dan lugar a

dispersión elástica la luz, es decir, sin cambio de frecuencia. Sin embargo, las fluctuaciones en la densidad del medio que están asociadas con las vibraciones atómicas dispersan la luz inelásticamente. La dispersión inelástica de la luz por vibraciones moleculares se observó experimentalmente por primera vez por Raman [62]. Hoy en día, la dispersión Raman se ha convertido en una herramienta estándar en espectroscopía de semiconductores. La Figura 7.15 muestra los principales procesos de interación elástica (Rayleigh) e inelástica (Stokes y Anti-Stokes) de la luz con la materia.

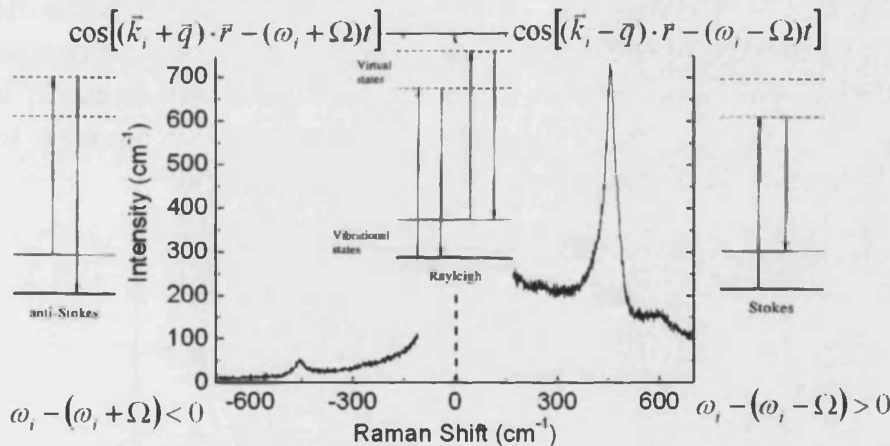

Figure 7.15: Principales procesos de interación elástica e inelástica de la luz con la materia.

Como técnica de caracterización electrica se utiliza la microscopía de fuerzas atómicas conductiva. La microscopía de fuerzas atómicas ha encontrado aplicaciones en muchos procesos importantes de la nanotecnología: la investigación de la superficie de los procesos de pulido y el grabado, la evaluación de la oxidación y la de los procesos de metalización, para medir la fuerza eléctrica en la superficie, obtener la capacidad de la superficie o técnicas que involucran el flujo de corriente entre el contacto punta-muestra. En esta Sección se explican los principios del AFM para la medición en las configuraciones más comunes (contacto y dinámico), así como las modificaciones necesarias para llevar a cabo mediciones eléctricas.

Caracterización de heteroestructuras de GaN/AlN no polares

En este Capítulo se ha analizado las caracteristicas de la emisión proveniente de heteroestructuras de pozos y puntos cuanticos de GaN/AlN crecidas a lo largo de

la dirección no polar a de la wurtzita.

En el caso de los pozos cuánticos se ha hecho un estudio en función del espesor del pozo entre 2 y 16 nm. Las medidas de fotoluminiscencia muestran un comportamiento peculiar en cuanta a la polarización de la emisión. Se observa que el grado de polarización decrece conforme la anchura del pozo aumenta, contrario a lo esperado si tenemos en cuenta que la polarización en el GaN masivo es cercana al 99estructurales mediante RS, XRD y TEM. El resumen de los resultados se muestra en la Figura 7.16. Los símbolos llenos conrresponden a la combinación experimental de las técnicas XRD y TEM, los símbolos vacios hacen referencia a los resultados extraidos de la dispersíon Raman. Todos ellos se comparan con el resultado de un modelo elástico teórico (líneas). Hay que destacar, la fuerte relajación que sufre la estructura cristalina en la muestra con pozos de 16 nm de grosor a lo largo de la dirección y.

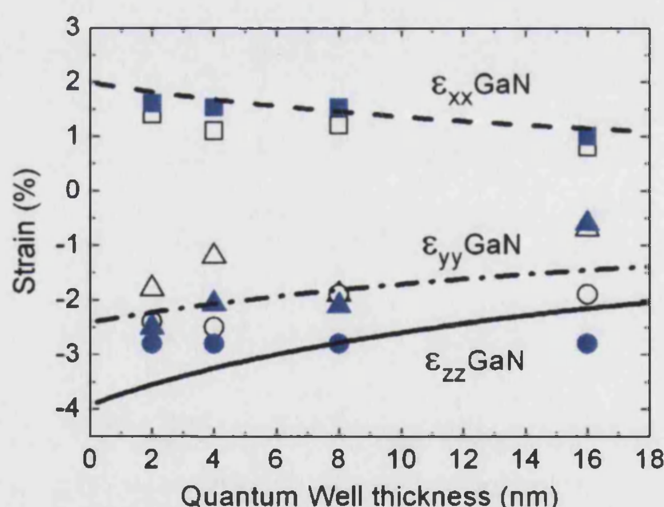

Figure 7.16: Comparación experimental de los valores obtenidos mediante XRD/TEM (símbolos llenos) con los resultados extraidos de la dispersión Raman (símbolos vacíos) y con un modelo elástico teórico (líneas). Los cuadrados corresponden a la dirección de la wurtzita x mientras que los triangulos y los circulos corresponden a las direcciones en el plano de crecimiento a lo largo de y y z.

Haciendo uso de un modelo teórico desarrollado en el marco de la teoría $\mathbf{k} \cdot \mathbf{p}$ [14], se calcula la fuerza de oscilador para la primera transicion a lo largo de las direcciones principales en el plano de crecimiento, y y z, en función de la deformación a lo largo de estas direcciones. Además de verificar que el efecto de confinamiento no influye sobre las bandas electrónicas, se obtiene un mapa del grado de polarización como el de la Figura 7.17, en el cual se han pintado los valores experimentales de deformación para los pozos cuánticos de 2 y 16 nm de

espesor. Se observa que para obtener un grado de polarización de la luz negativo la estructura debe de estar fuertemente comprimida a lo largo del eje z mientras que a lo largo del eje y la compresión debe de ser moderada. Como se puede observar, solo para el caso de los pozos cuánticos de 16 nm se obtiene un grado de polarización negativo.

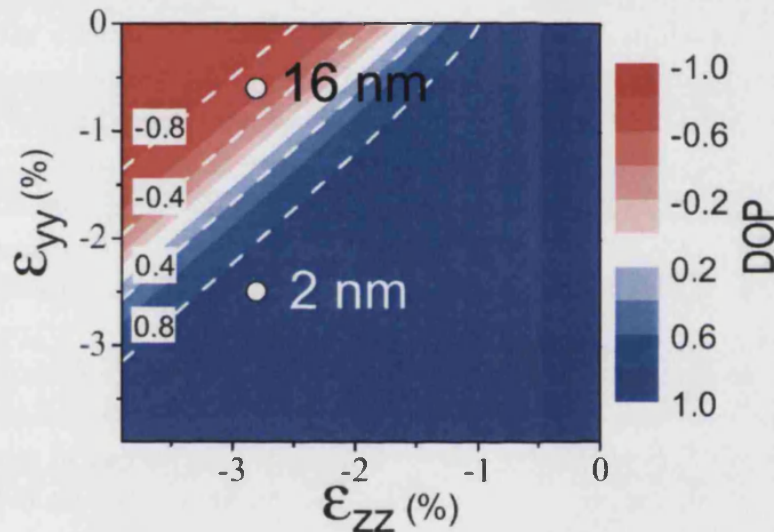

Figure 7.17: Grado de polarización calculado para para la primera transición en función de la deformación a lo largo de las direcciones del plano, y y z. Los puntos blancos indican el grado de polarización para las componentes de la deformación determinadas por Raman en los pozos cuánticos de 2 y 16 nm de grosor.

En el caso de los puntos cuánticos crecidos a lo largo de la dirección a de la wurtzita, se han estudiado diferentes muestras con diferentes morfologias y densidades. En una de las muestras también se observa un grado de polarización negativo mediante el estudio de la emisión. Se realiza un estudio estructural y morfologico sobre varias muestras de la serie. Los grados de deformación a la que están sometidas estas heteroestructuras no son suficientes para demostrar la inversión de la polarización de la luz. Sin embargo, del studio morfológico y con el apoyo de simulaciones teóricas se concluye que la forma del punto cuántico y la orientación del eje z en el punto también influyen sobre las propiedades ópticas.

Crecimiento y morfología de nanohilos de GaN

Con ayuda de un trabajo experimental realizado por Calleja y colaboradores, se pretende especificar las condiciones óptimas para el crecimiento de nanohilos de

GaN. Calleja *et al.* [104] realizó un estudio de la tasa de crecimiento de GaN como función del flujo de Ga, para una cantidad de nitrógeno activo dado, y para tres temperaturas diferentes de crecimiento. Se encontró que para bajos flujos de Ga, la tasa de crecimiento de GaN aumenta continuamente con el flujo de Ga. Un aumento del flujo de Ga finalmente satura la tasa de crecimiento. Este estado se llama crecimiento en estequeometría. Por otro lado, un aumento de la temperatura de crecimiento requiere de un mayor flujo de Ga para saturar el tasa de crecimiento, ya que la tasa de desorción Ga aumenta con la temperatura. Sin embargo, los Autores observan la presencia en la muestra de diversas morfologías al cambiar el flujo de Ga durante un proceso de crecimiento individual. Específicamente, se observan capas bidimensionales y una morfología nanocolumnar en condiciones de flujos altos y bajos de Ga, respectivamente. En particular, la morfología nanocolumnar se logra cuando, a partir de las condiciones estequiométricas a una temperatura determinada y una cantidad fija de nitrógeno activo, el flujo de Ga se reduce gradualmente. De forma paralela, un incremento en la temperatura de crecimiento aumentará no sólo la desorción del Ga, sino también la difusión de los átomos de Ga en la superficie del substrato, por lo que el aumento de la temperatura de crecimiento favorecerá la formación nanocolumnar del GaN.

Una vez establecidas las condiciones para el crecimiento de nanohilos de GaN, se crecen nanohilos de GaN con capas tampón de AlN y directamente sobre substratos de Si(111). De estas últimas, se realiza un estudio morfológico del nanohilo en función de la temperatura del substrato mediante imagenes SEM. Dado que hay un gradiente de temperatura entre 780°C y 805°C a lo largo del radio del substrato, se crecen dos muestas bajo las mismas condiciones pero con distintos tiempos de crecimiento, 3 horas y 20 minutos. De las muestras se obtienen nanohilos y los primeros estados de nucleación del nanohilo, también llamados precursores, respectivamente. Del estudio estadístico se observa que la densidad, tanto de los nanohilos como de los precursores, disminuye conforme aumenta la temperatura del substrato. Esto está de acuerdo con la desorción del Ga a temperaturas superiores a 800°C [115]. El diametro de los precursores permanece constante en torno a 12 nm en todo el rango de temperaturas, indicando que el proceso de nucleatión no está dominado por la cinética. Por otro lado, de la muestra de nanohilos se obtiene un diámetro medio que decrece con la temperatura, para converger al diámetro de los precursores en el rango de temperaturas más altas. Esto nos indica que el crecimiento lateral del nanohilo no es despreciable a bajas temperaturas debido a una disminución de la difusividad del Ga. Por último, la Figura 7.18 muestra la longitud media de los nanohilos junto con la dispersión de la longitud en funcion de la temperatura. Podemos observar como al aumentar la temperatura la longitud

media disminuye debido a la mayor desorción del Ga. Sin embargo, la dispersión en longitudes aumenta con la temperatura indicando que hay precursores que se forman en momentos distintos durante el proceso de crecimiento, dando lugar a nuevos nanohilos y finalmente a un aumento en la dispersión de la longitud.

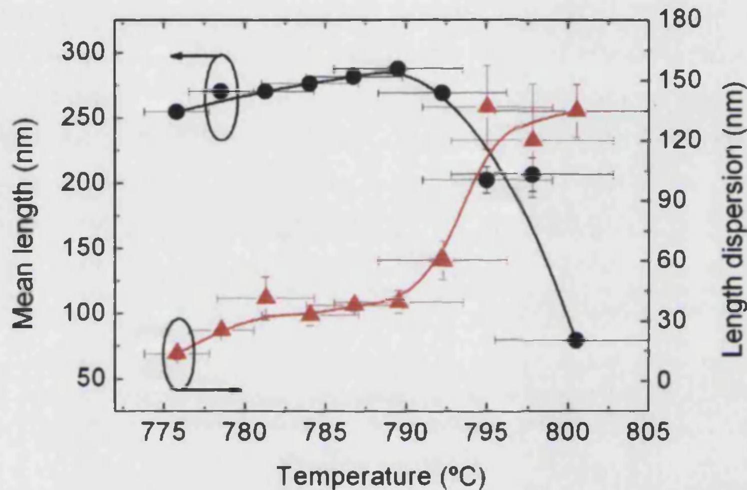

Figure 7.18: Longitud media de los nanohilos (circulos negros) junto a su dispersion de longitud (triangulos rojos) en funcion de la temperatura de crecimiento.

Caracterización estructural y óptica de nanohilos de GaN

Las propiedades estructurales de nanohilos de GaN se analizan mediante la técnica Raman en configuración de retrodispersión ($z(-,-)\bar{z}$), donde z es paralelo al eje c de la wurtzita. Las reglas de selección de la estructura wurtzita predicen la aparición de los modos E_{2h} y $A_1(LO)$ en esta configuración. Estos picos son claramente identificados en los espectros, además de la fuerte señal del sustrato de silicio. Los modos de $A_1(TO)$ y $E_1(TO)$ también son visibles, a pesar de que estos modos están prohibidos en esta configuración de polarización. Atribuimos esta ruptura de las reglas de selección debido a las múltiples reflexiones de la luz en los laterales de los nanohilos, además de la posible contribución debida a nanohilos inclinados. Como aspectos a destacar, la frecuencia del modo E_{2h} del GaN se encuentra aproximadamente 1 cm^{-1} desplazada a bajas energías respecto de su emisión en el GaN masivo. Este cambio ya se ha observado en nanohilos de

GaN crecidos en Si(111) y Si(100) [120]. Su origen no está claro, pero puede estar relacionado con el aumento de la superficie en relación al volumen del nanohilo. Además de los modos de vibración esperados en el GaN masivo, nos encontramos con una estructura en torno a 700 cm^{-1} que se atribuye a la emisión de los modos ópticos de superficie. Sobre esta emisión se ha realizado un estudio en función de la densidad de los nanohilos. La interacción dipolar entre los nanohilos y el medio envolvente se puede describir mediante la aproximación de Maxwell-Garnet [149]. Este modelo describe las propiedades ópticas del sistema nanohilo-aire mediante la función dieléctrica efectiva que depende de la cobertura (o densidad) de los nanohilos en el substrato [123]. En la Figura 7.19 se presenta el análisis de la emisión Raman relacionada con los modos superficiales y el modo $A_1(LO)$ en función de la cobertura (densidad) de los nanohilos, junto con la descripción teórica pintada con líneas discontinuas.

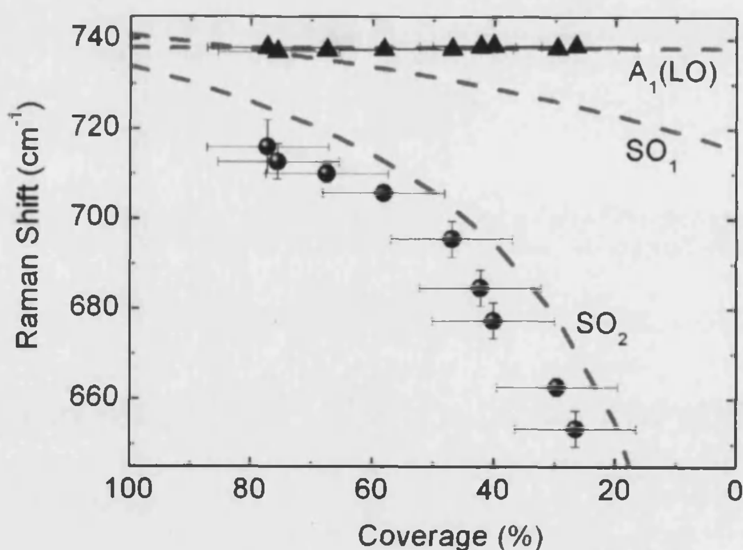

Figure 7.19: Frecuencia del modo superficial (esferas negras) junto con la del modo A_1(LO) (triangulos negros) en función de la cobertura (densidad) de los nanohilos. Se incluye los resultados de la teoría en líneas discontinuas.

Respecto al análisis de las propiedades ópticas, en la Figura 7.20 se muestra los espectros de PL a baja temperatura de dos muestras con diferentes nanoestructuras columnares, como se observa en las imágenes SEM a la derecha de la Figura. La muestra 1076 presenta una densidad mucho más alta ($2,36 \times 10^9$ NWrs/cm^2) en comparación con la muestra 1025 ($3,38 \times 10^8$ NWrs/cm^2). Además, las dimensiones de los nanohilos varian de una muestra a otra. Los espectros de PL de ambas muestras a baja temperatura presentan una fuerte emisión en 3.469 eV asociada a la

recombinación del excitón ligado a los donores D^0X_A. Este pico tiene una anchura a la semialtura de 4 meV, comparable con los reportados en la literatura [120, 131], lo que indica la buena calidad cristalina de estas nanoestructuras. Además, se puede identificar un hombro relacionado con la recombinación del excitón libre X_A en 3.475 eV. La asignación que hemos hecho se basa en estudios en función de la temperatura y potencia de excitación. En el lado de baja energía del borde de la banda, hay tres picos más de emisión presentes en ambas muestras: una emisión a 3.449 eV asociada a la emisión de estados excitados del donor (TES), una emisión ancha en 3.415 eV relacionada con los defectos planares (BPSF) formados en la base de lo nanohilos y una emisión débil en 3.354 eV relacionada con defectos chimenea (PSF) que siempre se forman en las terminaciones de los defectos planares. La emisión de la banda amarilla, asociado al nitrógeno, vacantes y otros defectos, no está presente en ambas muestras, corroborando la alta calidad cristalina de estos nanohilos. La polarización de la emisión se ha estudiado en función de la temperatura. Todas las emisiones siguen las reglas de selección del GaN masivo excepto la que se localiza cerca de 3.45 eV. Esta emisión muestra un grado de polarización negativo que se pierde rápidamente al aumentar la temperatura.

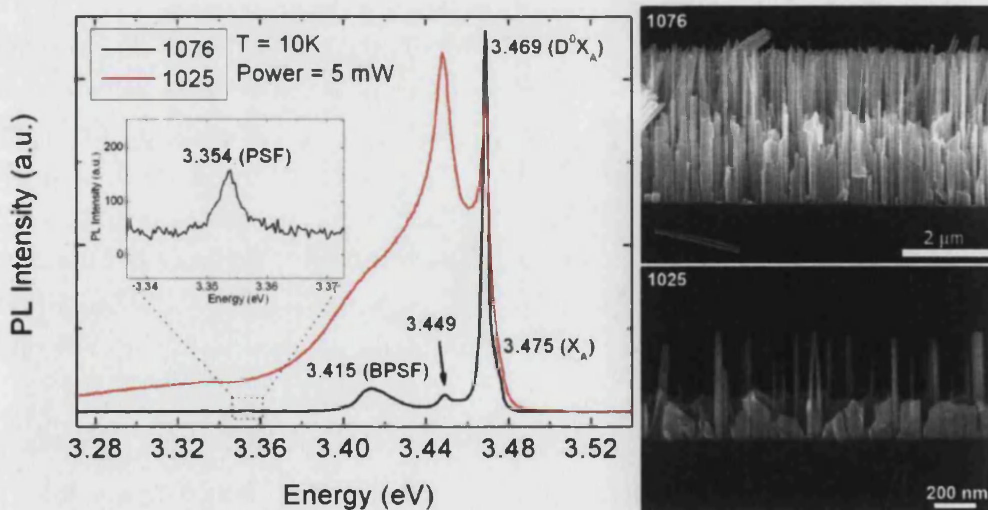

Figure 7.20: Espectros de fotoluminiscencia de dos muestras distintas de nanohilos. Ambos espectros están normalizados al mismo tiempo de acquisición, temperatura y potencia de excitación. Las correspondientes imagenes SEM se muestran en la parte derecha de la Figura.

Heteroestructuras de GaN/AlN crecidas sobre nanohilos de GaN

Como heteroestructuras de GaN/AlN crecidas sobre nanohilos de GaN, en primer lugar se han estudiado inserciones axiales, o también llamados nanodiscos. Dos muestras de nanohilos con nanodiscos de 1 (I1) y 2.5 nm (I2.5) de espesor han sido analizadas. Los espectros Raman de las dos muestras están representados en la Figura 7.21. Los picos Raman relevantes aparecen alrededor de 570 cm $^{-1}$ y 650 cm $^{-1}$ y se han atribuido los modos E_{2h} del GaN y AlN presentes en el nanohilo. El espectro de las muestra I2.5 se asemeja al de los nanohilos de GaN sin inserciones, que se muestra con una línea de puntos en la parte inferior de la gráfica a modo de referencia, debido a su gran contenido de GaN. Se observa un pico muy intenso a 566,7 cm $^{-1}$, que corresponde a la longitud de onda esperada para el modo E_{2h} del GaN relajado. Por otro lado, en el espectro de la muestra I1 después de la cuidadosa substracción del espectro del Si, se observan dos picos débiles atribuidos al GaN. Estos picos se etiquetan como $E_{2h}(1)$ a 570,3 cm^{-1} y $E_{2h}(2)$ a 580,2 cm^{-1}. Ambos picos están desplazados al azul respecto a la referencia, lo que indica una compresión del GaN. En cuanto a la región espectral del AlN, el modo E_{2h} aparece en 653,0 cm^{-1} y 648,1 cm^{-1} para las muestras I1 y I2.5, respectivamente, es decir, desplazado al rojo con respecto al valor de referencia. Esto indica una tensión en el material, que es más grande para I2.5. Mediante la relación de los potenciales de deformación de los modos, se obtienen los componentes de la deformación en las direcciones principales de la wurtzita. Para I1, se obtiene una deformación axial correspondiente a los picos $E_{2h}(1)$ y $E_{2h}(2)$ con un valor de 0,12 % y 0,60 %, respectivamente. Esta gran diferencia sugiere que las emisiones (1) y (2) se originan a partir de la dispersión de luz por las diferentes regiones del nanohilo: a la base del nanohilo le correspondería el pico (1), mientras que a los nanodiscos de GaN, rodeados de AlN y mostrando una mayor dilatación axial, le correspondería la emisión del pico (2).

En relación a los resultados observados anteriormente, la existancia de dislocaciones en nanohilos se ha predicho teóricamente en heteroestructuras axiales [152] y radiales [157], en función del desajuste de red. Como ejemplo nos referiremos a la muestra I2.5. Esta muestra se ha estudiado mediante HRTEM y se han encontrado dislocaciones en la intercara entre el GaN y el AlN, como se ilustra en la Figura 7.22. La imagen (a) muestra tres inclusiones sucesivas. De esta imagen se puede ver que las dislocaciones se producen a la misma distancia a lo largo del lado oblicuo en las tres inclusiones, correspondiente al grosor de la capa de AlN, es decir, alrededor de 3 nm. Debemos hacer hincapié en que la situación es diferente

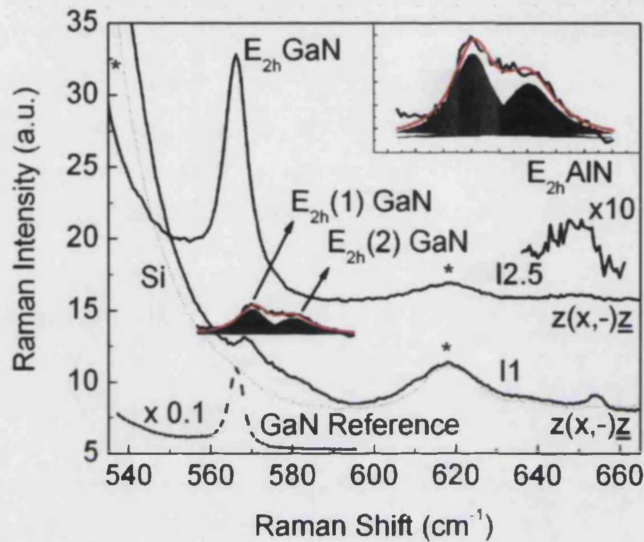

Figure 7.21: Espectos Raman a temperatura ambiente de las muestras I1 y I2.5. Espectros correspondientes a los nanohilos de GaN y al sustrato de Si están incluidos en la gráfica como referencias.

en el caso de I1. Más precisamente, proponemos que las dislocaciones (se muestra en la Fig.7.22) están relacionadas tanto con la forma redondeada de la inserción de GaN inserciones como con el proceso de deposición del AlN. En la Figura 7.22(b) se amplia una única dislocación para determinar la inclusión de un nuevo plano de átomos.

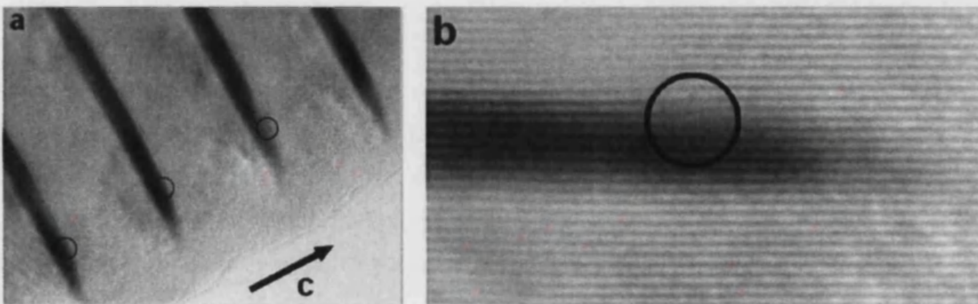

Figure 7.22: (a) Imagen HRTEM de la muesra I2.5 donde se aprecian dislocaciones en la interfase AlN/GaN. (b) Aumento de una única inserción de GaN.

UNIVERSITAT DE VALÈNCIA BIBLIOTECA DE CIENCIES

Nanohilos de GaN dopados con Si

Una serie de muestras con nanohilos de GaN dopados con Si han sido crecidas con diferentes flujos de Si para variar el dopado en las distintas muestras. Las muestras han sido etiquetadas con las temperaturas usadas en la célula de Si: Si850, Si875, Si900, Si950 y SI1000.

Las propiedades estructurales de los nanohilos de GaN dopados con Si han sido estudiados por medio de μ-RS a temperatura ambiente. Las muestras fueron iluminados a lo largo del eje z del nanohilo y la luz se recogió en geometría de retrodispersión. De los espectros Raman observamos el modo de fonón E_{2h} de GaN. Además de este pico, las muestras Si950 y SI1000 presentan un hombro en $\approx$ 558 cm^{-1} atribuido al modo $E_1(A)$. La emisión de este modo está prohibida en nuestra configuración Raman ($z(-,-)\bar{z}$), pero puede ser observado, debido a las múltiples reflexiones de la luz sobre las caras laterales de los nanohilos. La frecuencia del modo se mantiene casi constante para temperaturas bajas de la célula de Si, y aumenta de forma abrupta (5 cm^{-1}) para la muestra Si1000. La FWHM del modo sigue la misma tendencia, manteniéndose casi constante a 4 cm $^{-1}$ en los niveles bajos de dopado, a excepción de la muestra Si1000, que aumenta a 11 cm^{-1}. Atribuimos estos cambios al alto grado de coalescencia de los nanohilos en esta muestra, junto con los cambios observados en la morfología de las imágenes SEM. En la región de frecuencia correspondiente al modo $A_1(LO)$, alrededor de 734 cm^{-1}, no hay ninguna evidencia de picos Raman. La ausencia del modo $A_1(LO)$ se puede atribuir a la amortiguación de la resonancia plasmon-fonón, así como a la calidad del material. Ambos aspectos pueden contribuir al aumento de la anchura de este modo y a la disminución de su intensidad.

En la Figura 7.23 se muestran los espectros de fotoluminiscencia a baja temperatura de las muestras Si850, Si875, Si900 y Si950. La muestra Si1000 ha sido excluida, ya que su emisión de PL está ausente para la potencia de excitación usada (90 μW). La emisión de fotoluminiscencia de nanohilos de GaN sin dopar ha sido añadida como referencia. Además de las líneas características de nanohilos de GaN que se observan en la muestra de referencia, se observan varias emisiones nuevas relacionadas con los donores de Si. El espectro de Si850 (línea en negro) presenta dos anchas bandas de emisión entre 3.1 y 3.3 eV, características de las transiciones donor-aceptor (DAP). Una vez los donores se han incorporado en el nanohilo, aumentan la probabilidad de recombinación con aceptores intrínsecos. En la muestra Si875, con mayor contenido de silicio, se observa una disminución en la intensidad de las transiciones de DAP. Esto se atribuye a la parcial saturación de los estados aceptores con el aumento de dopaje. Además, se observa un pico de

emisión en 3.43 eV que se atribuye a la formación de un nivel de nuevos donores $D-VB$ por debajo del nivel del donor intrinseco que se asocia al Si ($Si-VB$). Al aumentar el contenido de Si, como es el caso de de Si900 (Espectro de color verde), las emisiones relacionadas con la transición DAP desaparecen debido a la compensación total de aceptores intrínsecos por los electrones de los átomos de silicio. Por otro lado, las transiciones $Si-VB$ se desplazan hacia altas energías. Este cambio se atribuye a un aumento de la energía de Fermi hacia la banda de conducción. Esta emisión ya se ha observado en nanohilos de GaN moderadamente dopados con Si [177]. Sin embargo, en esta referencia los autores atribuyen esta emisión a los BPSF. La muestra Si950 presenta unas propiedades ópticas muy diferentes. Podemos señalar la ausencia de los picos relacionados con las transiciones DAP. Además de esto, se observa un corrimiento al azul en la energía de emisión y un ensanchamiento de la emisión, todo ello relacionado con el llenado de la banda de conducción por la alta densidad de los electrones libres.

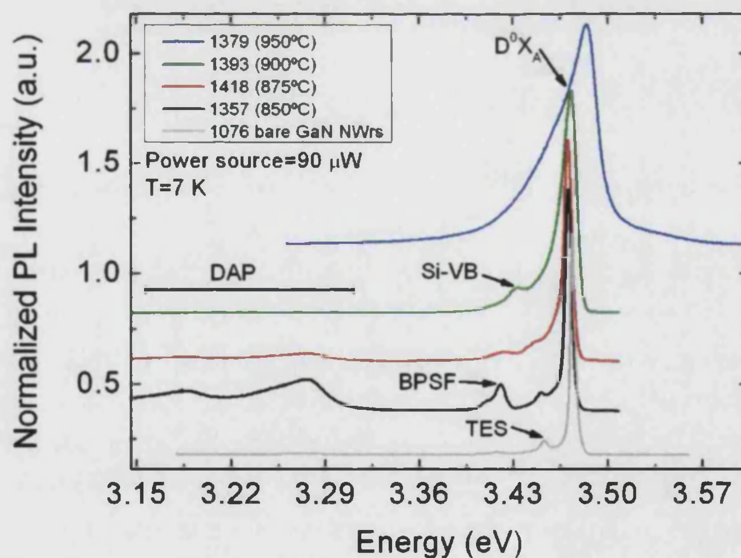

Figure 7.23: Espectros de fotoluminiscencia de las muestras con nanohilos de GaN dopados con Si.

Antes de la adquisición de la curvas I-V, es necesario obtener una imagen de AFM de la parte superior de los nanohilos, con el fin de determinar su distribución y seleccionar los nanohilos apropiados para los estudios eléctricos. Con este propósito se explora un área en el modo de no contacto (tapping) para evitar los nanohilos con la punta de AFM. Como ejemplo representativo de el resultado de este procedimiento, en la Figura 7.24 se muestra una imagen de AFM de 2×2 μm^2 de la muestra Si950. Se puede distinguir la forma hexagonal de la parte superior

de los nanohilos. De la imagen, es posible seleccionar un solo nanohilo y colocar la punta en la parte superior del mismo, utilizando el modo contacto de medida.

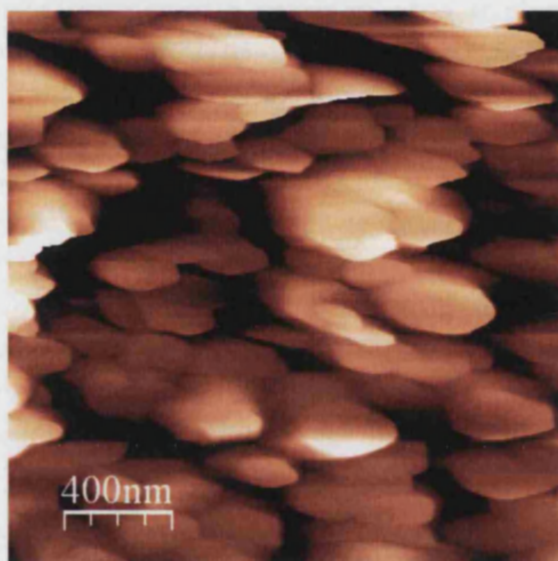

Figure 7.24: Imágen 2×2 μm^2 de la part superior de los nanohilos de GaN dopados con Si.

Un análisis estadístico de las curvas I-V se lleva a cabo mediante la repetición del experimento en condiciones similares en unos 20 nanohilos en cada una de las muestras estudiadas. Las variaciones entre las curvas I-V pertenecientes a la misma muestra son posiblemente debido a pequeñas diferencias en su contenido de silicio, mientras que las mediciones realizas en el mismo nanohilo dan resultados muy reproducibles. En cualquier caso, las diferencias en las características de las curvas I-V entre las diferentes muestras son mucho mayores que entre nanohilos de la misma muestra. La Figura 7.25 muestra las curvas I-V representativas de las diferentes muestras. La mayoría de las curvas I-V muestran un comportamiento típico de contactos Schottky, el cual se puede relacionar con el contenido en Si de las muestras. Sólo la muestra Si1000, con el más alto contenido de silicio, presenta un contacto óhmico. Conforme aumenta el contenido de silicio, se observa una disminución en el valor absoluto de la tensión de ruptura en polarización inversa. Al mismo tiempo, en polarización directa la corriente empieza a fluir para potenciales menores. Este comportamiento corresponde a una disminución en la pendiente de la curva IV en un gráfico con escala logarítmica, como el que se muestra en el recuadro interno de la Figura.

Las 20 curvas I-V de cada muestra se han representado en escala logarítmica. En esta representación, la ausencia del efecto resistencia series se verifica. Por otra parte, se ajusta la región lineal de la representación logarítmica, y el punto

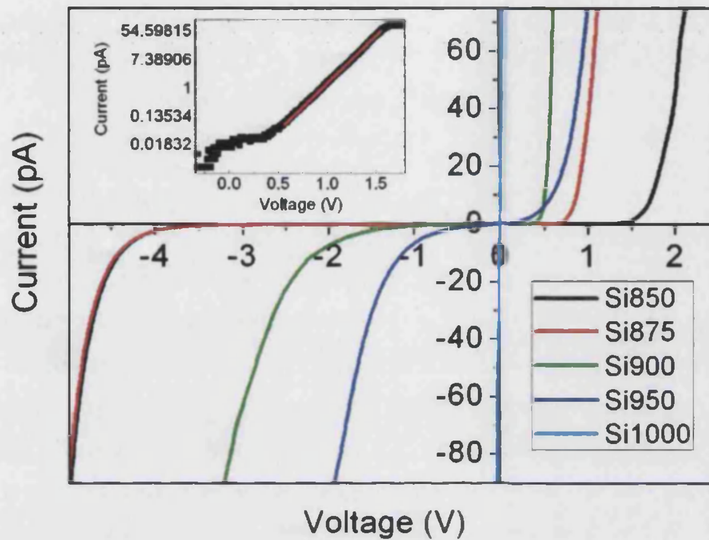

Figure 7.25: Curvas I-V representativas de las muestras con nanohilos de GaN dopados con distintos contenidos de Si. La gráfica interior es una representación en escala logarítmica.

de corte con el eje de corriente se puede relacionar mediate la teoría termoniónica de la difusión-emisión con el valor de I_0:

$$I = I_0 \left[\exp\left(\frac{qV}{\eta kT} \right) - 1 \right] . \tag{7.5}$$

Los valores de I_0 y el factor de idealidad (η) se obtienen con el ajuste. Los valores del factor de idealidad obtenidos se encuentrasn en el rango entre 2 y 15, dependiendo de la muestra y el nanohilo investigado. La gran variación de η es debido a diferentes procesos de flujo que no se han tenido en cuenta en la interpretación, tales como daños en el nanohilo, daños de la punta y variaciones en las propiedades de contacto metal-semiconductor. Las propiedades eléctricas de cada muestra están representadas por un valor de I_0 que se obtiene como el promedio de las corrientes de todos los nanohilos estudiados en la muestra. Para determinar la densidad de corriente correspondiente J_0, dividimos I_0 por el valor de la superficie de contacto de la punta con la parte superior del nanohilo. Estimamos que nuestro radio del contacto es de alrededor de $r = 4$ nm. La resultando del área de contacto es de $A = 5 \cdot 10^{-13}$ cm ^{2}. Como prueba, se calcula el área correspondiente al radio máximo de la punta ($\sim$ 10 nm) y los resultados del estudio eléctrico finales sólo cambian un 8% en comparación con nuestra estimación anterior. Finalmente, se calcula el valor experimental de J_0 para cada muestra. De acuerdo con la teoría

de la difusión de la emisión termoiónica, J_0 vieme dada por:

$$J_0 = A^{**}T^2 \exp\left(-\frac{q\phi_{Bn}}{kT}\right). \tag{7.6}$$

Donde, A^{**} es la constante reducida de Richardson, tomada aquí como 24 A/cm^2K^2 [180], T es la temperatura (300 K), q la carga del electrón ($1.602 \cdot 10^{-19}$ C) y k la constante de Boltzmann. A partir del valor experimental de J_0 obtenemos el valor de la barrera Schottky ($q\phi_{bn}$) para cada muestra. Esta barrera de energía potencial se puede descomponer en tres contribuciones: el término del potencial carácteristico asociado al contacto (Pt-GaN) $q\phi_0$, el potencial asociado al nivel de dopado $q\phi_n$ y el término de la barrera correspondiente a la reducción debida a la fuerza imágen $q\Delta\phi$. Paralelamente a los calculos anteriores, para la muestra Si1000 la teoría de Schottky no se puede aplicar, ya que presenta un comportamiento óhmico. Sin embargo, experimentalmente se puede obtener la resistencia equivalente R_c mediante la pendiente de la curva en polarización directa. Para la descripción de sus propiedades eléctricas usamos la teoría óhmica que describe la resistencia equivalente R_c mediante la ecuación:

$$R_c = \frac{k}{A^{**}Tq} \exp\left(\frac{q\phi_{Bn}}{kT}\right). \tag{7.7}$$

Una vez se ha obtenido el valor de la barrera Schottky $q\phi_{Bn}$ se toman en consideración diferentes apróximaciones para aplicar diferentes teorías a los distintos términos de la barrera con el fin de extraer el nivel de dopado en cada muestra. El siguiente par de ecuaciones representa los diferentes terminos considerados para los casos de bajo dopado, en los que el nivel de Fermi no se encuentra degenerado con la banda de conducción y en los que, al menos, hay un solapamiento de la densidad de estados de los niveles dopantes con la banda de conducción.

$$\begin{aligned} q\phi_{Bn} &= q\phi_0 + kT\ln(N_c/N_D) - q\left[\frac{q^2 N_D q\phi_0}{8\pi^2\varepsilon_s^3}\right]^{1/4} \quad \text{Non degenerated} \\ q\phi_{Bn} &= q\phi_0 - \frac{(3\pi^2 N_D)^{2/3}\hbar^2}{2m_e^*} - q\left[\frac{q^2 N_D q\phi_0}{8\pi^2\varepsilon_s^3}\right]^{1/4} \quad \text{Degenerated} \end{aligned} \tag{7.8}$$

En la siguiente gráfica 7.26 se representa el valor de la barrera en función de la densidad de impurezas dadoras. Se han representado ambos casos expuestos anteriormente, para los cuales se ha tomado el valor de $N_D = 10^{18}$ cm^{-3} como límite entre casos no degenerado y degenerado. Las curvas se han representado para valores de $q\phi_0$ entre 0.3 y 0.7 eV y están limitadas verticalmente por los

valores experimentales de $q\phi_{Bn}$, mientras que horizontalmente se encuentran comprendidas entre el valor de N_D intrinseco del GaN y el valor de la muestra Si1000.

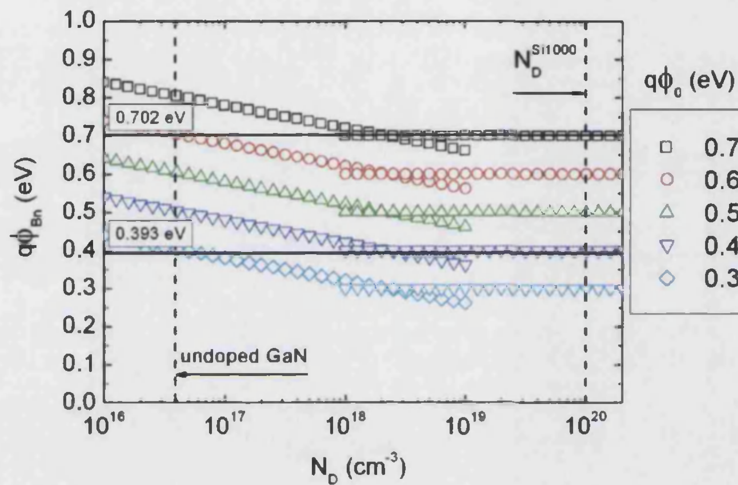

Figure 7.26: Barrera Schottky $q\phi_{Bn}$ en función de la concentración de impurezas dadoras N_D.

Tomando todas las consideraciones oportunas y teniendo el cuenta la incertidumbre tan elevada en estas medidas, se estima que el dopado de la serie de muestras con nanohilos de GaN dopados con Si está comprendido entre 10^{16} y 10^{20} cm^{-3}.

Bibliography

[1] I. Vurgaftman and J. R. Meyer. Band parameters for nitrogen-containing semiconductors. *Journal of Applied Physics* **94**(6), 3675–3696 (2003)

[2] N. Zheludev. The life and times of the LED-a 100 year history-. *Nature Photonics* **1**, 189 -192 (2007)

[3] URL `http://www.fhi-berlin.mpg.de`

[4] P. Waltereit, O. Brandt, A. Trampert, H. T. Grahn, J. Menniger, M. Ramsteiner, M. Reiche, and K. H. Ploog. Nitride semiconductors free of electrostatic fields for efficient white light-emitting diodes. *Nature* **406**, 865–868 (2000)

[5] O. Ambacher, J. Smart, J. R. Shealy, N. G. Weimann, K. Chu, M. Murphy, W. J. Schaff, L. F. Eastman, R. Dimitrov, L. Wittmer, M. Stutzmann, W. Rieger, and J. Hilsenbeck. Two-dimensional electron gases induced by spontaneous and piezoelectric polarization charges in N- and Ga-face AlGaN/GaN heterostructures. *Journal of Applied Physics* **85**(6), 3222–3233 (1999)

[6] F. Bernardini, V. Fiorentini, and D. Vanderbilt. Spontaneous polarization and piezoelectric constants of III-V nitrides. *Phys. Rev. B* **56**(16), R10024–R10027 (1997)

[7] A. Dal Corso, M. Posternak, R. Resta, and A. Baldereschi. Ab initio study of piezoelectricity and spontaneous polarization in ZnO. *Phys. Rev. B* **50**(15), 10715–10721 (1994)

[8] J. G. D. O'Clock and M. T. Duffy. Acoustic surface wave properties of epitaxially grown aluminum nitride and gallium nitride on sapphire. *Applied Physics Letters* **23**(2), 55–56 (1973)

[9] A. D. Bykhovski, B. L. Gelmont, and M. S. Shur. Elastic strain relaxation and piezoeffect in GaN-AlN, GaN-AlGaN and GaN-InGaN superlattices. *Journal of Applied Physics* **81**(9), 6332–6338 (1997)

[10] M. A. Littlejohn, J. R. Hauser, and T. H. Glisson. Monte carlo calculation of the velocity-field relationship for gallium nitride. *Applied Physics Letters* **26**(11), 625–627 (1975)

[11] N. M. K. Tsubouchi. *IEEE Trans. Sonics Ultrason.* **32**, 634 (1985)

[12] A. Polian, M. Grimsditch, and I. Grzegory. Elastic constants of gallium nitride. *Journal of Applied Physics* **79**(6), 3343–3344 (1996)

[13] A. F. Wright. Elastic properties of zinc-blende and wurtzite AlN, GaN, and InN. *Journal of Applied Physics* **82**(6), 2833–2839 (1997)

[14] S. L. Chuang and C. S. Chang. $\mathbf{k} \cdot \mathbf{p}$ method for strained wurtzite semiconductors. *Phys. Rev. B* **54**(4), 2491–2504 (1996)

[15] J. J. Sakurai. *Modern quantum mechanics* (Addison-wesley Publishing Company, Inc., 1985)

[16] J. A. B. Marcilla. *Efecto de las deformaciones en las propiedades estructurales, electrónicas y ópticas de puntos cuánticos auto-ensamblados de GaN/AlN*. Doctoral Thesis, University of Valencia (2011)

[17] P. P. Paskov, T. Paskova, P. O. Holtz, and B. Monemar. Polarized photoluminescence study of free and bound excitons in free-standing GaN. *Phys. Rev. B* **70**(3), 035210 (2004)

[18] M. Suzuki and T. Uenoyama. Strain effect on electronic and optical properties of GaN/AlGaN quantum-well lasers. *Journal of Applied Physics* **80**(12), 6868–6874 (1996)

[19] H. Callen, E. Callen, and Z. Kalva. Crystal symmetry and macroscopic laws. II. *American Journal of Physics* **38**(11), 1278–1284 (1970)

[20] J. M. Zhang, T. Ruf, M. Cardona, O. Ambacher, M. Stutzmann, J.-M. Wagner, and F. Bechstedt. Raman spectra of isotopic GaN. *Phys. Rev. B* **56**(22), 14399–14406 (1997)

[21] V. Y. Davydov, Y. E. Kitaev, I. N. Goncharuk, A. N. Smirnov, J. Graul, O. Semchinova, D. Uffmann, M. B. Smirnov, A. P. Mirgorodsky, and R. A.

Evarestov. Phonon dispersion and raman scattering in hexagonal GaN and AlN. *Phys. Rev. B* **58**(19), 12899–12907 (1998)

[22] A. Cros, N. Garro, A. Cantarero, J. Coraux, H. Renevier, and B. Daudin. Raman scattering as a tool for the evaluation of strain in GaN/AlN quantum dots: The effect of capping. *Phys. Rev. B* **76**(16), 165403 (2007)

[23] R. J. Briggs and A. K. Ramdas. Piezospectroscopic study of the raman spectrum of cadmium sulfide. *Phys. Rev. B* **13**(12), 5518–5529 (1976)

[24] V. Darakchieva, T. Paskova, M. Schubert, H. Arwin, P. P. Paskov, B. Monemar, D. Hommel, M. Heuken, J. Off, F. Scholz, B. A. Haskell, P. T. Fini, J. S. Speck, and S. Nakamura. Anisotropic strain and phonon deformation potentials in GaN. *Phys. Rev. B* **75**(19), 195217 (2007)

[25] F. Demangeot, J. Frandon, P. Baules, F. Natali, F. Semond, and J. Massies. Phonon deformation potentials in hexagonal GaN. *Phys. Rev. B* **69**(15), 155215 (2004)

[26] V. Y. Davydov, N. S. Averkiev, I. N. Goncharuk, D. K. Nelson, I. P. Nikitina, A. S. Polkovnikov, A. N. Smirnov, M. A. Jacobson, and O. K. Semchinova. Raman and photoluminescence studies of biaxial strain in GaN epitaxial layers grown on 6H-SiC. *Journal of Applied Physics* **82**(10), 5097–5102 (1997)

[27] P. Y. Yu and M. Cardona. *Fundamentals of Semiconductors - Physics and Materials Properties* (Springer - Verlag, 2001)

[28] H. Harima. Properties of GaN and related compounds studied by means of Raman scattering. *Journal of Physics: Condensed Matter* **14**(38), R967 (2002)

[29] H. S. H. Harima and S. Nakashima. Raman microprobe measurement of under damper LO-phonon-plasmon coupled mode in n-type GaN. *Material Science Forum* **264-268**, 1363–1366 (1998)

[30] P. Perlin, J. Camassel, W. Knap, T. Taliercio, J. C. Chervin, T. Suski, I. Grzegory, and S. Porowski. Investigation of longitudinal-optical phonon-plasmon coupled modes in highly conducting bulk GaN. *Applied Physics Letters* **67**(17), 2524–2526 (1995)

[31] T. Kozawa, T. Kachi, H. Kano, Y. Taga, M. Hashimoto, N. Koide, and K. Manabe. Raman scattering from LO phonon-plasmon coupled modes in gallium nitride. *Journal of Applied Physics* **75**(2), 1098–1101 (1994)

[32] F. Widmann, J. Simon, B. Daudin, G. Feuillet, J. L. Rouvière, N. T. Pelekanos, and G. Fishman. Blue-light emission from GaN self-assembled quantum dots due to giant piezoelectric effect. *Phys. Rev. B* **58**(24), R15989–R15992 (1998)

[33] D. A. B. Miller, D. S. Chemla, T. C. Damen, A. C. Gossard, W. Wiegmann, T. H. Wood, and C. A. Burrus. Band-edge electroabsorption in quantum well structures: The quantum-confined stark effect. *Phys. Rev. Lett.* **53**(22), 2173–2176 (1984)

[34] M. D. Craven, P. Waltereit, J. S. Speck, and S. P. DenBaars. Well-width dependence of photoluminescence emission from *a*-plane GaN/AlGaN multiple quantum wells. *Applied Physics Letters* **84**(4), 496–498 (2004)

[35] R. Langer, J. Simon, V. Ortiz, N. T. Pelekanos, A. Barski, R. André, and M. Godlewski. Giant electric fields in unstrained GaN single quantum wells. *Applied Physics Letters* **74**(25), 3827–3829 (1999)

[36] M. E. Lin, Z. Ma, F. Y. Huang, Z. F. Fan, L. H. Allen, and H. Morkoç. Low resistance ohmic contacts on wide band-gap GaN. *Applied Physics Letters* **64**(8), 1003–1005 (1994)

[37] K. K. N. S. M. Sze. *Physics of Semiconductor Devices, 3rd Edition* (WILEY-INTERSCIENCE, 2007)

[38] W. Spicer, P. Chye, C. Garner, I. Lindau, and P. Pianetta. The surface electronic structure of 3-5 compounds and the mechanism of fermi level pinning by oxygen (passivation) and metals (schottky barriers). *Surface Science* **86**, 763 – 788. Proceedings of the International Conference on Solid Films and Surfaces Tokyo, Japan, 5-8 July 1978 (1979)

[39] W. E. Spicer, I. Lindau, P. Skeath, C. Y. Su, and P. Chye. Unified mechanism for schottky-barrier formation and III-V oxide interface states. *Phys. Rev. Lett.* **44**(6), 420–423 (1980)

[40] A. Y. Cho. Film deposition by molecular-beam techniques. *Journal of Vacuum Science and Technology* **8**(5), S31–S38 (1971)

[41] A. Y. Cho and J. R. Arthur. Molecular beam epitaxy. *Prog. in Solid State Chemistry* **10**, 157–192 (1975)

[42] URL `http://commons.wikimedia.org/`

[43] Y. Horio, Y. Hashimoto, and A. Ichimiya. A new type of rheed apparatus equipped with an energy filter. *Applied Surface Science* **100-101**, 292 – 296 (1996)

[44] R. Songmuang, O. Landré, and B. Daudin. From nucleation to growth of catalyst-free GaN nanowires on thin AlN buffer layer. *Applied Physics Letters* **91**(25), 251902 (pages 3) (2007)

[45] K. Kanaya and S. Okayama. Penetration and energy-loss theory of electrons in solid targets. *Journal of Physics D: Applied Physics* **5**(1), 43 (1972)

[46] N. Metropolis and S. Ulam. The monte carlo method. *Journal of the American Statistical Association* **44**(247), 335–341 (1949)

[47] T. E. Everhart and R. F. M. Thornley. Wide-band detector for micro-microampere low-energy electron currents. *Journal of Scientific Instruments* **37**(7), 246 (1960)

[48] URL `http://www.zeiss.com/`

[49] M. Fox. *Optical Properties of Solids* (Oxford University Press, USA, May 2001)

[50] L. Pavesi and M. Guzzi. Photoluminescence of $Al_xGa_{1-x}As$ alloys. *Journal of Applied Physics* **75**(10), 4779–4842 (1994)

[51] W. van Roosbroeck and W. Shockley. Photon-radiative recombination of electrons and holes in germanium. *Phys. Rev.* **94**(6), 1558–1560 (1954)

[52] P. P. Paskov, B. Monemar, A. Toropov, J. P. Bergman, and A. Usui. Two-electron transition spectroscopy of shallow donors in bulk GaN. *physica status solidi (c)* **4**(7), 2601–2604 (2007)

[53] B. Gil, P. Bigenwald, M. Leroux, P. P. Paskov, and B. Monemar. Internal structure of the neutral donor-bound exciton complex in cubic zinc-blende and wurtzite semiconductors. *Phys. Rev. B* **75**(8), 085204 (2007)

[54] B. J. Skromme, J. Jayapalan, R. P. Vaudo, and V. M. Phanse. Low-temperature luminescence of exciton and defect states in heteroepitaxial GaN grown by hydride vapor phase epitaxy. *Applied Physics Letters* **74**(16), 2358–2360 (1999)

[55] G. Martínez-Criado, C. R. Miskys, A. Cros, O. Ambacher, A. Cantarero, and M. Stutzmann. Photoluminescence study of excitons in homoepitaxial GaN. *Journal of Applied Physics* **90**(11), 5627–5631 (2001)

[56] B. Monemar. Fundamental energy gap of GaN from photoluminescence excitation spectra. *Phys. Rev. B* **10**(2), 676–681 (1974)

[57] D. Gogova, H. Larsson, R. Yakimova, Z. Zolnai, I. Ivanov, and B. Monemar. Fast growth of high quality GaN. *physica status solidi (a)* **200**, 13–17 (2003)

[58] B. Monemar, H. Larsson, C. Hemmingsson, I. Ivanov, and D. Gogova. Growth of thick GaN layers with hydride vapour phase epitaxy. *Journal of Crystal Growth* **281**(1), 17 – 31 (2005)

[59] R. Pässler. Semi-empirical descriptions of temperature dependences of band gaps in semiconductors. *Physica Status Solidi (b)* **236**, 710–728 (2003)

[60] R. Dingle, D. D. Sell, S. E. Stokowski, and M. Ilegems. Absorption, reflectance, and luminescence of GaN epitaxial layers. *Phys. Rev. B* **4**(4), 1211–1218 (1971)

[61] K. Kornitzer, T. Ebner, K. Thonke, R. Sauer, C. Kirchner, V. Schwegler, M. Kamp, M. Leszczynski, I. Grzegory, and S. Porowski. Photoluminescence and reflectance spectroscopy of excitonic transitions in high-quality homoepitaxial GaN films. *Phys. Rev. B* **60**(3), 1471–1473 (1999)

[62] C. V. Raman and K. S. Krishnan. A new type of secondary radiation. *Nature* **121**, 501–502 (1928)

[63] R. Loudon. The Raman effect in crystals. *Advances in Physics* **13**, 423–482 (1964)

[64] S. P. S. Porto. *Light scattering spectra of solids* (Springer Verlag, New York 1969)

[65] T. Livneh, J. Zhang, G. Cheng, and M. Moskovits. Polarized raman scattering from single *gan* nanowires. *Phys. Rev. B* **74**(3), 035320 (2006)

[66] G. Binnig, H. Rohrer, C. Gerber, and E. Weibel. Tunneling through a controllable vacuum gap. *Applied Physics Letters* **40**(2), 178–180 (1982)

[67] G. Binnig, C. F. Quate, and C. Gerber. Atomic force microscope. *Phys. Rev. Lett.* **56**(9), 930–933 (1986)

[68] URL `http://www.nanosensors.com/`

[69] URL `http://www.nanotec.es/`

[70] H. J. Butt and M. Jaschke. Calculation of thermal noise in atomic force microscopy. *Nanotechnology* **6**(1), 1 (1995)

[71] R. A. Oliver. Advances in afm for the electrical characterization of semiconductors. *Reports on Progress in Physics* **71**(7), 076501 (2008)

[72] Y. Martin, C. C. Williams, and H. K. Wickramasinghe. Atomic force microscope force mapping and profiling on a sub 100-Å scale. *Journal of Applied Physics* **61**(10), 4723–4729 (1987)

[73] R. García and R. Pérez. Dynamic atomic force microscopy methods. *Surface Science Reports* **47**(6-8), 197 - 301 (2002)

[74] M. V. Salapaka, D. J. Chen, and J. P. Cleveland. Linearity of amplitude and phase in tapping-mode atomic force microscopy. *Phys. Rev. B* **61**(2), 1106–1115 (2000)

[75] O. Sahin and A. Atalar. Analysis of tip-sample interaction in tapping-mode atomic force microscope using an electrical circuit simulator. *Applied Physics Letters* **78**(19), 2973–2975 (2001)

[76] F. A. Ponce and D. P. Bour. Nitride-based semiconductors for blue and green light-emitting devices. *Nature* **386**(6623), 351–359 (1997)

[77] S.-H. Park and S.-L. Chuang. Crystal-orientation effects on the piezoelectric field and electronic properties of strained wurtzite semiconductors. *Phys. Rev. B* **59**(7), 4725–4737 (1999)

[78] S. Founta. *Croissance d'hétérostructures GaN/AlN à champ électrique interne réduit*. Doctoral Thesis, Université Joseph Fourier, Grenoble, France (2007)

[79] S. Founta, C. Bougerol, H. Mariette, B. Daudin, and P. Vennéguès. Anisotropic morphology of nonpolar a-plane GaN quantum dots and quantum wells. *Journal of Applied Physics* **102**(7), 074304 (pages 6) (2007)

[80] R. Mata, A. Cros, J. A. Budagosky, A. Molina-Sánchez, N. Garro, A. García-Cristóbal, J. Renard, S. Founta, B. Gayral, E. Bellet-Amalric, C. Bougerol, and B. Daudin. Reversed polarized emission in highly strained a-plane GaN/AlN multiple quantum wells. *Phys. Rev. B* **82**(12), 125405 (2010)

[81] T. J. Badcock, P. Dawson, M. J. Kappers, C. McAleese, J. L. Hollander, C. F. Johnston, D. V. S. Rao, A. M. Sanchez, and C. J. Humphreys. Optical polarization anisotropy of a-plane GaN/AlGaN multiple quantum well structures grown on r-plane sapphire substrates. *Journal of Applied Physics* **105**(12), 123112 (pages 6) (2009)

[82] C. Adelmann, E. Sarigiannidou, D. Jalabert, Y. Hori, J.-L. Rouvière, B. Daudin, S. Fanget, C. Bru-Chevallier, T. Shibata, and M. Tanaka. Growth and optical properties of GaN/AlN quantum wells. *Applied Physics Letters* **82**(23), 4154–4156 (2003)

[83] P. P. Paskov, R. Schifano, B. Monemar, T. Paskova, S. Figge, and D. Hommel. Emission properties of a-plane GaN grown by metal-organic chemical-vapor deposition. *Journal of Applied Physics* **98**(9), 093519 (pages 7) (2005)

[84] S. W. King, C. Ronning, R. F. Davis, M. C. Benjamin, and R. J. Nemanich. Dependence of (0001) GaN/AlN valence band discontinuity on growth temperature and surface reconstruction. *Journal of Applied Physics* **84**(4), 2086–2090 (1998)

[85] A. D. Andreev and E. P. O'Reilly. Theory of the electronic structure of GaN/AlN hexagonal quantum dots. *Phys. Rev. B* **62**(23), 15851–15870 (2000)

[86] A. A. Yamaguchi. Anisotropic optical matrix elements in strained GaN quantum wells on semipolar and nonpolar substrates. *Japanese Journal of Applied Physics* **46**, L789–L791 (2007)

[87] M. H. Meynadier, J. A. Brum, C. Delalande, M. Voos, F. Alexandre, and J. L. Liévin. Optical studies of impurity trapping at the GaAlAs/GaAs interface in quantum well structures. *Journal of Applied Physics* **58**(11), 4307–4312 (1985)

[88] S. Founta, F. Rol, E. Bellet-Amalric, J. Bleuse, B. Daudin, B. Gayral, H. Mariette, and C. Moisson. Optical properties of GaN quantum dots grown on nonpolar (11-20) SiC by molecular-beam epitaxy. *Applied Physics Letters* **86**(17), 171901 (pages 3) (2005)

[89] S. Founta, J. Coraux, D. Jalabert, C. Bougerol, F. Rol, H. Mariette, H. Renevier, B. Daudin, R. A. Oliver, C. J. Humphreys, T. C. Q. Noakes, and P. Bailey. Anisotropic strain relaxation in a-plane GaN quantum dots. *Journal of Applied Physics* **101**(6), 063541 (pages 7) (2007)

[90] J. E. Northrup and J. Neugebauer. Theory of GaN $(10\bar{1}0)$ and $(11\bar{2}0)$ surfaces. *Phys. Rev. B* **53**(16), R10477–R10480 (1996)

[91] J. Simon, N. T. Pelekanos, C. Adelmann, E. Martinez-Guerrero, R. André, B. Daudin, L. S. Dang, and H. Mariette. Direct comparison of recombination dynamics in cubic and hexagonal GaN/AlN quantum dots. *Phys. Rev. B* **68**(3), 035312 (2003)

[92] T. Schmidt, K. Lischka, and W. Zulehner. Excitation-power dependence of the near-band-edge photoluminescence of semiconductors. *Phys. Rev. B* **45**(16), 8989–8994 (1992)

[93] D. Bimberg, M. Sondergeld, and E. Grobe. Thermal dissociation of excitons bounds to neutral acceptors in High-Purity GaAs. *Phys. Rev. B* **4**(10), 3451–3455 (1971)

[94] J. M. L. Montolio. *Estructura electrónica y propiedades ópticas de puntos cuánticos auto-organizados*. Doctoral Thesis, Universidad de Valencia (2006)

[95] E. Calleja, M. A. Sánchez-García, F. J. Sánchez, F. Calle, F. B. Naranjo, E. Muñoz, U. Jahn, and K. Ploog. Luminescence properties and defects in GaN nanocolumns grown by molecular beam epitaxy. *Phys. Rev. B* **62**(24), 16826–16834 (2000)

[96] A. Kikuchi, M. Kawai, M. Tada, and K. Kishino. InGaN/GaN Multiple Quantum Disk Nanocolumn Light-Emitting Diodes Grown on (111) Si Substrate. *Japanese Journal of Applied Physics* **43**(12A), L1524–L1526 (2004)

[97] C. Bougerol, R. Songmuang, D. Camacho, Y. M. Niquet, R. Mata, A. Cros, and B. Daudin. The structural properties of GaN insertions in GaN/AlN nanocolumn heterostructures. *Nanotechnology* **20**(29), 295706 (2009)

[98] K. Hestroffer, R. Mata, D. Camacho, C. Leclere, G. Tourbot, Y. M. Niquet, A. Cros, C. Bougerol, H. Renevier, and B. Daudin. The structural properties of GaN/AlN core/shell nanocolumn heterostructures. *Nanotechnology* **21**(41), 415702 (2010)

[99] H. Sekiguchi, K. Kishino, and A. Kikuchi. GaN/AlGaN nanocolumn ultraviolet light-emitting diodes grown on n-(111) Si by RF-plasma-assisted molecular beam epitaxy. *Electronics Letters* **44**(2), 151–152 (2008)

[100] R. S. Wagner and W. C. Ellis. Vapor-liquid-solid mechanism of single crystal growth. *Applied Physics Letters* **4**(5), 89–90 (1964)

[101] S.-K. Lee, H.-J. Choi, P. Pauzauskie, P. Yang, N.-K. Cho, H.-D. Park, E.-K. Suh, K.-Y. Lim, and H.-J. Lee. Gallium nitride nanowires with a metal initiated metal-organic chemical vapor deposition (MOCVD) approach [phys. stat. sol. (b) 241, 2775 (2004)]. *phys. stat. sol. (b)* **242**(3), 763–763 (2005)

[102] M. Sánchez-García, E. Calleja, E. Monroy, F. Sanchez, F. Calle, E. Muñoz, and R. Beresford. The effect of the III/V ratio and substrate temperature on the morphology and properties of GaN- and AlN-layers grown by molecular beam epitaxy on Si(1 1 1). *Journal of Crystal Growth* **183**(1-2), 23 – 30 (1998)

[103] M. Yoshizawa, A. Kikuchi, N. Fujita, K. Kushi, H. Sasamoto, and K. Kishino. Self-organization of $GaN/Al_{0.18}Ga_{0.82}N$ multi-layer nanocolumns on (0 0 0 1) Al_2O_3 by RF molecular beam epitaxy for fabricating GaN quantum disks. *Journal of Crystal Growth* **189-190**, 138 – 141 (1998)

[104] E. Calleja, J. Ristic, S. Fernández-Garrido, L. Cerutti, M. A. Sánchez-García, J. Grandal, A. Trampert, U. Jahn, G. Sanchez, A. Griol, and B. Sanchez. Growth, morphology, and structural properties of group-III-nitride nanocolumns and nanodisks. *phys. stat. sol. (b)* **244**(8), 2816–2837 (2007)

[105] O. Landré, C. Bougerol, H. Renevier, and B. Daudin. Nucleation mechanism of GaN nanowires grown on (111) Si by molecular beam epitaxy. *Nanotechnology* **20**(41), 415602 (2009)

[106] V. Consonni, M. Hanke, M. Knelangen, L. Geelhaar, A. Trampert, and H. Riechert. Nucleation mechanisms of self-induced GaN nanowires grown on an amorphous interlayer. *Phys. Rev. B* **83**(3), 035310 (2011)

[107] V. Consonni, M. Knelangen, L. Geelhaar, A. Trampert, and H. Riechert. Nucleation mechanisms of epitaxial GaN nanowires: Origin of their self-induced formation and initial radius. *Phys. Rev. B* **81**(8), 085310 (2010)

[108] T. Suzuki and Y. Hirabayashi. First observation of the Si(111)-$7 \times 7 \leftrightarrow 1 \times 1$ phase transition by the optical second harmonic generation. *Japanese Journal of Applied Physics* **32**(Part 2, No. 4B), L610–L613 (1993)

[109] C. W. Hu, H. Hibino, T. Ogino, and I. S. T. Tsong. Hysteresis in the $(1 \times 1) - (7 \times 7)$ first-order phase transition on the Si(111) surface. *Surface Science* **487**(1-3), 191 – 200 (2001)

[110] C. Chèze, L. Geelhaar, A. Trampert, and H. Riechert. In situ investigation of self-induced gan nanowire nucleation on Si. *Applied Physics Letters* **97**(4), 043101 (pages 3) (2010)

[111] R. Calarco, R. J. Meijers, R. K. Debnath, T. Stoica, E. Sutter, and H. Lüth. Nucleation and Growth of GaN Nanowires on Si(111) Performed by Molecular Beam Epitaxy. *Nano Letters* **7**(8), 2248–2251 (2007)

[112] S. Fernández-Garrido, J. Grandal, E. Calleja, M. A. Sánchez-García, and D. López-Romero. A growth diagram for plasma-assisted molecular beam epitaxy of GaN nanocolumns on Si(111). *Journal of Applied Physics* **106**(12), 126102 (pages 3) (2009)

[113] V. Consonni, M. Knelangen, A. Trampert, L. Geelhaar, and H. Riechert. Nucleation and coalescence effects on the density of self-induced GaN nanowires grown by molecular beam epitaxy. *Applied Physics Letters* **98**(7), 071913 (pages 3) (2011)

[114] S. D. Carnevale, J. Yang, P. J. Phillips, M. J. Mills, and R. C. Myers. Three-dimensional GaN/AlN nanowire heterostructures by separating nucleation and growth processes. *Nano Letters* **11**(2), 866–871 (2011)

[115] N. Grandjean, J. Massies, F. Semond, S. Y. Karpov, and R. A. Talalaev. GaN evaporation in molecular-beam epitaxy environment. *Applied Physics Letters* **74**(13), 1854–1856 (1999)

[116] N. Gogneau, D. Jalabert, E. Monroy, T. Shibata, M. Tanaka, and B. Daudin. Structure of GaN quantum dots grown under "modified stranski-krastanow" conditions on AlN. *Journal of Applied Physics* **94**(4), 2254–2261 (2003)

[117] H. Sekiguchi, T. Nakazato, A. Kikuchi, and K. Kishino. Structural and optical properties of GaN nanocolumns grown on (0 0 0 1) sapphire substrates by rf-plasma-assisted molecular-beam epitaxy. *Journal of Crystal Growth* **300**(1), 259 – 262. First International Symposium on Growth of Nitrides - ISGN-1 (2007)

[118] M. Niebelschutz, V. Cimalla, O. Ambacher, T. Machleidt, K.-H. Franke, J. Ristic, J. Grandal, M. A. Sánchez-García, and E. Calleja. Space charged region in GaN and InN nanocolumns investigated by atomic force microscopy. *physica status solidi (c)* **5**(6), 1609–1611 (2008)

[119] F. Furtmayr, M. Vielemeyer, M. Stutzmann, J. Arbiol, S. Estradé, F. Peirò, J. R. Morante, and M. Eickhoff. Nucleation and growth of GaN nanorods on

si (111) surfaces by plasma-assisted molecular beam epitaxy - the influence of Si- and Mg-doping. *Journal of Applied Physics* **104**(3), 034309 (pages 7) (2008)

[120] L. Cerutti, J. Ristić, S. Fernández-Garrido, E. Calleja, A. Trampert, K. H. Ploog, S. Lazic, and J. M. Calleja. Wurtzite GaN nanocolumns grown on Si(001) by molecular beam epitaxy. *Applied Physics Letters* **88**(21), 213114 (pages 3) (2006)

[121] G. D. Mahan, R. Gupta, Q. Xiong, C. K. Adu, and P. C. Eklund. Optical phonons in polar semiconductor nanowires. *Phys. Rev. B* **68**(7), 073402 (2003)

[122] D. Spirkoska, G. Abstreiter, and A. F. i Morral. Size and environment dependence of surface phonon modes of gallium arsenide nanowires as measured by raman spectroscopy. *Nanotechnology* **19**(43), 435704 (2008)

[123] A. Sarua, J. Monecke, G. Irmer, I. M. Tiginyanu, G. GÃ¤rtner, and H. L. Hartnagel. Fröhlich modes in porous III-V semiconductors. *Journal of Physics: Condensed Matter* **13**(31), 6687 (2001)

[124] P.-M. Chassaing, F. Demangeot, V. Paillard, A. Zwick, N. Combe, C. Pagès, M. L. Kahn, A. Maisonnat, and B. Chaudret. Surface optical phonons as a probe of organic ligands on ZnO nanoparticles: An investigation using a dielectric continuum model and raman spectrometry. *Phys. Rev. B* **77**(15), 153306 (2008)

[125] S. Bhattacharya, A. Datta, S. Dhara, and D. Chakravorty. Surface optical raman modes in GaN nanoribbons. *Journal of Raman Spectroscopy* (2010)

[126] N. Begum, A. S. Bhatti, F. Jabeen, S. Rubini, and F. Martelli. Lineshape analysis of raman scattering from LO and SO phonons in iii-v nanowires. *Journal of Applied Physics* **106**(11), 114317 (pages 5) (2009)

[127] I. M. Tiginyanu, A. Sarua, G. Irmer, J. Monecke, S. M. Hubbard, D. Pavlidis, and V. Valiaev. Fröhlich modes in GaN columnar nanostructures. *Phys. Rev. B* **64**(23), 233317 (2001)

[128] K. Adu, Q. Xiong, H. Gutierrez, G. Chen, and P. Eklund. Raman scattering as a probe of phonon confinement and surface optical modes in semiconducting nanowires. *Applied Physics A: Materials Science & Processing* **85**, 287–297. 10.1007/s00339-006-3716-8 (2006)

[129] C.-L. Hsiao, L.-W. Tu, T.-W. Chi, M. Chen, T.-F. Young, C.-T. Chia, and Y.-M. Chang. Micro-raman spectroscopy of a single freestanding GaN nanorod grown by molecular beam epitaxy. *Applied Physics Letters* **90**(4), 043102 (pages 3) (2007)

[130] L. Zhang, J.-j. Shi, and T. L. Tansley. Polar vibration spectra of interface optical phonons and electron-interface optical phonon interactions in a wurtzite gan-aln nanowire. *Phys. Rev. B* **71**(24), 245324 (2005)

[131] O. Brandt, C. Pfüller, C. Chèze, L. Geelhaar, and H. Riechert. Sub-mev linewidth of excitonic luminescence in single GaN nanowires: Direct evidence for surface excitons. *Phys. Rev. B* **81**(4), 045302 (2010)

[132] P. Corfdir, P. Lefebvre, J. Ristić, P. Valvin, E. Calleja, A. Trampert, J.-D. Ganière, and B. Deveaud-Plédran. Time-resolved spectroscopy on GaN nanocolumns grown by plasma assisted molecular beam epitaxy on si substrates. *Journal of Applied Physics* **105**(1), 013113 (pages 8) (2009)

[133] E. Calleja, M. A. Sánchez-García, D. Basak, F. J. Sánchez, F. Calle, P. Youinou, E. Muñoz, J. J. Serrano, J. M. Blanco, C. Villar, T. Laine, J. Oila, K. Saarinen, P. Hautojärvi, C. H. Molloy, D. J. Somerford, and I. Harrison. Effect of Ga/Si interdiffusion on optical and transport properties of GaN layers grown on Si(111) by molecular-beam epitaxy. *Phys. Rev. B* **58**(3), 1550–1559 (1998)

[134] R. Liu, A. Bell, F. A. Ponce, C. Q. Chen, J. W. Yang, and M. A. Khan. Luminescence from stacking faults in gallium nitride. *Applied Physics Letters* **86**(2), 021908 (pages 3) (2005)

[135] S. Fischer, G. Steude, D. M. Hofmann, F. Kurth, F. Anders, M. Topf, B. K. Meyer, F. Bertram, M. Schmidt, J. Christen, L. Eckey, J. Holst, A. Hoffmann, B. Mensching, and B. Rauschenbach. On the nature of the 3.41 eV luminescence in hexagonal GaN. *Journal of Crystal Growth* **189-190**, 556 - 560 (1998)

[136] Y. T. Rebane, Y. G. Shreter, and M. Albrecht. Stacking Faults as Quantum Wells for Excitons in Wurtzite GaN. *physica status solidi (a)* **164**(1), 141–144 (1997)

[137] J. B. Schlager, K. A. Bertness, P. T. Blanchard, L. H. Robins, A. Roshko, and N. A. Sanford. Steady-state and time-resolved photoluminescence from

relaxed and strained GaN nanowires grown by catalyst-free molecular-beam epitaxy. *Journal of Applied Physics* **103**(12), 124309 (pages 6) (2008)

[138] L. H. Robins, K. A. Bertness, J. M. Barker, N. A. Sanford, and J. B. Schlager. Optical and structural study of GaN nanowires grown by catalyst-free molecular beam epitaxy. i. near-band-edge luminescence and strain effects. *Journal of Applied Physics* **101**(11), 113505 (pages 8) (2007)

[139] W. Bludau, A. Onton, and W. Heinke. Temperature dependence of the band gap of silicon. *Journal of Applied Physics* **45**(4), 1846 –1848 (1974)

[140] P. Dawson, O. Rubel, S. D. Baranovskii, K. Pierz, P. Thomas, and E. O. Göbel. Temperature-dependent optical properties of InAs/GaAs quantum dots: Independent carrier versus exciton relaxation. *Phys. Rev. B* **72**(23), 235301 (2005)

[141] Y. P. Varshni. Temperature dependence of the energy gap in semiconductors. *Physica* **34**(1), 149 – 154 (1967)

[142] L. Viña, S. Logothetidis, and M. Cardona. Temperature dependence of the dielectric function of germanium. *Phys. Rev. B* **30**(4), 1979–1991 (1984)

[143] N. Sarkar and S. Ghosh. Temperature dependent band gap shrinkage in GaN: Role of electron-phonon interaction. *Solid State Communications* **149**(31-32), 1288 – 1291 (2009)

[144] M. Leroux, N. Grandjean, B. Beaumont, G. Nataf, F. Semond, J. Massies, and P. Gibart. Temperature quenching of photoluminescence intensities in undoped and doped GaN. *Journal of Applied Physics* **86**(7), 3721–3728 (1999)

[145] C. X. Shan, Z. Liu, and S. K. Hark. Photoluminescence polarization in individual CdSe nanowires. *Phys. Rev. B* **74**(15), 153402 (2006)

[146] Y. J. Sun, O. Brandt, U. Jahn, T. Y. Liu, A. Trampert, S. Cronenberg, S. Dhar, and K. H. Ploog. Impact of nucleation conditions on the structural and optical properties of M-plane GaN$(1\bar{1}00)$ grown on gamma-$LiAlO_2$. *Journal of Applied Physics* **92**(10), 5714–5719 (2002)

[147] A. A. Pomarico, D. Huang, J. Dickinson, A. A. Baski, R. Cingolani, H. Morkoç, and R. Molnar. Current mapping of GaN films by conductive atomic force microscopy. *Applied Physics Letters* **82**(12), 1890–1892 (2003)

[148] K. Karch, J.-M. Wagner, and F. Bechstedt. Ab initio study of structural, dielectric, and dynamical properties of GaN. *Phys. Rev. B* **57**(12), 7043–7049 (1998)

[149] J. C. M. Garnett. *Colours in Metal Glasses and in Metallic Films* (Phil. Trans. R. Soc. Lond., A203, 385 (1904))

[150] P. Ramvall, S. Tanaka, S. Nomura, P. Riblet, and Y. Aoyagi. Observation of confinement-dependent exciton binding energy of GaN quantum dots. *Applied Physics Letters* **73**(8), 1104–1106 (1998)

[151] M. Diarra, Y.-M. Niquet, C. Delerue, and G. Allan. Ionization energy of donor and acceptor impurities in semiconductor nanowires: Importance of dielectric confinement. *Phys. Rev. B* **75**(4), 045301 (2007)

[152] F. Glas. Critical dimensions for the plastic relaxation of strained axial heterostructures in free-standing nanowires. *Phys. Rev. B* **74**(12), 121302 (2006)

[153] J. Ristić, E. Calleja, M. A. Sánchez-García, J. M. Ulloa, J. Sánchez-Páramo, J. M. Calleja, U. Jahn, A. Trampert, and K. H. Ploog. Characterization of GaN quantum discs embedded in $Al_xGa_{1-x}N$ nanocolumns grown by molecular beam epitaxy. *Phys. Rev. B* **68**(12), 125305 (2003)

[154] J. B. Schlager, N. A. Sanford, K. A. Bertness, J. M. Barker, A. Roshko, and P. T. Blanchard. Polarization-resolved photoluminescence study of individual GaN nanowires grown by catalyst-free molecular beam epitaxy. *Applied Physics Letters* **88**(21), 213106 (pages 3) (2006)

[155] M. Tchernycheva, C. Sartel, G. Cirlin, L. Travers, G. Patriarche, J.-C. Harmand, L. S. Dang, J. Renard, B. Gayral, L. Nevou, and F. Julien. Growth of GaN free-standing nanowires by plasma-assisted molecular beam epitaxy: structural and optical characterization. *Nanotechnology* **18**(38), 385306 (2007)

[156] J. Renard, R. Songmuang, C. Bougerol, B. Daudin, and B. Gayral. Exciton and biexciton luminescence from single GaN/AlN quantum dots in nanowires. *Nano Letters* **8**(7), 2092–2096 (2008)

[157] S. Raychaudhuri and E. T. Yu. Critical dimensions in coherently strained coaxial nanowire heterostructures. *Journal of Applied Physics* **99**(11), 114308 (pages 7) (2006)

[158] J. Ristic, E. Calleja, S. Fernández-Garrido, L. Cerutti, A. Trampert, U. Jahn, and K. H. Ploog. On the mechanisms of spontaneous growth of III-nitride nanocolumns by plasma-assisted molecular beam epitaxy. *Journal of Crystal Growth* **310**(18), 4035 – 4045 (2008)

[159] P. N. Keating. Effect of invariance requirements on the elastic strain energy of crystals with application to the diamond structure. *Phys. Rev.* **145**(2), 637–645 (1966)

[160] J. Eymery, F. Rieutord, V. Favre-Nicolin, O. Robach, Y.-M. Niquet, L. Fröberg, T. Mårtensson, and L. Samuelson. Strain and shape of epitaxial InAs/InP nanowire superlattice measured by grazing incidence X-ray techniques. *Nano Letters* **7**(9), 2596–2601 (2007)

[161] Y. M. Niquet. Effects of a shell on the electronic properties of nanowire superlattices. *Nano Letters* **7**(4), 1105–1109 (2007)

[162] C.-H. Hsieh, M.-T. Chang, Y.-J. Chien, L.-J. Chou, L.-J. Chen, and C.-D. Chen. Coaxial metal-oxide-semiconductor (MOS) $Au/Ga_2O_3/GaN$ nanowires. *Nano Letters* **8**(10), 3288–3292. PMID: 18778107 (2008)

[163] J. Ristić, E. Calleja, A. Trampert, S. Fernández-Garrido, C. Rivera, U. Jahn, and K. H. Ploog. Columnar AlGaN/GaN nanocavities with AlN/GaN bragg reflectors grown by molecular beam epitaxy on Si(111). *Phys. Rev. Lett.* **94**(14), 146102 (2005)

[164] O. Landré, V. Fellmann, P. Jaffrennou, C. Bougerol, H. Renevier, A. Cros, and B. Daudin. Molecular beam epitaxy growth and optical properties of AlN nanowires. *Applied Physics Letters* **96**(6), 061912 (pages 3) (2010)

[165] R. Songmuang, T. Ben, B. Daudin, D. GonzÃ¡lez, and E. Monroy. Identification of III-N nanowire growth kinetics via a marker technique. *Nanotechnology* **21**(29), 295605 (2010)

[166] X. H. Ji, Q. Y. Zhang, S. P. Lau, H. X. Jiang, and J. Y. Lin. Temperature-dependent photoluminescence and electron field emission properties of AlN nanotip arrays. *Applied Physics Letters* **94**(17), 173106 (pages 3) (2009)

[167] H.-M. Wu and J.-Y. Liang. Optical properties of single-crystalline wurtzite aluminum nitride nanowires. In *Nanoelectronics Conference (INEC), 2010 3rd International*, pages. 795–796 (2010)

[168] J. Yoon, A. M. Girgis, I. Shalish, L. R. Ram-Mohan, and V. Narayanamurti. Size-dependent impurity activation energy in GaN nanowires. *Applied Physics Letters* **94**(14), 142102 (pages 3) (2009)

[169] D. Camacho Mojica and Y.-M. Niquet. Stark effect in GaN/AlN nanowire heterostructures: Influence of strain relaxation and surface states. *Phys. Rev. B* **81**(19), 195313 (2010)

[170] M. Tchernycheva, C. Sartel, G. Cirlin, L. Travers, G. Patriarche, L. Largeau, O. Mauguin, J.-C. Harmand, L. S. Dang, J. Renard, B. Gayral, L. Nevou, and F. Julien. GaN/AlN free-standing nanowires grown by molecular beam epitaxy. *physica status solidi (c)* **5**(6), 1556–1558 (2008)

[171] C. Foxon, S. Novikov, J. Hall, R. Campion, D. Cherns, I. Griffiths, and S. Khongphetsak. A complementary geometric model for the growth of GaN nanocolumns prepared by plasma-assisted molecular beam epitaxy. *Journal of Crystal Growth* **311**(13), 3423 - 3427 (2009)

[172] Y. Park, S.-H. Lee, J.-E. Oh, C.-M. Park, and T.-W. Kang. Self-assembled GaN nano-rods grown directly on (111) Si substrates: Dependence on growth conditions. *Journal of Crystal Growth* **282**(3-4), 313 - 319 (2005)

[173] V. I. Belitsky, A. Cantarero, M. Cardona, C. Trallero-Giner, and S. T. Pavlov. Feynman diagrams and fano interference in light scattering from doped semiconductors. *Journal of Physics: Condensed Matter* **9**(27), 5965 (1997)

[174] K. Arya, M. A. Kanehisa, M. Jouanne, K. P. Jain, and M. Balkanski. Pseudopotential calculation of the discrete-continuum interference in p-Si Raman spectra. *Journal of Physics C: Solid State Physics* **12**(18), 3843 (1979)

[175] V. Magidson and R. Beserman. Fano-type interference in the Raman spectrum of photoexcited Si. *Phys. Rev. B* **66**(19), 195206 (2002)

[176] J. Sánchez-Páramo, J. M. Calleja, M. A. Sánchez-García, and E. Calleja. Optical investigation of strain in Si-doped GaN films. *Applied Physics Letters* **78**(26), 4124–4126 (2001)

[177] F. Furtmayr, M. Vielemeyer, M. Stutzmann, A. Laufer, B. K. Meyer, and M. Eickhoff. Optical properties of Si- and Mg-doped gallium nitride nanowires grown by plasma-assisted molecular beam epitaxy. *Journal of Applied Physics* **104**(7), 074309 (pages 7) (2008)

[178] E. F. Schubert, I. D. Goepfert, W. Grieshaber, and J. M. Redwing. Optical properties of Si-doped GaN. *Applied Physics Letters* **71**(7), 921–923 (1997)

[179] B. Pérez-García, J. Zúñiga-Pérez, V. Muñoz-Sanjosé, J. Colchero, and E. Palacios-Lidón. Formation and Rupture of Schottky Nanocontacts on ZnO Nanocolumns. *Nano Letters* **7**(6), 1505–1511. PMID: 17511510 (2007)

[180] K. Suzue, S. N. Mohammad, Z. F. Fan, W. Kim, O. Aktas, A. E. Botchkarev, and H. Morkoç. Electrical conduction in platinum-gallium nitride schottky diodes. *Journal of Applied Physics* **80**(8), 4467–4478 (1996)

[181] W. Götz, N. M. Johnson, C. Chen, H. Liu, C. Kuo, and W. Imler. Activation energies of Si donors in GaN. *Applied Physics Letters* **68**(22), 3144–3146 (1996)

[182] H. Wang and A.-B. Chen. Calculation of shallow donor levels in GaN. *Journal of Applied Physics* **87**(11), 7859–7863 (2000)

[183] S. K. Noh, C. R. Lee, S. E. Park, I. H. Lee, I. H. Choi, S. J. Son, K. Y. Lim, and H. J. Lee. Doping characteristics of Si-doped n-GaN Epilayers grown by low-pressure metal-organic chemical-vapor deposition. *J. Korean Phys. Soc* **32**, 851–856 (1998)

[184] S. Nakamura, T. Mukai, and M. Senoh. Si- and Ge-Doped GaN Films Grown with GaN Buffer Layers. *Japanese Journal of Applied Physics* **31**(Part 1, No. 9A), 2883–2888 (1992)

[185] T. Richter, H. L. R. Meijers, R. Calarco, and M. Marso. Doping Concentration of GaN Nanowires Determined by Opto-Electrical Measurements. *Nano Letters* **8**(9), 3056–3059 (2008)

[186] M. Ilegems. Vapor epitaxy of gallium nitride. *Journal of Crystal Growth* **13-14**, 360–364. Third International Conference on Crystal Growth (1972)

Curriculum Vitae in Science

Personal data

Name:	**Rafael Mata Sanz**
Place and date of birth:	Valencia (Spain), 10th of April of 1978
Nationality:	Spanish
Personal address:	C/ Dr. Gómez Ferrer 59-6
	46910 Alfafar(Valencia) Spain
Mobile phone:	+34 699891883
E-mail:	rafael.mata@uv.es
	rafa.matasanz@gmail.com

Languages of scientific interest

	(Regular, Sufficient, Well)		
Language	Speak	Read	Write
English	Well	Well	Well
German	Well	Sufficient	Regular
Italian	Well	Well	Regular
Spanish	Mather lang.	Mather lang.	Mather lang.

Academic studies

Title:	Degree in Physics
Center:	University of Valencia
Date:	18/07/2006
Country:	Spain
Region:	Comunidad Valenciana
Mark:	Pass (1.5/4)
Title:	Curso de Aptitud Pedagógica: Física y Química
Center:	University of Valencia
Date:	02/03/2009
Country:	Spain
Region:	Comunidad Valenciana
Mark:	Pass (2.0/4)
Title:	Master in Advanced Physics: Photonic and Devices
Center:	University of Valencia
Date:	10/07/2008
Country:	Spain
Region:	Comunidad Valenciana
Mark:	Excellent (3.0/4)

Thesis, master thesis and research reports

Key:	Master of thesis in Advanced Physics
Title:	Study of the anisotropic emission of auto-assembled GaN quantum dots grown along non-polar directions
Director of thesis:	Dr. Ana Cros Stötter and Dr. Núria Garro
University:	University of Valencia
Faculty / School:	Faculty of Physics, Department of Applied Physics and Electromagnetism
Year:	2008
Mark:	Excellent (3.0/4)

Research stays abroad

Center:	University of Ulm
Place:	Ulm
Country:	GERMANY
Year:	2005
Duration:	5 months
Issue:	Design and build the circuitry of an Atomic Force Microscope.
Key:	Student contract
Center:	OSRAM-Optosemiconductors, Department of Analysis and Models
Place:	Regensburg
Country:	GERMANY
Year:	2006
Duration:	6 months
Issue:	Photoluminescence and Electroluminescence measurements of Light Emitting Diodes of Nitride semiconductors.
Key:	Practice in company
Center:	Department of Physics of the University of Florence
Place:	Florence
Country:	ITALY
Year:	2007
Duration:	4 months
Issue:	Characterization of GaN Superlattices quantum dots by means of time integrated and time resolved photoluminescence.
Key:	Marie Curie Predoctoral fellowship

Center:	University of Cambridge, Department of Material Science and Metalurgy
Place:	Cambridge
Country:	UNITED KINGDOM
Year:	2009
Duration:	3 months
Issue:	Perform Conductive AFM, Chatodoluminiscence and Kelvin Probe on GaN nanowires, GaN quantum dots and quantum wires grown along non polar direccion.
Key:	Research stay within the Ph.D. fellowship
Center:	Commissariat à l'Énergie Atomique (CEA). Institut nanosciences en cryogenie, service de physique des materiaux et microstuctures. Laboratoire de nanostructrues et physique des semiconducteurs.
Place:	Grenoble
Country:	FRANCE
Year:	2010
Duration:	3 months
Issue:	Radio Frequency Plasma Assisted Molecular Beam Epitaxy of GaN nanowires: AlN/GaN superlattices, GaN/AlN core/shell heterostructures and Si-doped nanowires.
Key:	Research stay within the Ph.D. fellowship
Center:	Department of Physics of the University of Aveiro.
Place:	Aveiro
Country:	PORTUGAL
Year:	2011
Duration:	1 week
Issue:	Characterization of Si doped GaN nanowires by means of InfraRed.
Key:	Invited

Center:	Commissariat à l'Énergie Atomique (CEA). Institut nanosciences en cryogenie, service de physique des materiaux et microstuctures. Laboratoire de nanostructrues et physique des semiconducteurs.
Place:	Grenoble
Country:	FRANCE
Year:	2011
Duration:	1 week
Issue:	Characterization of Si doped GaN nanowires by means of Time Resolved Photoluminescence.
Key:	Invited

Conference contributions

Authors:	R. Mata, N. Garro, A. García-Cristóbal, J. Budagosky, A. Cantarero, A. Cros and B. Daudin
Title:	Optical emission in GaN/AlN non-polar heterostructures
Participation:	Poster
Conference:	V National meeting of Solid State Physics of the Specializing Group of Solid State Physics GEFES
Place:	Santiago de Compostela (SPAIN)
Year:	2008
Authors:	R. Mata, N. Garro, A. García-Cristóbal, J. Budagosky, A. Cros, A. Vinattieri, M. Gurioli, E. Bellet-Amalric and B. Daudin
Title:	Anisotropic Polarization of Non-Polar GaN Quantum Dot Emission
Participation:	Oral presentation
Conference:	International Workshop of Nitrides Semiconductors 2008
Place:	Montreux (SWITZERLAND)
Year:	2008

Authors:	R. Mata, A. Cros, N. Garro, J. A. Budagosky, A. Molina, A. García-Cristóbal, J. Renard, E. Bellet-Amalric and B. Daudin
Title:	Study of the polarized emission from non polar GaN/AlN QWs and QDs superlattices
Participation:	Poster
Conference:	Prominas Training Course TC4 and Workshop: "Growth and Structural Characterization of Semiconductor Nanostructures"
Place:	Grenoble (FRANCE)
Year:	2009
Authors:	R. Mata, A. Cros, D. Camacho, Y.M. Niquet, G. Tourbot, J. Renard, B. Gayral and B. Daudin
Title:	Optical and structural characterization of GaN/AlN core-shell nanowires grown by MBE
Participation:	Invited presentation
Conference:	ICNS8
Place:	Jeju (REPUBLIC OF KOREA)
Year:	2009
Authors:	R. Mata, A. Cros, R. A. Oliver, G. Tourbot and B. Daudin
Title:	Electrical and optical study of silicon doped GaN nanowires
Participation:	Poster
Conference:	VI Reunión del Grupo Especializado de Física del Estado Sólido 2010
Place:	Zaragoza (SPAIN)
Year:	2010
Authors:	R. Mata, A. Cros, N. Garro, J. A. Budagosky, A. Molina-Sánchez, A. García-Cristóbal, J. Renard, S. Founta, B.Gayral, E. Bellet-Amalric, and B. Daudin
Title:	Reversed optical polarization in nonpolar GaN/AlN quantum wells: role of strain and confinement
Participation:	Oral presentation
Conference:	ICNS8
Place:	Jeju (REPUBLIC OF KOREA)
Year:	2009

Authors:	R. Mata, J. Budagosky, K. Hestroffer, A. Cros, A. García-Cristóbal, B. Gayral, C. Bougerol, H. Renevier and B. Daudin
Title:	Nucleation of GaN Nanowires Grown by Molecular Beam Epitaxy: The Effect of Temperature
Participation:	Oral presentation
Conference:	IWN2010
Place:	Tampa (UNITED STATES)
Year:	2010
Authors:	K.Hestroffer, R. Mata, D.Camacho, C.Leclere, G.Tourbot, Y-M.Niquet, A.Cros, C.Bougerol, H.Renevier and B.Daudin
Title:	Structural Properties of GaN/AlN Core-shell Nanowire Heterostructures
Participation:	Oral presentation
Conference:	IWN2010
Place:	Tampa (UNITED STATES)
Year:	2010
Authors:	R. Mata, J. Budagosky, K. Hestroffer, A. Cros, A. García-Cristóbal, B. Gayral, C. Bougerol, H. Renevier and B. Daudin
Title:	Length dispersion of GaN nanowires grown by molecular beam epitaxy: the effect of temperature and of nucleation memory
Participation:	Oral presentation
Conference:	5th Nanowire Growth Workshop NWG 2010
Place:	Roma (ITALY)
Year:	2010

Authors:	<u>J. Wang</u>, F. Demangeot, R. Pechou, A. Ponchet, R. Mata, A. Cros and B. Daudin
Title:	Raman scattering studies of GaN nanowires: doping and surface effects
Kind of participation:	Poster
Conference:	9th ICNS
Place of celebration:	Glasgow (ENGLAND)
Year:	2011
Authors:	R. Mata, <u>A. Cros</u>, S. Agouram, B. Gayral and B. Daudin
Title:	Surface phonon modes of MBE grown GaN nanowires: dependence on nanowire density
Kind of participation:	Poster
Conference:	9th ICNS
Place of celebration:	Glasgow (ENGLAND)
Year:	2011
Authors:	R. Mata, A. Cros, J. Budagosky, C. Bougerol, A. García-Cristóbal, B. Gayral, K. Hestroffer, H. Renevier, O. Landré and <u>B. Daudin</u>
Title:	Nucleation of GaN nanowires grown by molecular beam epitaxy: its relation to length distribution
Kind of participation:	Oral presentation
Conference:	E-MRS
Place of celebration:	Nice (FRANCE)
Year:	2011

Journal publications

Authors:	C. Bougerol, R. Songmuang, D. Camacho, Y. M. Nique, R. Mata, A. Cros and B. Daudin
Title:	Structural properties of GaN insertions in GaN/AlN nanocolumn heterostructures
Journal:	909342 - Nanotechnology
Volume:	20
Number:	295706
Year:	2009

Authors:	R. Mata, N. Garro, A. Cros, J. A. Budagosky, A. García-Cristóbal, A. Vinattieri, M. Gurioli, S. Founta, E. Bellet-Amalric and B. Daudin
Title:	Anisotropic polarization of non-polar GaN quantum dot emission
Journal:	Physica Status Solidi (c)
Volume:	1
Number:	4
Year:	2009

Authors:	K. Hestroffer, R. Mata, D. Camacho, C. Lèclere, G. Tourbot, Y. M. Niquet, A. Cros, C. Bougerol, H. Renevier and B. Daudin
Title:	The structural properties of GaN/AlN core-shell nanocolumn heterostructures
Journal:	909342 - Nanotechnology
Volume:	21
Number:	415702
Year:	2010

Authors:	R. Mata, A. Cros, J. A. Budagosky, A. Molina-Sánchez, N. Garro, A. García-Cristóbal, J. Renard, S. Founta, B. Gayral, E. Bellet-Amalric, C. Bougerol and B. Daudin
Title:	Reversed polarized emission in highly strained *a*-plane GaN/AlN multiple quantum wells
Journal:	903342 - Physical Review B
Volume:	82
Number:	125405
Year:	2010

Authors:	R. Mata, K. Hestroffer, J. Budagosky, A. Cros, C. Bougerol, H. Renevier and B. Daudin
Title:	Nucleation of GaN nanowires grown by plasma-assisted molecular beam epitaxy: the effect of temperature
Journal:	Submitted
Year:	2011
Authors:	R. Mata, A. Cros, S. Agouram, B. Gayral and B. Daudin
Title:	Surface phonon modes of MBE grown GaN nanowires: dependence on nanowire density
Journal:	Under elaboration
Year:	2011

Other merits

Intensive Course of German Ausias March school. Valencia, Spain. Period: from 01/06/2004 to 31/07/2004.

Exchange Exchange awarded with fellowship for a year in the University of Ulm (Germany) with the aim to course the last year in physics degree under the program Socrates-Erasmus. Period: from 01/10/2004 to 31/07/2005.

Teaching experience Course given entitle "Manejo básico del microscopio de fuerzas atómicas y software libre de image nanotec para el análisis de superficies". Servei de formació permanent. University of Valencia. Period: from 23/02/2009 to 06/03/2009.

Attendance Advanced school on hybrid nanostructured materials for photovoltaic applications, Valencia (SPAIN) in March of 2009.

Teaching experience Teacher of laboratory group of the first course in biology degree in the University of Valencia. Total hours teaching 30 in 2010.

International school "Prominas" "Growth and Structural Characterization of Semiconductor Nanostructures", in the framework of the Marie Curie action of the VI European Project, in Grenoble at the CEA Research Center, from 1st to 14th September 2009.

Attendance Course entitled "High resolution X-ray diffraction on monocrystalline thin layers" on 1st, 2nd, 4th, 5th and 8th of March of 2010 in Commissariat a l'Energie Atomique, Institut Nanosciences et Cryogenie, Service de Physique des Materiaux et Microstructures, Laboratoire de Nanostructures et Physique des Semiconducteurs. Grenoble, France.

Attendance Workshop Nano2csf II, nanotechnology and nanomaterials for solar photovoltaic conversion, Valencia (SPAIN) in November of 2010.

Teaching experience Course given entitle "Manejo básico del microscopio de fuerzas atómicas y software libre de image nanotec para el análisis de superficies" 2nd Edition. Servei de formació permanent. University of Valencia. Period: from 4/04/2011 to 1/04/2011.

Teaching experience Teacher of laboratory group of the first course in biology biotechnology degree in the University of Valencia. Total hours teaching 30 in 2011.

References

Dr. Ana Cros
Institute of Material Science
University of Valencia
Department of Applied Physics and Magnetism
Polígono La Coma
46980 Valencia
Spain
Tel: +34 963543602
E-mail: Ana.Cros@uv.es

Dr. Bruno Daudin
CEA-Grenoble,INAC SP2M/NPSC
17 rue des martyrs
38054 Grenoble Cedex 9
France
Tel: +33 (0)4 38 78 37 50
E-mail: bruno.daudin@cea.fr

Dr. Rachel Oliver
Royal Society University Research Fellow
Department of Materials Science and Metallurgy
University of Cambridge
Pembroke Street Cambridge CB2 3QZ
United Kingdom
Tel: +44 (0)1223 334469
E-mail: rao28@hermes.cam.ac.uk

Dr. Anna Vinattieri
Dipartimento di Fisica
University of Florence
Via Sansone 1 50019
Sesto Fiorentino
Italy
Tel: +39 (0)55 4572049
E-mail: vinattieri@fi.infn.it

Aquí me encuentro buceando con una tortuga en el Mar Rojo, en una de las tres veces que durante los años de doctorado he recorrido en crucero Los Canales de Suez y Aqaba para disfrutar de sus maravillosos fondos marinos.

UNIVERSITAT DE VALÈNCIA **FACULTAT DE FISICA**

Reunit el Tribunal que susbscriu, en el dia de la data, acorda d atorgar, aquesta Tesi Doctoral d'En/Na/N' ...Rafael....Mata...Sanz..................
la qualificació de...excel·lent cum laude.....................
València a ...23.... d.....setembre.......de 20..11...

El President

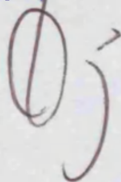

El Secretari.